

CHAPTER 6

SURFACE DEPOSITION OF POLLUTANT MATERIAL

6.1 Introduction

A significant process that influences the concentration predictions of the airshed model is the interaction of the pollutants with the ground. Roberts (1975), for example, estimated that in the Los Angeles Basin almost half of the sulfur oxides are removed at the ground before air parcels leave the airshed. The objective of this section is to develop an upper limit expression for the rate at which gaseous material is removed at the surface. In most models the deposition rate is described by a single quantity, the pollutant deposition velocity v_g . The flux of material, F , directed towards the lower boundary surface is defined by

$$F = v_g c(z_r) \quad (6.1)$$

where $c(z_r)$ is the concentration of the material at some reference height z_r . A basic problem with (6.1) is that it does not explicitly represent the fact that dry deposition involves a complex linkage between turbulent diffusion in the surface boundary layer, molecular scale motion at the air-ground interface and chemical interaction of the material with the surface. Various physical processes are involved including gravitational settling, turbulent and molecular diffusion, inertial impaction, phoretic and electrical effects. In

addition to these removal phenomena, deposited material can be desorbed or mechanically resuspended. Reviews of the general subject of dry deposition are included in the works of Chamberlain (1966), Hill and Chamberlain (1974), Kneen and Strauss (1969), Liu and Ilori (1974), Sehmel and Hodgson (1974), Slinn (1974), Davidson (1977), National Academy of Sciences (1978), McMahon and Denison (1979), and Sehmel (1980).

As a first step towards improving upon the model (6.1) it is necessary to recognize that there are two basic components associated with pollutant removal: one is the transport of material to the ground and the other is the interaction of the pollutants with the surface. Unless extensive field experiments have been made in the airshed, it is not possible to accurately characterize the second component of the dry deposition process. An alternative approach, and the focus of this chapter, is to develop an upper limit for v_g in terms of the transport processes and the concentration at a reference point above the surface. (Typically the height of the lowest computational grid point in the airshed model.) A secondary goal is to identify the significant meteorological variables and surface properties needed to either correlate different measurements of v_g or to modify the results for different experimental conditions.

6.2 Deposition in the Constant Flux Layer

Consider the idealized representation of the airshed surface shown in Figure 6.1. Within the layer $0 \leq z \leq z_r$ the deposition is assumed to be a one-dimensional, steady-state, constant flux process occurring

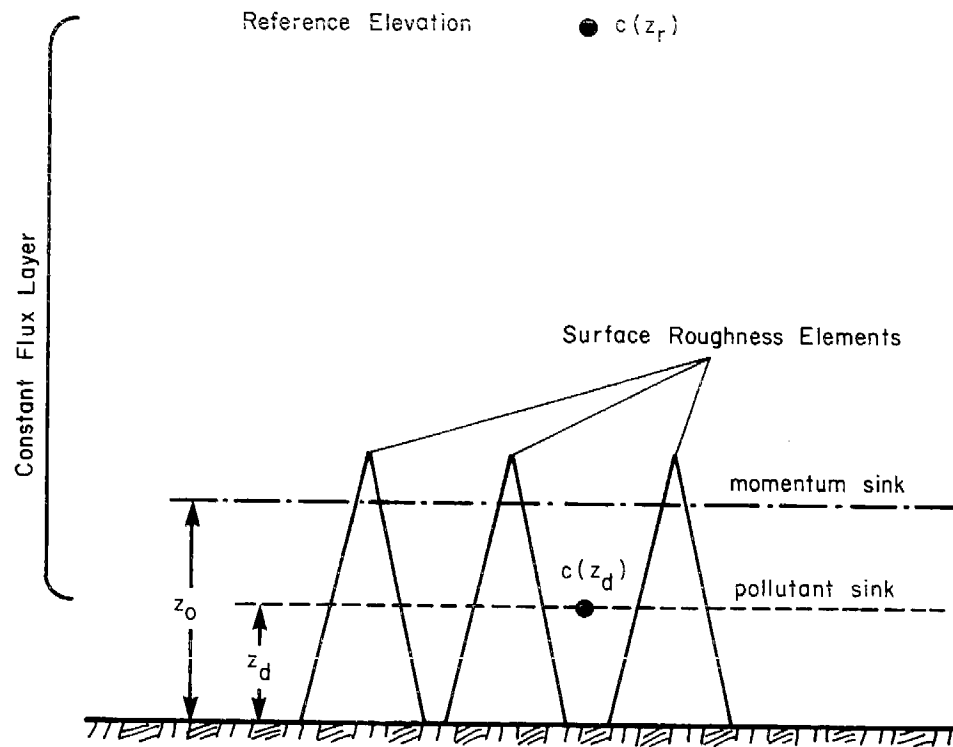


FIGURE 6.1

Idealized Representation of the Airshed Surface

without re-entrainment and, in the case of aerosols, without particle agglomeration. With these assumptions the deposition flux is described by

$$F = [K_p(z) + D] \frac{dc}{dz} + v_t c(z) \quad (6.2)$$

where $K_p(z)$ is the pollutant eddy diffusion coefficient, D the molecular diffusion coefficient of the material in air and v_t the terminal settling velocity for particulate material. Equating the fluxes in expressions (6.1) and (6.2) gives

$$\int_{z_d}^{z_r} \frac{dz}{[K_p(z) + D]} = \int_{c(z_d)}^{c(z_r)} \frac{dc}{[v_g c(z_r) - v_t c(z)]} \quad (6.3)$$

The lower limits of integration z_d and $c(z_d)$ refer to the elevation and concentration of material at the effective pollutant sink height. It is important to note that z_d is not in general equal to the surface roughness z_0 , a height associated with the momentum sink (Brutsaert, 1975). If the terminal settling velocity is set to zero for the case of gaseous materials then (6.3) can be written in the simpler form

$$v_g = \frac{\left[1 - \frac{c(z_d)}{c(z_r)} \right]}{\int_{z_d}^{z_r} \frac{dz}{[K_p(z) + D]}} \quad (6.4)$$

6.3 Eddy Diffusion of Momentum and Scalar Contaminants in the Surface Layer

Since the model is intended to be used primarily in the surface layer of the atmosphere, an expression for $K_p(z)$ can be developed using Monin-Obukhov similarity theory. The velocity shear and the pollutant eddy diffusion coefficient, $K_p(z)$, are given by

$$\frac{\partial u}{\partial z} = \frac{u_*}{kz} \phi_m\left(\frac{z}{L}\right) \quad (6.5)$$

and

$$K_p(z) = \frac{k u_* z}{\phi_p\left(\frac{z}{L}\right)} \quad (6.6)$$

where k is the von Karman constant, u_* the friction velocity, L the Monin-Obukhov length and ϕ_p , ϕ_m are universal functions which must be determined by experiment (Monin and Yaglom, 1971). The ϕ functions are basically correct for the effects of buoyancy on turbulence. Businger et al. (1971) have constructed expressions for momentum ϕ_m and heat ϕ_H from an analysis of field data taken under a wide variety of stability conditions. A survey of the results of some experiments directed at developing these functions is shown in Table 6.1. For the present model the expressions adopted for momentum are

$$\phi_m\left(\frac{z}{L}\right) = \begin{cases} [1 + 4.7(\frac{z}{L})] & \text{Stable; } \frac{z}{L} > 0 \\ 1 & \text{Neutral; } \frac{z}{L} = 0 \\ [1 - 15(\frac{z}{L})]^{-\frac{1}{4}} & \text{Unstable; } \frac{z}{L} < 0 \end{cases} \quad (6.7)$$

TABLE 6.1

Estimates of Turbulence Constants from Surface-Layer Measurements
(Source: Busch, 1973)

$$\phi_m = \begin{cases} 1 + \beta_m \frac{z}{L} & ; \frac{z}{L} > 0 \\ (1 - \alpha_m \frac{z}{L})^{-\frac{1}{4}} & ; \frac{z}{L} < 0 \end{cases} \quad \phi_H = \begin{cases} 1 + \beta_H \frac{z}{L} & ; \frac{z}{L} > 0 \\ (1 - \alpha_H \frac{z}{L})^{-\frac{1}{2}} & ; \frac{z}{L} < 0 \end{cases}$$

REFERENCE	MOMENTUM		HEAT		$\phi_H(0)$	$\phi_M(0)$
	α_m	β_m	α_H	β_H		
Businger et al. (1971)	15	4.7	9	6.4	0.74	---
Paulson (1970) Badgley et al. (1972)	16	7	16	7	1	1
Webb (1970)	18	5.2	9	5.2	1	1
Dyer and Hicks (1970)	16	---	16	---	1	1

In addition to the transport relations for momentum there are some data for ϕ functions associated with water vapor ϕ_w and heat ϕ_H . Unfortunately, there are few direct experimental measurements of pollutant fluxes in the atmospheric surface layer.

A decision must be made as to the form of the ϕ function for a generalized passive scalar contaminant. For unstable conditions ($z/L < 0$) the experimental evidence of Dyer and Hicks (1970) indicates that $\phi_H, \phi_w = \phi_m^2$. Galbally (1971) measured ozone profiles and fluxes in the surface layer and concluded that the eddy transport mechanism for O_3 is similar to that for heat rather than momentum. On the basis of these two studies and the data of Businger et al. (1971) the following ϕ functions have been adopted for pollutant transport.

$$\phi_p\left(\frac{z}{L}\right) = \begin{cases} 0.74 + 4.7\left(\frac{z}{L}\right) & \text{Stable; } \frac{z}{L} > 0 \\ 0.74 & \text{Neutral; } \frac{z}{L} = 0 \\ 0.74\left[1 - 9\left(\frac{z}{L}\right)\right]^{-\frac{1}{2}} & \text{Unstable; } \frac{z}{L} < 0 \end{cases} \quad (6.8)$$

6.4 Upper Limit Deposition Model

Within the surface layer defined by $z_d \leq z \leq z_r$ the bulk contribution to the diffusive transport from molecular diffusion is negligible. Applying this assumption to equation (6.4) and in addition substituting the flux gradient relation (6.6) for $K_p(z)$ gives the following upper limit to the deposition velocity.

$$v_g = \frac{k \left[1 - \frac{c(z_d)}{c(z_r)} \right]}{\int_{z_d}^{z_r} \frac{1}{zu_*} \phi_p \left(\frac{z}{L} \right) dz} \quad (6.9)$$

Since u_* is approximately constant with height in the surface layer (Busch, 1973) and $\phi_p \approx 1$ for $z_d \leq z \leq z_o$, the denominator of (6.9) can be expanded to give

$$v_g = \frac{k^2 u(z_r) \left[1 - \frac{c(z_d)}{c(z_r)} \right]}{\left[\int_{z_o}^{z_r} \phi_m \left(\frac{z}{L} \right) \frac{dz}{z} \right] \left[\ln \left(\frac{z_o}{z_d} \right) + \int_{z_o}^{z_r} \phi_p \left(\frac{z}{L} \right) \frac{dz}{z} \right]} \quad (6.10)$$

Evaluation of the term $\ln(z_o/z_d)$ in the denominator of equation (6.10) requires a knowledge of z_d and of the transfer processes at the surface. Based on a survey of the heat transfer literature and in particular the work of Brutsaert (1975), Wesely and Hicks (1977) assumed that

$$\ln \left(\frac{z_o}{z_d} \right) = 2 \left(\frac{Sc}{Pr} \right)^{\frac{2}{3}} \quad (6.11)$$

where Sc and Pr are the Schmidt and Prandtl numbers associated with the pollutant material in air. The complete model is then

$$v_g = \frac{k^2 u(z_r) \left[1 - \frac{c(z_d)}{c(z_r)} \right]}{\left[\int_{z_o}^{z_r} \phi_m \left(\frac{z}{L} \right) \frac{dz}{z} \right] \left[2 \left(\frac{Sc}{Pr} \right)^{\frac{2}{3}} + \int_{z_o}^{z_r} \phi_p \left(\frac{z}{L} \right) \frac{dz}{z} \right]} \quad (6.12)$$

The integrals required to evaluate v_g are shown in Table 6.2.

6.5 Application of Deposition Model

The final result exposes a number of the limitations of the basic model (6.1), in particular, the fact that v_g is directly influenced by the prevailing meteorology and atmospheric stability. The effect of stability is particularly apparent; consider for example, the conditions shown in Table 6.3 for a range of Sc/Pr ratios. With z/L in the range -1.5 to +1.5, the deposition velocities vary by almost a factor of five. This result indicates that under typical conditions there could be a significant diurnal variation in the surface removal of pollutant material. The functional dependence of v_g on the elevation above the surface highlights the need for reporting the reference height z_r in field or laboratory studies. If v_g , z_r , z_o and $u(z_r)$ are measured, then it is possible to evaluate $c(z_d)/c(z_r)$ and, in turn, v_g for elevations other than the reference height. This is a useful approach for developing the deposition velocities for air quality models in which z_r may be of 0(10-50 m). The variation of v_g as a function of z/L is shown in Figure 6.2.

TABLE 6.2

Momentum and Pollutant Integrals for Different Stability Conditions

INTEGRAL	STABILITY CONDITION		
	STABLE $\frac{z}{L} > 0$	NEUTRAL $\frac{z}{L} = 0$	UNSTABLE $\frac{z}{L} < 0$
MOMENTUM			
$\int_{z_0}^{z_r} \phi_m \left(\frac{z}{L} \right) \frac{dz}{z}$	$\ln \left(\frac{z_r}{z_0} \right) + \frac{4.7}{L} (z_r - z_0)$	$\ln \left(\frac{z_r}{z_0} \right)$	$\ln \left[\frac{\left(\frac{z_r}{1-15 \frac{r}{L}} \right)^{\frac{1}{4}} - 1}{\left(\frac{z}{1-15 \frac{r}{L}} \right)^{\frac{1}{4}} + 1} \right] - \ln \left[\frac{\left(\frac{z_0}{1-15 \frac{r}{L}} \right)^{\frac{1}{4}} - 1}{\left(\frac{z}{1-15 \frac{r}{L}} \right)^{\frac{1}{4}} + 1} \right]$
POLLUTANT			
$\int_{z_0}^{z_r} \phi_p \left(\frac{z}{L} \right) \frac{dz}{z}$	$0.74 \ln \left(\frac{z_r}{z_0} \right) + \frac{4.7}{L} (z_r - z_0)$	$0.74 \ln \left(\frac{z_r}{z_0} \right)$	$\left\{ \ln \left[\frac{\left(\frac{z_r}{1-9 \frac{r}{L}} \right)^{\frac{1}{2}} - 1}{\left(\frac{z_r}{1-9 \frac{r}{L}} \right)^{\frac{1}{2}} + 1} \right] - \ln \left[\frac{\left(\frac{z_0}{1-9 \frac{r}{L}} \right)^{\frac{1}{2}} - 1}{\left(\frac{z_0}{1-9 \frac{r}{L}} \right)^{\frac{1}{2}} + 1} \right] \right\} + 2 \arctan \left(1-15 \frac{r}{L} \right)^{\frac{1}{4}} - 2 \arctan \left(1-15 \frac{r_0}{L} \right)^{\frac{1}{4}}$

TABLE 6.3

Deposition Velocity as a Function of Stability and Ratio of Sc/Pr^*

Deposition velocity v_g as a function of stability (z/L)							
$\frac{Sc}{Pr}$	-1.5	-1.0	-0.5	0	0.5	1.0	1.5
0.6	1.36	1.26	1.13	0.51	0.49	0.31	0.21
0.8	1.28	1.20	1.07	0.50	0.47	0.30	0.21
1.0	1.22	1.14	1.02	0.48	0.46	0.29	0.20
1.2	1.17	1.09	0.98	0.47	0.44	0.29	0.20
1.4	1.12	1.05	0.95	0.46	0.43	0.28	0.19
1.6	1.09	0.91	0.92	0.44	0.42	0.27	0.19
1.8	1.05	0.98	0.89	0.43	0.41	0.27	0.19
2.0	1.02	0.95	0.86	0.42	0.41	0.27	0.19
2.2	0.99	0.92	0.84	0.42	0.40	0.26	0.18
2.4	0.96	0.90	0.82	0.41	0.39	0.26	0.18
2.6	0.93	0.87	0.80	0.40	0.38	0.25	0.18
2.8	0.91	0.85	0.78	0.39	0.38	0.25	0.18
3.0	0.89	0.84	0.76	0.39	0.37	0.25	0.17

*Conditions for calculations

$$u = 2.5 \text{ m/sec}, z_o = 0.01\text{m}, z_r = 10\text{m}, c(z_d) = 0$$

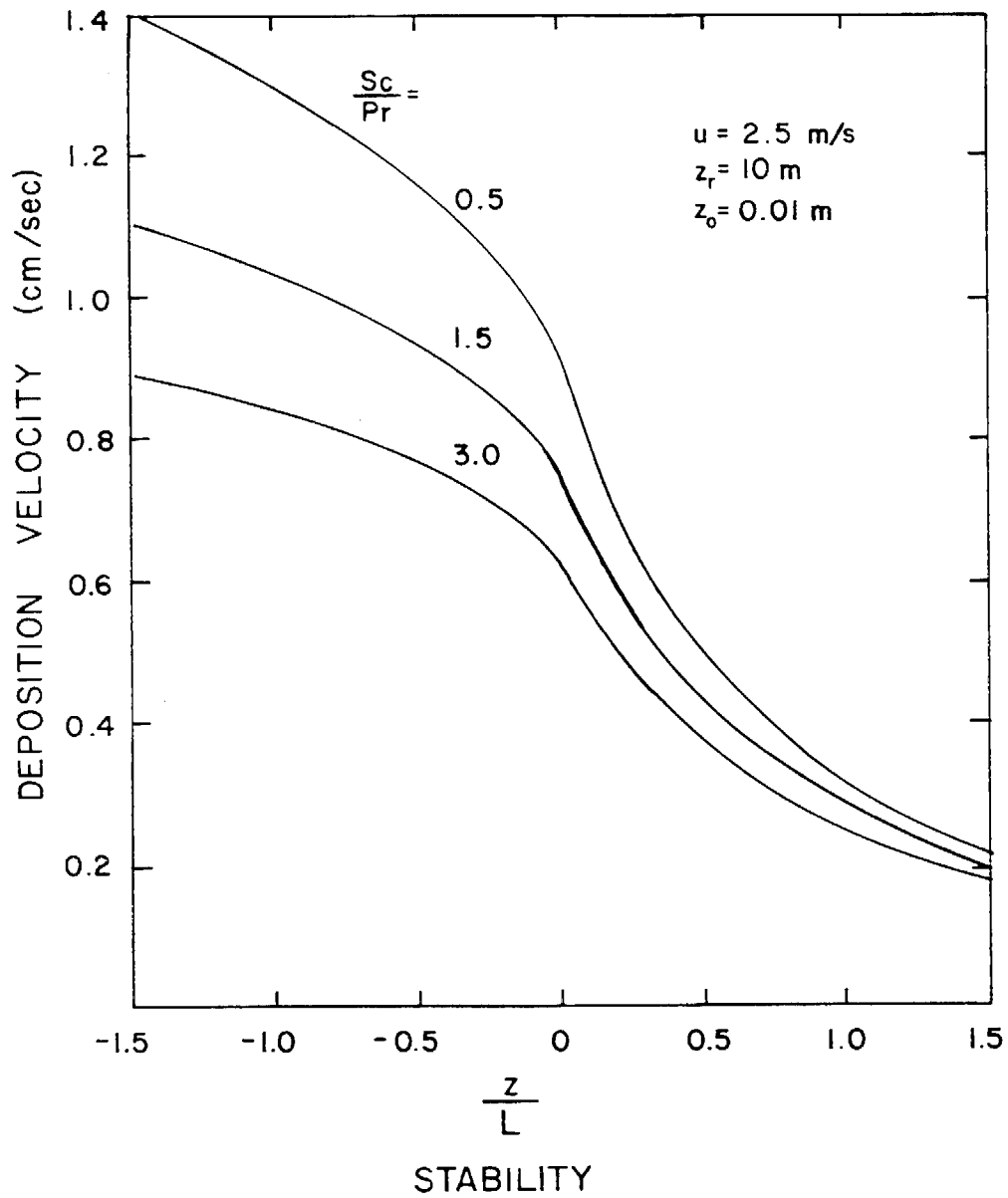


FIGURE 6.2

Variation of Surface Deposition Velocity v_g as a Function of Atmospheric Stability and Pollutant Sc/Pr Ratio

Once the pollutant deposition velocity has been established, either by direct measurement or estimated using the proposed model, the next step is to develop a formal procedure for calculating the amount of material removed at the ground. At the lower surface of the airshed the pollutant removal is typically described by the boundary condition:

$$F \equiv - K_p(z) \left. \frac{\partial c}{\partial z} \right|_{z = z_r} = - v_g(z_r) c(z_r) \quad (6.13)$$

Where z_r is a reference elevation, $v_g(z_r)$ and $c(z_r)$ are the pollutant deposition velocity and concentration at that height. Because of the nonlinear nature of $K_p(z)$, most mathematical descriptions of pollutant transport require numerical solution. This can pose a problem in that the elevation of the lowest computational grid point is typically much higher than the reference height, z_r , used to establish the pollutant deposition velocities. The situation is illustrated in Figure 6.3 where Δz is the height of the bottom cell and $\Delta z \gg z_r$. Because of the need to approximate the vertical concentration profile in discrete increments $c(z_r)$ is not readily available. When coupled with the observation that v_g varies with height there is a need to develop an equivalent deposition velocity \bar{v}_g that, when applied to the cell average concentration, c_1 , correctly predicts the flux at the lower boundary. One way to develop such a model is to assume that most of the lowest cell is within the surface or constant flux layer. If this is the case then the cell deposition velocity is given by

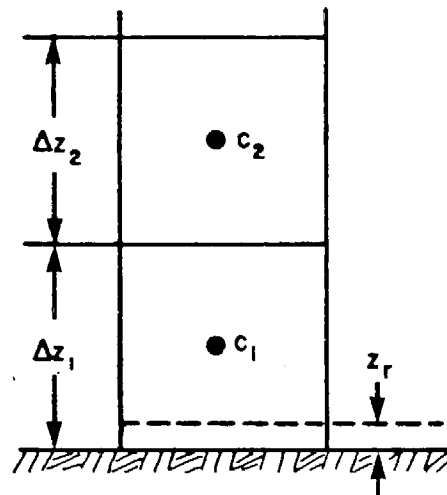


FIGURE 6.3

(a) Computational Cell Nomenclature

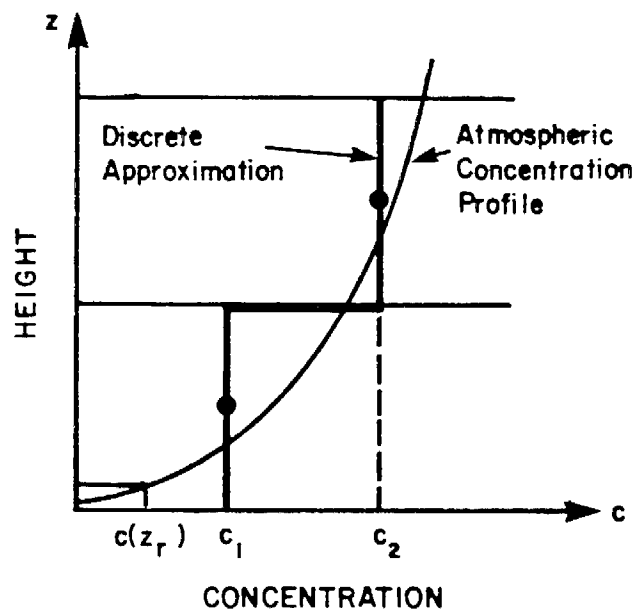


FIGURE 6.3

(b) Discrete Approximation of Vertical Concentration Profile

$$\bar{v}_g = \frac{v_g(z_r)c(z_r)}{c_1} \quad (6.14)$$

If c_1 is to represent the average value of the actual vertical concentration distribution in the range $z_r \leq z \leq \Delta z$ then it must be equivalent to

$$c_1 = \frac{1}{\Delta z - z_r} \int_{z_r}^{\Delta z} c(z) dz \quad (6.15)$$

Within the constant flux layer $c(z)$ is given by

$$c(z) = c(z_r) \left[1 + v_g(z_r) \int_{z_r}^z \frac{1}{K_p(z)} dz \right] \quad (6.16)$$

The equivalent cell deposition velocity can now be determined by combining (6.16), (6.15), (6.14) and (6.6) to give

$$\bar{v}_g = \frac{v_g(z_r)}{1 + \frac{v_g(z_r)}{ku_*(\Delta z - z_r)} \int_{z_r}^{\Delta z} \int_{z_r}^z \phi_p\left(\frac{x}{L}\right) \frac{dx}{x} dz} \quad (6.17)$$

The integrals needed to evaluate the denominator of (6.17) are shown in Table 6.3. An example of the variation of \bar{v}_g with cell size and atmospheric stability is shown in Figure 6.4, and, as can be expected, the equivalent deposition velocity becomes smaller as Δz increases. The

TABLE 6.4

Integrals Required to Calculate the Cell Average Deposition Velocity

STABILITY CONDITION	$\phi_p \left(\frac{z}{L} \right)$	INTEGRAL $I = \int_{z_r}^{\Delta z} \int_{z_r}^z \phi_p \left(\frac{x}{L} \right) \frac{dx}{x} dz$
Stable $\left(\frac{z}{L} > 0 \right)$	$\phi_p \left(\frac{z}{L} \right) = 0.74 + 4.7 \left(\frac{z}{L} \right)$	$I = 0.74(\Delta z) \ln \frac{\Delta z}{z_r} - \Delta z + z_r + \frac{2.35}{L} (\Delta z - z_r)^2$
Neutral $\left(\frac{z}{L} = 0 \right)$	$\phi_p \left(\frac{z}{L} \right) = 0.74$	$I = 0.74(\Delta z) \ln \frac{\Delta z}{z_r} - \Delta z + z_r$
Unstable $\left(\frac{z}{L} < 0 \right)$	$\phi_p \left(\frac{z}{L} \right) = 0.74 \left[1 - 9 \frac{z}{L} \right]^{-\frac{1}{2}}$	$I = 0.74 \Delta z \ln \left[\left(\frac{\sqrt{1 - 9 \frac{\Delta z}{L}} - 1}{\sqrt{1 - 9 \frac{z_r}{L}} - 1} \right) \left(\frac{\sqrt{1 - 9 \frac{z_r}{L}} + 1}{\sqrt{1 - 9 \frac{\Delta z}{L}} + 1} \right) \right]$ $+ 0.104 L \left[\sqrt{1 - 9 \frac{\Delta z}{L}} - \sqrt{1 - 9 \frac{z_r}{L}} \right]$

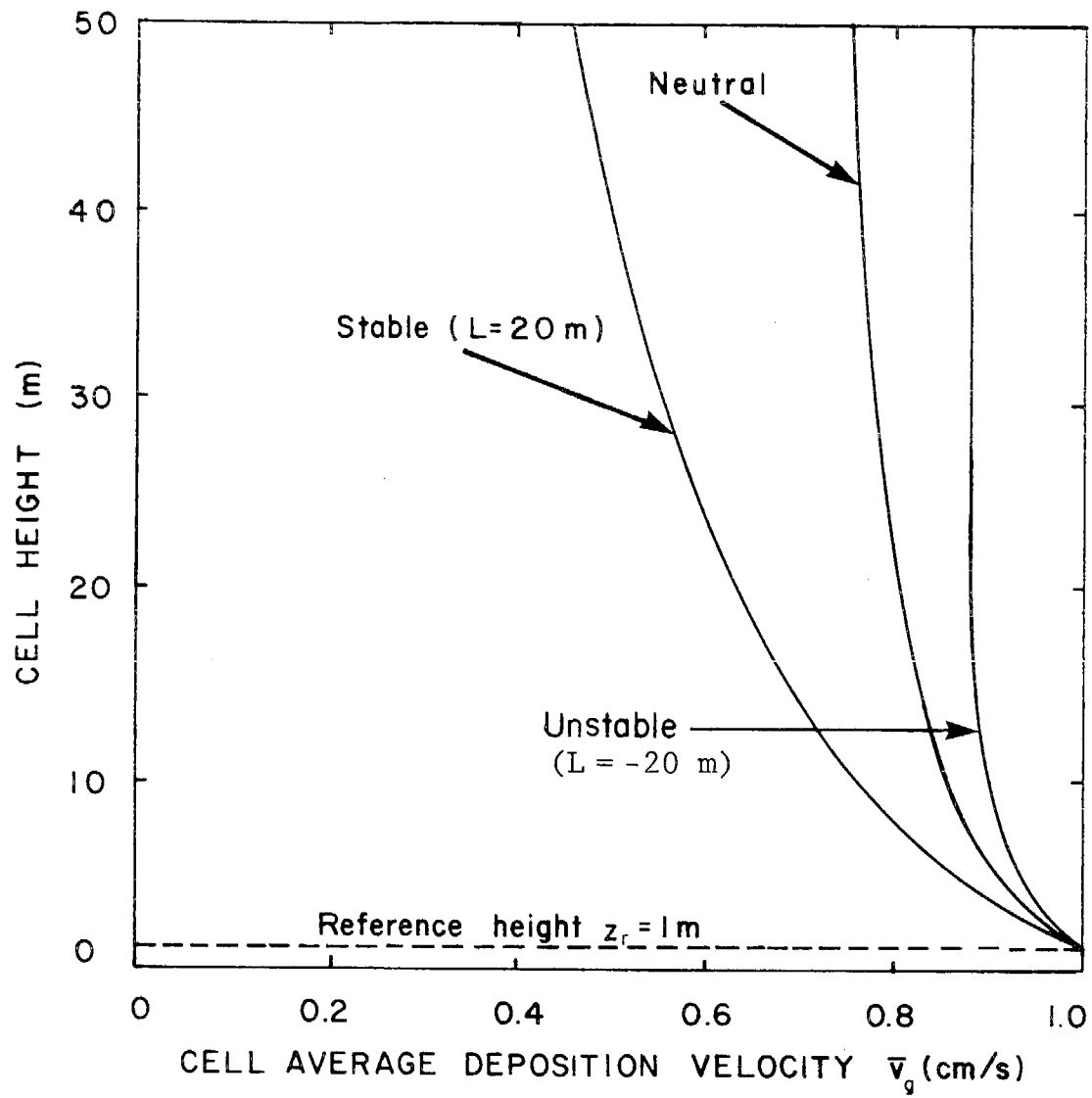


FIGURE 6.4

Variation of Average Deposition Velocity as a
Function of Atmospheric Stability and the Cell Height
($z_o = 0.01$ m, $\bar{u} = 2.5$ m/s, $v_g(z_r) = 0.01$ m/s)

variation is most pronounced under stable conditions because of the reduced vertical mixing. One implication of this result is that if $v_g(z_r)$, rather than \bar{v}_g , were to be used in a practical calculation then the surface removal flux would be considerably overestimated.

In order to illustrate how diurnal variations in atmospheric stability influence the surface removal processes consider a column of air of height H containing an initial distribution, $c(z,0)$, of a non-reacting species. If there are no other competing processes the fraction of material remaining in the column at time t is given by

$$M_f(t) = \frac{\int_0^h c(z,t) dz}{\int_0^h c(z,0) dz} \quad (6.18)$$

By neglecting both vertical wind shear and advection the pollutant transport can be described by

$$\frac{\partial c}{\partial t} = \frac{\partial}{\partial z} K_p(z) \frac{\partial c}{\partial z} \quad (6.19)$$

with the boundary conditions at the surface and at the column top given by

$$K_p(z) \frac{\partial c}{\partial z} = 0 \quad ; \quad z = H \quad (6.20)$$

and

$$K_p(z) \frac{\partial c}{\partial z} = v_g c \quad ; \quad z = z_r \quad (6.21)$$

Once the initial conditions $v_g(z_r)$ and $K_p(z)$ have been specified the numerical procedures described in Chapter 8 can be used to predict the evolution of the vertical concentration distribution. As an illustration, Figures 6.5 and 6.6 depict the variations of $c(z,t)$ and $M_f(t)$ within an air parcel as it traverses a typical urban airshed. There is quite a pronounced variation in both the vertical diffusion and surface deposition rate during the diurnal cycle. The surface depletion rate, expressed in terms of the deposition velocity, and the total material loss show a complex dependence on the time of day, the extent of vertical mixing and surface conditions. The point of this calculation is to illustrate that the use of a single diurnal average v_g could lead to a significant over-prediction of the amount of material removed during the nighttime. This conclusion further reinforces the need for careful reporting of atmospheric conditions during field studies directed at establishing surface removal fluxes.

6.6 Experimental Methods for Determining Deposition Velocities

In the previous section primary attention was directed at developing an upper limit estimate of the rate at which pollutants can be transported to the ground. Whether this flux corresponds to the actual removal rate depends to a large extent on the conditions and type of the underlying surface. Garland (1974), for example, has observed an order of magnitude difference in the ozone (O_3) deposition velocity over different soil types. If $c(z_d)$ is the pollutant concentration at the effective sink height, z_d , then the upper and lower limits on v_g correspond to

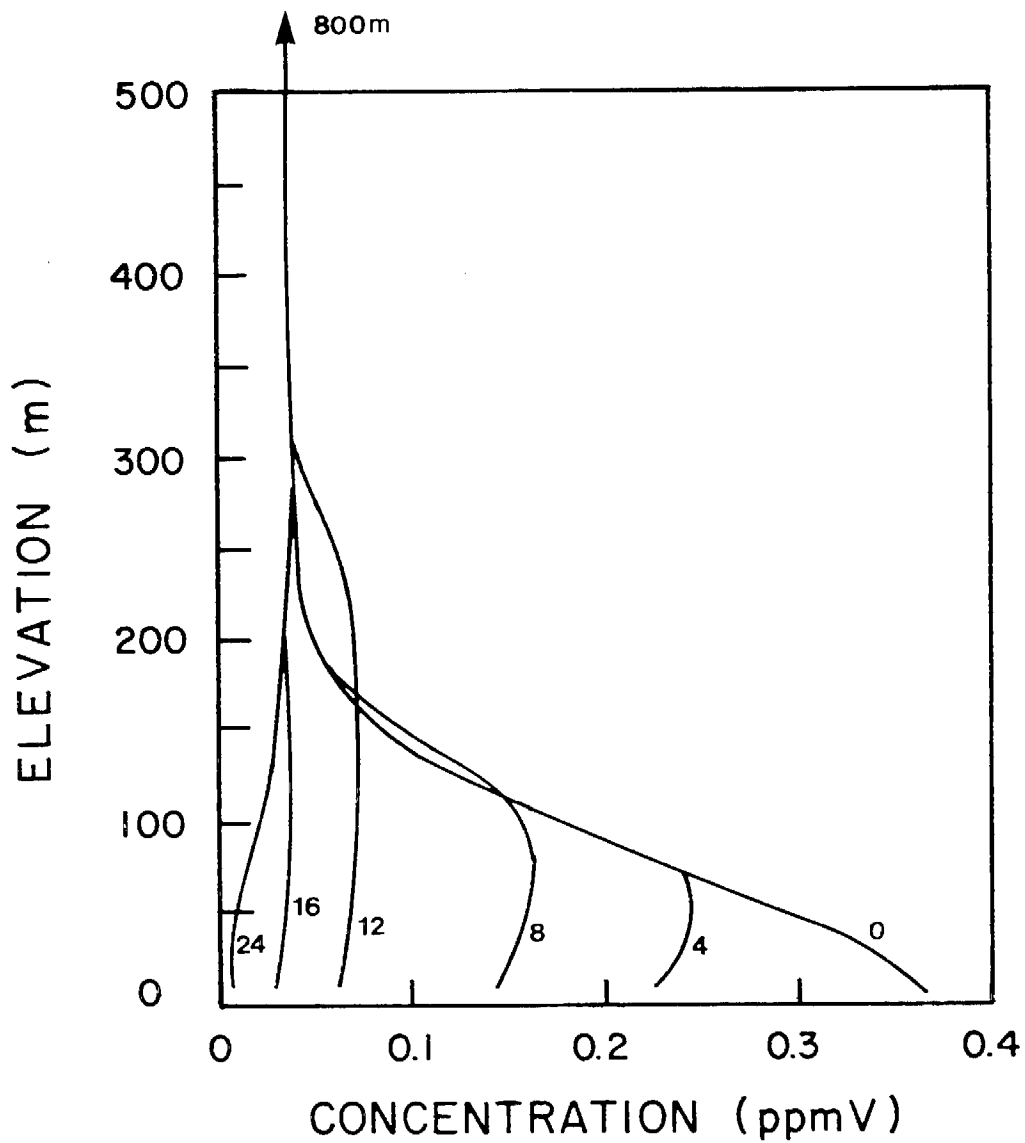
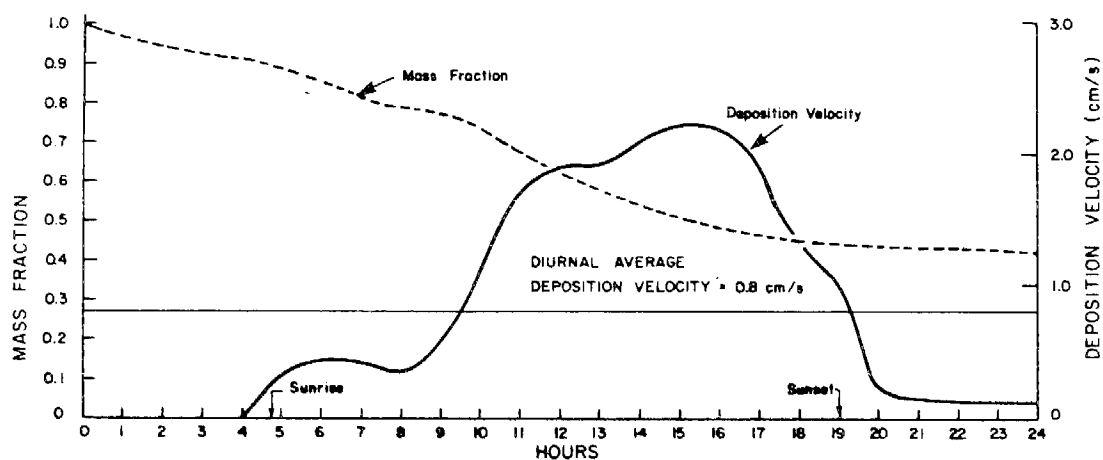


FIGURE 6.5

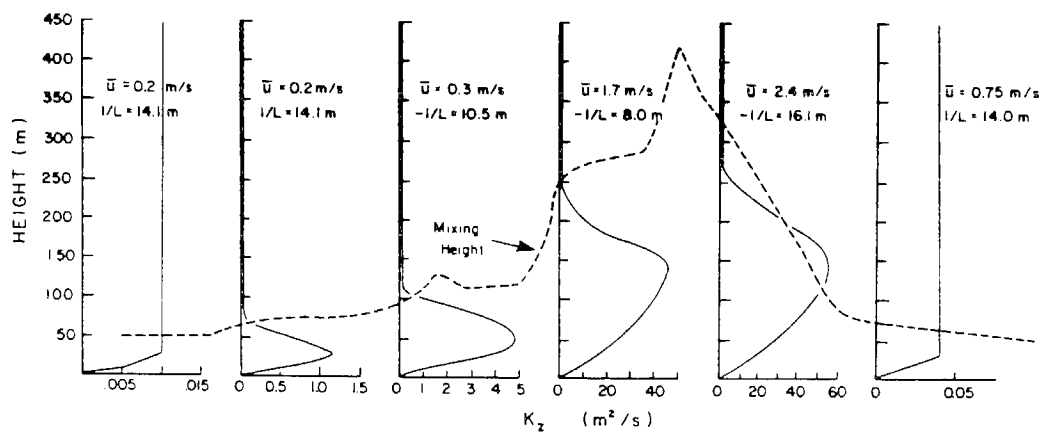
Time Evolution of a Typical Vertical Concentration Profile
for an Air Parcel Traversing an Urban Airshed

($\Delta z = 20$ m, $z_o = 0.01$ m, $z_r = 10$ m, $v_g = 0.01$ m/s)



(a)

Diurnal Variation of Column Mass Fraction and
Cell Average Deposition Velocity



(b)

Diurnal Variation of Vertical Diffusivity
(Profiles are drawn every four hours)

FIGURE 6.6

the conditions $c(z_d) = 0$ and $c(z_r) = c(z_d)$. If a lower bound on v_g is required then it is important to be able to estimate the concentration difference $c(z_r) - c(z_d)$. At present the only satisfactory means for establishing the surface condition is by experimental measurement. This section presents a brief survey of field and laboratory techniques for determining deposition velocities for gaseous species which participate in photochemical reaction processes.

Whether pollutant deposition velocities are measured in the field or under laboratory conditions usually one of three basic techniques is employed. These methods include: the use of radioactive tracers, free stream concentration decay measurements and gradient or profile determinations. The most common laboratory procedure is called the flux method which equates free stream concentration decay rates to the surface removal fluxes. Garland and Penkett (1976) measured the concentration decay of peroxy acetyl nitrate (PAN) as it passed over different surfaces in a wind tunnel. Given the concentration difference, the travel time over the surface and the wind tunnel dimensions, it is a simple task to infer the net deposition flux and in turn determine the deposition velocity. A similar technique was used by Hill and Chamberlain (1974) to establish the pollutant influx required to maintain a constant concentration over different plant canopies. More recently the emergence of fast response pollutant detectors has enabled a direct measurement of the vertical turbulent flux. Wesely et al. (1977) recorded the velocity, w' , and concentration, c' , fluctuations at a

reference height of $z_r = 5$ m and evaluated v_g directly using

$$v_g(z_r) = \left. \frac{\overline{w'c'}}{\bar{c}} \right|_{z = z_r} \quad (6.23)$$

where $\overline{w'c'}$ is the time averaged vertical turbulent flux and \bar{c} the average concentration. The averaging time for the results reported in Wesely et al. (1977) was 0(10 minutes).

Another means for determining deposition velocities is to employ isotopic labelling techniques. If isotopes, with low natural abundances, are used then the task of differentiating between material previously present at the surface and the amount deposited during the experiment is considerably simplified. Owens and Powell (1974) released sulfur dioxide (SO_2), labelled with the sulfur isotope $^{35}_{16}S$, and measured the accumulation of $^{35}SO_2$ at the ground. Given the exposure time, T , and the $^{35}SO_2$ concentration at the reference elevation the deposition velocity is given by

$$v_g(z_r) = \frac{^{35}SO_2 \text{ Activity at the Ground}}{T \ ^{35}SO_2(z_r)} \quad (6.24)$$

Chamberlain (1966) used thorium - B ($^{212}_{82}Pb$), in a wind tunnel, to measure the vertical flux of pollutant materials towards grass and similar surfaces as a function of the concentration difference between the reference height and the surface.

The most common technique used in field studies is the gradient or profile method. This procedure utilizes measurements at two or more elevations to establish the vertical concentration gradient $\partial c / \partial z$. If the momentum, heat, water vapor, and pollutant fluxes are constant within the surface layer then the Monin-Obukhov similarity hypothesis, coupled with the measured vertical gradient, gives the pollutant deposition velocity

$$v_g(z_r) = \frac{K_p(z)}{c(z)} \left. \frac{\partial c}{\partial z} \right|_{z = z_r} \quad (6.25)$$

The turbulent eddy diffusivity $K_p(z)$ can be estimated using the methods presented in Chapter 4 or determined from energy budget measurements using a mass transfer analogy. An alternative approach is to assume that the pollutant transport is similar to that of water vapor and employ a stability dependent bulk transfer coefficient to approximate the surface flux. Given the measured concentration profile the deposition velocity is simply

$$v_g(z_r) = \bar{C}u(z_h) \left(\frac{c(z_h) - c(z_d)}{c(z_r) - c(z_d)} \right) \quad (6.26)$$

where C is the aerodynamic transfer coefficient and $\bar{u}(z_h)$ is the mean wind speed at an elevation z_h above the ground. Whelpdale and Shaw (1974) used (6.26) to evaluate SO_2 deposition velocities over different surfaces for a range of stability conditions. Further, more detailed discussions of the profile and other methods are given in Garland (1974) and Droppo and Hales (1974).

6.7 Literature Survey of Deposition Velocity Measurements

A major goal of developing the upper limit deposition model was to establish the surface removal rates for those species which participate in photochemical reactions. A partial list of these species includes nitric oxide (NO), nitrogen dioxide (NO₂), ozone (O₃), peroxy acetyl nitrate (PAN), hydrogen peroxide (H₂O₂), nitrous acid (HONO), nitric acid (HNO₃), carbon monoxide (CO), reactive hydrocarbons, organic and inorganic radicals. An extensive literature search was carried out to identify experimental determinations of ground level deposition velocities for each of these species. The results, presented in Table 6.5, include additional values excerpted from the comprehensive surveys conducted by Droppo (1976), Slinn et al. (1978) and McMahon and Denison (1979). In constructing the table an attempt has been made to summarize those factors which influence the estimates, namely the experimental technique, reference height, type of surface, moisture conditions and the atmospheric conditions.

Considering the important role of deposition in establishing ambient concentration levels the most striking feature of Table 6.5 is the paucity of reported results. The problem is further compounded by inadequate documentation of the atmospheric conditions prevailing during each of the experiments. Unless sufficient meteorological data are reported it is difficult to separate whether the turbulent transport or chemical nature of the underlying surface is controlling the deposition. The limited data reported in the table are, unfortunately, insufficient to adequately verify the quantitative performance of the upper limit model.

TABLE 6.5

Literature Survey of Deposition Velocity Data for Species
Involved in Photochemical Reaction Processes

SPECIES	DEPOSITION VELOCITY v_g (cm/s)	SURFACE CONDITIONS	MEASUREMENT METHOD	METEOROLOGICAL DATA REPORTED	REFERENCE
O_3	1.67	Alfalfa	Flux	\bar{u}	Hill and Chamberlain (1974)
	0.10-2.10	Soil, Short Grass	Profile	$z/L, R_{f_b}, u_*, z_r=4m, T, RH, z_o$	Galbally (1971)
	0.47-0.55	Grass, Soil, Water	Flux	$\bar{u}, u_*, z_o, z_r=10cm$	Garland and Penkett (1976)
	0.20-0.80	Maize	Flux	$\bar{u}, u_*, z_o, w, T, z_r=4-5m$	Wesely et al. (1978)
	0.60-6.30	---	---	---	Droppo (1976)
	0.02-1.80	---	---	---	McMahon and Denison (1979)
	0.29-0.84	Soybean field	Eddy-correlation	$\bar{u}, z_r=5.2m, L$	Wesley et al. (1982)
<hr/>					
NO	0.10	Alfalfa	Flux	\bar{u}	Hill and Chamberlain (1974)
NO ₂	1.90	Alfalfa	Flux	\bar{u}	Hill and Chamberlain (1974)
	0.50-2.00	---	---	---	McMahon and Denison (1979)
	0.05-0.56	Soybean field	Eddy-correlation	$\bar{u}, z_r=5.2m, L$	Wesley et al. (1982)
<hr/>					
CO	0.00-0.002	Vegetation	---	---	McMahon and Denison (1979)
PAN	0.14-0.30	Grass, Soil	Flux	$\bar{u}, u_*, z_o, z_r=10cm$	Garland and Penkett (1976)
	0.63	Alfalfa	Flux	\bar{u}	Hill and Chamberlain (1974)

A qualitative indication can, however, be gained by examining the study of sulfur dioxide (SO_2) deposition carried out by Whelpdale and Shaw (1974). Their results, presented in Table 6.6, clearly demonstrate that the influence of atmospheric stability is consistent with the calculated variation shown in Figure 6.2. During stable conditions the deposition flux is primarily controlled by the rate at which material can be transported to the surface. Such circumstances are likely to occur at night. During the daytime the deposition rate is much more likely to be influenced by the chemical interaction at the surface.

Table 6.7 summarizes the deposition velocities derived from the literature survey. The accompanying concentration ratios, based on a reference elevation $z_r = 1 \text{ m}$, are for use in the airshed model. The data should only be considered as estimates.

6.8 Conclusions

In this chapter a simple upper limit model for pollutant deposition velocities has been presented. The principal features of the formulation are: an explicit treatment of atmospheric stability and a formal procedure for determining equivalent cell average deposition velocities for use in numerical calculations. The fact that atmospheric stability has such a pronounced effect on the surface fluxes points to the need for careful reporting of meteorological conditions during field studies. This would enable an independent assessment of whether the limits on v_g are set by the eddy diffusion or by the ability of the underlying surface to assimilate the material. In terms of future work considerably more

TABLE 6.6

Average Deposition Velocity of SO₂ for
Different Surface and Stability Conditions^a

SURFACE	STABILITY	NUMBER OF EXPERIMENTS	DEPOSITION VELOCITY v_g (cm/s)
Grass	$Ri_b < -0.02$	10	2.4
	$-0.02 < Ri_b < 0.02$	3	2.6
	$Ri_b > 0.02$	2	0.5
Snow	$Ri_b < -0.02$	1	1.6
	$-0.02 < Ri_b < 0.02$	3	0.52
	$Ri_b > 0.02$	8	0.05
Water	$Ri_b < -0.02$	7	4.0
	$-0.02 < Ri_b < 0.02$	7	2.2
	$Ri_b > 0.02$	4	0.16

a. Source: Whelpdale and Shaw (1974)

b. Stability is defined in terms of the bulk Richardson Number Ri_b

$$Ri_b = \frac{g}{T} \Delta z \frac{\Delta \theta}{(\Delta \bar{u})^2}$$

where T is the ambient temperature, Δz difference in sampling heights, $\Delta \theta$ the potential temperature difference and $\Delta \bar{u}$ the wind speed.

TABLE 6.7

Summary of Deposition Velocity Data
and Concentration Ratios

SPECIES	DEPOSITION VELOCITY RANGE v_g (cm/s)	CONCENTRATION RATIO
		$1 - \frac{c(z_d)}{c(z_r)}$
O ₃	0.025 - 6.3	0.8
NO ₂	0.5 - 2.0	0.6
PAN	0.14 - 0.63	0.25
CO	0.0 - 0.03	0.0
NO	0.0 - 0.10	0.1

attention needs to be given to characterizing the physical and chemical processes occurring in the layer $z_d \leq z \leq z_o$. At present there are no satisfactory theoretical treatments of the mass transfer close to the surface. Even more serious is the limited amount of field data on pollutant uptake at the surface.

A basic limitation of the model is the reliance on Monin-Obukhov similarity theory to characterize the material fluxes. While this formally restricts applications to steady conditions and values $|z/L| < 1$, the model is, nevertheless, capable of producing useful limits for surface deposition fluxes for a range of the species encountered in photochemical applications.

CHAPTER 7

TREATMENT OF POINT AND AREA SOURCE EMISSIONS

7.1 Introduction

A primary determinant of pollutant concentration levels within an urban environment is the emission of contaminant materials into the atmosphere. These emissions, which can be produced from a variety of different activities, enter the airshed model either through the boundary conditions or as source terms in the conservation equations. This chapter describes the procedures used to allocate emissions into the appropriate computational cells. Particular attention is given to: the mode of material injection, effective release height, near source chemistry and the influence of turbulent diffusion. The issues which need to be considered when compiling a comprehensive emission inventory for a specific region are discussed in Chapter 13.

7.2 Point and Area Source Emissions

Despite the diversity of different source types, pollutants and modes of material discharge, most emissions can be considered to be released from either point locations or areal regions. Point sources, by definition, need to be treated as direct inputs to the species continuity equations in much the same manner as the chemical reaction terms. If a point source emits a typical species at the rate $E_p(\underline{x}_p, t)$ from the discharge point \underline{x}_p , then the contribution to the rate of concentration change at \underline{x} is given by

$$S(\underline{x}, t) = E_p(\underline{x}_p, t) \alpha(\underline{x}, \underline{x}_p) \quad (7.1)$$

where $\alpha(\underline{x}, \underline{x}_p)$ is given by

$$\alpha(\underline{x}, \underline{x}_p) = \begin{cases} 1 & ; \underline{x} = \underline{x}_p \\ 0 & ; \underline{x} \neq \underline{x}_p \end{cases} \quad (7.2)$$

Area sources are typically located at the ground and as a result they enter the airshed model through the boundary conditions. For the problem under consideration the flux balance at the surface results in an expression of the form

$$v_g c - K_{zz} \frac{\partial c}{\partial z} = E_a(\underline{x}, t) \quad (7.3)$$

where v_g is the deposition velocity of species c , K_{zz} the turbulent diffusivity and $E_a(\underline{x}, t)$ is the emission flux at the ground. In a typical urban airshed there are often a very large number of point sources within an area defined by a typical computational cell. Rather than considering each source separately, a common practice is to aggregate all the ground level point sources within each cell and develop a comparable source term. If there are n ground level point sources located within an area, A , then the equivalent, uniformly distributed flux is given by

$$E_a(\underline{x}, t) = \frac{1}{n} \sum_{i=1}^n E_p(\underline{x}_i, t) \quad ; \underline{x}_i \in A \quad (7.4)$$

Most airshed models cannot resolve spatial scales smaller than the size of an individual computational cell. Because of this, point and area emissions are often treated as volume source terms. In order

to determine the incremental contribution from emissions into a particular cell consider the one shown in Figure 7.1, which is of arbitrary base area A and uniform height $h(t)$. Given the mass emission rate from either a point source $E_p(\underline{x}_p, t)$ or an area source $E_a(\underline{x}, t)$, the corresponding cell mass concentrations $Q_p(t)$ and $Q_a(t)$ are of the form

$$Q_p(t) = \frac{E_p(\underline{x}_p, t)}{h(t) A} \quad (7.5)$$

and

$$Q_a(t) = \frac{\iint_A E_a(\underline{x}_p, t) d\underline{x}}{h(t)} \quad (7.6)$$

To be useful in comparisons against ambient air quality standards the expressions (7.5 - 7.6) need to be converted to a system of concentration units expressed in terms of parts per million by volume. This is accomplished by assuming that all species can be described by the ideal gas laws. Under these conditions the volume occupied by one mole of an ideal gas is given by RT/P where R is the Universal gas constant, T the absolute temperature in $^{\circ}K$, and P the pressure in standard atmospheres. If M is the molecular weight of species k then the conversion is given by

$$\text{Concentration (ppmv)} = \frac{RT}{MP} \text{Concentration } (\mu\text{gm}/\text{m}^3) \quad (7.7)$$

The source conversion factor, S , expressed in units of ppm sec^{-1} is then given by

$$S = \frac{RT}{MP} 10^9 Q(\text{Kgm}/\text{m}^3\text{-s}) \quad (7.8)$$

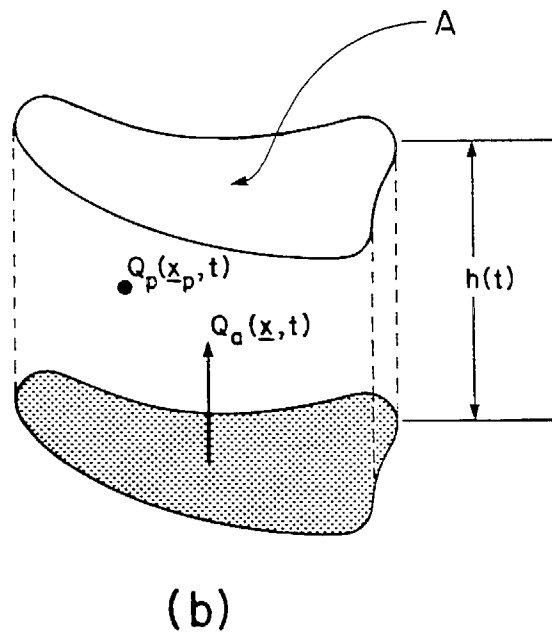
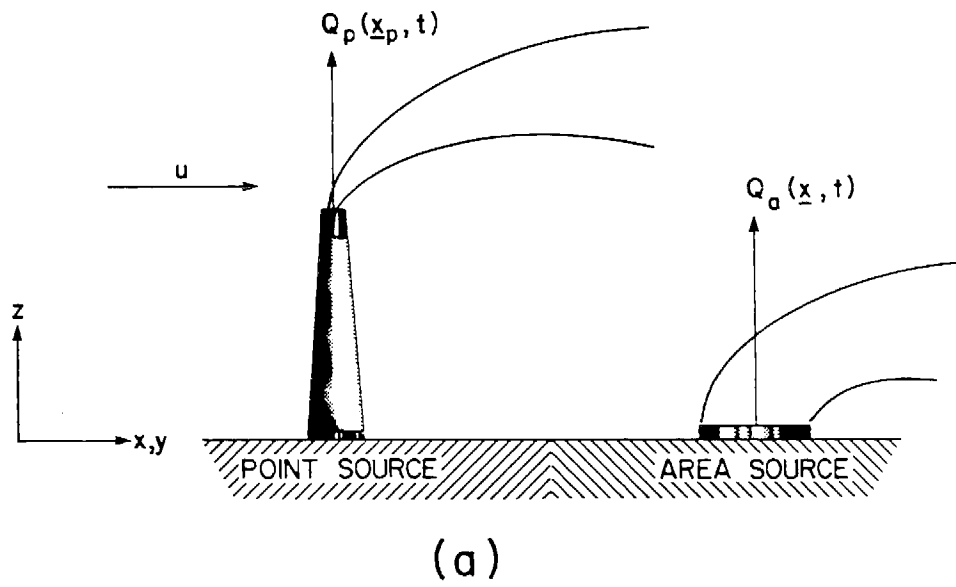


FIGURE 7.1
Point and Area Source Representation

For the most common case of a regular cell of volume V and source emissions E_p and E_a the above expressions reduce to:

$$S_p(t) = \frac{RT}{MP} \frac{10^9}{V} E_p(\underline{x}, t) \quad (7.9)$$

$$S_a(t) = \frac{RT}{MP} \frac{10^9}{h(t)} E_a(\underline{x}, t) \quad (7.10)$$

In order to illustrate an application of the above formulae consider an area source with an emission flux density of $E_a(t) = 1 \text{ Kgm/m}^2\text{-s}$ and a point release of $E_p(t) = 1 \text{ Kgm/s}$. If the ambient conditions are $T = 25^\circ\text{C} = 298^\circ\text{K}$, $P = 1 \text{ atm}$ and $R = 8.314 \text{ Joule/gm-mole-}^\circ\text{K}$ ($RT/P = 0.02450$), then the source conversion factors for a unit cell volume and height can be readily calculated from (7.9) and (7.10). Some typical results for a range of different species are shown in Table 7.1.

Both concentration conversion formulae require a knowledge of the molecular weights. This does not pose a problem for most species; however, a difficulty arises when treating hydrocarbons because there are hundreds of them present in a typical urban atmosphere. Since it is not practical to consider the reactions of each individual hydrocarbon, the most common approach is to treat the chemistry of a series of lumped classes. A typical grouping could be aldehydes, olefins, aromatics, alkanes and other non-reactive species.

TABLE 7.1

Conversion Factors for Point and Area Sources^(a)

SPECIES (k)	MOLECULAR WEIGHT (gm)	CONVERSION FACTORS ^(b) $(\frac{\mu\text{gm}}{3} / \text{ppm})$	SOURCE EMISSION ^(c) FACTORS $(S_p^k, S_a^k \text{ h})$
CO	28	1143	8.75×10^5
NO	30	1224	8.17×10^5
NO ₂	46	1878	5.33×10^5
SO ₂	64	2612	3.83×10^5
SO ₃	80	3625	3.06×10^5
CH ₄	16	653	15.31×10^5
C ₃ H ₈	44	1796	5.57×10^5
HCHO	30	1224	8.17×10^5
NH ₃	17	694	14.41×10^5

(a) Ambient conditions $p = 1 \text{ atm}$ and $T = 298^\circ\text{K}$ (b) Example calculation, 1.5 ppmV of nitric oxide (NO) = $1.5 \times 1224 = 1836 \mu\text{gm}/\text{m}^3$

(c) The conversion factors are based on $E_a = 1 \text{ Kgm}/\text{m}^2\text{-sec}$ and $E_p = 1 \text{ Kgm}/\text{sec}$. As an example consider a large point source emitting 0.1 Kgm/sec ($\approx 10 \text{ tons/day}$) of nitric oxide (NO) into a grid cell of dimension 5000 x 5000 x 30 m, then

$$S_p(\text{NO}) = \frac{RT}{MP} \frac{10^9}{V} E_p(\text{NO}) = \frac{8.17 \times 10^5 \times 0.1}{5000 \times 5000 \times 30} = 1.14 \times 10^{-4} \frac{\text{ppm}}{\text{sec}} \approx 7 \frac{\text{ppb}}{\text{min}}$$

In the present study the i -th hydrocarbon class average molecular weight, MW_i , is determined from

$$MW_i = \frac{\sum_{k=1}^n E_k}{\sum_{k=1}^n E_k / M_k} \quad (7.11)$$

where E_k and M_k are the emissions and molecular weight of species k in the i -th class.

7.3 Effective Release Height for Emissions

In the previous section no consideration was given to either the physical stack height or the buoyant rise of hot exhaust gases when locating the effective discharge point, x_p . Within the airshed model the actual height, H , for emission release is considered to be the sum of the stack elevation, h_s , and the plume rise, h_p . Depending upon the value of H and the size of the first computational cell, Δz , the emissions can be treated as either ground level or elevated releases. Clearly when $h_s > \Delta z$ the emissions need to be considered as elevated point sources. When $h_s < \Delta z$ the distinction between ground level and elevated sources, and their mode of numerical treatment, is no longer clear cut. As a result it is necessary to establish selection criteria which can be used to distinguish between the two cases. One approach for creating such a division is shown in Figure 7.2 and illustrates the need to address two basic issues: the computational cost and the magnitude of the concentration increment.

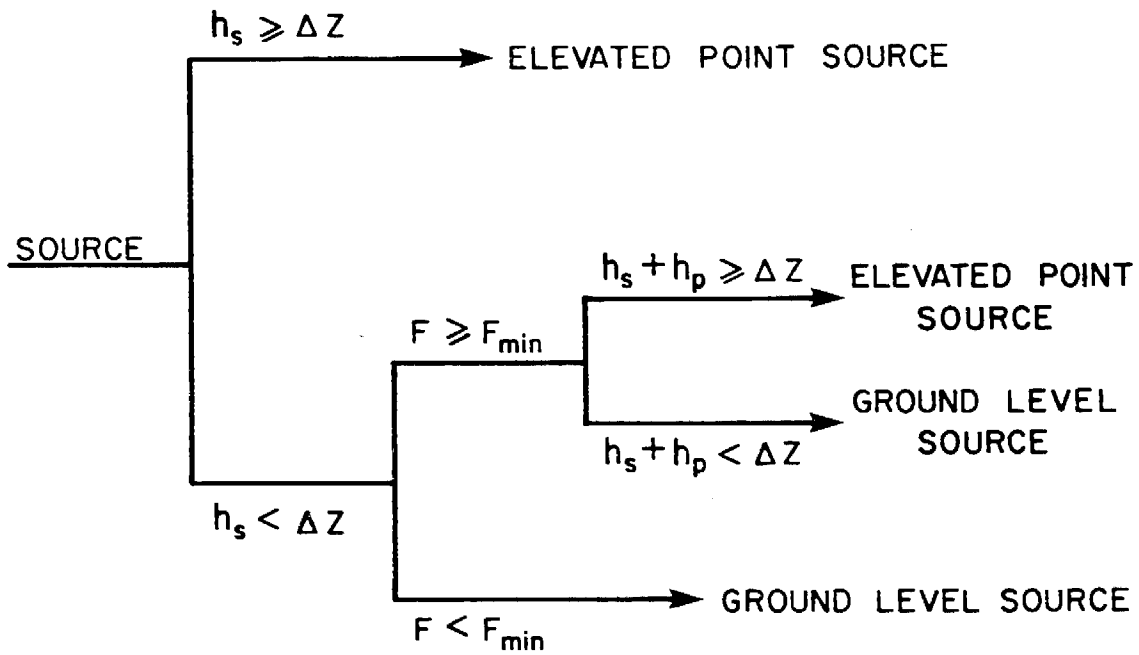


FIGURE 7.2

Selection Criteria for Ground Level and Elevated Sources

The critical problem, in either case, is to determine if the plume rise above the stack top is greater than Δz . Since most of the exhaust plumes encountered in an urban environment are dominated by buoyancy rather than momentum, an initial selection can be made on the basis of the magnitude of the buoyancy flux, F , emitted by the source. This flux is defined as

$$F = \frac{g Q_H}{\pi C_p \rho T_s} \quad (7.12)$$

where Q_H is the heat output from the source, T_s the stack gas temperature, C_p and ρ the specific heat and density of the exhaust gases. In the present model the source emissions are treated as ground level releases if the effluent buoyancy is below a minimum value, F_{\min} . Assigning a lower value effectively reduces the the number of sources treated as individual point releases. This latter factor is quite important as an extensive set of calculations must be performed in order to correctly account for the material dispersion from each source. In practice the exact value of the cutoff depends on the number of sources and the magnitude of their emissions. Chapter 13 discusses the choice of F_{\min} for an urban airshed.

When the source buoyancy exceeds F_{\min} the next step is to determine if the equilibrium height of the effluent plume is above the top of the first computational cell. If the plume rise plus the stack height exceeds Δz then the source is treated as an elevated point source. When $h_s + h_p < \Delta z$ the point source is added to the ground level flux term in (7.3). Clearly a crucial element of the selection

process is the determination of h_p and this is the subject of the next section.

7.4 Plume Rise and Effective Stack Height

Characterization of the plume rise above the stack top in terms of the exhaust gas properties and the ambient atmospheric state is a complex problem. A recent review by Briggs (1975) indicates that no single formula adequately predicts plume rise for the range of commonly encountered meteorological conditions; indeed, the predictions of different formulations can vary by factors of 2 to 10. Given such a large range of uncertainty it is natural to ask the question: what procedures can be used in the airshed model to predict the plume rise from individual point sources? The objective of this section is to present the formulae embedded in the airshed model.

As might be expected, there is an extensive literature on plume rise modeling; however, it is beyond the scope of this study to consider the details of the different formulations. This background information is comprehensively reviewed in the works of Briggs (1969,1975), Fischer et al. (1979), Fabrick et al. (1977) and Tesche et al. (1976). An examination of this literature indicates that the approaches can be broadly classified into three basic categories. The most detailed involves solving the coupled conservation equations of mass, momentum, energy and species. This method is generally not used in airshed models because of the prohibitive cost of the numerical solution. An alternative approach, introduced by Morton et al. (1956), is to consider the integrated form of the conservation equations. This method

involves integrating the equations across a section normal to the plume trajectory and assuming that all turbulent transport terms vanish at the plume boundary. Several variations of the general equations for the integral method are available for different flow geometries and the ambient conditions. A thorough discussion of the development of the general equations for a buoyant jet in a density-stratified cross flow are given by Hirst (1972), Omms (1972), Wright (1977), Schatzmann (1979), Koh and Brooks (1975), Csanady (1973), Hoult et al. (1969) and Fischer et al. (1979).

Although there are many plume rise formulae, the ones proposed by Briggs (1969, 1975) are the most widely employed in practice (CRSTER, 1977). Extensive sets of field observations, dimensional analyses and theoretical formulations were used by Briggs in developing the plume models. Near the source h_p is adequately predicted using the momentum conservation equations and a simple entrainment assumption.

For neutral and unstable conditions Briggs developed the following expression:

$$h_p = \frac{1.6 [F x^2]^{1/3}}{u} \quad (7.13)$$

where x is downwind distance from source (m), and u is the horizontal wind speed (m/s). The buoyancy flux, in $m^4 s^{-3}$, is defined by

$$F = \frac{gd^2 V_s (T_s - T_a)}{4T_s} \quad (7.14)$$

where g is the gravitational acceleration ($9.8 m s^{-2}$), d is the stack

inside diameter (m), V_s the exhaust gas velocity (m/s), T_a is the ambient air temperature ($^{\circ}\text{K}$), and T_s the stack exhaust gas temperature. Based on early experimental evidence, Briggs concluded that the final plume rise, h_p , occurred at a downwind distance of ten stack heights. Later results indicated that the the downwind distance at which the final plume rise occurred was a function of buoyancy. The distances are as follows

$$x_d = \begin{cases} 14 F^{5/8} & ; F < 55 \\ 34 F^{2/5} & ; F \geq 55 \end{cases} \quad (7.15)$$

The limiting plume rise predictions as a function of the buoyancy flux parameter F are shown in Figure 7.3.

Under stable ambient stratification Briggs (1975) indicates that the plume rise can be described by

$$h_p = \begin{cases} 2.6 [F/us]^{1/3} & ; \text{for windy conditions} \\ 5.0 [F^2/s^3]^{1/8} & ; \text{for near calm conditions} \end{cases} \quad (7.17)$$

In these expressions s is stability parameter defined in terms of the vertical potential temperature gradient.

$$s = \frac{g}{T} \frac{\partial \theta}{\partial z} \quad (7.19)$$

When calculating the plume rise h_p , the smaller of the values estimated by (7.17) and (7.18) should be used. The downwind distance

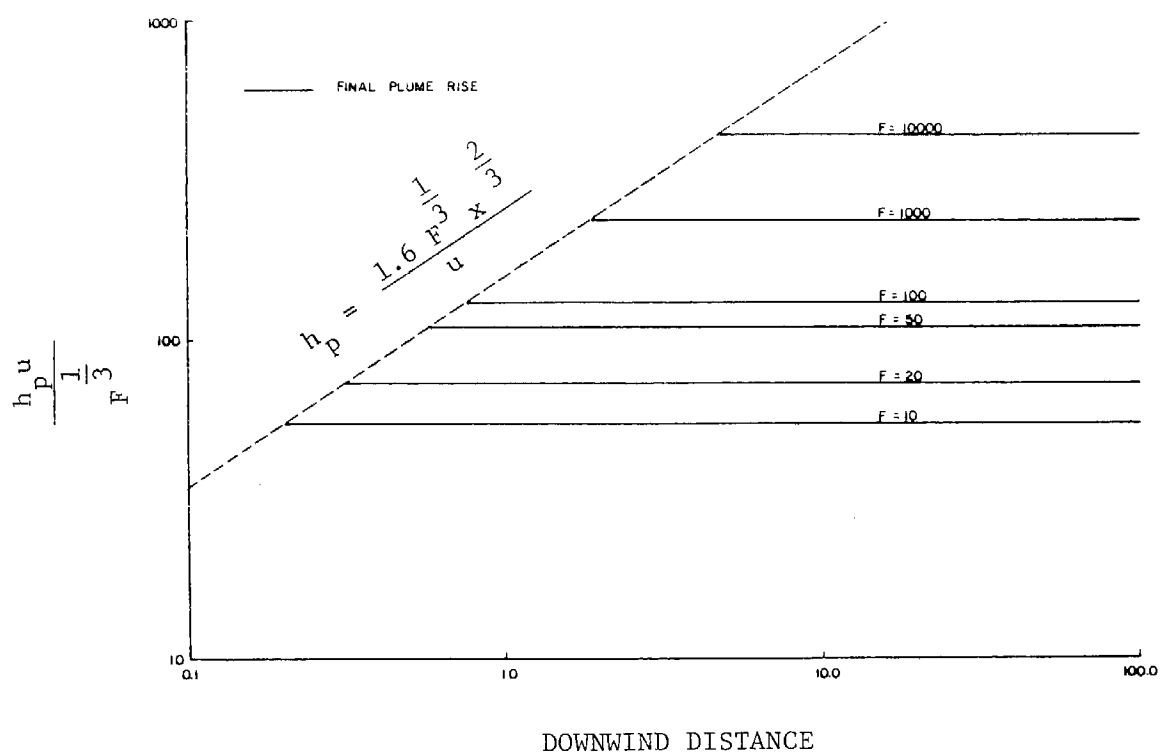


FIGURE 7.3
Limiting Plume Rise as a Function of the
Buoyancy Flux Parameter F .

to the final plume rise is given by

$$x_d = \pi u / \sqrt{s} \quad (7.20)$$

In some circumstances the appropriate field data will not be available for direct determination of the stratification parameter; for these situations s can be approximated using the information presented in Table 7.2.

7.5 Plume Penetration Into Elevated Stable Layers

In urban environments the surface layer is often capped by an elevated stable layer. Since the formulae presented in the previous sections are only valid for conditions of uniform stratification they provide little guidance in assessing the ability of buoyant plumes to penetrate into the inversion. This section presents a simple model that enables the study of plume penetration in an environment composed of a surface neutral layer below a stable, elevated temperature inversion. A schematic representation of the problem is shown in Figure 7.4. Note that for the purposes of the following analysis the inversion is considered to be deeper than the final plume rise.

As a first approximation consider the classic Morton et al. (1956) approach to plume rise in which there is no cross flow. If the Boussinesq approximation is invoked then the conservation equations for mass, momentum and buoyancy can be written in the form

$$\frac{d}{dz} (b^2 w) = 2\alpha b w \quad (7.21)$$

TABLE 7.2
Relationship Between Pasquill-Gifford Stability
Classes and Temperature Stratification

STABILITY CLASS	AMBIENT TEMPERATURE GRADIENT $\partial T / \partial z$ ($^{\circ}\text{C}/100\text{m}$)	POTENTIAL TEMPERATURE* GRADIENT $\partial \theta / \partial z$ ($^{\circ}\text{C}/100\text{m}$)
A (extremely unstable)	<-1.9	<-0.9
B (moderately unstable)	-1.9 to -1.7	-0.9 to -0.7
C (slightly unstable)	-1.7 to -1.5	-0.7 to -0.5
D (neutral)	-1.5 to -0.5	-0.5 to 0.5
E (slightly stable)	-0.5 to 1.5	0.5 to 2.5
F (moderately stable)	>1.5	>2.5

* Calculated by assuming $\frac{d\theta}{dz} \approx \frac{dT}{dz} + \Gamma$ where Γ is the adiabatic lapse rate ($0.986^{\circ}\text{C}/100\text{m}$).

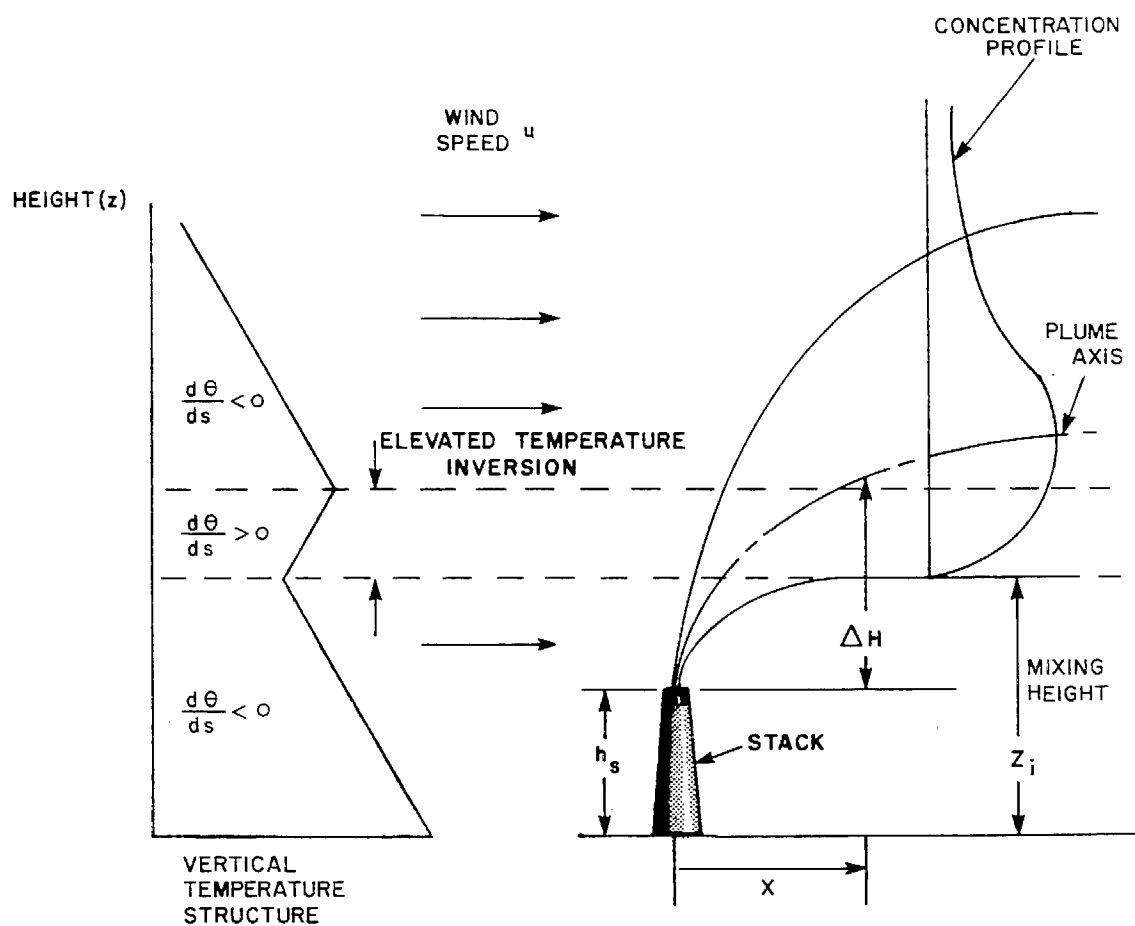


FIGURE 7.4

Nomenclature for Plume Rise Calculations

$$\frac{d}{dz} (b^2 w^2) = b^2 g \frac{T_1 - T}{T_a} \quad (7.22)$$

$$\frac{d}{dz} \left(b^2 w g \frac{T_1 - T}{T_a} \right) = b^2 w g \frac{dT_a}{dz} \quad (7.23)$$

where α is the entrainment coefficient, $w(z)$ the vertical velocity component, $b(z)$ the plume radius as a function of elevation z , T and T_1 are the temperatures inside and outside the plume. (T_a is a reference temperature, typically the ambient value at the same elevation as the top of the stack.) In the above formulation the vertical velocity and temperature have been assumed to be constant across the plume at any height. This formulation can be easily extended to the more conventional approaches of Csanady (1973) and Koh and Brooks (1975) in which the profiles are assumed to be Gaussian.

The buoyancy flux in (7.23) is given by

$$F_z = b^2 w g \frac{T_1 - T}{T_a} \quad (7.24)$$

Under neutral conditions $d(F_z)/dz$ is constant and so F_z is equal to F , the buoyancy flux at the stack exit. Equations (7.21) and (7.22) can be solved to give an expression for the change in buoyancy flux as a function of elevation and the temperature stratification parameter s , i.e.

$$\frac{dF_z}{dz} = -\frac{6\alpha}{5} \left(\frac{9\alpha}{10} \right)^{1/3} s F_z^{1/3} z^{5/3} \quad (7.25)$$

Starting at the stack top, where $F_z = F$, (7.25) can be integrated to find the elevation at which $F_z = 0$. This height defines the vertical extent of the plume rise. Since $s=0$ for $0 \leq z \leq Z_i$ the integral can be written in the form

$$\int_F^0 dfz = \frac{6\alpha}{5} \left(\frac{9\alpha}{10}\right)^{1/3} s F^{1/3} \int_{Z_i}^{z_e} z^{5/3} dz \quad (7.26)$$

Where z_e is the height of final plume rise. Evaluating the integral gives

$$z_e = Z_i \left[1 + \frac{20}{9\alpha} \left(\frac{10}{9\alpha}\right)^{1/3} \frac{1}{s} \left(\frac{F}{Z_i^4}\right)^{2/3} \right]^{3/8} \quad (7.27)$$

Which for a typical value of the entrainment coefficient, $\alpha = 0.124$, (Briggs, 1975) gives the following approximate expression for z_e

$$z_e = Z_i \left[1 + \frac{37}{s} \left(\frac{F}{Z_i^4}\right)^{2/3} \right]^{3/8} \quad (7.28)$$

Considering the finite size of the plume, complete penetration is likely to occur when $z_e = 1.3Z_i$. A similar analysis can be performed for the uniform cross flow case which results in an equilibrium plume rise of the form

$$z_e = Z_i \left[1.8 + \frac{19F}{usZ_i^4} \right]^{1/3} \quad (7.29)$$

A surprising feature of (7.29), also noted by Briggs (1975), is that

50% penetration ($z_e = z_i$) requires only 1/28 of the buoyancy required for 100% penetration ($z_e > 2z_i$). Within the airshed model the plume is considered to have penetrated the inversion base if

$$F > 0.3 u s z_i^3 \quad (7.30)$$

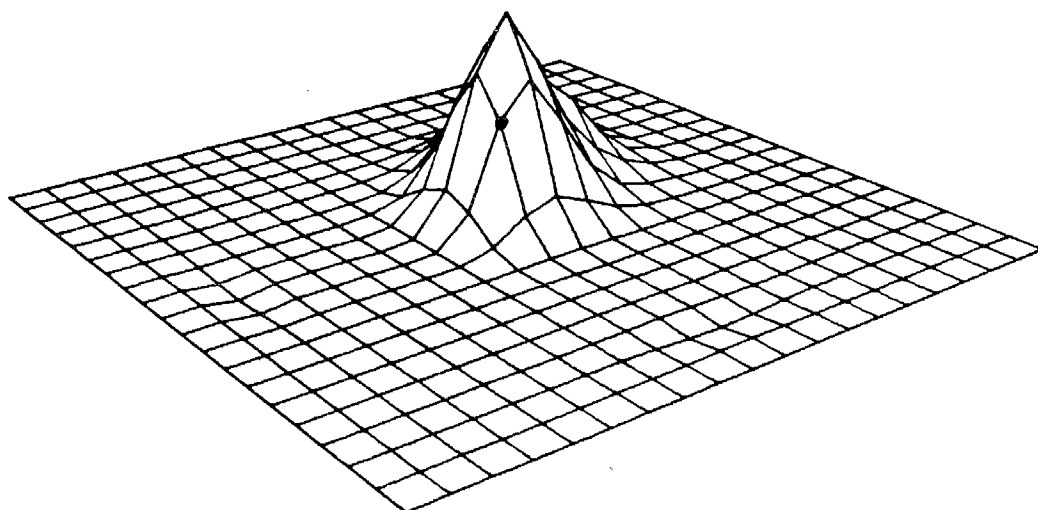
Because of the finite depth of the plume, partial penetration of elevated inversions probably occurs more often than total penetration. In either case it is important to have some estimate of the amount of material injected into the inversion. Manins (1979) presents laboratory results and a theoretical model of the conditions under which plumes can penetrate sharp, elevated temperature inversions. Of particular interest is the fact that his model can be used to predict the fraction of material trapped in the inversion layer and which will be available for subsequent fumigation. One of the more interesting findings of Manins' work was that so long as the plume remains in the inversion layer the amount of material trapped per unit downwind distance is approximately independent of wind speed.

In many situations the boundary layer temperature structure is more complicated than the simple two layer system described above. There are a number of integral plume models which can be used to predict plume dispersion in arbitrarily stratified environments. Some examples are described in the works of Schatzmann (1979), Ommes (1972), Briggs (1975) and Hirst (1972). Unfortunately none of these models result in simple analytic expressions and as a result they must be solved numerically.

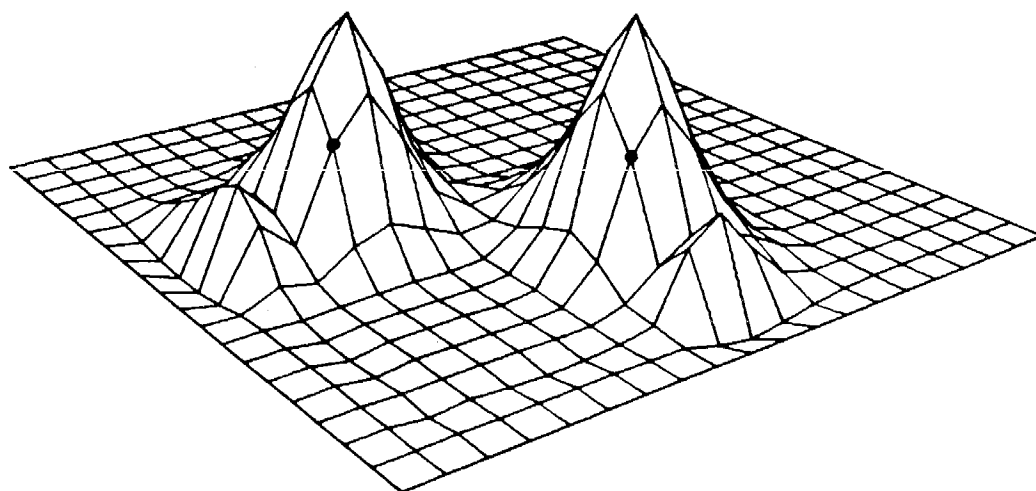
7.6 Treatment of Elevated Point Sources

Most previous models have either ignored the dispersion of pollutant material from elevated point sources (MacCracken et al., 1978) or treated them in a highly simplified manner (Reynolds et al, 1973). This is unfortunate since the contribution to both local and more distant pollutant levels can be quite significant. For example when the effective stack height is below the top of the mixed layer, the effluents can be rapidly downmixed within a short distance of the source. If the emissions are injected into the inversion the plume material can remain aloft for many hours, effectively isolated from the ground, until convective mixing erodes the stable layer. The point at which the fumigation occurs may be a considerable distance downwind from the source. This phenomenon was discussed in Chapter 5.

The most common allocation scheme for elevated point sources is to add the emissions from the source into the grid cell at the effective stack height. If all the material is injected into one cell the near source air quality impact can be overestimated. An even more serious drawback with this approach is that an isolated source can induce numerical dispersion errors that in turn can produce severe instabilities during numerical solution of the chemical kinetics. These errors can become even more severe when multiple sources are considered because the dispersive waves from each release can interact and be amplified (Figure 7.5). Some of these computational difficulties can be overcome by using the solution procedures described in Chapter 10.



(a)



(b)

FIGURE 7.5

Concentration Distributions Resulting from
Direct Point Source Injection into the
Computational Cells indicated by Dots

($u=v=2.2$ m/s, $t = 1.6$ hrs, $\Delta t = \Delta x = \Delta y = 3.2$ Km, $K_{xx}=K_{yy} = 100\text{m}^2/\text{sec}$)

In an earlier effort to avoid some of these problems, Reynolds et al. (1973) allocated the emissions to downwind computational cells on the basis of some Gaussian plume dispersion estimates. During the day-time the plume was considered to be well mixed in the vertical direction within a horizontal distance of two grid cells downwind from the source. Perhaps the most critical limitation of their procedure was that emissions injected above the top of the mixed layer were ignored.

The approach adopted in this study is to disperse the emissions downwind, taking into account the actual vertical and lateral spread of the plume as well as whether the effective stack height is above or below the top of the mixed layer. Lateral and vertical dimensions of the plume are obtained by assuming a Gaussian profile in each direction. In each direction the plume halfwidth is assumed to be 2σ which includes 95% of the plume mass. The dispersion coefficients σ_y and σ_z are functions of solar radiation, cloud cover, wind speed and surface roughness. The plume is assumed to extend downwind for a distance $u\Delta t$ where Δt is the averaging time of the wind data. If the vertical thickness of the plume, $4\sigma_z$, exceeds the mixed layer depth, the vertical thickness is taken to be the mixing height. Over the averaging time of the wind data, the plume is assumed to be uniformly mixed and to be essentially conical (Figure 7.6). With this assumption the fraction, F_{ijk} , of the elliptical cone volume that is within a given downwind grid cell, (i,j,k) , can be used to calculate the magnitude of the source contribution

$$S_{ijk} = \frac{E_p \Delta t}{\Delta x \Delta y \Delta z} F_{ijk} \quad (7.31)$$

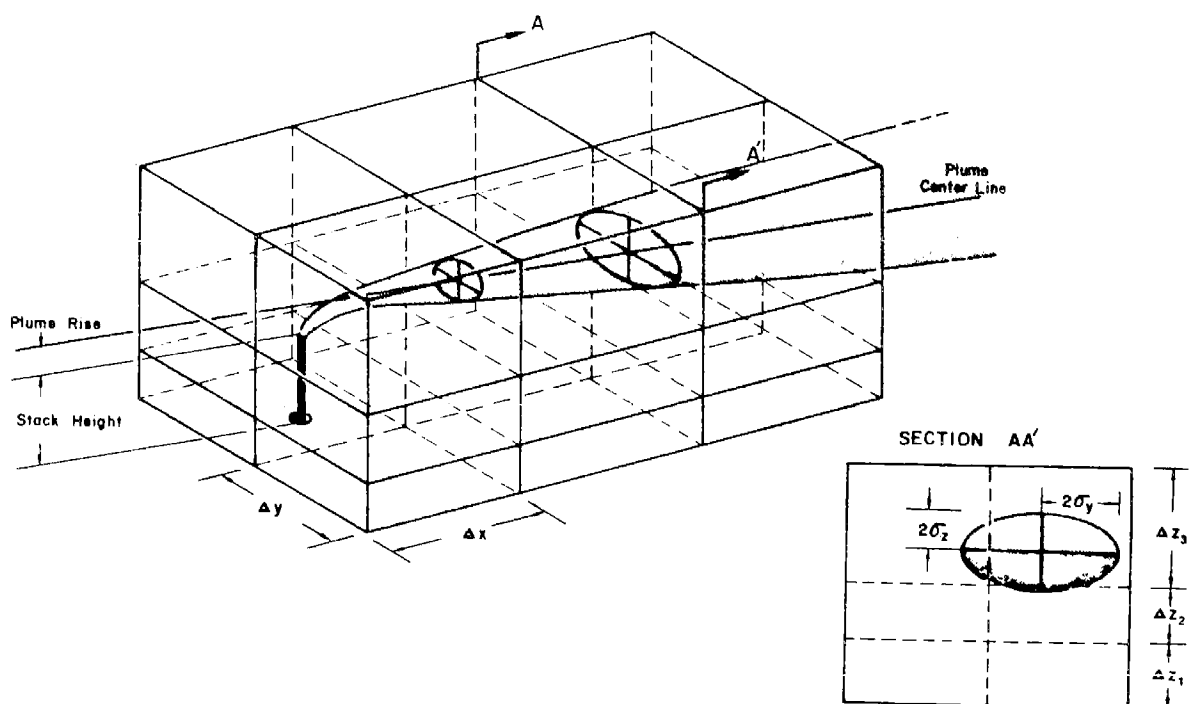
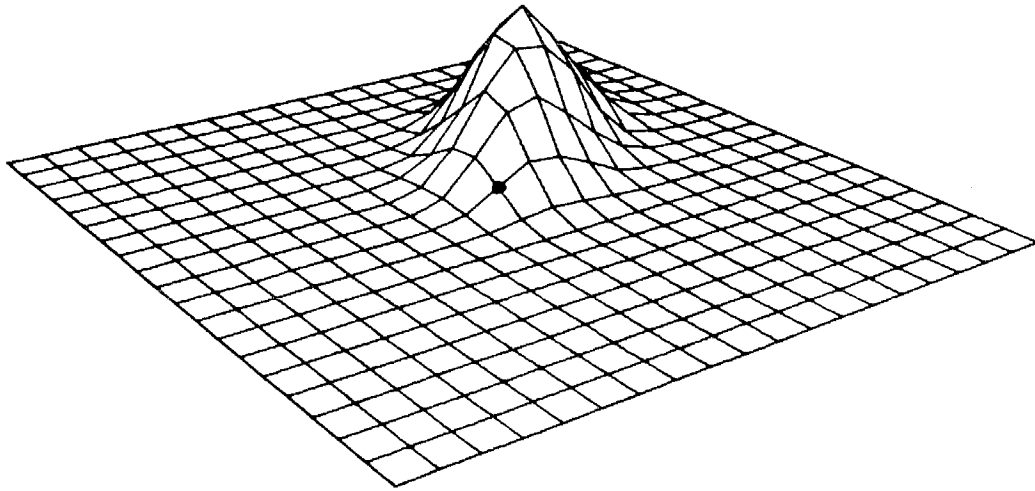
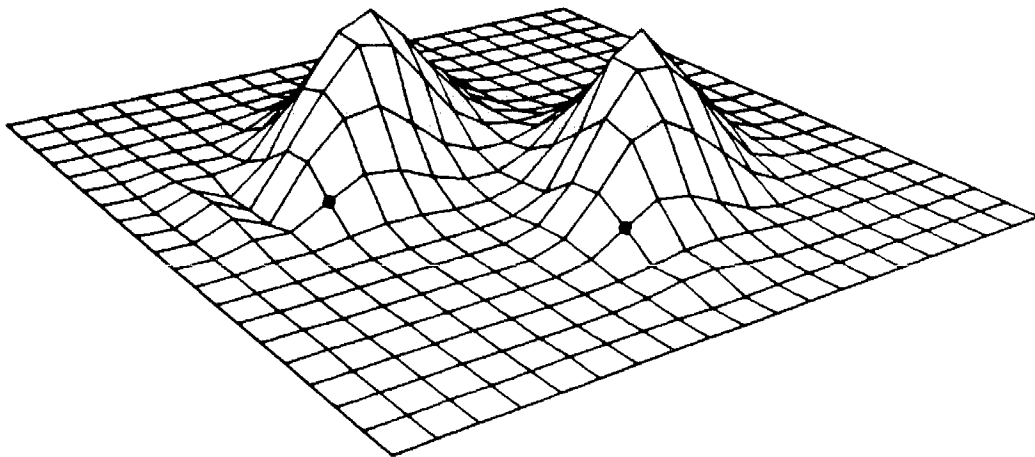


FIGURE 7.6
Plume Dispersion in Computational Grid

Figure 7.7(a) displays the concentration distribution resulting from a single source using this dispersion procedure. The upwind negative concentrations are much smaller than those resulting from the single cell source injection. Figure 7.7(b) shows the concentration distribution resulting from the same computational procedure but with two sources. The upwind dispersion errors, in both cases, are substantially less than those shown in Figure 7.5.



(a)



(b)

FIGURE 7.7

Same as Figure 7.6 except that the source injection is performed using the algorithm described in the text

7.7 Plume Dispersion Parameters

A key element of the source allocation procedure introduced in the previous section was the characterization of the plume growth in terms of the dispersion parameters σ_y and σ_z . While there is an extensive literature on procedures for estimating the coefficients, most of the commonly adopted schemes utilize the formulation presented in Turner (1970). Unfortunately the Turner Workbook is based on a limited set of field data and, more importantly, it does not accurately describe dispersion under unstable conditions. (Hanna et al., 1977; Gifford, 1976; and Pasquill, 1975, 1976). The recent work of Willis and Dear-dorff (1976, 1978), Lewellen and Teske (1975) and Lamb (1978, 1979) indicates that under convectively driven conditions both the mixed layer depth and the convective velocity scale have a significant impact on pollutant diffusion from elevated sources. Neither of these variables are included in typical Gaussian plume calculations. The objective of this section is to present an algorithm for predicting the plume growth in terms of readily available or estimated meteorological information. The procedure supplements the material presented in Chapter 4 and is partly based on the measurements and literature results assembled by Irwin (1979).

When describing the plume geometry it is important to ensure that the averaging times of the turbulence statistics and requirements for the concentration predictions are consistent. The basic problem is illustrated in Figure 7.8. As seen by a stationary observer, the mean concentration is influenced by meandering of the plume during the

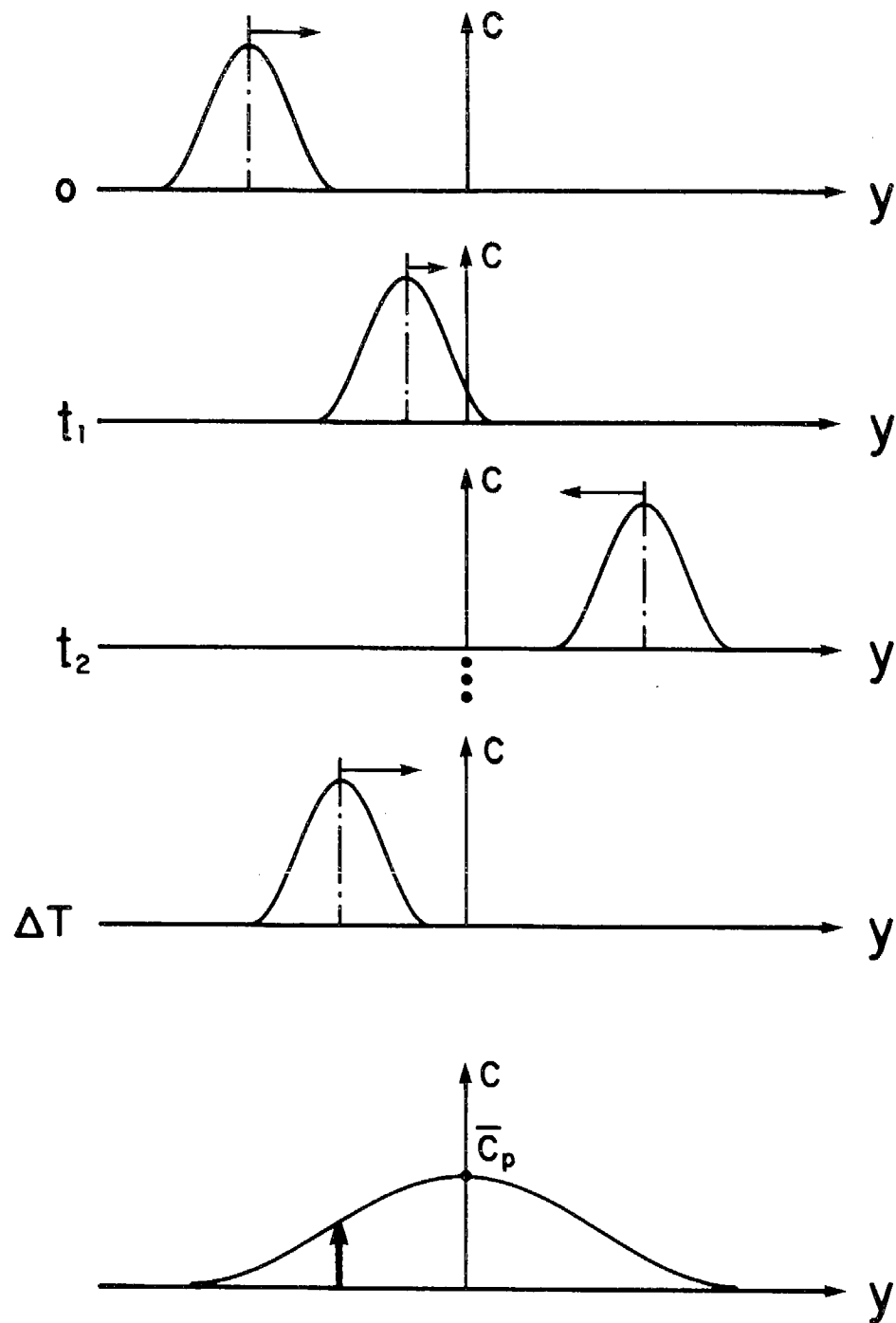


FIGURE 7.8
Instantaneous Concentrations and the Effect
of Temporal Averaging

experiment. Taylor (1921) addressed this issue and proposed a model for the average plume dimensions expressed in terms of the motion of single particles released from the point source. At a particular instant, however, the plume outline is defined by the trajectories of two particles released simultaneously by the source. The instantaneous plume width is described by the particle separation and the meander by the position of their center of mass. The need for distinguishing between the two cases becomes apparent when it is recognized that the plume chemistry is controlled by the instantaneous values and the observed ground level concentration by the average profile. Some initial ideas on the relationship between averaging times and particle statistics for different observed wind velocity spectra are presented in Sheih (1980). Further, more definitive work will require field data from a wider range of conditions. For the purposes of the present study it has been assumed that the averaging times for the dispersion coefficients are comparable with those of the meteorological data.

In the atmosphere σ_y and σ_z reflect the influence of the different physical phenomena acting on the plume. If the assumption is made that the various processes are additive (Pasquill, 1975) then the total dispersion in each direction can be represented by

$$\sigma_y^2 = \sigma_{a(y)}^2 + \sigma_{b(y)}^2 + \sigma_{s(y)}^2 \quad (7.32)$$

$$\sigma_z^2 = \sigma_{a(z)}^2 + \sigma_{b(z)}^2 \quad (7.33)$$

where the subscript a refers to the contribution from atmospheric

turbulence, b the fraction induced by the inherent buoyancy of the plume and s the additional cross wind spread arising from vertical wind shear. Since the primary purpose of the source allocation procedure is to maintain the plume integrity only until it has grown to the size of a typical computational cell, the effect on lateral dispersion from changes in the wind direction and speed with elevation can be ignored. Most of the research work and field investigations have been directed at formulating the contribution from atmospheric turbulence.

Under suitable assumptions on atmospheric stationarity and homogeneity Taylor (1921) showed that the diffusion parameters can be written in the general form

$$\sigma_{a(y)}^2 = 2 \overline{v'^2} \int_0^T \int_0^t R_y(\xi) d\xi dt \quad (7.34)$$

$$\sigma_{a(z)}^2 = 2 \overline{w'^2} \int_0^T \int_0^t R_z(\xi) d\xi dt \quad (7.35)$$

where T is the diffusion time and $R_{y,z}$ are the Lagrangian autocorrelations associated with the wind fluctuations v' , w' in the y and z directions. Close to the source $R(\xi) = 1$. In the limits of long diffusion times it is highly likely that the velocity fluctuations are uncorrelated and as a result $R(\xi) = 0$. For intermediate times measurement difficulties complicate characterization of the functional form of $R(\xi)$. In an effort to overcome some of the practical difficulties, Pasquill (1971) suggested an alternative definition that retained the

essential features of the Taylor formulation but which was more amenable to parameterization in terms of readily determined Eulerian quantities. In its most general form, as adopted by Draxler (1976), Hanna et al. (1977), and Irwin (1979), the Pasquill representation results in dispersion coefficients of the form

$$\sigma_{a(y)} = \sigma_v(\underline{P}) + F_y(\underline{P}) \quad (7.36)$$

$$\sigma_{a(z)} = \sigma_w(\underline{P}) + F_z(\underline{P}) \quad (7.37)$$

where the standard deviation of the wind fluctuations σ_v and σ_w and $F_{y,z}$ are universal functions of a set of parameters \underline{P} which specify the characteristics of the atmospheric boundary layer over a range of stability conditions.

The variables which comprise \underline{P} were introduced in Chapter 4 and include the friction velocity u_* , the Monin-Obukhov length L , the Coriolis parameter f , the mixed layer depth Z_i , the convective velocity scale w_* , the surface roughness z_0 and the height of the pollutant release above the ground z , i.e., $\underline{P} = \{ z, Z_i, u_*, w_*, z_0, L, f \}$. Details of the procedures used to determine these variables are discussed in Chapter 4.

For lateral dispersion, the standard deviation of the horizontal wind fluctuations can be written in the form

$$\sigma_v = \begin{cases} 1.78u_* \left[1 + 0.059 \left(-\frac{z_i}{L} \right) \right]^{\frac{1}{3}} & ; \frac{z_i}{L} < 0 \\ 1.78u_* & ; \frac{z_i}{L} \geq 0 \end{cases} \quad (7.38)$$

Irwin (1979) developed (7.38) by combining the results of Nieuwstadt and van Duuren (1979), Deardorff and Willis (1975), and Draxler (1976). For neutral and stable conditions, σ_v is based on the calculations described in Binkowski (1979).

Normally Monin-Obukhov similarity is valid only for $z/L < -2$; however, for convective conditions mixed-layer scaling can be applied throughout the whole boundary layer (Panofsky et al., 1977; Nieuwstadt, 1980). Using these results Irwin (1979) proposed the following forms for F_y .

$$F_y = \begin{cases} \frac{1}{1 + \left(\frac{t}{T_i} \right)^{\frac{1}{2}}} ; \frac{1}{T_i} = \frac{2.5u_*}{z_i} \left[1 + 0.0013 \left(-\frac{z_i}{L} \right) \right]^{\frac{1}{3}} ; \frac{z_i}{L} \leq 0 \\ \frac{1}{1 + 0.9 \left(\frac{t}{T_0} \right)^{\frac{1}{2}}} ; \frac{1}{T_0} = 1.001 ; \frac{z_i}{L} > 0 \end{cases} \quad (7.40)$$

(7.41)

An examination of (7.38-7.41) indicates that they have the same limiting behaviour predicted by the Taylor theory i.e. $\sigma_v \propto t$ for $t \rightarrow 0$ and $\sigma_v \propto \sqrt{t}$ for $t \rightarrow \infty$. Another interesting feature of the model is that there is no functional dependence on release height.

In contrast, the standard deviation of the vertical velocity fluctuations are closely related to the height of the pollutant release above the surface. The reason for this is that under unstable conditions the appropriate similarity variables are the convective velocity w_* and the mixed layer height Z_i (Willis and Deardorff, 1976). Using these variables a wide range of field and laboratory measurements can be described by a universal function of the form

$$\sigma_w = w_* G(z/Z_i) \quad (7.42)$$

Irwin (1979) has assembled a number of different data sets which characterize $G(z/Z_i)$. His results, shown in Figure 7.9, have been incorporated into the airshed model.

During neutral and stably stratified conditions the formulation developed by Binkowski (1979) can be used

$$\sigma_w = u_* \left[\frac{\phi_m\left(\frac{z}{L}\right) - \frac{z}{L}}{3kf_m} \right]^{\frac{1}{3}} \quad ; \quad \frac{z}{L} \geq 0 \quad (7.43)$$

In (7.43) k is the von Karman constant and $\phi_m(z/L)$ is given by

$$\phi_m\left(\frac{z}{L}\right) = 1 + 4.7 \left(\frac{z}{L}\right) \quad (7.44)$$

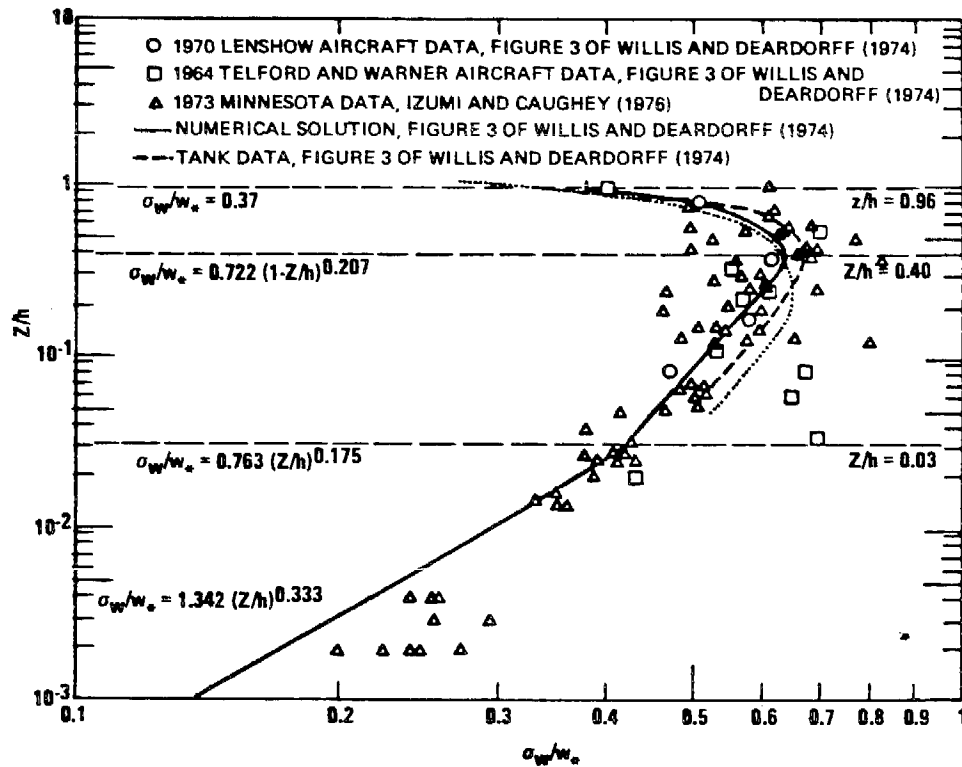


FIGURE 7.9

Vertical Profile of σ_w/w_* for Fully Convective Conditions
(After Irwin, 1979)

The reduced frequency f_m (Busch, 1973) at which the vertical velocity spectrum has its peak is given by

$$f_m = \begin{cases} 0.4 \left[1 + 3.9 \left(\frac{z}{L} \right) - 0.25 \left(\frac{z}{L} \right)^2 \right] & ; \frac{z}{L} \leq 2 \\ 0.4 \left[6.78 + 2.39 \left(\frac{z}{L} - 2 \right) \right] & ; \frac{z}{L} > 2 \end{cases} \quad (7.45)$$

$$(7.46)$$

Once the standard deviations of the wind velocity fluctuations have been established the next step is to complete parameterization of the vertical dispersion coefficients by specifying F_z . Some field and laboratory results for unstable conditions are shown in Figure 7.10, where the data have been plotted as a normalized function of the convective time scale Z_i/w_* . From an inspection of these graphs it is apparent that there are two different dispersion regimes, one for discharges above $0.1Z_i$ and the other for surface releases. Lamb (1979) has shown that locus of maximum concentration of a non-buoyant elevated plume ($z_s > 0.1Z_i$) follows a descending path that intercepts the ground at a downwind distance $x \sim 2z_s u/w_*$. For a surface source the locus of the maximum concentration ascends beginning at a distance of approximately $x = Z_i u/w_*$. The important features of the concentration field can be reproduced by the Gaussian plume model if the actual source elevation is replaced by a "virtual source height" H_e (Lamb, 1979). At present there are, unfortunately, no simple analytic expressions which describe the variation in F_z or H_e as a function of release height and stability. For the present study the data shown in Figure 7.10 are

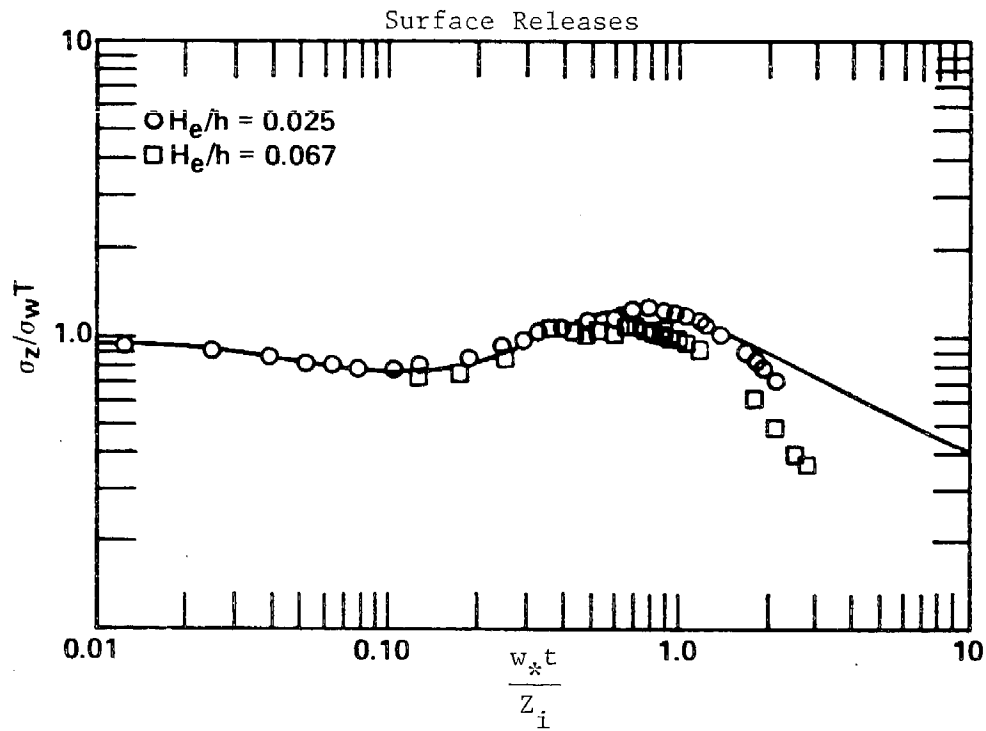
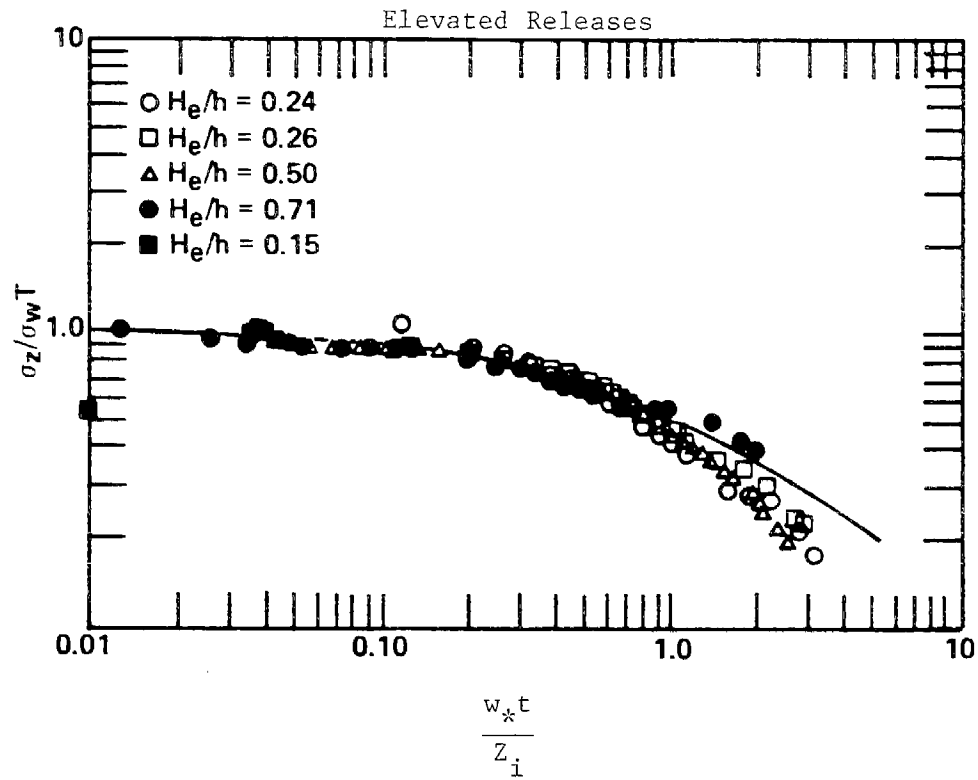


FIGURE 7.10

Values of F_z for Elevated Releases and
Near-Surface Releases during Convectively Unstable Conditions
(After Irwin, 1979)

employed directly in combination with (7.42). Between neutral conditions and $-Z_i/L$ less than 10 an interpolation formula due to Irwin (1979) is used.

Draxler (1976) developed the following results for neutral and stable conditions.

$$F_z = \begin{cases} \frac{1}{1 + 0.9 \left(\frac{t}{T_0} \right)^{\frac{1}{2}}} & ; \quad z < 50\text{m} \\ \frac{1}{1 + 0.945 \left(\frac{t}{T_0} \right)^{0.8}} & ; \quad z \geq 50\text{m} \end{cases} \quad (7.47)$$

The field data which formed the basis of (7.47-7.48) are shown in Figure 7.11. Both expressions require specification of the characteristic time T_0 . While an initial estimate of 50 seconds was given by Draxler, Irwin (1979) proposed the following functions after an analysis of additional field experiments and laboratory studies

$$T_0(\text{s}) = \begin{cases} 50 & ; \quad z < 50\text{m} \\ 1.52 - 25 & ; \quad 50 \leq z < 150\text{m} \\ 200 & ; \quad z \geq 150\text{m} \end{cases} \quad (7.49)$$

Even though most of the data examined by Irwin were for near neutral conditions the results are likely to have wider applicability because turbulence levels during stable conditions are relatively low.

So far in the discussion the plumes have been considered to be at the same temperature as the environment. If the source effluent is hot then the dispersion is influenced by both the ambient turbulence and

the buoyancy induced entrainment. Unfortunately there are few published studies which assess the relative importance of each process. As a result most descriptions of the source induced dispersion are based on theoretical formulations. Close to the stack the Taylor entrainment hypothesis predicts a linear relationship between the plume radius and the height of ascent. This is partially supported by the data reported in Briggs (1969) which indicate that the vertical spread is comparable to plume rise h_p . Pasquill (1975,1976) used this result to develop an estimate of the dispersion caused by the plume buoyancy. The Pasquill model assumes that the concentration distribution, across any cross section, is uniform. When modified for equivalent Gaussian profiles, the thermal dispersion coefficients utilized in the airshed model are given by

$$\sigma_b(y,z) = \frac{h_p}{2\sqrt{3}} \approx 0.3 h_p \quad (7.50)$$

As in all the previous formulations there is a clear need for additional field and laboratory data which can be used to test different models over a wide range of atmospheric conditions. This lack of suitable verification information considerably hampers the development of more refined descriptions of the dispersion of buoyant and passive exhaust gases.

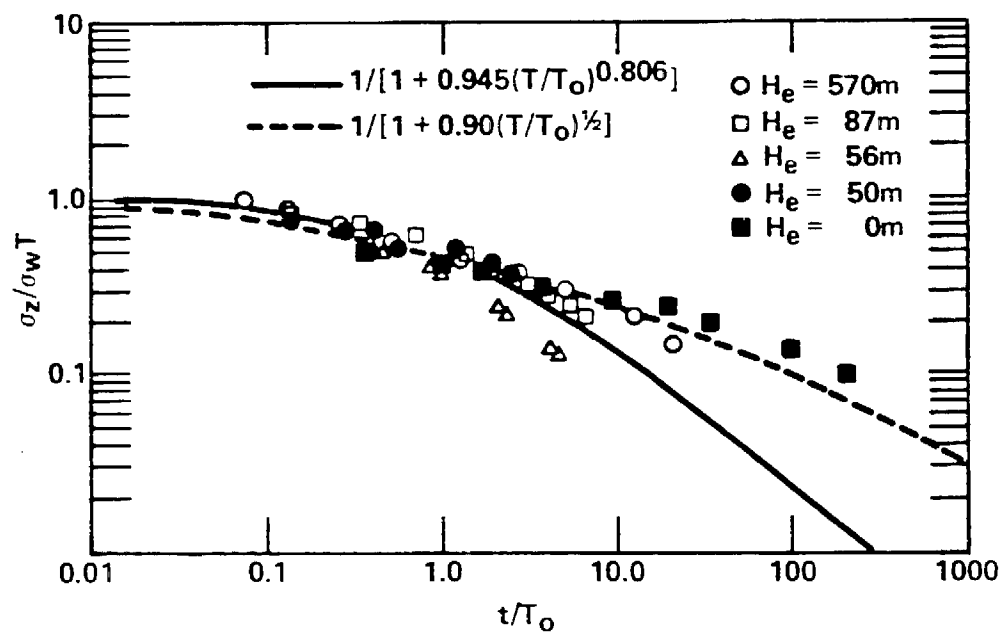


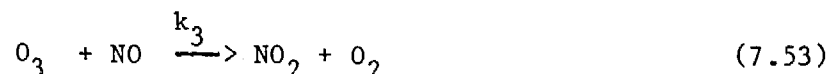
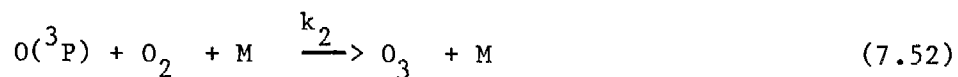
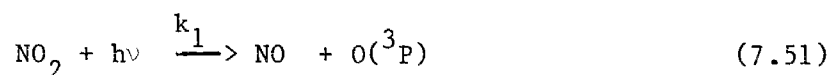
FIGURE 7.11

Values of F_z for Surface and Elevated Releases
During Neutral and Stable Conditions

(After Irwin, 1979)

7.8 Near Source Plume Chemistry

The combustion products from large point sources are rich in nitrogen oxides and typically have low concentrations of reactive hydrocarbons. As a result the near source plume chemistry is dominated by the following reactions.



Once the plume has grown to the size of a typical computational cell the full airshed model reaction mechanism, with its hydrocarbon and radical interactions, is more appropriate. The purpose of this section is to present a simple model which can be used to estimate the fraction of nitric oxide (NO) which is converted to nitrogen dioxide (NO_2) during the initial phase of plume dispersion.

Given a background ozone concentration of 0.04 ppm a simple calculation, using the rate constant data published in Hampson and Garvin (1977), predicts a typical NO half life of a few seconds. This calculation assumes that every available NO molecule in the plume encounters an ozone molecule. In reality the background ozone must diffuse into the NO rich plume. Because the chemical kinetics are so fast, relative to the characteristic mixing times, the overall conversion rates are

limited by the entrainment processes. There have been a number of theoretical studies (Kewley, 1978; Shu et al., 1978; White, 1979) as well as field measurements (White, 1977 and Hegg et al., 1977) which support this hypothesis for the reaction system (7.51 - 7.53).

At night the dominant reaction is (7.53); however, during daylight hours when $k_1 > 0$, an equilibrium is established amongst NO, NO₂, and O₃ which depends on the sunlight intensity. The NO₂ concentration levels are given by the photostationary approximation

$$\text{NO}_2 = \frac{k_3 \text{NO O}_3}{k_1} \quad (7.54)$$

An additional source of NO₂ is the thermal conversion process



In this reaction the NO₂ formation is proportional to (NO)² and, as a result, (7.55) is only significant when the NO concentration levels are high. This is the rationale for omitting the step in most photochemical reaction mechanisms. There are some circumstances, however, where the thermal oxidation can be important and these conditions are discussed in Section 7.9.

Ignoring, for the present, the NO₂ conversion from reaction (7.55), additional constraints are imposed on the NO-NO₂-O₃ system because of the fact that NO₂ + O₃ + O(³P) and NO + NO₂ are stoichiometric invariants. If surface removal processes are unimportant and the plume is considered to be well mixed across a transverse section, then the nitrogen and excess oxygen balances require that

Nitrogen:

$$\text{NO}_x(t) = \text{NO}_2(t) + \text{NO}(t) = D(t)\text{NO}_x(0) + [1 - D(t)]\text{NO}_x^b \quad (7.56)$$

Excess Oxygen (Ignoring $\text{O}({}^3\text{P})$):

$$\text{O}_x(t) = \text{NO}_2(t) + \text{O}_3(t) = D(t)[\text{NO}_2(0) + \text{O}_3(0)] + [1 - D(t)](\text{NO}_2^b + \text{O}_3^b) \quad (7.57)$$

In these expressions $D(t)$ refers to the plume dilution at time t , and $\text{NO}_x(0)$ to the stack concentrations and the superscript "b" to the background values. The dilution can be defined in terms of the change in the plume cross sectioned area as a function of time. If the initial transverse area is A_0 and is $A(t)$ at some later time t , then $D(t) = A_0/A(t)$. There is a simple relation between the dilution and the growth of a cross sectional segment of unit thickness; this expression is

$$\frac{1}{A(t)} \frac{dA(t)}{dt} = - \frac{1}{D(t)} \frac{dD(t)}{dt} \quad (7.58)$$

In addition to the dilution $D(t)$, the change in cross section can be expressed in terms of the dispersion coefficients, σ_y and σ_z ,

$$\frac{1}{A(t)} \frac{dA(t)}{dt} = \frac{1}{\sigma_y \sigma_z} \frac{d\sigma_y \sigma_z}{dt} \quad (7.59)$$

If the functional forms given by (7.36 - 7.37) are substituted into (7.59) then the dilution is given by

$$\frac{1}{A(t)} \frac{dA(t)}{dt} = \frac{\sigma_w}{\sigma_z} \left[F_z\left(\frac{t}{T_i}\right) + t \frac{dF_z}{dt} \right] + \frac{\sigma_v}{\sigma_y} \left[F_y\left(\frac{t}{T_i}\right) + t \frac{dF_y}{dt} \right] \quad (7.60)$$

When using expressions of the form (7.59 - 7.60) it is important to ensure that the dispersion parameters describe the instantaneous plume profile and not the time averaged envelope (White, 1977). The reason for this is that the meandering has no effect on the plume chemistry. The large scale fluctuations in wind direction do, however, influence the time averaged concentrations.

Since the ozone concentration in the stack exhaust gases is usually negligible, (7.57) can be written in the form

$$O_3(t) = b - NO_2(t) \quad (7.61)$$

where

$$b = D(t)NO_2(0) + [1 - D(t)](NO_2^b + O_3^b) \quad (7.62)$$

and the NO concentration is given by (7.56)

$$NO(t) = a - NO_2(t) \quad (7.63)$$

where

$$a = D(t)NO_x(0) + [1 - D(t)]NO_x^b \quad (7.64)$$

Combining (7.54, 7.61-7.64) produces a quadratic expression for $NO_2(t)$, the only physically realistic solution of which is given by

$$NO_2(t) = \frac{1}{2} \left[\left(a + b + \frac{k_1}{k_3} \right) - \sqrt{\left(a + b + \frac{k_1}{k_3} \right)^2 - 4ab} \right] \quad (7.65)$$

The variables a and b can be calculated from measurements of NO/NO_x in the stack exhaust, the dilution and the background concentrations of NO , NO_2 and O_3 . Given the rate constant ratio k_1/k_3 the downwind NO_2 concentration within the plume can be readily evaluated.

Some of the necessary corrections for the effects of turbulent fluctuations and concentration inhomogeneities are discussed in Shu et al. (1978) and White (1979). A variety of other methods for estimating short-term NO_2 impacts are reviewed in Cole and Summerhays (1979) and Peters and Richards (1977). One advantage of the formulation presented in this section is that it can be used in conjunction with conventional Gaussian plume models.

7.9 An Examination of the Contribution of Thermal NO Oxidation to the Formation of NO₂.

When nitrogen oxides (NO_x) are reported in source inventories they are frequently expressed in terms of equivalent emissions of nitrogen dioxide (NO₂) even though the exhaust NO_x is composed primarily of nitric oxide (NO). Unless the initial NO₂/NO_x ratio is specified from instack measurements it is necessary to establish appropriate fractions for reconstructing the actual emission levels of NO and NO₂. Depending on the source, and the characteristics of its combustion process, the fraction can vary from approximately 1 to 10%. In addition to the NO₂ formed during combustion, some small quantities can be formed in the exhaust gases by the third order reaction



This reaction step is normally ignored in photochemical reaction mechanisms because of the low ambient levels of nitric oxide. The objective of this section is to present a very simple model which can be used to estimate the fraction of NO which is converted to NO₂ in the vicinity of the source. The intent is not to add an additional reaction step to the airshed model chemistry but rather to develop a simple approach for augmenting the emission inventory NO₂/NO_x ratio.

If the plume is considered to be well mixed across each transverse section then the nitric oxide (NO) decay rate is given by

$$\frac{d(\text{NO})}{dt} = -2 k_4(T)(\text{NO})^2(\text{O}_2) + \frac{1}{D(t)} \frac{dD(t)}{dt} (\text{NO} - \text{NO}^b) \quad (7.67)$$

where $D(t)$ is the plume dilution as defined in Section 7.8 and NO^b is the background concentration of nitric oxide. The nitrogen mass constraint enables the direct calculation of NO_2 from

$$\text{NO}_2(t) = D(t)\text{NO}_x(0) + [1 - D(t)]\text{NO}_x^b - \text{NO}(t) \quad (7.68)$$

In (7.67) the second order reaction rate constant, in $\text{ppm}^{-2}\text{-min}^{-1}$ units, is of the form (Baulch et al., 1978)

$$k_4(T) = \frac{1.066 \times 10^{-5}}{T^2} \exp(530/T) \quad (7.69)$$

Even though the above expressions are straightforward, the NO concentration dynamics downwind from the stack are not immediately obvious. While entrainment of cool ambient air into the plume causes an increase in the magnitude of $k_4(T)$ (Figure 7.12), the plume dilution also results in a reduction of NO. This interplay between cooling and dilution can be described by integrating the species rate equation. If the background contribution in (7.67) is ignored then the NO concentration decay is given by

$$\text{NO}(t) = \frac{\text{NO}(0) D(t)}{1 + 2\text{NO}(0) \int_0^t k_4(T) \{D(t)\text{O}_2 + [1 - D(t)]\text{O}_2^b\} D(t) dt} \quad (7.70)$$

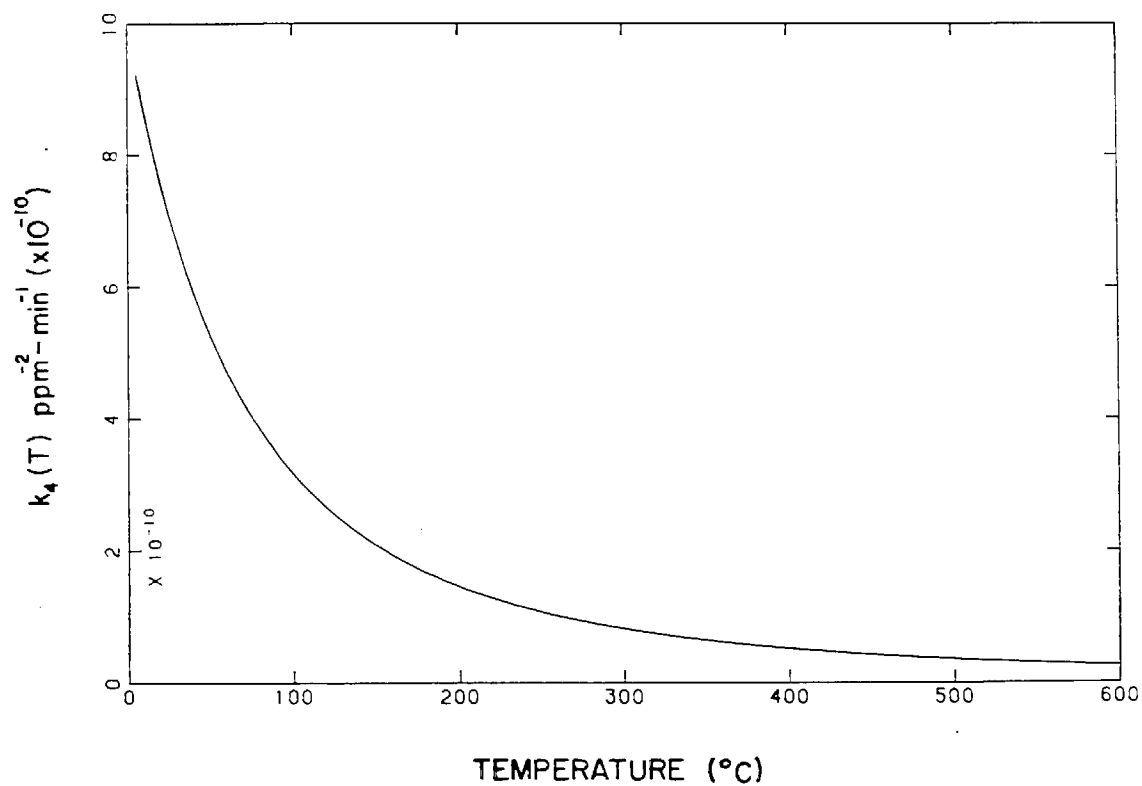


FIGURE 7.12
 Variation of $\text{NO} + \text{NO} + \text{O}_2 \xrightarrow{k_4(T)} 2\text{NO}_2$ Reaction Rate
 Constant as a Function of Temperature

Within the plume, the oxygen and temperature distributions are given by

$$O_2(t) = O_2^b + D(t)[O_2(0) - O_2^b] \quad (7.71)$$

$$T(t) = T^b + D(t)[T(0) - T^b] \quad (7.72)$$

While details of near source dilution characteristics can be found in Fischer et al. (1979), an approximate form was adopted in this study

$$D(t) = \exp[-0.15t] \quad ; \quad t < 30 \text{ s} \quad (7.73)$$

Given the initial and background conditions for NO_x , T and O_2 the system of equations (7.67 - 7.73) can be solved to give the conversion fractions for short travel times. Figure 7.13 presents the results of one such calculation where the initial $NO_2(0)/NO_x$ ratio was 5.0%, $O_2(0) = 3\% = 30000 \text{ ppmV}$, and the instack NO was varied from 200 to 2000 ppmV. A comparison between the pure dilution cases and those in which the chemistry was included indicates that between 2 and 12% of the increase in NO_2 concentration at any travel time can be explained by thermal oxidation. Two conclusions are apparent from this investigation. The first is that, close to the source, the reaction step can be significant, which in turn implies that more attention needs to be given to characterizing the stack exhaust gas concentration and temperature distributions when assembling emission inventory information. Since the effects of thermal oxidation are minimal when the dilution is high, there is no need to include the reaction step (7.66) in the airshed model. The incremental conversion can be incorporated by simply increasing the initial NO_2/NO_x emission inventory ratio.

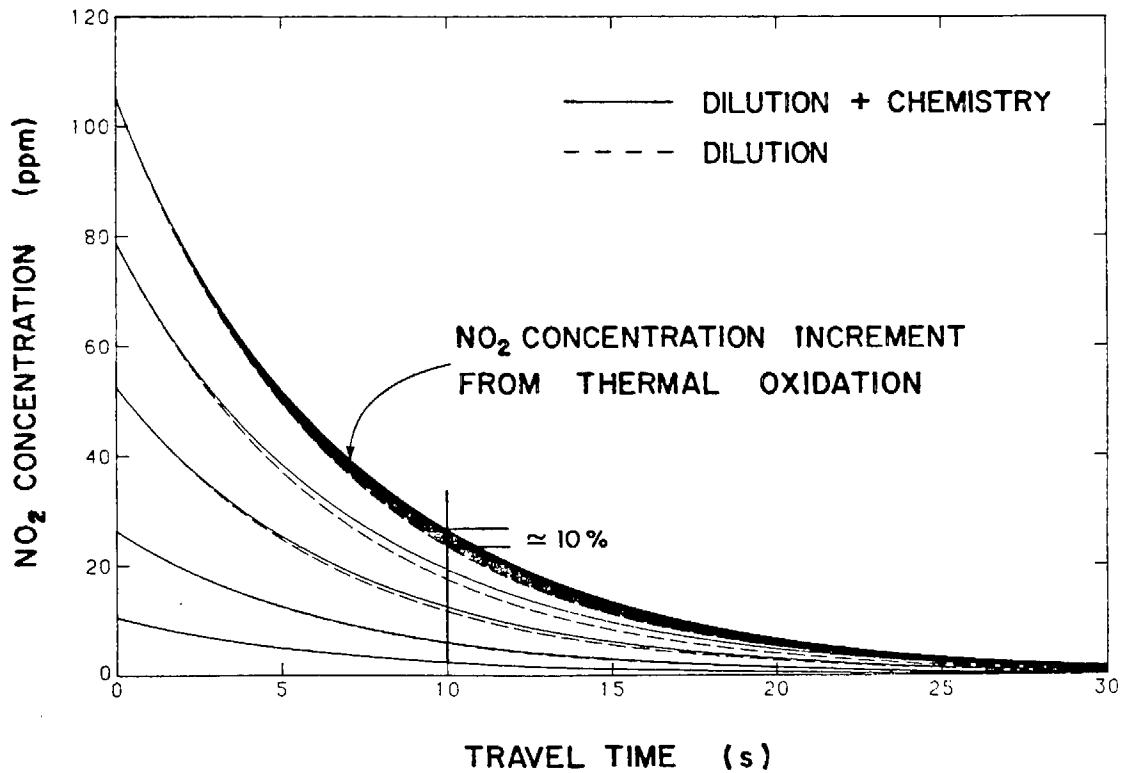
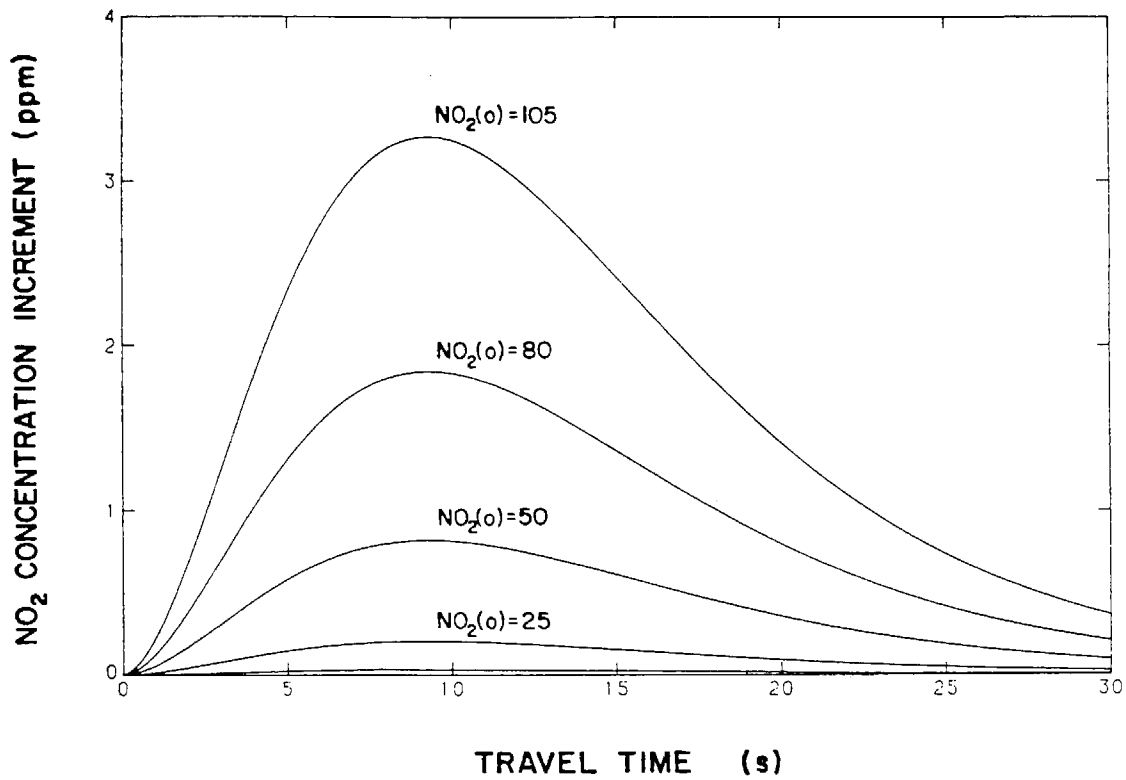


FIGURE 7.13

NO_2 Concentrations as a Function of Travel Time
 Stack conditions $T = 250^\circ\text{C}$, $\text{O}_2 = 3\%$, $\text{NO}_2(o)/\text{NO}_x = 0.05$, $\text{NO}_2^b = 0.02$.

7.10 Conclusions

This chapter has described how both point and area source emissions are treated in the airshed model. Of particular interest is an improved method for allocating elevated emissions discharges into a three-dimensional computational grid. When coupled with suitable selection criteria that identify whether a particular source should be treated as an elevated release, the procedure significantly reduces the numerical dispersion errors associated with conventional allocation schemes. Some preliminary work on the treatment of plume rise in a non-uniformly stratified environment resulted in a simple criterion that establishes whether a plume can penetrate an elevated temperature inversion. In addition to formulating the plume rise models some consideration was given to the characteristics of the near source chemistry and, in particular, the role of thermal oxidation of nitric oxide to NO_2 .

There is a critical need for more field measurements which can be used to verify different models of plume dispersion, trapping and subsequent fumigation.

CHAPTER 8

PRACTICAL IMPLEMENTATION OF A PHOTOCHEMICAL
REACTION MECHANISM WITHIN AN AIRSHED MODEL8.1 Introduction

Photochemical air pollution is formed as a result of a complex interaction between sunlight, meteorology and primary emissions of nitrogen oxides and reactive hydrocarbons. The development of a reaction mechanism that accurately describes the atmospheric chemistry and which, at the same time, is computationally tractable is a complex undertaking. The task is complicated by the need to maintain a balance between the level of chemical detail and minimizing, for numerical reasons, the number of species and reaction pathways. This dilemma is particularly apparent when considering hydrocarbon chemistry. In a typical urban atmosphere literally hundreds of different hydrocarbons are present. Under most circumstances it is simply not feasible to incorporate the reaction steps for each species. As a result two basic approaches have been developed to characterize the hydrocarbon chemistry: surrogate and lumped reaction mechanisms.

Surrogate mechanisms are those in which the organic species in a particular class, e.g. olefins, are represented by one or more members of that class, e.g. propylene. In general these mechanisms, typified by Graedel et al. (1976) and Dodge (1977), tend to have a large number of reaction steps and are not practical in situations where the meteorological transport model involves more than a few computational

cells. The second approach to the problem is to use chemical lumping in which one or more reactants, of similar structure and reactivity, are grouped together into a single class. A basic objective is to take advantage of the common features of the hydrocarbons and free radicals in order to minimize the number of species while at the same time maintaining a high degree of detail for the inorganic reactions. In the present study the lumped mechanism, developed by Falls and Seinfeld (1978), has been used. Their mechanism represents the atmospheric hydrocarbon mixture by six classes: ethylene, other olefins, alkanes, aromatics, formaldehyde and higher aldehydes. Other examples of lumped mechanisms are described in Eschenroeder and Martinez (1972), Gelinas and Skewes-Cox (1975), Hecht and Seinfeld (1972), Hecht et al. (1974), MacCracken and Sauter (1975) and Whitten et al. (1979).

The basic objective of this chapter is to provide sufficient information regarding initial conditions, rate constants and stoichiometry to allow an independent verification of the Falls and Seinfeld (1978) mechanism. Their mechanism was selected, for the airshed model, because it incorporates recent information on rate constants, mechanistic structure and, in addition, has been successfully validated against a wide range of smog chamber experiments. Since an extensive analysis of the chemical basis of the reaction scheme is available in the cited reference it will not be repeated here. Subsequent sections of this chapter present the results of a series of tests designed to examine the numerical properties of the kinetics, the adequacy of some

psuedo steady state approximations and the mechanism consistency as evidenced by mass balance checks. While primary emphasis is given to the Falls and Seinfeld (1978) formulation, much of the discussion in subsequent sections can be easily applied to other mechanisms.

8.2 Chemical Reaction Source Term and Mechanism Definition

Within the airshed model the ambient chemistry is represented by the presence of reaction terms, R_i ; $i = 1, 2, \dots, n$, in the atmospheric diffusion equation. This section presents the detailed formulation of the mathematical form and structure of these terms. Consider a homogeneous, isothermal, isobaric system in which n single phase species, c_i , $i = 1, 2, \dots, n$, simultaneously participate in m elementary reaction steps. Formally, the reaction set can be written in terms of linear combinations of species called complexes (Horn and Jackson, 1972).

$$\sum_{i=1}^n r_{ji} c_i \rightarrow \sum_{i=1}^n p_{ji} c_i \quad j = 1, 2, \dots, m \quad (8.1)$$

The reactant and product stoichiometry in reaction step j is defined by the coefficients r_{ji}, p_{ji} . In general, these coefficients are such that mass is conserved in each elementary reaction; however, there are circumstances, to be discussed later, in which this condition must be relaxed. Note that the sum in (8.1) extends over all n species to allow for the possibility that a given species can participate in a reaction step as both a product and a reactant. Equation (8.1) can be written

in a more compact matrix notation in which $\{c\}$ is interpreted as a concentration vector $c = [c_1, c_2, \dots, c_n]^T$ and where the reactant and product stoichiometric matrices $[R]$, $[P]$ are of dimension $m \times n$:



If the rates f_j of the m individual reactions are given, the following set of ordinary differential equations, together with appropriate initial conditions, is a basis for describing the kinetics of the reaction set embedded in the airshed model (Cavalas, 1968; Aris, 1965).

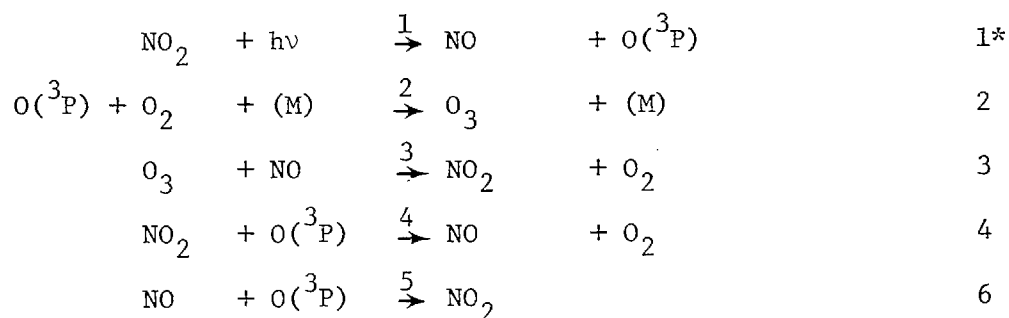
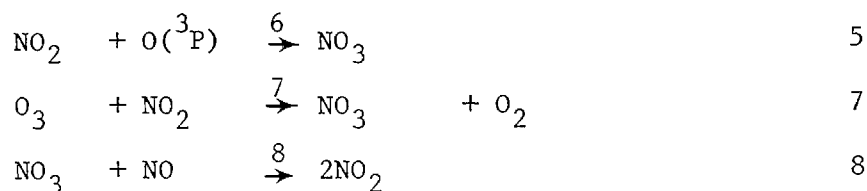
$$\frac{d\{c\}}{dt} \equiv \{\dot{c}\} = [S]^T \{F\} = g(c) \quad (8.3)$$

where $[S]$ is the $m \times n$ stoichiometric matrix defined by $[P] - [R]$, $\{F\}$ is an $m \times 1$ vector of rate functions f_j , and $g(c)$ can be interpreted as a non-linear transformation which maps points from \mathbb{R}^m into \mathbb{R}^n . In general the matrix $[S]$ has no special properties, such as symmetry, band or block structure, except that the number of differential equations clearly has the upper bound: $\text{rank}(S) \leq \min(m, n)$.

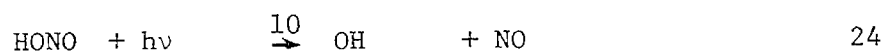
For definitional purposes the chemical mechanism embedded in the airshed model is reproduced in Table 8.1. Each species and its symbolic representation is shown in Table 8.2. In this latter table the last column indicates whether the species is described by one of the following mathematical types: a differential equation (D), a pseudo steady state approximation (PSSA), a constant (C) or as an uncoupled

TABLE 8.1

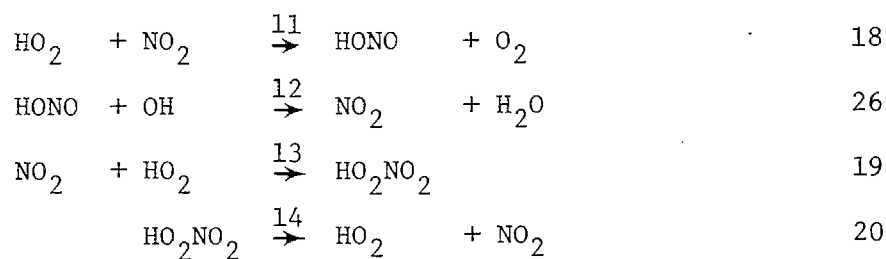
CHEMICAL MECHANISM USED WITHIN AIRSHED MODEL

Photolysis of NO_2 and basic NO - NO_2 - O_3 photolytic cycleChemistry of NO_3 (nitrogen trioxide)

Nitrous acid and peroxy nitrous acid chemistry

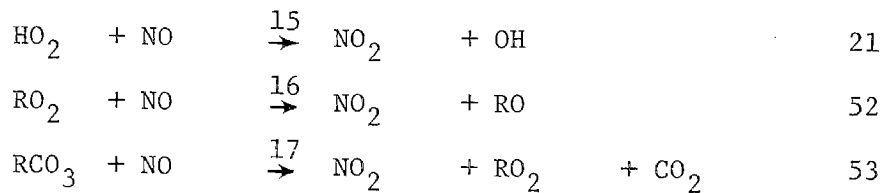
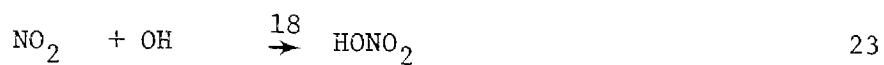
Photolysis of HONO 

Nitrous acid chemistry

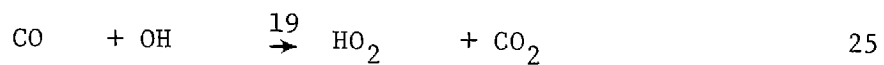


*These numbers correspond to reactions presented in Tables I-III of Falls and Seinfeld (1978)

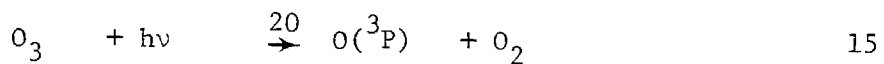
TABLE 8.1 (Continued)

Conversion of NO to NO₂Nitric acid (HONO₂) formation

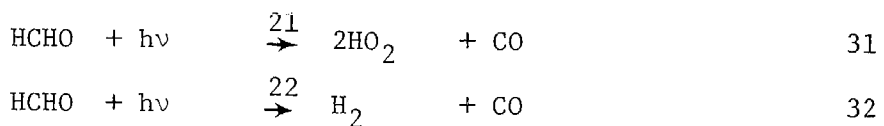
Hydroperoxyl radical formation



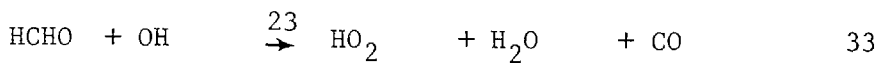
Photolysis of ozone



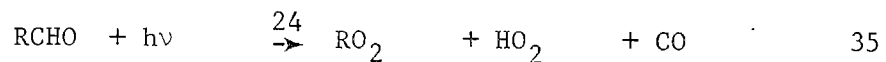
Photolysis of formaldehyde



Formaldehyde chemistry



Photolysis of higher aldehydes

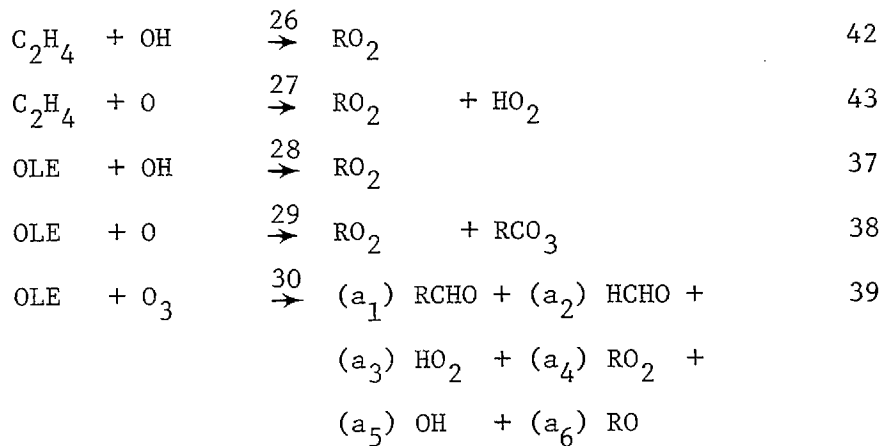


Higher aldehyde chemistry

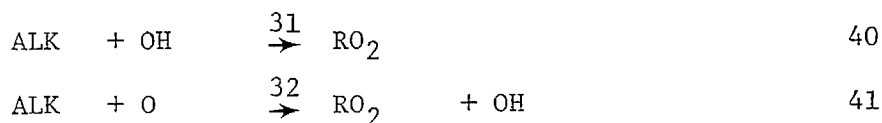


TABLE 8.1 (Continued)

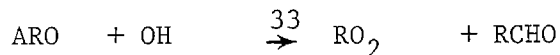
Olefin chemistry (OLE)



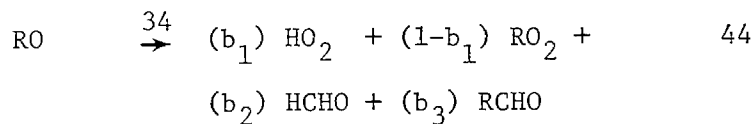
Alkane chemistry (ALK)



Aromatic chemistry (ARO)



Alkoxy radical chemistry



Photolysis and chemistry of RONO

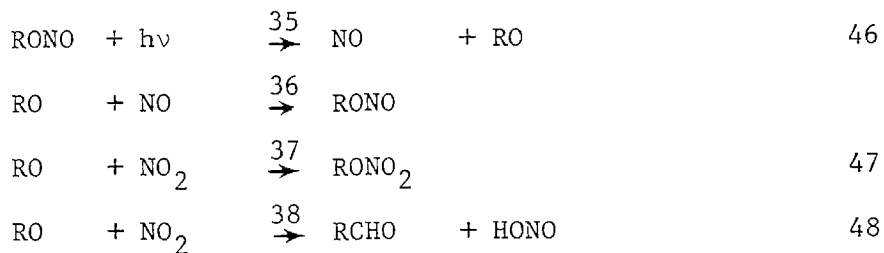
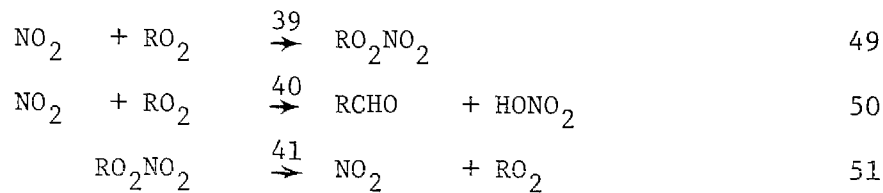
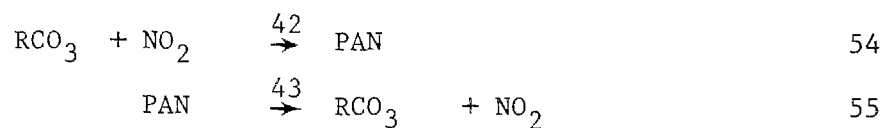
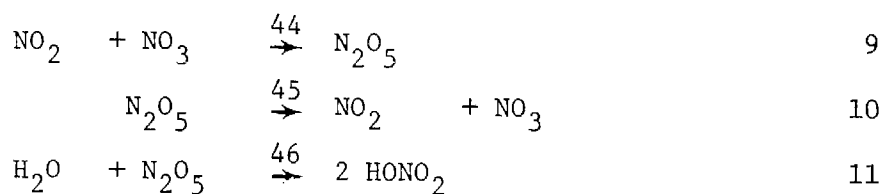


TABLE 8.1 (Continued)

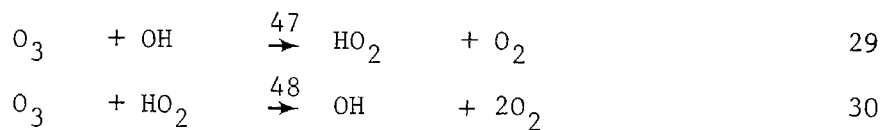
Peroxy nitrate chemistry



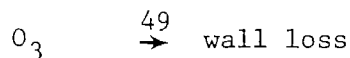
Peroxyacyl nitrate (PAN) chemistry

Dinitrogen pentoxide (N_2O_5) chemistry

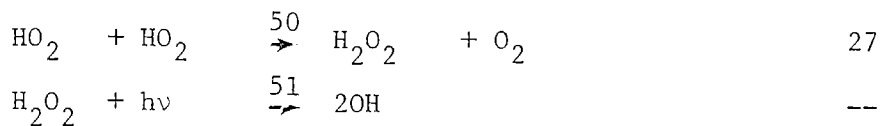
Ozone removal steps



Ozone wall loss term for smog chamber experiments



Hydrogen peroxide production and photolysis



Recombination Reaction for peroxyalkyl radicals



TABLE 8.2

Chemical Species Participating in Photochemical Reaction Mechanism

SPECIES ^a		NAME	TREATMENT IN AIRSHED MODEL ^b
1	NO	Nitric Oxide	D
2	NO ₂	Nitrogen Dioxide	D
3	O ₃	Ozone	D
4	HCHO	Formaldehyde	D
5	RCHO	Higher Aldehydes	D
6	OLE	Lumped Olefins	D
7	ALK	Lumped Alkanes	D
8	ARO	Lumped Aromatics	D
9	C ₂ H ₄	Ethylene	D
10	CO	Carbon Monoxide	D
11	H ₂ O ₂	Hydrogen Peroxide	D
12	PAN	Peroxyacetyl nitrate	D
13	HONO	Nitrous Acid	D
14	RONO	Alkyl Nitrite	D
15	RNO ₄	Peroxyalkyl Nitrate	D
16	N ₂ O ₅	Dinitrogen Pentoxide	PSSA
17	HNO ₄	Peroxynitric Acid (HO ₂ NO ₂)	PSSA
18	RCO ₃	Peroxyacyl Radical	PSSA
19	HO ₂	Hydroperoxyl Radical	PSSA
20	NO ₃	Nitrogen Trioxide	PSSA
21	RO ₂	Alkylperoxy Radical	PSSA

TABLE 8.2 (Continued)

SPECIES ^a		NAME	TREATMENT IN AIRSHED MODEL ^b
22	OH	Hydroxyl Radical	PSSA
23	RO	Alkoxyl Radical	PSSA
24	O	Atomic Oxygen	PSSA
25	CO ₂	Carbon Dioxide	P
26	RNO ₃	Alkyl Nitrate (RONO ₂)	P
27	HNO ₃	Nitric Acid (HONO ₂)	P
28	H ₂	Hydrogen	P
29	LOSS	Ozone loss term for smog chamber experiments	P
30	H ₂ O	Water	C
31	O ₂	Oxygen	C
32	M	Third Body	C

Notes:

- a. Species name is restricted to four characters for computational reasons.
- b. Treatment of species within the airshed model chemistry
- D - Differential Equation
 - PSSA - Pseudo Steady State Approximation
 - C - Constant species during one integration step
 - P - Product species ignored in some applications.

differential form (P). The structure and interrelation among all elements of the mechanism are shown in Figure 8.1.

The Jacobian matrix of the system of differential equations is frequently required as a component of numerical solution procedures and for sensitivity analyses. For the set of equations defined by (8.3) and (8.4) the Jacobian is given by

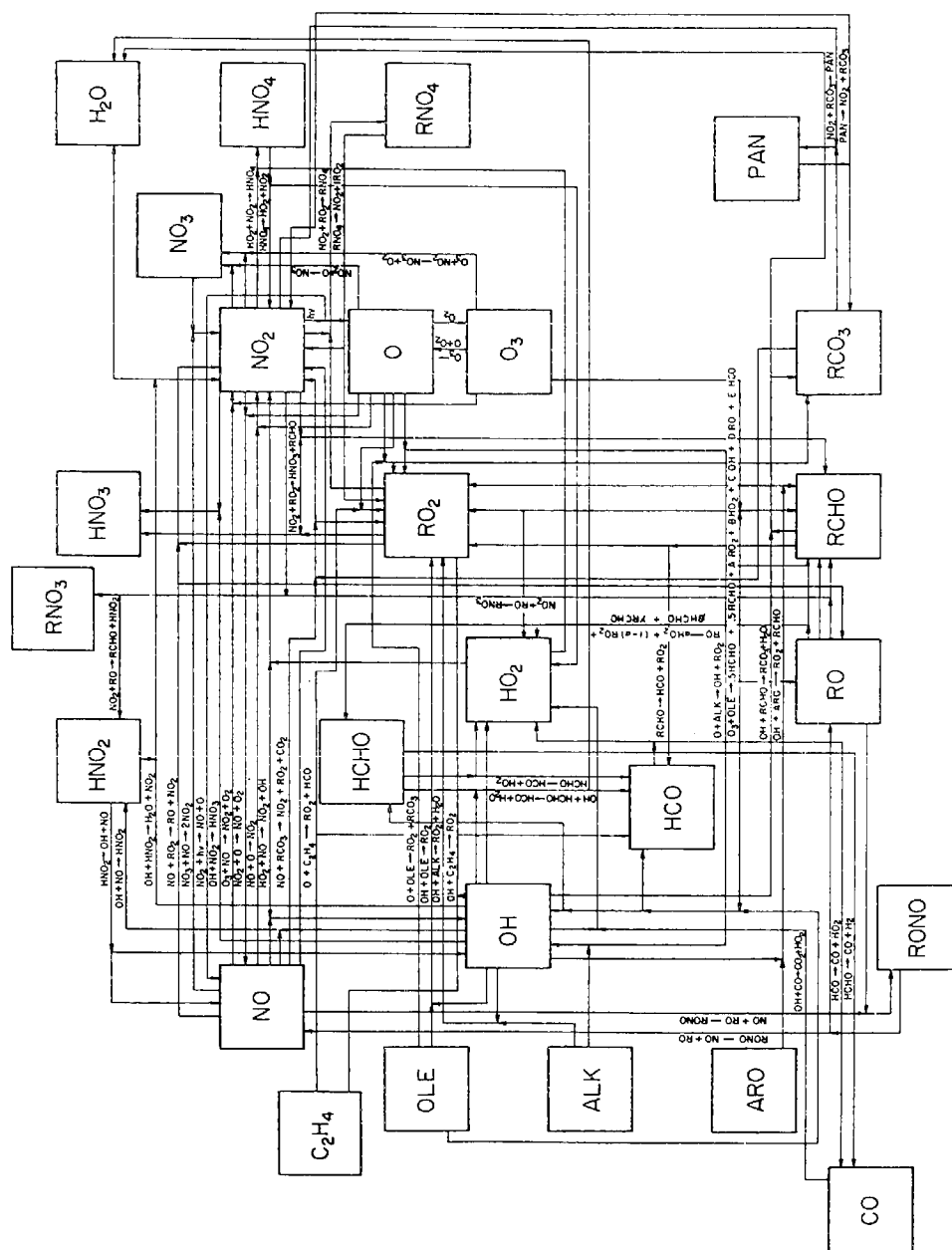
$$J \equiv \frac{\partial \{\dot{c}\}}{\partial \{c\}} = [S]^T \frac{\partial \{F\}}{\partial \{c\}} \quad (8.4)$$

A number of species in the mechanism appear only as products and as a result can be treated as uncoupled differential equations. Partitioning the concentration vector to reflect this division, (8.3) can be written as

$$\{\dot{c}\} = \begin{Bmatrix} \dot{c}_c \\ \dot{c}_p \end{Bmatrix} = \begin{Bmatrix} g_c(c_c) \\ g_p(c_c) \end{Bmatrix} \quad (8.5)$$

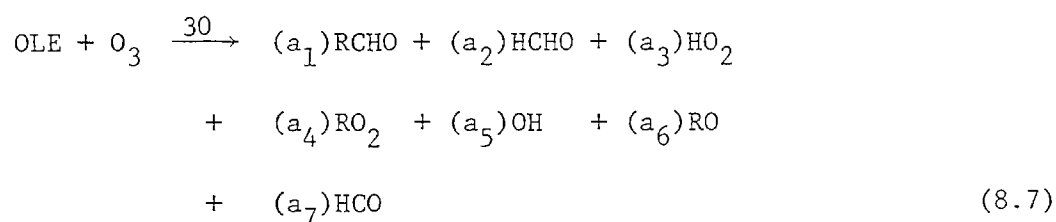
where the subscripts refer to the coupled (c) and product (p) species. Since the $\{c_p\}$ can be expressed as functions of $\{c_c\}$, their concentrations are readily determined for any interval $[t_0, T]$ by standard numerical quadrature procedures by evaluating integrals of the form

$$\{c_p(T)\} = \{c_p(t_0)\} + \int_{t_0}^T \{g_p(c_c)\} dt \quad (8.6)$$



8.3 Stoichiometric Coefficients for the Lumped Reactions

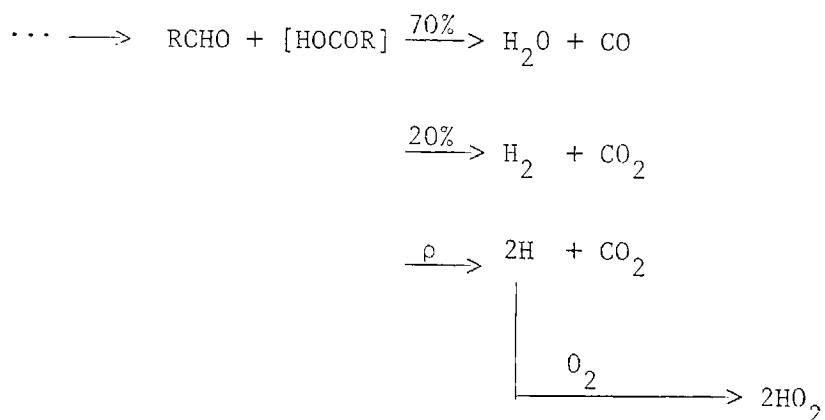
Two reactions in the Falls and Seinfeld (1978) mechanism require specification of stoichiometric coefficients. The first is the lumped ozone-olefin chemistry which is shown schematically in Figure 8.2 and can be expressed in the form



where the stoichiometric coefficients are given by

$$\begin{aligned}
 a_1 &= (1 - 0.5\delta) \\
 a_2 &= 0.5\delta \\
 a_3 &= 0.5 \varepsilon (\xi + \eta) (1-0.5\delta) + \rho\delta \\
 a_4 &= 0.5 \varepsilon (2\xi + \eta) (1-0.5\delta) \\
 a_5 &= 0.5 \varepsilon \xi (1-0.5\delta) \\
 a_6 &= 0.5 \varepsilon \eta (1-0.5\delta) \\
 a_7 &= 0.5 \varepsilon \eta (1-0.5\delta)
 \end{aligned} \tag{8.8}$$

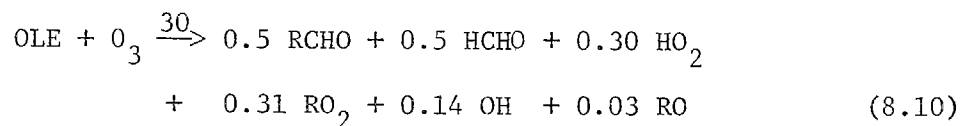
where δ equals the fraction of olefins with terminal double bonds, $1-\varepsilon$ the fraction of RCHOO reactions that proceed by collisional stabilization, ξ and η the fractions of RCHOO to [RCHOO]* and [HOCOR]* respectively. All other splits are assumed to be 50/50 except for the step



where ρ is 10% (Dodge, 1978). For the purposes of calculating the stoichiometric coefficient for HO_2 production, ρ has been assumed to be 0.1. From a computational point of view, it is desirable to minimize the number of species. Since the formyl radical (HCO) reacts very rapidly with oxygen to form hydroperoxyl (HO_2), HCO can be eliminated with the reaction step



Applying this result, together with the interpretation by Dodge (1978) of the Herron and Huie (1977) ozone-olefin experiments, the stoichiometric coefficients can be calculated from $\epsilon = 0.8$, $\xi = 0.68$, $\eta = 0.17$, $\delta = 1$, and $\rho = 0.1$. Substituting these values into the expressions for a_1, \dots, a_6 gives



where the HO_2 coefficient is derived from $a_3 + a_7$, i.e.

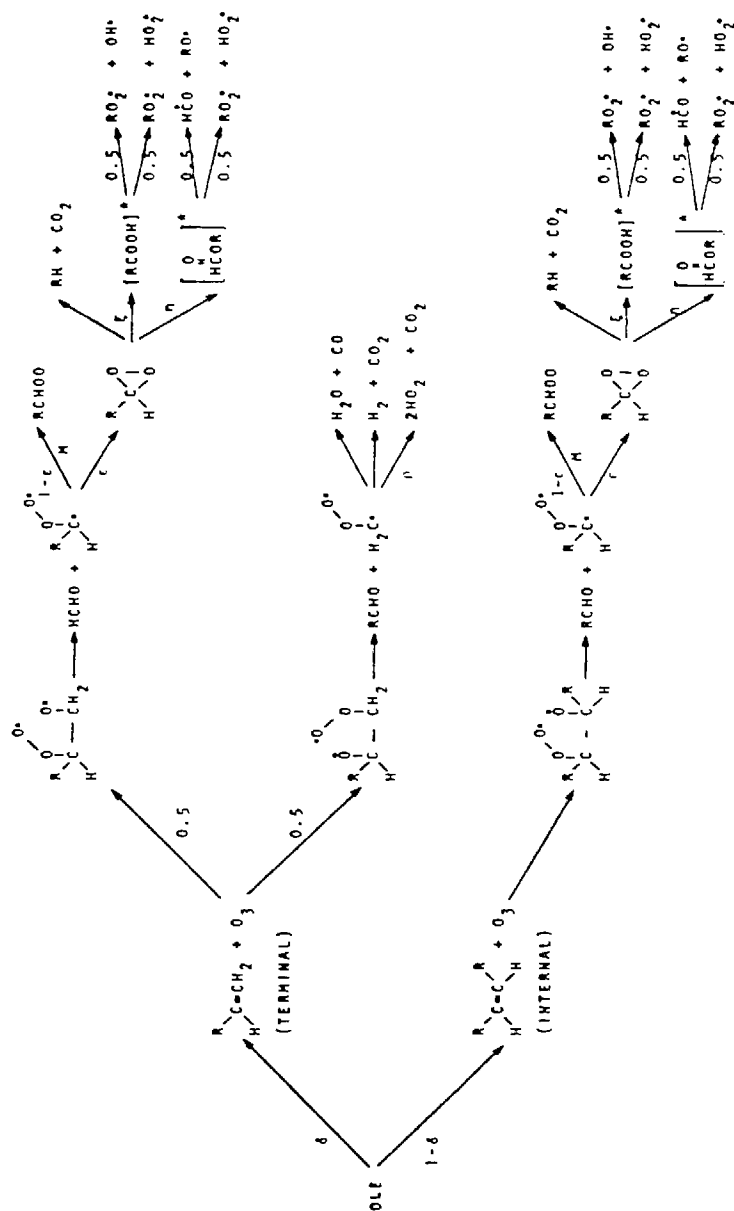
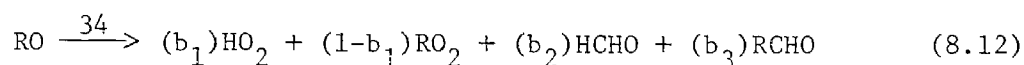


FIGURE 8.2
General Ozone-Olefin Reaction Mechanism
with Reaction Products as Proposed by Dodge (1978)

$$a_3 + a_7 = [0.5\epsilon(\xi+\eta)(1-0.5\delta) + \rho\delta] + [0.5\epsilon\eta(1-0.5\delta)] = 0.304 \quad (8.11)$$

The decomposition, reaction with O_2 , and isomerization of the alkoxy and hydro-alkoxy classes in the airshed mechanism have been concentrated in the reaction step



Since the RO lumped species represents a large class of different-sized radicals and because splits between reaction paths even for specific radicals are unknown, b_1 can have a value in the range 0 to 1. For the present model, the coefficients have been assigned the following values: $b_1 = 1$, $b_2 = 0.5$, and $b_3 = 0.5$, so that (8.12) can be written in the simpler form



8.4 Specification of the Reaction Rate Constants

Three basic types of reaction rate data are needed to complete the mechanism kinetics: inorganic, lumped hydrocarbon and photolysis rates. The determination of individual species reaction rates $\{F\}$ is a major area of experimental and theoretical investigation. For dilute chemical systems, a frequently employed model for correlating experimental data is the so-called 'mass action law' which is based on an analogy to

molecular collision (Pratt, 1969). In its simplest statement this model results in a polynomial expression for the rate, f_j of the form

$$f_j = k_j \prod_{i=1}^n c_i^{r_{ji}} \quad (8.14)$$

where k_j is a temperature dependent rate constant given by,

$$k_j(T) = A_j \exp [-B_j/T] \quad (8.15)$$

Expression (8.15) is the Arrhenius equation, the coefficients of which are derived from measurements of individual reaction rates as a function of temperature and pressure. The rate data for the inorganic reactions in the Falls and Seinfeld (1978) are presented in Table 8.3 together with appropriate literature citations. Baulch et al. (1980) have recently published an evaluated review of kinetic data for atmospheric chemistry. In some cases there are differences between their recommendation and the values used in the model evaluation studies described in subsequent chapters of this study. While future work with the mechanism will incorporate the new information, Table 8.3 serves as documentation of the rate constants employed in calculations to date. A discussion of procedures for developing the rate data for the lumped hydrocarbon reaction is presented in the next section. For more detailed analyses of the kinetic model (8.14) the reader is referred to Krambeck (1970), Horn and Jackson (1972) and Bowen (1976).

TABLE 8.3

Summary of Rate Constants Excluding Photolysis and Lumped Hydrocarbon Steps

RATE CONSTANTS (ppm-min units)			
REACTION		VALUE AT 298°K	REFERENCE ^a
$O(^3P) + O_2 \xrightarrow{+M} O_3 + M$	$\frac{0.346}{T^2} \exp(510/T)$	2.16×10^{-5}	[1]
$O_3 + NO \xrightarrow{3} NO_2 + O_2$	$\frac{9.24 \times 10^5}{T} \exp(-1450/T)$	2.39×10^1	[1]
$NO_2 + O(^3P) \xrightarrow{4} NO + O_2$	$\frac{3.99 \times 10^6}{T}$	1.34×10^4	[1]
$NO + O(^3P) \xrightarrow{5} NO_2$	$\frac{1.67 \times 10^5}{T} \exp(584/T)$	3.98×10^3	[1]
$NO_2 + O(^3P) \xrightarrow{6} NO_3$	$\frac{1.07 \times 10^6}{T}$	3.59×10^3	[1]
$O_3 + NO_2 \xrightarrow{7} NO_3 + O_2$	$\frac{5.19 \times 10^4}{T} \exp(-2450/T)$	4.68×10^{-2}	[1]
$NO_3 + NO \xrightarrow{8} 2NO_2$	$\frac{8.05 \times 10^6}{T}$	2.70×10^4	[2]
$NO + OH \xrightarrow{9} HONO$	$\frac{5.07 \times 10^6}{T}$	1.70×10^4	[1]
$HO_2 + NO_2 \xrightarrow{11} HONO + O_2$	$k_{11} = 0.001 k_{13}$	1.70	[3]
$HONO + OH \xrightarrow{12} NO_2 + H_2O$	$\frac{2.91 \times 10^6}{T}$	9.77×10^3	[1]
$NO_2 + HO_2 \xrightarrow{13} HO_2NO_2$	$\frac{1.73 \times 10^4}{T} \exp(1006/T)$	1.70×10^3	[4]
$HO_2NO_2 \xrightarrow{14} HO_2 + NO_2$	$1.80 \times 10^{15} \exp(-9950/T)$	5.68	[4]
$HO_2 + NO \xrightarrow{15} NO_2 + OH$	$\frac{3.58 \times 10^6}{T}$	1.20×10^4	[1]
$RO_2 + NO \xrightarrow{16} NO_2 + RO$	$\frac{3.58 \times 10^6}{T}$	1.20×10^4	[5]

TABLE 8.3 (Continued)

REACTION		RATE CONSTANTS (ppm-min units)		VALUE AT 298°K	REFERENCE ^a
$\text{RCO}_3 + \text{NO}$	$\xrightarrow{17} \text{NO}_2 + \text{RO}_2 + \text{CO}_2$	$\frac{1.13 \times 10^6}{T}$		3.79×10^3	[6]
$\text{NO}_2 + \text{OH}$	$\xrightarrow{18} \text{HONO}_2$	$\frac{4.53 \times 10^{6e}}{T}$		1.52×10^4	[1]
$\text{CO} + \text{OH}$	$\xrightarrow{19} \text{HO}_2 + \text{CO}_2$	$\frac{1.31 \times 10^5}{T}$		4.40×10^2	[1]
RO	$\xrightarrow{34} b_1 \text{HO}_2$ $+ b_2 \text{HCHO}$ $+ b_3 \text{RCHO}$ $+ (1-b_1) \text{RO}_2$	2.0×10^5		2.0×10^5	[7]
$\text{RO} + \text{NO}$	$\xrightarrow{36} \text{RONO}$	$\frac{4.38 \times 10^6}{T}$		1.47×10^4	[8]
$\text{RO} + \text{NO}_2$	$\xrightarrow{37} \text{RONO}_2$	$\frac{2.19 \times 10^6}{T}$		7.35×10^3	[8]
$\text{RO} + \text{NO}_2$	$\xrightarrow{38} \text{RCHO} + \text{HONO}^b$	$k_{38} = 0.087 k_{37}$		6.39×10^2	[9]
$\text{NO}_2 + \text{RO}_2$	$\xrightarrow{39} \text{RO}_2\text{NO}_2$	$\frac{1.64 \times 10^6}{T}$		5.50×10^3	[10]
$\text{NO}_2 + \text{RO}_2$	$\xrightarrow{40} \text{RCHO} + \text{HONO}_2$	$\frac{1.64 \times 10^3}{T}$		5.50	[10]
RO_2NO_2	$\xrightarrow{41} \text{NO}_2 + \text{RO}_2$	same as k_{14}		5.68	[5]
$\text{RCO}_3 + \text{NO}_2$	$\xrightarrow{42} \text{PAN}$	$\frac{6.17 \times 10^5}{T}$		2.07×10^3	[6]
PAN	$\xrightarrow{43} \text{RCO}_3 + \text{NO}_2$	$4.77 \times 10^{16} \exp(-12516/T)$		2.74×10^{-2}	[6]
$\text{NO}_2 + \text{NO}_3$	$\xrightarrow{44} \text{N}_2\text{O}_5$	$\frac{2.20 \times 10^6}{T}$		7.39×10^3	[13]
N_2O_5	$\xrightarrow{45} \text{NO}_2 + \text{NO}_3$	$3.44 \times 10^{16} \exp(-10600/T)$		1.22×10^1	[13]

TABLE 8.3 (Continued)

REACTION		RATE CONSTANTS (ppm-min units)			REFERENCE ^a
		VALUE AT 298°K			
H ₂ O	+ N ₂ O ₅ $\xrightarrow{46}$ 2HONO ₂	$\frac{4.47 \times 10^{-3}}{T}$		1.50 × 10 ⁻⁵	[1]
O ₃	+ OH $\xrightarrow{47}$ HO ₂ + O ₂	$\frac{6.62 \times 10^5}{T} \exp(-1000/T)$		7.75 × 10 ¹	[1]
O ₃	+ HO ₂ $\xrightarrow{48}$ OH + 2O ₂	$\frac{4.85 \times 10^3}{T} \exp(-580/T)$		2.32	[11]
O ₃	$\xrightarrow{49^c}$ wall loss	0.0		Depends on the equipment	
HO ₂	+ HO ₂ $\xrightarrow{50}$ H ₂ O ₂ + O ₂	$\frac{3.4 \times 10^4}{T} \exp(1100/T) + \frac{5.8 \times 10^{-5}}{T^2} \exp(5800/T) [\text{H}_2\text{O}]^f$		8.28 × 10 ³	[11]
RO ₂	+ RO ₂ $\xrightarrow{52}$ 2RO	$\frac{2.04 \times 10^4}{T} \exp(223/T)$		1.45 × 10 ²	[12]

- a) [1] Hampson and Garvin (1978)
 [2] Graham and Johnston (1978)
 [3] Graham, Winer and Pitts (1977)
 [4] Graham, Winer and Pitts (1978)
 [5] Estimate
 [6] Cox and Roffey (1977)
 [7] Baldwin, Barker, Golden and Hendry (1977)
 [8] Batt and Rattray (1979)
 [9] Baker and Shaw (1965)
 [10] Simonaitis and Heicklen (1974)
 [11] NASA (1981)
 [12] Sander and Watson
 [13] Baulch et al. (1980)

b) $\frac{k_{37}}{k_{37} + k_{38}} = 0.92$ for CH_3 , $k_{38} = 0.087 k_{37}$

c) Wall loss term for modeling smog chamber experiments, k_{49} depends on experimental conditions.

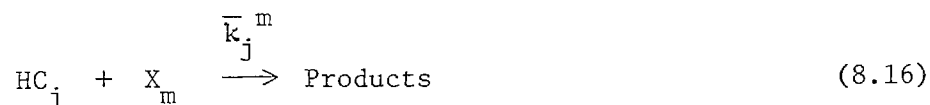
d) Rate constants for reactions 39 and 40 are based on the assumption that $k_{16}/(k_{39} + k_{40}) = 2.2$.

e) Determined from $1.477 \times 10^{15} \times 10^{-\left(\frac{11.6T}{17.4+T}\right) \sqrt{\frac{280}{T}}}$

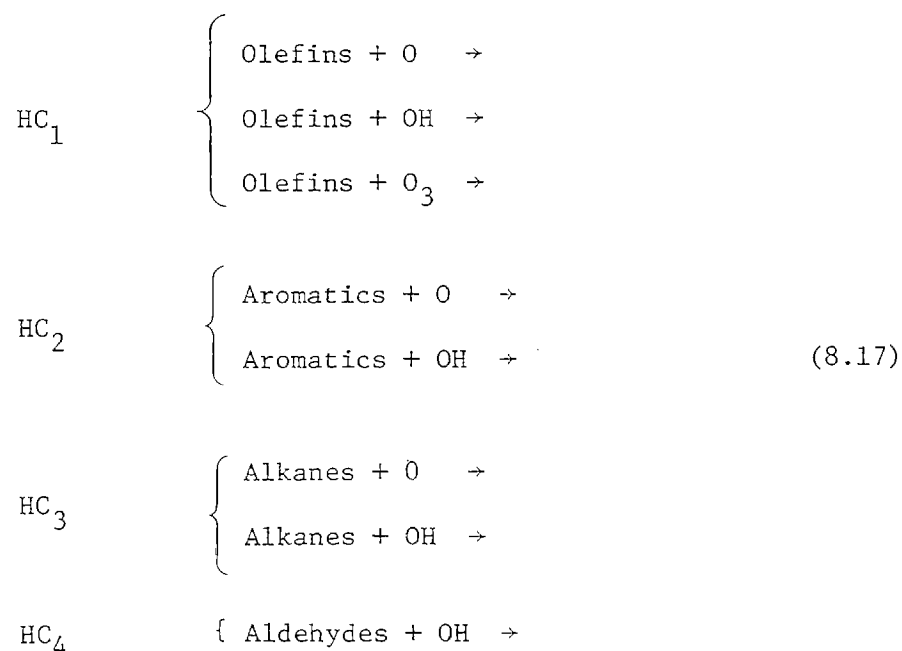
f) Water concentration in ppm, value at 298°K based on 20,000 ppm.

8.5 Lumped Hydrocarbon Reaction Rate Constants

Most lumped photochemical mechanisms represent atmospheric hydrocarbon chemistry by reactions of the form



The step (8.16) involves a reaction between X_m , typically atomic oxygen (O), hydroxyl radical (OH) or ozone (O_3), and the j th hydrocarbon class. In the case of the Falls and Seinfeld (1978) mechanism the organics, present in ambient air, are divided into one of four classes: alkanes, olefins, aromatics and oxygenated compounds like aldehydes. Since each class is composed of many different species the lumped reaction rate constant, \bar{k}_j^m , is composition dependent. This section describes the procedures used to generate the rate constants for reactions of the type



The basis for calculating the lumped rates are the kinetic data and concentrations of individual species in each class. Consider a typical class, j , which is composed of p_j individual species. The mole weighted lumped rate constant \bar{k}_j^m is given by

$$\bar{k}_j^m = \frac{\sum_{i=1}^{p_j} k_i^m n_i}{\sum_{i=1}^{p_j} n_i} \quad (8.18)$$

where n_i is the number of moles of species c_i in class j and k_i^m is the rate constant for the reaction between c_i and X_m . The expression (8.18) is the form adopted for use in calculating the lumped rate constants either from emissions data or concentration measurements. In order to evaluate (8.18) an extensive literature search was carried out to identify the basic kinetic data for individual organic species and their reaction with O_3 , OH and O . The results of this survey are too voluminous to be presented however, for additional details, the reader is referred to the rate data contained in Hampson and Garvin (1978), Atkinson et al. (1978) and Lloyd et al. (1976).

As an illustration of the procedure consider the calculation of the lumped rates for a typical smog chamber experiment. The composition of the hydrocarbon mixture for the smog chamber experiment SUR-119J (Pitts et al., 1976) is shown in Table 8.4. Individual species concentrations were chosen so that the overall mixture was representative

TABLE 8.4

Hydrocarbon Composition of Smog Chamber Experiment SUR-119J
Excluding Methane, Acetylene, and Acetone

LUMPED HYDROCARBON CLASS SPECIES		CONCENTRATION	
		ppbV	ppbC
ALKANES	Ethane (C_2H_6)	76.8	154
	Propane (C_3H_8)	17.0	51.0
	Isobutane (C_4H_{10})	0.2	0.8
	N-butane	166	664
	2,3-Dimethyl Butane ($C_4H_8-(CH_3)_2$)	97.6	586
		<u>357.6</u>	<u>1455.8</u>
OLEFINS	Ethene (C_2H_4)	43.2	86.4
		<u>43.2</u>	<u>86.4</u>
	Propene (C_3H_6)	10.6	31.8
	Trans-2-Butene (C_4H_8)	0.7	2.8
	Cis-2-Butene (C_4H_8)	13.0	52.0
	2-methyl Butene-2 ($C_4H_7-CH_3$)	14.8	74.0
		<u>39.1</u>	<u>160.6</u>
AROMATICS	Benzene (C_6H_6)	1.6	9.6
	Toluene ($C_6H_5-CH_3$)	16.8	118
	Ethyl Benzene ($C_6H_5-C_2H_5$)	6.4	51.2
	Meta-xylene ($C_6H_4-(CH_3)_2$)	42.4	339
	Isopropyl Benzene ($C_6H_5-C_3H_7$)	0.4	3.6
	n-Propyl Benzene ($(C_6H_4-C_3H_7)_n$)	0.1	0.9
	Meta-Ethyl Toluene ($C_6H_4-CH_3-C_2H_5$)	1.0	9.0
	1,2,3 Trimethyl Benzene ($C_6H_3-(CH_3)_3$)	1.6	14.4
		<u>70.3</u>	<u>545.7</u>

TABLE 8.4 (Continued)

LUMPED HYDROCARBON CLASS SPECIES		CONCENTRATION	
		ppbV	ppbC
ALDEHYDES	Formaldehyde (HCHO)	38.0	38.0
	Acetaldehyde (CH ₃ CHO)	20.0	40.0
	Propionaldehyde (C ₂ H ₅ CHO)	3.2	9.6
		<hr/> 23.2	<hr/> 49.6
	TOTALS FOR MIXTURE	571.4	2336.0

of the 6-9 AM ambient pollutant burden in the Los Angeles atmosphere. Species have been grouped into each of the lumped classes with the concentration, c_i , expressed both in terms of volume as ppbV and by carbon atom as ppbC. Tables 8.5-8.7 present the individual species rate data for reactions with OH, O, and O_3 derived from the literature survey. Given this information and (8.18) the rate constants for the lumped reaction in the Falls and Seinfeld (1978) mechanism are shown in Table 8.8. For comparison purposes the lumped rate constants based on species emission data are also presented in the same table. Details of the emissions inventory and its composition are described in Chapter 13. As a caution it is important to note that in a smog chamber experiment the more reactive components in each class are consumed first. Applying a mole weighted scheme under these circumstances has the effect of underestimating the reaction rates at the beginning of the experiment and overestimating them at the end of a run. This is not a particularly serious problem in urban modeling application because there is a continued injection of source material.

As can be seen from the previous exercise, detailed composition data are required to develop the lumped rate constants. Since most monitoring agencies only report total (THC) and non-methane (NMHC) hydrocarbon concentration levels it is necessary to develop a procedure to partition the broad groupings into the appropriate lumped class for establishing initial conditions. One way to do this is to develop splitting factors from detailed compositional studies and then apply

TABLE 8.5

Rate Constant Data for Reaction with OH

CLASS	SPECIES	RATE CONSTANT (298°K) (cm ³ /molecule-sec)	ppbv k_i	LUMPED RATE CONSTANT (cm ³ /molecule-sec)
ALKANES	Ethane (C ₂ H ₆)	2.8x10 ⁻¹³	2.15x10 ⁻¹¹	
	Propane (C ₃ H ₈)	1.47x10 ⁻¹²	2.5x10 ⁻¹¹	
	Isobutane (C ₄ H ₁₀)	2.4x10 ⁻¹²	4.8x10 ⁻¹³	
	N-butane	2.7x10 ⁻¹²	4.48x10 ⁻¹⁰	
	2,3 Dimethylbutane (C ₄ H ₈ -(CH ₃) ₂)	6.54x10 ⁻¹²	6.38x10 ⁻¹⁰	
			1.14x10 ⁻⁹	$\bar{k} = 3.18 \times 10^{-12}$
293				
OLEFINS	Ethene (C ₂ H ₄)	7.9x10 ⁻¹²	3.41x10 ⁻¹⁰	$\bar{k} = 7.89 \times 10^{-12}$
	Propene (C ₃ H ₆)	2.5x10 ⁻¹¹	2.65x10 ⁻¹⁰	
	Trans-2-Butene (C ₄ H ₈)	7x10 ⁻¹¹	4.9x10 ⁻¹¹	
	Cis-2-Butene (C ₄ H ₈)	5.4x10 ⁻¹¹	7.02x10 ⁻¹⁰	
	(2-methyl butene-2) (C ₄ H ₇ -CH ₃)	8.7x10 ⁻¹¹	1.28x10 ⁻⁹	
			2.296x10 ⁻⁹	$\bar{k} = 5.87 \times 10^{-11}$

TABLE 8.5 (Continued)

CLASS	SPECIES	RATE CONSTANT (298°K) (cm ³ /molecule-sec)	ppbv k_i	LUMPED RATE CONSTANT (cm ³ /molecule-sec)
AROMATICS	Benzene (C ₆ H ₆)	1.2x10 ⁻¹²	1.92x10 ⁻¹²	
	Toluene (C ₆ H ₅ -CH ₃)	6.1x10 ⁻¹²	1.02x10 ⁻¹⁰	
	EthylBenzene (C ₆ H ₅ -C ₂ H ₅)	8x10 ⁻¹²	5.12x10 ⁻¹¹	
	Meta-xylene (C ₆ H ₄ -(CH ₃) ₂)	2.4x10 ⁻¹¹	1.01x10 ⁻⁹	
	Isopropyl Benzene (C ₆ H ₅ -C ₃ H ₇)	6.2x10 ⁻¹²	2.48x10 ⁻¹²	
	n-Propyl Benzene (C ₆ H ₄ -C ₃ H ₇) _n	6.2x10 ⁻¹²	6.2x10 ⁻¹³	
	meta-Ethyl Toluene (C ₆ H ₄ -CH ₃ -C ₂ H ₅)	1.95x10 ⁻¹¹	1.95x10 ⁻¹¹	
	1,2,3 Trimethylbenzene (C ₆ H ₃ -(CH ₃) ₃)	2.64x10 ⁻¹¹	4.22x10 ⁻¹¹	
			1.23x10 ⁻⁹	$\bar{k} = 1.75x10^{-11}$
ALDEHYDES	Formaldehyde	9.4x10 ⁻¹²	3.57x10 ⁻¹⁰	$\bar{k} = 9.4x10^{-12}$
	Acetaldehyde (CH ₃ CHO)	1.6x10 ⁻¹¹	3.2x10 ⁻¹⁰	
	Propionaldehyde (C ₂ H ₅ CHO)	3.06x10 ⁻¹¹	9.79x10 ⁻¹¹	
			4.18x10 ⁻¹⁰	$\bar{k} = 1.8x10^{-11}$

TABLE 8.6

Rate Constant Data for Reactions with O

CLASS	SPECIES	RATE CONSTANT (298°K) (cm ³ /molecule-sec)	ppbv k_i	LUMPED RATE CONSTANT (cm ³ /molecule-sec)
ALKANES	Ethane (C ₂ H ₆)	8.9x10 ⁻¹⁶	6.84x10 ⁻¹⁴	
	Propane (C ₃ H ₈)	8.6 x10 ⁻¹⁴	4.42x10 ⁻¹³	
	Isobutane (C ₄ H ₁₀)	1.07x10 ⁻¹³	2.14x10 ⁻¹⁴	
	N-butane	4.91x10 ⁻¹⁴	8.15x10 ⁻¹²	
	2,3 Dimethylbutane (C ₄ H ₈ -(CH ₃) ₂)	2.11x10 ⁻¹³	2.06x10 ⁻¹¹	
			2.93x10 ⁻¹¹	$\bar{k} = 8.19x10^{-14}$
OLEFINS	Ethylene (C ₂ H ₄)	8.25x10 ⁻¹³	3.56x10 ⁻¹¹	$\bar{k} = 8.25x10^{-13}$
	Propene (C ₃ H ₆)	3.6x10 ⁻¹²	3.82x10 ⁻¹¹	
	Trans-2-Butene (C ₄ H ₈)	2.3x10 ⁻¹¹	1.61x10 ⁻¹¹	
	Cis-2-Butene (C ₄ H ₈)	1.7x10 ⁻¹¹	2.21x10 ⁻¹⁰	
	2-methyl butene-2 (C ₄ H ₇ -CH ₃)	5.17x10 ⁻¹¹	7.65x10 ⁻¹⁰	
			1.04x10 ⁻⁹	$\bar{k} = 2.66x10^{-11}$

TABLE 8.6 (Continued)

CLASS	SPECIES	RATE CONSTANT (298°K) (cm ³ /molecule-sec)	ppbv _i k _i	LUMPED RATE CONSTANT (cm ³ /molecule-sec)
AROMATICS	Benzene (C ₆ H ₆)	2.2x10 ⁻¹⁴	3.52x10 ⁻¹⁴	
	Toluene (C ₆ H ₅ -CH ₃)	7.3x10 ⁻¹⁴	1.23x10 ⁻¹²	
	Ethyl Benzene (C ₆ H ₅ -C ₂ H ₅)	5.3x10 ⁻¹³	3.39x10 ⁻¹²	
	Meta-xylene (C ₆ H ₄ -(CH ₃) ₂)	3.4x10 ⁻¹³	1.44x10 ⁻¹¹	
	Isopropyl Benzene (C ₆ H ₅ -C ₃ H ₇)	6.0x10 ⁻¹³	2.40x10 ⁻¹³	
	n-Propyl Benzene (C ₆ H ₄ -C ₃ H ₇) _n	6.0x10 ⁻¹³	6.0 x10 ⁻¹⁴	
	meta-Ethyl Toluene (C ₆ H ₄ -CH ₃ -C ₂ H ₅)	4.0x10 ⁻¹³	4.0 x10 ⁻¹³	
	1,2,3 Trimethylbenzene (C ₆ H ₃ -(CH ₃) ₃)	1.15x10 ⁻¹²	1.84x10 ⁻¹²	
			<u>2.16x10⁻¹¹</u>	3.07x10 ⁻¹³

TABLE 8.7

Rate Constant Data for Reactions with O_3

CLASS	SPECIES	RATE CONSTANT (298°K) ($cm^3/molecule\text{-}sec$)	ppbv k_i	LUMPED RATE CONSTANT ($cm^3/molecule\text{-}sec$)
OLEFINS	Ethylene (C_2H_4)	1.67×10^{-18}	7.21×10^{-17}	$\bar{k} = 1.67 \times 10^{-18}$
	Propene (C_3H_6)	1.04×10^{-17}	1.1×10^{-16}	
	Trans-2-butene (C_4H_8)	1.76×10^{-16}	1.23×10^{-16}	
	Cis-2-butene (C_4H_8)	1.25×10^{-16}	1.63×10^{-15}	
	2-methyl butene-2 ($C_4H_7-CH_3$)	4.4×10^{-16}	6.51×10^{-15}	
			8.37×10^{-15}	$\bar{k} = 2.15 \times 10^{-16}$

TABLE 8.8

Rate Constants for Lumped Hydrocarbon Reaction Steps

REACTION STEP	RATE CONSTANTS (ppm ⁻¹ - min ⁻¹)	
	Smog Chamber Surrogate Hydrocarbon Mixture SUR-119J	Atmospheric Conditions in Los Angeles 27 June 1974
HCHO + OH $\xrightarrow{23}$ HO ₂ + H ₂ O + CO	13890.0	13890.0
RCHO + OH $\xrightarrow{25}$ RCO ₃	26600.0	25680.0
C ₂ H ₄ + OH $\xrightarrow{26}$ RO ₂	11660.0	11660.0
C ₂ H ₄ + O $\xrightarrow{27}$ RO ₂ + HO ₂	1219.0	1219.0
OLE + OH $\xrightarrow{28}$ RO ₂	86800.0	89142.0
OLE + O $\xrightarrow{29}$ RO ₂ + RCO ₃	39300.0	22118.0
OLE + O ₃ $\xrightarrow{30}$ (a ₁)RCHO + (a ₂)HCHO + (a ₃)HO ₂ (a ₄)RO ₂ + (a ₅)OH + (a ₆)RO	0.317	0.136
ALK + OH $\xrightarrow{31}$ RO ₂	4700.0	4700.0
ALK + O $\xrightarrow{32}$ RO ₂ + OH	121.0	99.8
ARO + OH $\xrightarrow{33}$ RO ₂ + RCHO	25900.0	16112.0

Variable Stoichiometric Coefficients for OLE + O₃ reactions

$$\begin{array}{lll}
 a_1 = 0.5 & a_2 = 0.5 & a_3 = 0.30 \\
 a_4 = 0.31 & a_5 = 0.14 & a_6 = 0.03
 \end{array}$$

these values to the routine non-methane hydrocarbon measurements. As an example consider the surrogate mixture in Table 8.4. Given the average carbon numbers for each class, C_j^a , and the carbon fraction, f_j , in each class then it is a straightforward task to develop the volume splitting factors from

$$v_j = \frac{f_j}{C_j^a} \quad (8.19)$$

where the average carbon number of class j is given by

$$C_j^a = \frac{\sum_{i=1}^{P_j} c_i \text{ (ppbC)}}{\sum_{i=1}^{P_j} c_i \text{ (ppbV)}} \quad (8.20)$$

The process is illustrated in Figure 8.3.

8.6 Photolytic Rate Constants

A key process in the formation of photochemical air pollution is the photolysis of such species as nitrogen dioxide (NO_2), formaldehyde (HCHO) and nitrous acid (HONO). In an urban atmosphere it is difficult either to measure the rates directly or to use routine monitoring data as a basis for indirect calculations. This section is devoted to a discussion of a priori methods for determining the diurnal variation of the photolysis rate constants.

		<u>LUMPED</u> <u>CLASS</u>	<u>CARBON</u> <u>FRACTION</u> <u>CARBON</u> <u>NUMBER</u>		<u>MOLE %</u>
x(ppbC) →		ALK	0.623 4.07	→ 0.153x(ppbV)	62.3
		C ₂ H ₄	0.037 2.0	→ 0.020x(ppbV)	8.1
		OLE	0.069 4.11	→ 0.0168x(ppbV)	6.8
		ARO	0.234 7.76	→ 0.030x(ppbV)	12.2
		HCHO	0.016 1.0	→ 0.016x(ppbV)	6.5
		RCHO	0.021 2.14	→ 0.0098x(ppbV)	4.0

FIGURE 8.3

Conversion of Total Reactive Hydrocarbon Measurements, Expressed in ppbC, to an Equivalent Volumetric Concentration (ppbV) of Lumped Hydrocarbon Species - The Specific Example is for the Atmospheric Surrogate Smog Chamber Experiment SUR-119J

For a typical species, A, the photodissociation step is commonly written in the form



with the forward reaction rate, R, given by

$$R \equiv - \frac{dA}{dt} = k[A] \quad (8.22)$$

The photolysis rate constant, k, of any pollutant, present in the atmosphere in small concentrations, is given by

$$k = \int_0^{\infty} \sigma[\lambda, T(h)] \phi[\lambda, T(h)] I[\lambda, N(t), \underline{x}] d\lambda \quad (8.23)$$

where $\sigma[\lambda, T(h)]$ (cm^2) is the wavelength, λ , dependent absorption cross section for the species at temperature, T, in most applications the atmospheric temperature is a function of the elevation, h. $\phi[\lambda, T(h)]$ is the quantum yield for the reaction and I is the actinic irradiance ($\text{photons}/\text{cm}^2\text{-sec}$) corresponding to an atmospheric state, N, at spatial location, \underline{x} , and time, t. N specifies the temporal variation of those variables which affect the transmission and absorption of solar radiation in the atmosphere. A typical example is the seasonal variation of turbidity.

Since the wavelength dependent absorption coefficients and quantum yields are fixed, the variation of the species rate constant in space and time depends primarily on the variation of the actinic flux.

Actinic irradiance is the radiometric energy incident on single molecules and, as conventionally defined, applies to ultraviolet (uv) wavelengths. This parameter is very difficult to estimate from customary solar radiation measurements; in particular those made with broad band 180° pyroheliometers. As a result most photolysis rate constants are based on theoretical calculations of the solar flux in the spectral band of interest. Many previous modeling studies employed the tabulation, by Leighton (1961), of photolysis rates as a function of zenith angle. His results were based on a radiative transfer calculation which, by necessity, employed many simplifying assumptions. The availability of more sophisticated radiative transfer models and more recent measurements of the upper atmospheric properties has led to considerable refinement in the calculation of solar fluxes.

Duewer et al. (1978) used the model of Luther and Gelinas (1976) as a basis for determining the photodissociation rate constants of the species NO_2 , HNO_2 , H_2O_2 , Aldehydes, RNO_2 , NO_3 , O_3 . For the present study the actinic irradiance, as a function of zenith angle, was obtained from the report by Peterson (1976). The actinic flux at ground level is shown in Table 8.9 for zenith angles in the range 0° - 86° as a function of wavelength in the spectral band 290-800 nm. Extrapolation of these values beyond 700 nm were obtained from Schere and Demerjian (1977). The calculations by Peterson were performed with a modified version of the program developed by Braslau and Dave (1973 a, b). It is beyond the scope of this chapter to discuss the details of the

TABLE 8.9

Ground Level Actinic Irradiance as a Function of
Zenith Angle and Wavelength (Photons/cm²-secx10⁻¹⁵)

WAVELENGTH RANGE (NM)	ZENITH ANGLES (DEG)									
	0.0	10.00	20.00	30.00	40.00	50.00	60.00	70.00	78.00	86.00
285 - 295	0.000	0.000	0.0	0.0	0.0	0.0	0.0	0.0	0.0	0.0
295 - 305	0.040	0.038	0.033	0.025	0.016	0.007	0.002	0.000	0.0	0.0
305 - 315	0.439	0.431	0.401	0.351	0.281	0.198	0.110	0.039	0.009	0.001
315 - 325	0.955	0.944	0.901	0.826	0.717	0.571	0.389	0.194	0.064	0.009
325 - 335	1.613	1.594	1.538	1.440	1.292	1.083	0.803	0.463	0.203	0.039
335 - 345	1.713	1.696	1.645	1.555	1.416	1.215	0.936	0.573	0.269	0.061
345 - 355	1.892	1.875	1.824	1.733	1.591	1.383	1.243	0.884	0.328	0.077
355 - 365	1.951	1.933	1.885	1.798	1.662	1.459	1.164	0.749	0.363	0.083
365 - 375	2.397	2.378	2.323	2.224	2.067	1.831	1.480	0.972	0.477	0.107
375 - 385	2.318	2.301	2.251	2.161	2.019	1.803	1.475	0.988	0.491	0.106
385 - 395	2.341	2.325	2.279	2.195	2.059	1.852	1.534	1.047	0.529	0.111
395 - 405	3.174	3.153	3.093	2.984	2.810	2.541	2.125	1.474	0.758	0.156
405 - 415	3.993	3.968	3.896	3.765	3.556	3.232	2.725	1.919	1.003	0.202
415 - 425	4.119	4.095	4.025	3.896	3.696	3.378	2.875	2.059	1.097	0.215
425 - 435	4.222	4.198	4.051	3.930	3.735	3.428	2.938	2.129	1.151	0.223
435 - 445	4.617	4.512	4.442	4.317	4.113	3.793	3.274	2.402	1.321	0.251
445 - 455	5.205	5.182	5.101	4.958	4.728	4.366	3.783	2.800	1.559	0.292
455 - 465	5.615	5.585	5.498	5.344	5.099	4.715	4.059	3.055	1.721	0.319
465 - 475	5.750	5.721	5.630	5.485	5.242	4.848	4.248	3.193	1.821	0.333
475 - 485	5.799	5.771	5.680	5.541	5.304	4.918	4.327	3.277	1.887	0.340
485 - 495	5.784	5.756	5.676	5.533	5.305	4.944	4.352	3.317	1.926	0.342
495 - 505	5.887	5.857	5.773	5.625	5.390	5.022	4.422	3.377	1.970	0.342
505 - 515	5.935	5.905	5.818	5.668	5.425	5.053	4.450	3.405	1.994	0.339
515 - 525	5.932	5.903	5.818	5.665	5.433	5.067	4.472	3.434	2.020	0.338
525 - 535	5.980	5.950	5.866	5.717	5.482	5.116	4.521	3.476	2.045	0.331
535 - 545	5.927	5.899	5.816	5.670	5.439	5.080	4.495	3.462	2.040	0.322
545 - 555	5.910	5.881	5.797	5.650	5.420	5.061	4.479	3.452	2.037	0.315
555 - 565	5.969	5.940	5.853	5.703	5.467	5.103	4.514	3.479	2.052	0.309
565 - 575	6.058	6.028	5.941	5.789	5.551	5.183	4.585	3.534	2.081	0.303
575 - 585	6.174	6.144	6.058	5.905	5.666	5.296	4.714	3.629	2.148	0.311
585 - 595	6.226	6.197	6.111	5.958	5.722	5.354	4.754	3.686	2.194	0.320
595 - 605	6.265	6.240	6.152	5.997	5.758	5.387	4.785	3.714	2.218	0.324
605 - 615	6.312	6.282	6.192	6.036	5.793	5.421	4.815	3.742	2.242	0.327
615 - 625	6.321	6.292	6.205	6.047	5.803	5.432	4.826	3.778	2.303	0.349
625 - 635	6.330	6.301	6.217	6.058	5.812	5.442	4.900	3.854	2.363	0.372
635 - 645	6.421	6.392	6.306	6.059	5.743	5.362	4.979	3.933	2.438	0.400
645 - 655	6.513	6.483	6.395	6.240	6.004	5.641	5.058	4.015	2.512	0.429
655 - 665	6.594	6.563	6.472	6.314	6.074	5.708	5.122	4.079	2.574	0.455
665 - 675	6.674	6.643	6.549	6.388	6.144	5.775	5.187	4.142	2.635	0.481
675 - 685	6.655	6.626	6.537	6.375	6.136	5.777	5.199	4.168	2.671	0.499
685 - 695	6.643	6.610	6.524	6.365	6.134	5.775	5.211	4.193	2.706	0.518
695 - 705	6.400	6.360	6.350	6.200	5.980	5.710	5.150	4.090	2.740	0.530
705 - 715	6.400	6.370	6.220	6.140	5.910	5.650	5.110	4.070	2.750	0.540
715 - 725	6.370	6.340	6.190	6.020	5.800	5.550	5.020	4.040	2.770	0.560
725 - 735	6.370	6.340	6.190	6.020	5.800	5.550	5.020	4.040	2.780	0.560
735 - 745	6.370	6.340	6.190	6.020	5.800	5.550	5.020	4.040	2.790	0.570
745 - 755	6.370	6.340	6.190	6.020	5.800	5.550	5.020	4.040	2.790	0.570
755 - 765	6.370	6.340	6.190	6.020	5.800	5.550	5.020	4.040	2.790	0.570
765 - 775	6.370	6.340	6.190	6.020	5.800	5.550	5.020	4.040	2.790	0.570
775 - 785	6.370	6.340	6.190	6.020	5.800	5.550	5.020	4.040	2.790	0.570
785 - 795	6.370	6.340	6.190	6.020	5.800	5.550	5.020	4.040	2.790	0.570
795 - 805	6.370	6.340	6.190	6.020	5.800	5.550	5.020	4.040	2.790	0.570

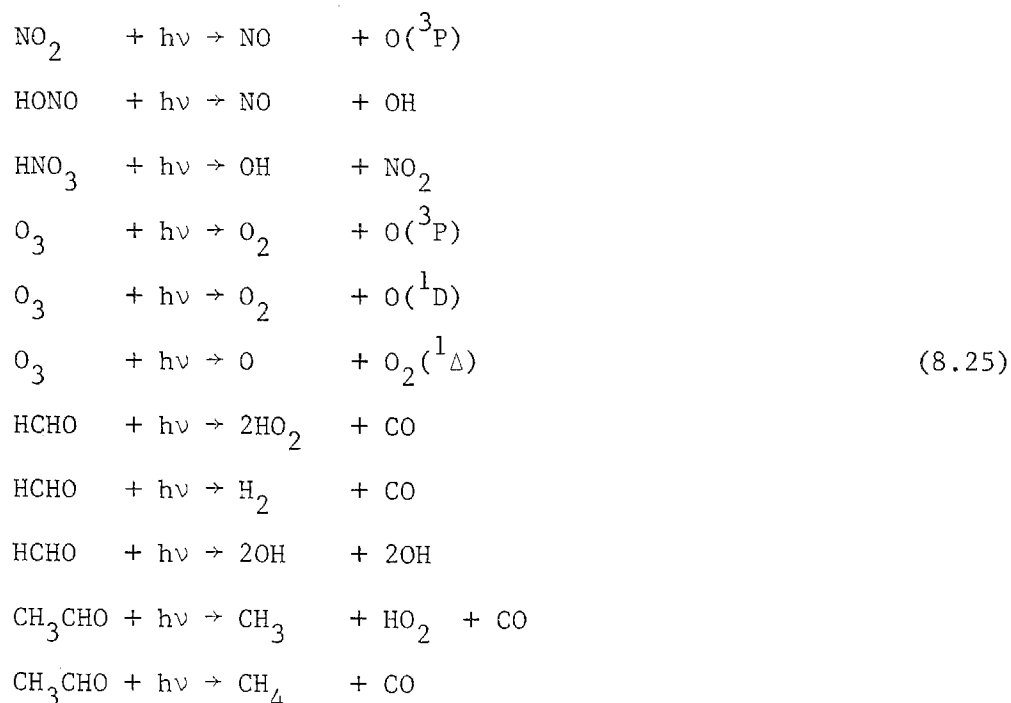
algorithms, it suffices to say however, that their model includes aerosol scattering and absorption, Rayleigh scattering, and ozone absorption. The atmospheric state, N , assumed in the model corresponds to annual average U.S. urban conditions, Flowers et al. (1969). This condition corresponds to a cloud-free atmosphere over a typical urban environment.

The photolysis rate constant for a particular species can be determined by evaluating (8.23) and in practice the integral can be approximated, with minimal error, by a finite interval summation of the form

$$k \approx \sum_{i=1}^n \overline{\sigma} [\lambda_i, \Delta\lambda_i] \overline{\phi} [\lambda_i, \Delta\lambda_i] \overline{I} [\lambda_i, \Delta t_i N(t), h, z] \quad (8.24)$$

where the overbar represents an average over a wavelength interval $\Delta\lambda_i$ centered at λ_i . The actinic irradiance at a particular time and elevation h is specified as a function of the zenith angle z . Compared to the total solar spectrum, the summation interval is quite small ($290 \leq \lambda \leq 800$ nm). The photochemistry of the lower atmosphere is dominated by the fact that virtually no solar radiation of wavelengths less than 290 nm reaches the troposphere. Essentially all the incident solar radiation at wavelengths below 290 nm is absorbed by gases in the upper atmosphere, principally the Hartley band of 220–295 nm and by oxygen in the Schumann continuum 175–145 nm (Coulson, 1975). The upper limit for λ is set by either the reduction of the species absorption cross section or reaction quantum yield as a function of increasing wavelength.

Data for the species absorption cross sections and quantum yields as a function of wavelength are required in order to evaluate (8.24). Tables 8.10 and 8.11 contain the appropriate information, compiled from Schere and Demerjian (1977), Demerjian (1977) and Demerjian et al. (1980), for the following reactions



The tables represent a collation of experimental information and have been assembled to enable an independent verification of the photolysis rate calculations. The species rate constants, as a function of the cosine of the zenith angle, are shown in Figures 8.4-8.14. The diurnal variation of the rate constants for any date or location can be easily evaluated using these figures and a knowledge of the solar declination angle δ . The local zenith angle, Z , can be determined from the expression (Sellers, 1969)

TABLE 8.10

Quantum Yield Data Averaged over 10 nm Wavelength Interval

Quantum yields for photolytic processes, 10 nm integral averaged, centered about λ for the reactions (8.25)										
λ (nm)	NO ₂	HONO	HONO ₂	O ₃ ^a	O ₃	HCHO	HCHO	CH ₃ CHO	CH ₃ CHO	H ₂ O ₂
290	1.0	1.0	1.0	0.0	1.0	.73	.28	.46	.31	1.0
300	1.0	1.0	1.0	0.0	1.0	.77	.23	.60	.19	1.0
310	1.0	1.0	1.0	1.0	.52	.75	.25	.72	.09	1.0
320	1.0	1.0	1.0	1.0	.01	.61	.39	.86		1.0
330	1.0	1.0		1.0		.31	.59	.98		1.0
340	1.0	1.0		1.0	1.0	.01	.42	1.00		1.0
350	1.0	1.0		1.0	1.0					1.0
360	1.0	1.0								
370	.99	1.0								
380	.97	1.0								
390	.91	1.0								
400	.65									
410	.22									
420	.02									
430										

^aO₃ quantum yield in the 450-750 nm region equal 1.0.

TABLE 8.11

Absorption Cross Section $\sigma(10^{-20} \text{ cm}^2 \text{ molecule}^{-1})$
 10 nm integral averaged, centered about λ

λ (nm)	NO ₂	HONO	HONO ₂	O ₃	HCHO	CH ₃ CHO	H ₂ O ₂
290	8.52		0.634	162.	3.18	4.66	1.23
300	12.83		0.276	44.4	3.25	4.09	0.71
310	18.26	0.3	0.095	11.9	3.15	2.96	0.41
320	24.74	3.4	0.018	3.36	2.34	1.69	0.24
330	30.95	6.6		0.88	2.37	0.69	0.14
340	37.39	13.3		0.19	1.98	0.13	0.08
350	44.90	17.0		0.04	0.84		0.05
360	50.11	9.6			0.18		
370	54.05	17.2					
380	56.99	10.9					
390	58.22	2.3					
400	59.52						
410	58.03						
420	54.52						
430	51.46						
440	48.50						
450	45.50			.020			
460				.036			
470				.054			
480				.075			
490				.096			
500				.131			
510				.174			
520				.220			
530				.276			
540				.331			
550				.378			
560				.454			
570				.509			
580				.493			
590				.515			
600				.552			
610				.498			
620				.417			
630				.361			
640				.318			
650				.269			
660				.217			
670				.179			
680				.152			
690				.126			
700				.098			
710				.081			
720				.068			
730				.056			
740				.048			
750				.041			

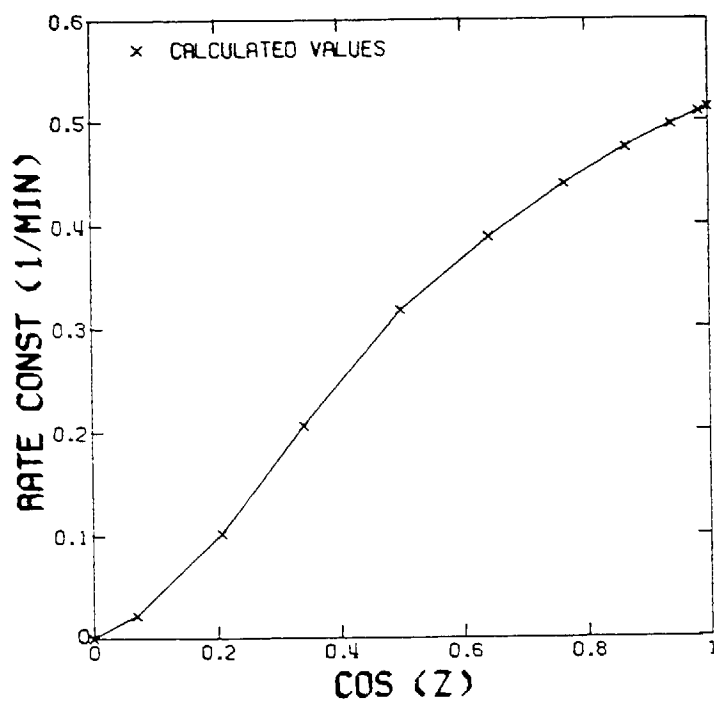


FIGURE 8.4

Photolysis Rate for $\text{NO}_2 + h\nu \xrightarrow{k} \text{NO} + \text{O}(^3\text{P})$ as a Function of Zenith Angle

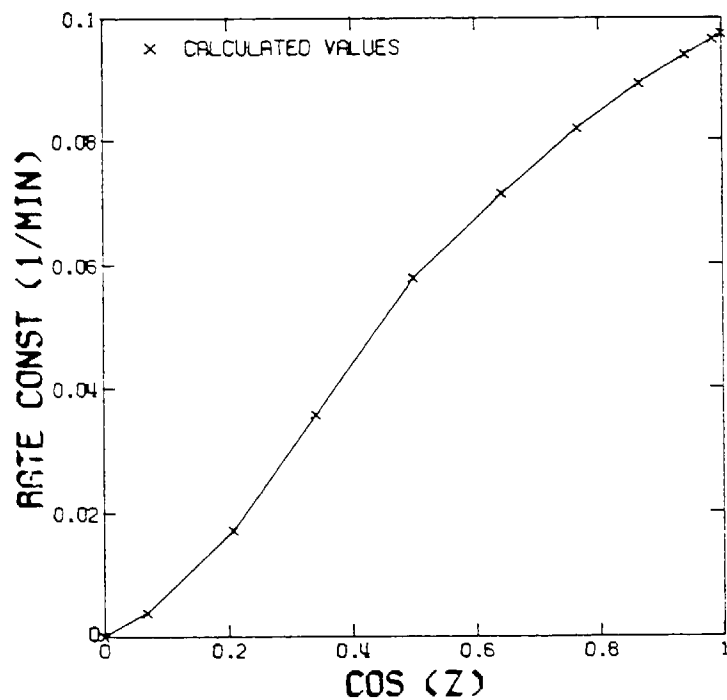


FIGURE 8.5

Photolysis Rate for $\text{HONO} + h\nu \xrightarrow{k} \text{OH} + \text{NO}$ as a Function of Zenith Angle

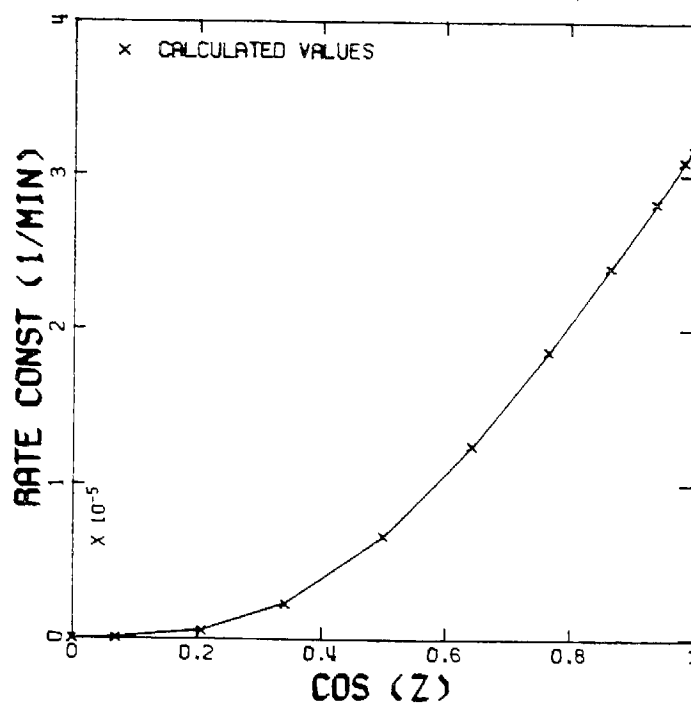


FIGURE 8.6

Photolysis Rate for $\text{HNO}_3 + h\nu \xrightarrow{k} \text{OH} + \text{NO}_2$ as a Function of Zenith Angle

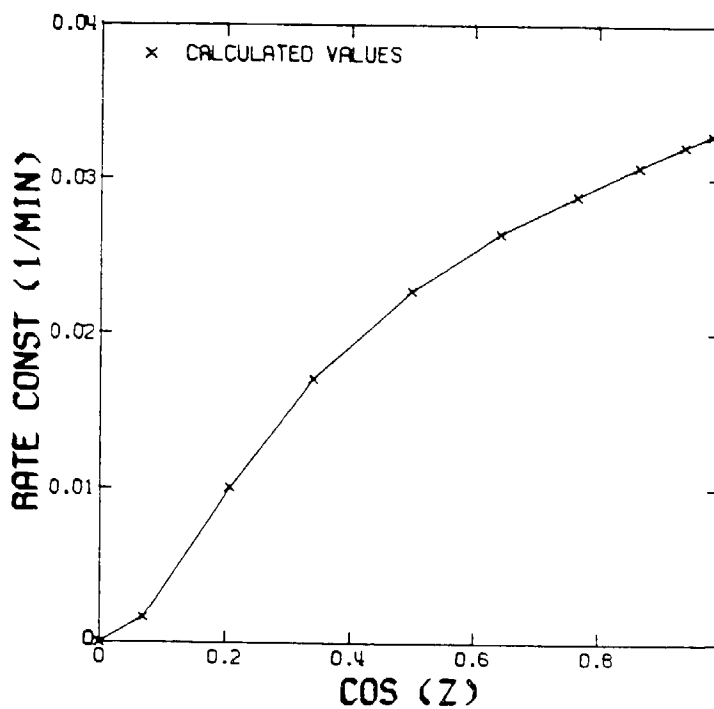


FIGURE 8.7

Photolysis Rate for $\text{O}_3 + h\nu \xrightarrow{k} \text{O}({}^3\text{P}) + \text{O}_2$ as a Function of Zenith Angle

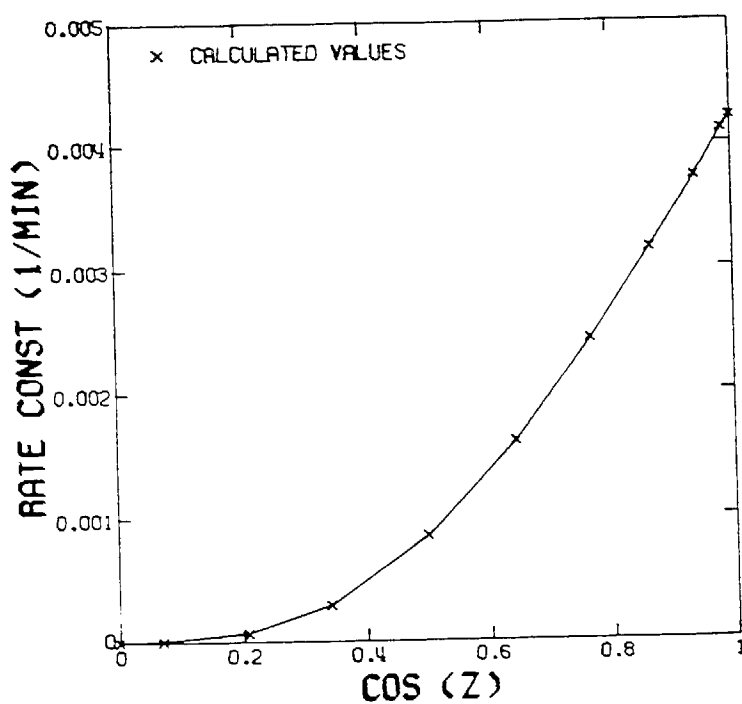


FIGURE 8.8

Photolysis Rate for $O_3 + hv \xrightarrow{k} O(^1D) + O_2$ as a Function of Zenith Angle

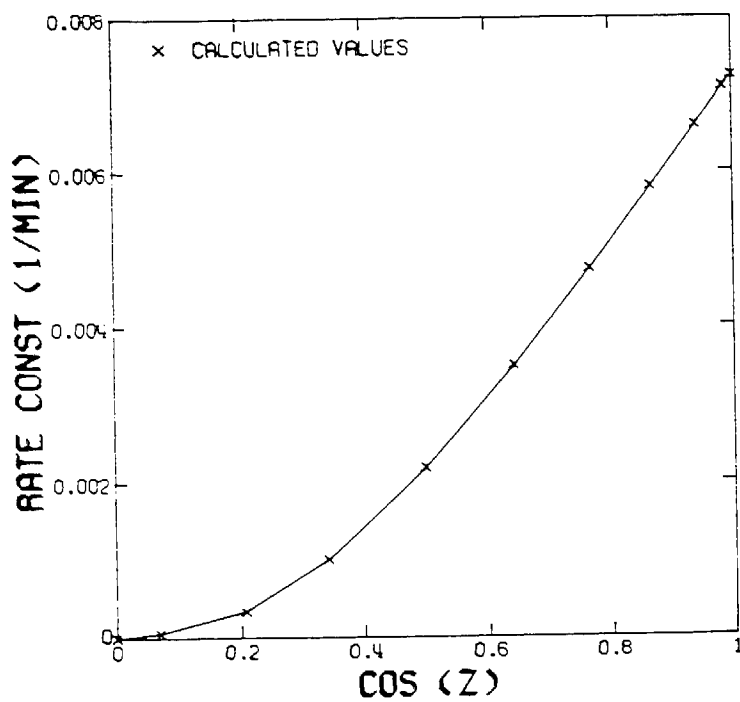


FIGURE 8.9

Photolysis Rate for $O_3 + hv \xrightarrow{k} O_2(^1\Delta) + O$ as a Function of Zenith Angle

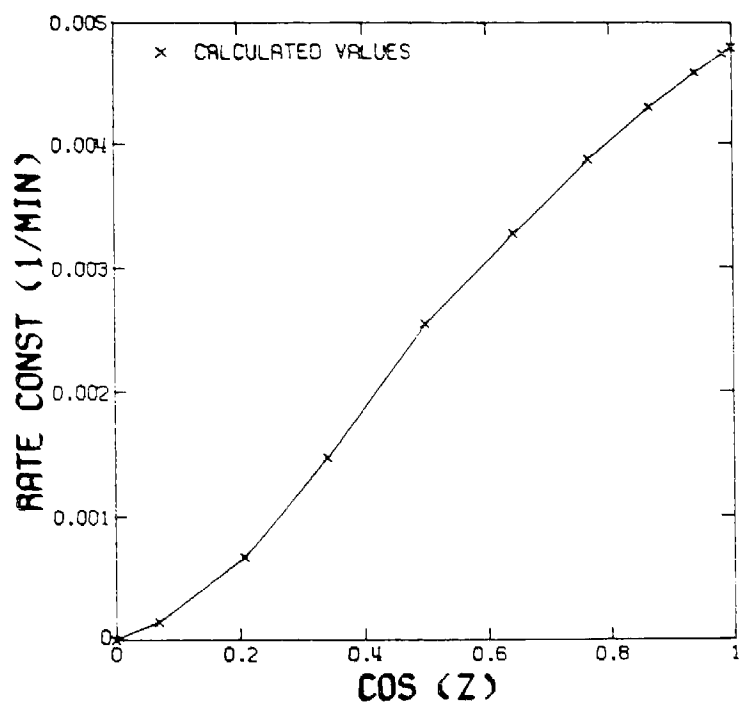


FIGURE 8.10

Photolysis Rate for $\text{HCHO} + h\nu \xrightarrow{k} \text{H}_2 + \text{CO}$ as a Function of Zenith Angle

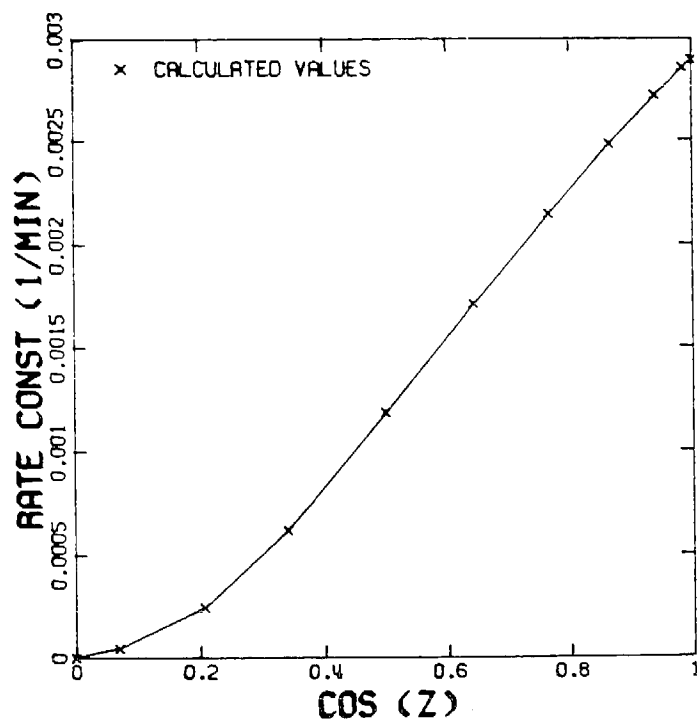


FIGURE 8.11

Photolysis Rate for $\text{HCHO} + h\nu \xrightarrow{k} 2\text{HO}_2 + \text{CO}$ as a Function of Zenith Angle

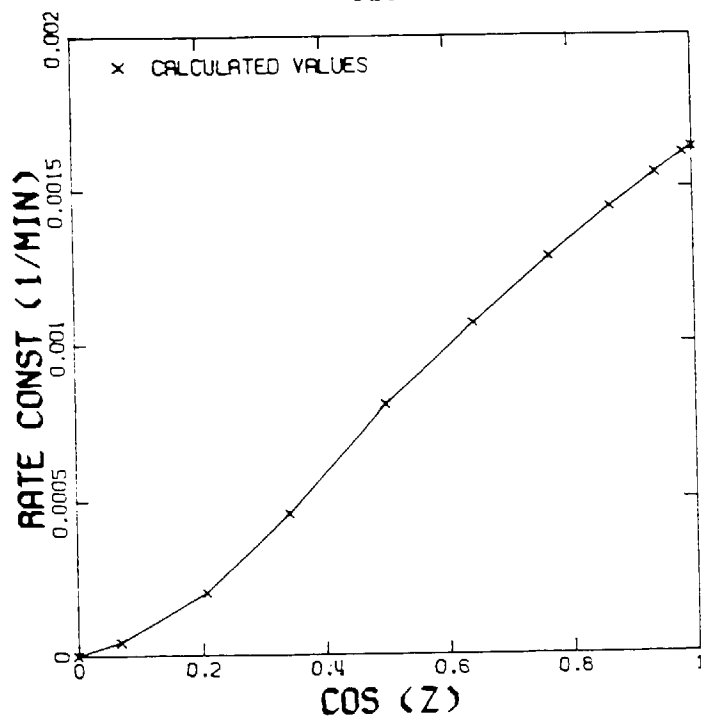


FIGURE 8.12

Photolysis Rate for $\text{H}_2\text{O}_2 + h\nu \xrightarrow{k} 2\text{OH}$ as a Function of Zenith Angle

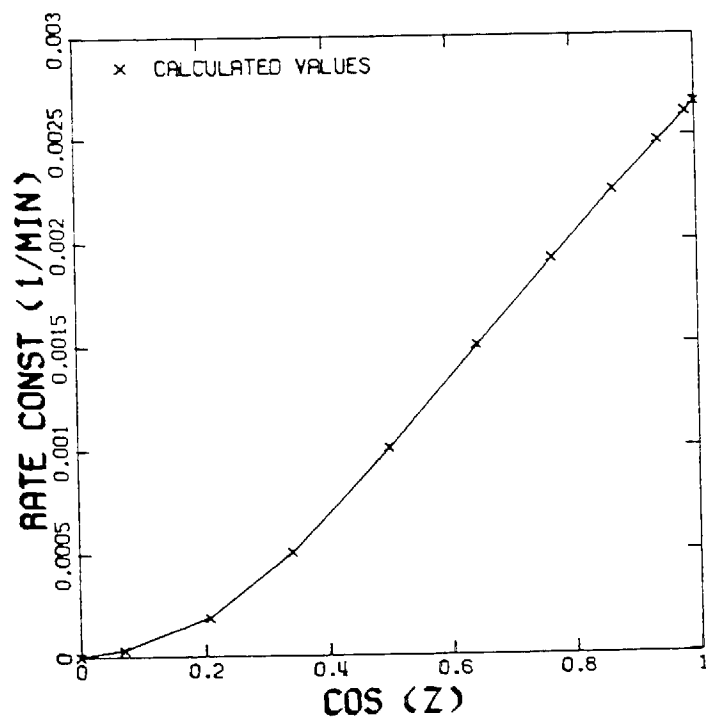


FIGURE 8.13

Photolysis Rate for $\text{CH}_3\text{CHO} + h\nu \xrightarrow{k} \text{CH}_3 + \text{HO}_2 + \text{CO}$ as a Function of Zenith Angle

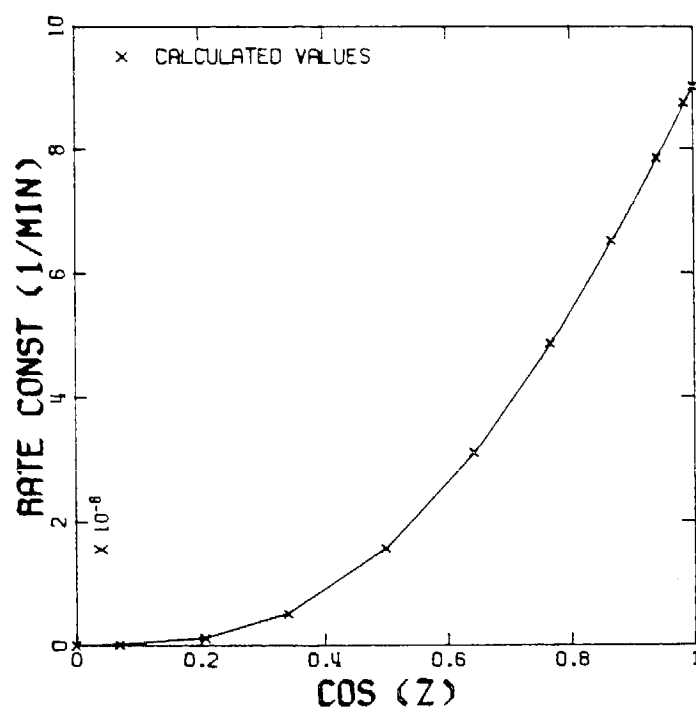


FIGURE 8.14

Photolysis Rate for $\text{CH}_3\text{CHO} + h\nu \xrightarrow{k} \text{CH}_4 + \text{CO}$ as a Function of Zenith Angle

$$\cos Z = \sin \phi \sin \delta + \cos \phi \cos \delta \cos h \quad (8.26)$$

where ϕ is the latitude and h the hour angle. The relationship between these angles is shown in Figure 8.15. At solar noon the hour angle is zero and as a result it is related to the local standard time and the longitude λ . The declination angle is a function only of the day of the year and it varies from $23^{\circ}27'$ on June 21 to $-23^{\circ}27'$ on December 22nd. Values for each day and hour can be obtained from a nautical almanac or calculated using the algorithm of Woolf (1967). This latter approach, together with a simple interpolation scheme, and Figures 8.4-8.14 is used to evaluate the photolysis rates in the airshed model. The expression (8.26) can also be employed to calculate the day length and in turn the sunrise and sunset times. A knowledge of these times is very useful for controlling the numerical procedures during the rapid chemical changes which take place during initiation or termination of the mechanism photolysis steps.

A typical diurnal variation in the NO_2 photolysis rate and a comparison against the experimental observations of Zafonte (1977), is shown in Figure 8.16. The predicted and measured values agree quite closely over most of the day. Scatter in the experimental measurements was primarily due to the presence of broken high cloud conditions (Zafonte, 1977). Schere and Demerjian (1977) attempted a similar correlation; however, most of the measurements available to them were for non clear sky conditions and, as a result, scaling of the calculated

results was required. Table 8.12 presents a summary of the photodissociation rates for the photolysis steps in the Falls and Seinfeld (1978) mechanism. Some preliminary results for ozone and the appropriate experimental techniques for formaldehyde (HCHO), nitrous acid (HONO), hydrogen peroxide (H_2O_2), and nitric acid (HNO_3) have been described by Stedman et al. (1977). An additional point to note about the results is that the rates have been calculated using ground level actinic irradiance data. Within the lowest 5-10 km of the atmosphere the actinic flux increases with elevation leading to higher photolysis rates. The results of Peterson et al. (1977) for NO_2 and HCHO show a significant increase with height. For example, at an elevation of 0.98 km the photolysis rate for NO_2 , depending on the zenith angle, is between 21 and 70% higher than the corresponding ground level value. The photolysis rates should be recalculated if the modeling region is at a high elevation.

Most theoretical calculations of the photolysis rate constants assume 'clear sky' conditions. A critical problem in practice is how to modify the calculated results when there is a perturbation to the basic atmospheric state employed in the radiative transfer calculations. Increased aerosol loadings or the presence of clouds would require scaling of the photodissociation rates.

When only broad band measurements of solar radiation are available correction of the calculated values can be based on the ratio of pyranometer observations to the theoretical clear sky transmission. Because pyranometer data reported by air pollution agencies typically only apply to total solar fluxes and the reaction rates depend on the ultraviolet (uv) flux densities, the scaling ratio may not be a good representation. Scattering is wavelength dependent and as a result the uv flux is more strongly affected than the total solar flux. Offsetting this to some extent, the flux density is much less sensitive to scattering than is the flux (Duewer et al., 1978).

In situations where uv pyranometer data are available another approach is possible. Zafonte et al. (1977) and Stedman et al. (1977) correlated their NO_2 photodissociation rate measurements with solar radiation in the uv portion of the spectrum. Radiometric data were obtained with Eppley uv pyranometers that have a full bandwidth sensitivity of 295–385 nm, a wavelength interval relevant to many photochemical reactions. The results of the correlations are shown in Figure 8.17. This graph provides a direct means of determining either the photolysis rate from the radiation measurements or the scaling ratios for the calculated values. Schere and Demerjian (1977) used uv measurements and the calculated clear sky solar flux to scale the rate constants. They reported substantial differences in some cases between theoretical clear sky and observed rate constants, however, the uv scaled calculated rates match the observations quite closely as in Figure 8.18.

TABLE 8.12

Photolysis Steps in Photochemical Reaction Mechanism^a

REACTION				Photolysis Rate (min ⁻¹)		
				7:24 AM ^b	Average ^c	Peak
NO ₂	+ hν	$\xrightarrow{1}$	NO + O(³ P)	0.320	0.339	0.508
HONO	+ hν	$\xrightarrow{10}$	OH + NO	0.0585	0.0631	0.0963
O ₃	+ hν	$\xrightarrow{20}$	O(³ P) + O ₂	0.0229	0.0232	0.0328
HCHO	+ hν	$\xrightarrow{21}$	2HO ₂ + CO	0.00121	0.00163	0.00284
HCHO	+ hν	$\xrightarrow{22}$	H ₂ + CO	0.00258	0.00296	0.00473
RCHO	+ hν	$\xrightarrow{24}$	RO ₂ + HO ₂ + CO	0.00103	0.00145	0.00260
RONO	+ hν	$\xrightarrow{35}$	NO + RO	0.0704 ^d	0.0746 ^d	0.1118 ^d
H ₂ O ₂	+ hν	$\xrightarrow{51}$	2OH	0.00082	0.00098	0.00161

a) All values are for Los Angeles California (latitude 34.06°, longitude 118.25°, time zone = 8.0)

b) Photolysis rates at 7:24 Pacific Standard Time, 26 June 1974.

c) Average of daylight hours.

d) Photolysis rate set to 0.22 of NO₂

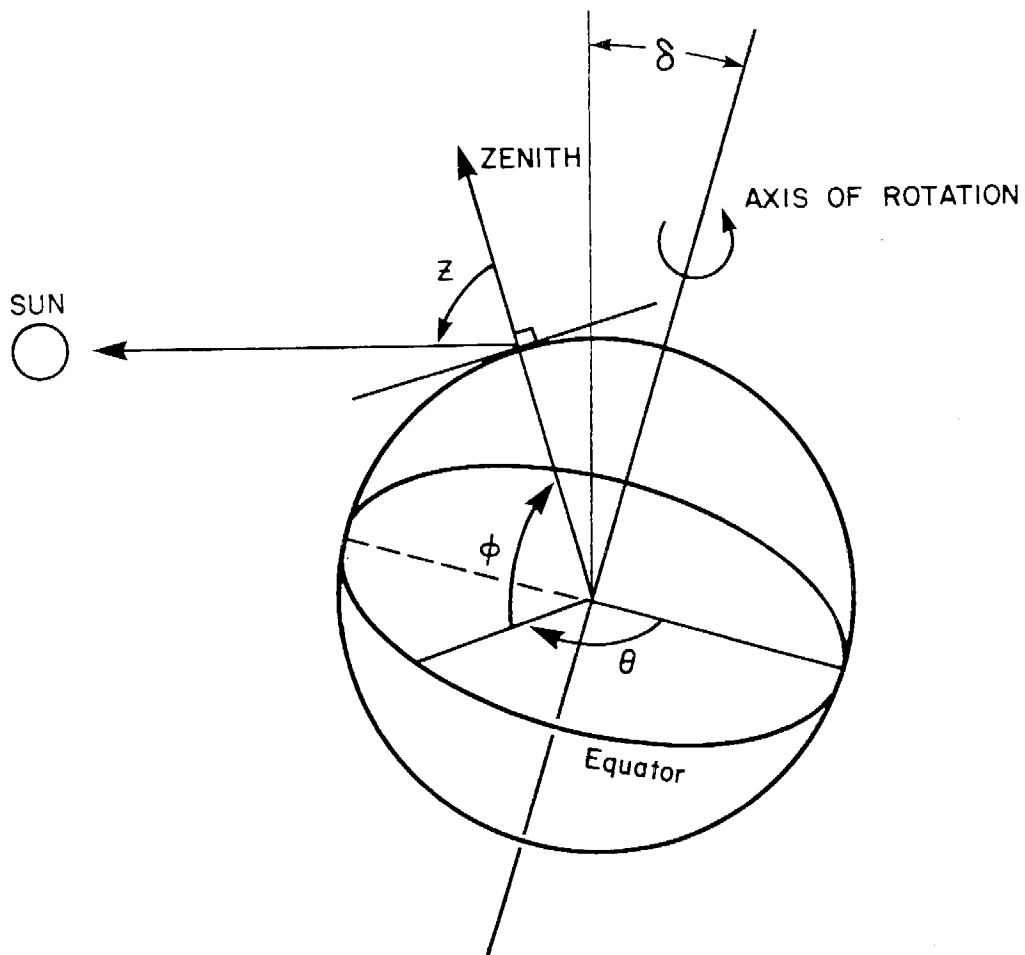


FIGURE 8.15

Relationship Between Latitude, Declination and Zenith Angles.

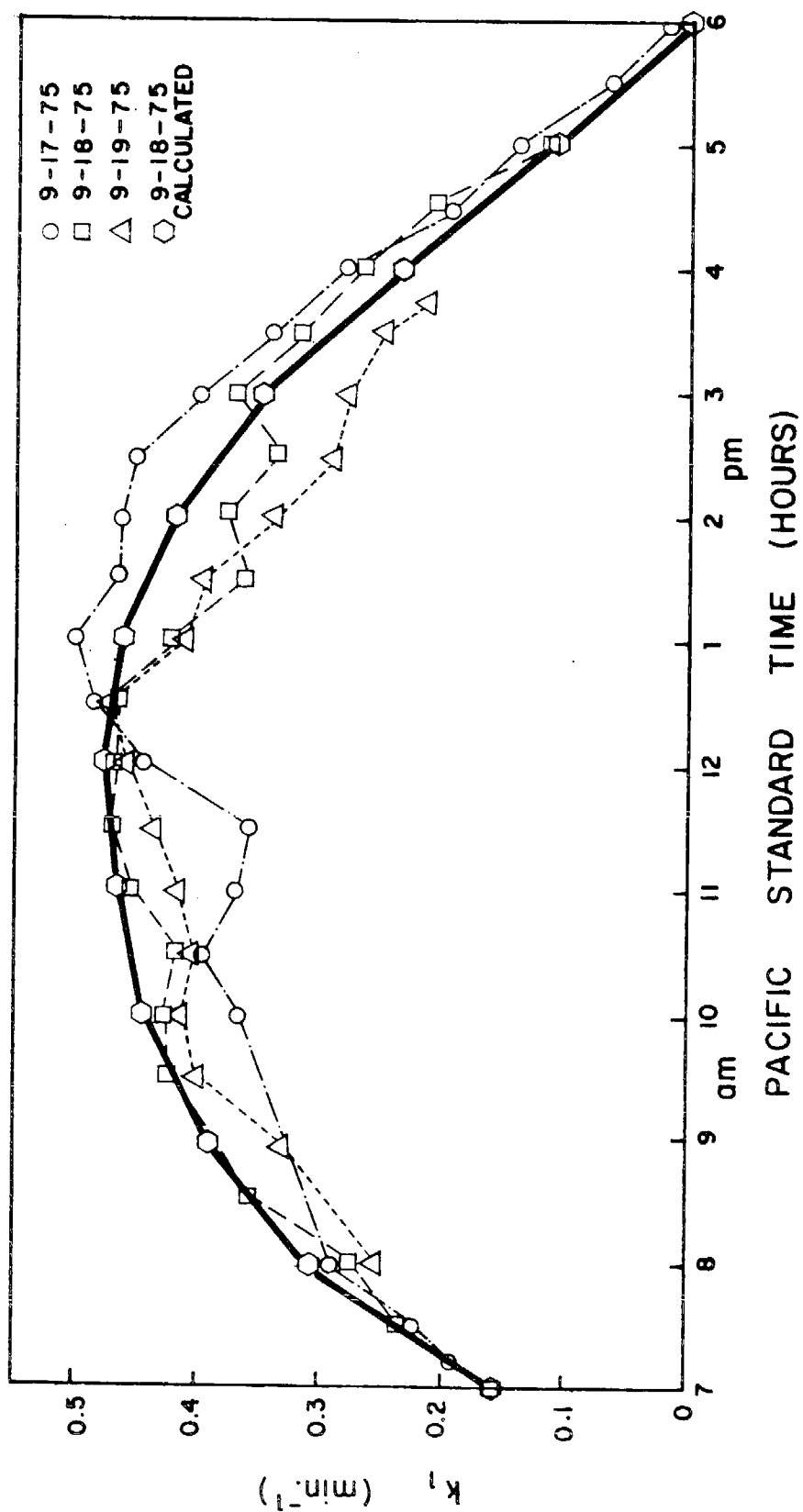


FIGURE 8.16

Comparison of Calculated Diurnal Variation of NO_2 Photolysis Rate with
Experimental Measurements of Zafonte et al. (1977)

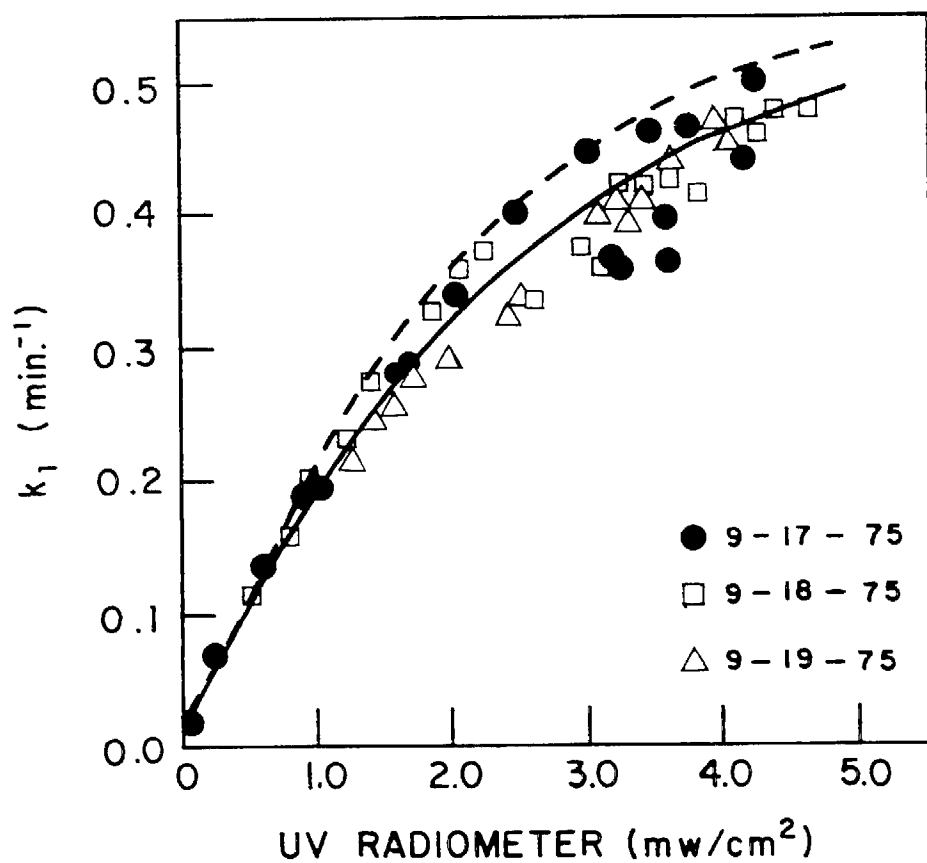


FIGURE 8.17

Correlation Between UV Radiometric Measurements and NO_2 Photolysis Rate - Experimental Points and Solid Line are from Zafonte et al. (1977), Dashed Line is Best Fit to Data of Stedman et al. (1977)

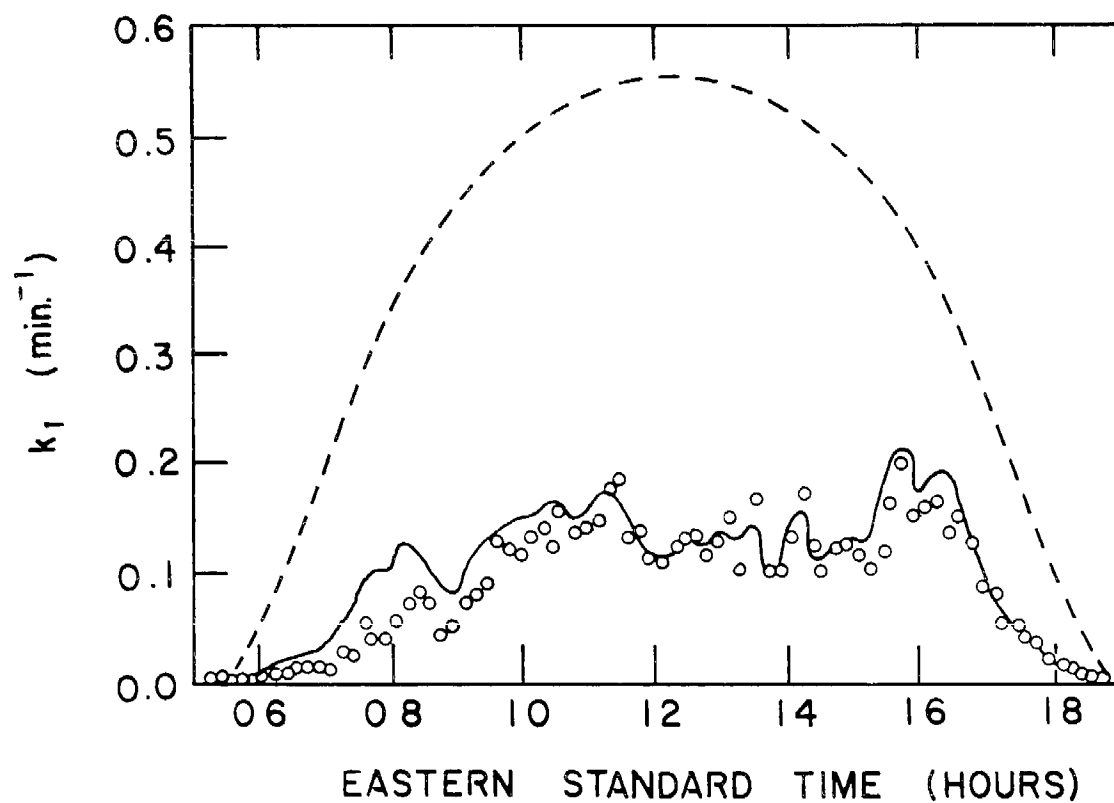


FIGURE 8.18

Comparison of the Experimental (Circles), Theoretical (Dashed Line), and UV Scaled Theoretical (Solid Line) Diurnal Variation of the Photolytic Rate Constant for the Photolysis of NO_2 Near Raleigh, N.C. (35.8°N , 78.6°W) on April 28, 1975
(Source: Schere and Demerjian, 1977).

8.7 Calculation of Atmospheric Water Vapor Concentration

Most photochemical reaction mechanisms require that the water vapor be expressed in terms of concentration units like ppmV or $\mu\text{g}/\text{m}^3$. While it is a straightforward task to determine the concentration given ambient measurements of temperature, pressure, and relative humidity, the need to employ psychrometric charts or tables considerably complicates automation of the process. This section presents a simple algebraic procedure, based on McRae (1980), which enables the water concentration to be determined to within 0.5% over the range of commonly encountered meteorological conditions.

For a given temperature, T , relative humidity, RH , is defined as the ratio of the observed vapor pressure to the saturation vapor pressure at the same conditions. An alternative approach is to define RH in terms of the mole fraction of water vapor in the moist atmosphere, y , to the mole fraction at saturation y_s . In either case the relative humidity is often expressed in percent so that

$$RH = 100 \frac{y}{y_s} \quad (8.27)$$

Since the mole fraction is equivalent to the volume fraction the water concentration in ppmv is given by

$$\text{H}_2\text{O}(\text{ppmv}) = 10^6 y = 10^4 RH y_s \quad (8.28)$$

By using the perfect gas laws (8.28) can be written in terms of the saturation vapor pressure $P_s(T)$ and the atmospheric pressure P_a . The

error involved in using Dalton's Law over a temperature range of -50 to 50°C is less than 0.5% (Threlkeld, 1970). With this approximation (8.28) can be written in the form:

$$H_2O(\text{ppmv}) = 10^4 RH \frac{P_s(T)}{P_a} \quad (8.29)$$

In order to evaluate this expression, the saturation vapor pressure must be known. While many tabulations and graphical forms exist in the literature relatively few are suitable for direct inclusion in the airshed model; what is required is an explicit algebraic expression. One of the first attempts to describe $P_s(T)$ - T experimental data in a functional form was the work of Goff and Gratch (1945). Their function, while quite accurate ($\sim 0.001\%$), involves a large number of constants and contains highly non-linear terms. An approximate expression for $P_s(T)$ in mb, applicable to a limited temperature range, is given by (Iribarne and Godson, 1973).

$$\log_{10}[P_s(T)] = -\frac{2937.4}{T_a} - 4.9283 \log_{10} T_a + 23.5518 \quad (8.30)$$

This form is sometimes called the Magnus formula and corresponds to the inclusion of second and third terms in the virial equation of state. For the purpose of this study the simple, but relatively unknown, polynomial expression of Richards (1971) was adopted. The functional form is given by:

$$P_s(T) = P_A \exp[13.3185t - 1.9760t^2 - 0.6445t^3 - 0.1299t^4] \quad (8.31)$$

where P_A is the standard atmospheric pressure of 1013.25 mb, the parameter t is defined in terms of the ambient temperature T_a ($^{\circ}\text{K}$) and the steam temperature $T_s \approx 373.15^{\circ}\text{K}$ at pressure P_a .

$$t = 1 - \frac{T_s}{T_a} \approx 1 - \frac{373.15}{T_a} \quad (8.32)$$

Equation (8.31) is more accurate than (8.30) and is valid to $\pm 0.1\%$ over a temperature range of -50 to 140°C . The variation of $P_s(T)$ over the range $T_a = -50$ to 40°C is shown in Figure 8.19. Table 8.13 illustrates the application of the procedure to some typical atmospheric conditions.

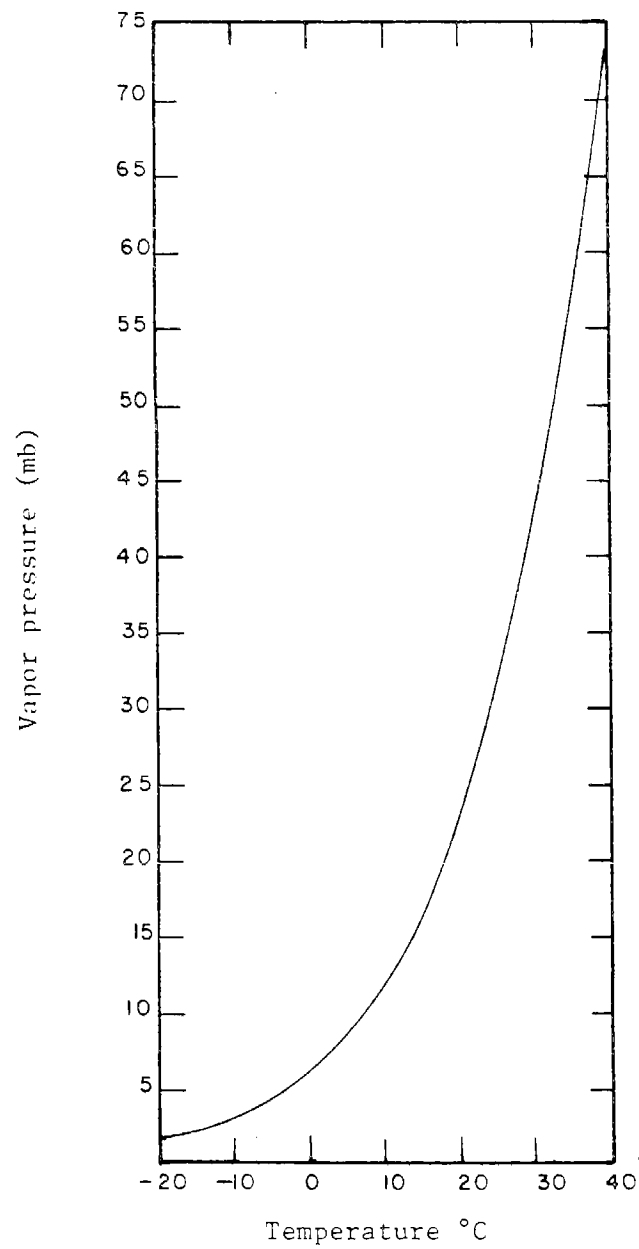


FIGURE 8.19

Saturation Vapor Pressure as a Function of Ambient Temperature
Evaluated Using the Polynomial Expression of Richards (1971)

TABLE 8.13
APPLICATION OF PROCEDURE FOR CALCULATING
ATMOSPHERIC WATER VAPOR CONCENTRATION ^a

T_a (°C)	$P_s(T_a)$ (mb)	$\frac{H_2O(\text{ppm})}{RH(\%)}$	H_2O at 50% RH (ppm)
-20	1.25	12.34	617
-15	1.91	18.85	942
-10	2.86	28.23	1411
-5	4.22	41.65	2082
0	6.11	60.30	3015
5	8.72	86.06	4303
10	12.28	121.19	6060
15	17.05	168.27	8413
20	23.39	230.84	11542
25	31.69	312.76	15638
30	42.45	418.95	20947
35	56.26	555.24	27762
40	73.80	728.35	36417
45	95.89	946.36	47318

^a Ambient conditions assumed for calculation $P_a = 1013.25$ mb
Steam temperature $T_s = 373.15^\circ\text{K}$.

8.8 A Simple Box Model for Testing Photochemical Reaction Mechanisms

Before a photochemical reaction scheme is used in an airshed model it is necessary to carry out a series of tests to evaluate the performance of the mechanism under a variety of conditions. A common approach is to compare the prediction of the mechanism against observational data from smog chamber experiments. While valuable, these comparisons do not adequately test the kinetics over the range of conditions likely to be encountered in the atmosphere. Specifically, few smog chamber experiments include the effects of continuous injection of source material or diurnal variations of solar radiation. This section presents the formulation of a simple box model in which the effects of different meteorological and surface removal processes can be isolated. When interpreted as a well mixed chemical reactor, the mathematical system can be used to model a wide variety of smog chamber experiments. The range of valid atmospheric applications, however, is restricted by the nature of the assumptions used in the model derivation.

The most elementary form of a box model is a well mixed, variable volume, chemical reactor. A variable volume formulation is needed in atmospheric applications because the vertical extent of pollutant dispersion is controlled by diurnal variations in the depth of the mixed layer. The effects of a capping inversion over an urban area can be best studied if the mixing height is included as an explicit variable.

In order to account for these effects consider a single cell located over a large, horizontally homogeneous, urban area (Figure 8.20).

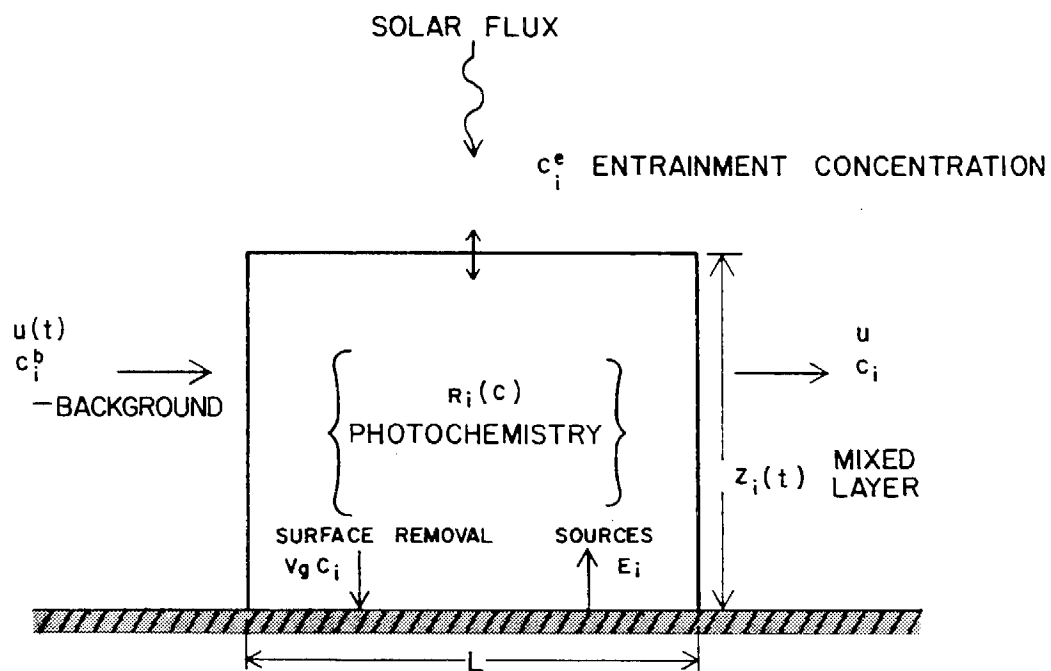


FIGURE 8.20

Schematic Representation of a Simple Box Model

The source strength per unit area for species $c_i, i=1,2,\dots,n$ is represented by E_i . The box is of dimension $LWZ_i(t)$ where L is the length parallel to the spatially uniform wind field $u(t)$. W is the box width and $Z_i(t)$ the current mixed layer depth. The ventilation cross section is WZ_i and the pollutant flux out of the box is simply $WZ_i u c_i$, where c_i is the average pollutant concentration in the well mixed box. If c_i^b is the background concentration, then the material flux into the box from outside the region is $WZ_i u c_i^b$. Generation or removal of species by chemical reaction is represented by $R_i(c_1, c_2, \dots, c_n)$. In the present model, surface interactions are parameterized in terms of simple deposition velocity v_g .

If pollutants, left at elevated levels from the previous day, are advected out of the box before sunrise on the current day then the mixed layer will grow into air containing ambient or background conditions. Denoting c_i^e as the concentration left above the current mixed layer, then if $c_i^e > 0$ the entrainment flux into the box is $LW c_i^e dZ_i/dt$. A collapsing mixed layer, however, does not act as an impenetrable lid. Ignoring the contribution from surface sources, the concentration within the box is not affected by the volume change. When the ventilation is weak, then c_i^e should be replaced by c_i so that the current concentration is entrained the next day. In this present study, chemical reactions amongst the species above the mixed layer are not considered.

Given the above assumptions and ignoring the effects of horizontal diffusion, the conservation equations for pollutant material within the box can be written as a set of ordinary differential equations.

$$\begin{aligned} \frac{d}{dt}(LWZ_i c_i) = & LWZ_i R_i(c) + LWE_i + WZ_i u(c_i^b - c_i) \\ & + LW \frac{\partial Z_i}{\partial t} c_i^e - LWv_g c_i \end{aligned} \quad (8.33)$$

$$i=1,2,\dots,n$$

Dividing through by the box volume and taking into account the temporal variations in Z_i , (8.33) can be written in the form

$$\frac{dc}{dt} = R(c) + \frac{E}{Z_i} + \frac{u}{L} (c^b - c) + \frac{(c^e - c)}{Z_i} \frac{dZ_i}{dt} - \frac{v_g c}{Z_i} \quad (8.34)$$

where the species index i has been dropped for convenience. For numerical solution purposes it is convenient to have the Jacobian of (8.34) which is given by (8.35) where $[I]$ is the identity matrix.

$$J = \frac{\partial}{\partial c} \left(\frac{dc}{dt} \right) = \frac{\partial R(c)}{\partial c} - \frac{u}{L} [I] - \frac{1}{Z_i} \frac{dZ_i}{dt} [I] - \frac{v_g}{Z_i} [I] \quad (8.35)$$

In the above expression the terms involving dZ_i/dt are set to zero if $dZ_i/dt < 0$. The form (8.35) is quite similar to the expression originally proposed by Lettau (1970). The principal differences are: the parameterization of the turbulent flux caused by entrainment, the chemical reactions and surface deposition terms. If the box moves with mean wind then (8.35) represents a one-dimensional trajectory model.

In view of the simplicity of the model, it is worthwhile to reiterate the basic assumptions used in its formulation. The most critical simplification is that the pollutants are well mixed up to the

capping inversion. Unless the characteristic turbulent mixing time is fast in comparison to the chemical reaction rates, then the box model is not representative of atmospheric conditions.

8.9 Numerical Solution Procedures

The algebraic forms of the ordinary differential equations which describe the kinetics of the mechanism shown in Table 8.1 are presented in Appendix A. This system, subject to the appropriate rate constants and initial conditions, was solved with the variable step, variable order, backward difference scheme of Hindmarsh and Byrne (1975). This method was chosen because it represents one of the best general purpose approaches to numerical integration of stiff ordinary differential equations. Selection of a method that was both robust and highly accurate was important because in a number of cases the numerical results of this appendix were used as standards for comparative evaluation of solution schemes described in Chapter 11.

Except for cases in which steady state approximations were used, the kinetics of each species were described by differential equations. Because of their high concentration, constant values were assigned to oxygen (2.1×10^5 ppmV) and the third body M (1.0×10^6 ppmV) which appears in the ozone formation step. In each case the starting and maximum step sizes were set to 10^{-5} and 10 minutes, respectively. Semi-relative error control, with a convergence tolerance of $\epsilon = 0.0001$, was selected because some species have an initial concentration of zero. From a

practical point of view there is little to be gained by using smaller values of ϵ . In fact, setting ϵ to be less than 10^{-4} in most cases gave no useful additional information and at the same time drastically increased the consumption of computer time.

8.10 Smog Chamber Experiments

A direct way of evaluating photochemical reaction mechanisms is to compare the predictions against carefully controlled laboratory studies. Falls and Seinfeld (1978), for example, tested their model against smog chamber experiments conducted at the Statewide Air Pollution Research Center (SAPRAC) of the University of California at Riverside. Extensive documentation of the experimental protocols, sampling procedures and measurement techniques used at that research center are given in Pitts et al. (1976), Pitts and Winer (1978) and Winer et al. (1980). The initial evaluation of the airshed mechanism employed propylene and n-butane as well as different combinations of the two compounds. Further experiments have been carried out using hydrocarbon mixtures which more closely correspond to atmospheric conditions. A representative sample of these results is presented in this section.

The initial conditions for one smog chamber experiment, SUR-119J (Pitts et al., 1976), are reproduced in Table 8.14. This information together with the photolysis and lumped hydrocarbon rate constants from Tables 8.8 and 8.12 is sufficient to enable an independent duplication of the mechanism performance. Table 8.15 and Figures 8.21 - 8.27

TABLE 8.14

Initial Conditions for Smog Chamber Experiment SUR-119J

SPECIES	CONCENTRATION (ppmv)
NO	0.301
NO ₂	0.041
HNO ₂	0.012
CO	7.45
HCHO	0.038
RCHO	0.023
ALK	0.358
OLE	0.039
C ₂ H ₄	0.043
ARO	0.07
H ₂ O	15500.0
O ₂	210000.0
M	1000000.0
Total Nitrogen	0.354
RHC(ppmV)	0.548
NO _x /RHC (ppmv/ppmV)	0.642
Relative Humidity (%)	58.5-53.0
Temperature (°C)	30.5-33.1

TABLE 8.15

Initial Conditions for Smog Chamber Experiments

Experiment ^a	Initial Conditions (ppmV)								k ₁ (min ⁻¹)	
	NO	NO ₂	OLE	ALK	ARO	ETH	HCHO	RCHO		HONO ^b
119J	0.301	0.041	0.039	0.358	0.070	0.043	0.038	0.023	0.0	0.32
121J	0.044	0.012	0.040	0.370	0.066	0.042	0.06	0.011	0.0	0.32
126J	0.302	0.040	0.039	0.372	0.075	0.046	0.043	0.007	0.0	0.32
132J	0.144	0.018	0.024	0.224	0.045	0.029	--	0.014	0.012	0.32
133J	0.084	0.013	0.023	0.227	0.046	0.032	0.005	0.011	0.012	0.32
134J	0.030	0.008	0.041	0.368	0.067	0.043	0.031	0.013	0.0	0.32
EC-237 ^c	0.377	0.106	0.15	1.488	0.177	0.875	0.0	0.0012	0.08	0.30

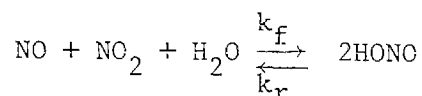
a Pitts et al. (1976)

b Assumed (see Text)

c Evacuable chamber O₃ wall loss rate = 2.3×10^{-3} min⁻¹, dilution 2.9×10^{-4} min⁻¹ (Pitts and Winer, 1978).

document these results as well as a number of other experiments. The model predictions closely match most of the observed data.

There is some evidence that nitrous acid is formed during the loading of smog chambers (Chan et al., 1976). Nitrous acid is produced in the dark by the reactions



and an equilibrium can be reached given sufficient time. The concentration of nitrous acid achieved in the dark is governed by

$$\frac{d[\text{HONO}]}{dt} = 2k_f [\text{NO}][\text{NO}_2][\text{H}_2\text{O}] - 2k_r [\text{HONO}]^2 \quad (8.36)$$

Solution of this rate equation subject to $[\text{HONO}]_0 = 0$ yields the concentration of nitrous acid as a function of time. As $t \rightarrow \infty$, the equilibrium concentration,

$$[\text{HONO}]_{\text{eq}} = \left[\frac{k_f [\text{NO}][\text{NO}_2][\text{H}_2\text{O}]}{k_r} \right]^{1/2} \quad (8.37)$$

is reached. Assuming that $[\text{NO}]$, $[\text{NO}_2]$ and $[\text{H}_2\text{O}]$ are constant, (8.36) can be integrated to yield

$$\frac{[\text{HONO}]}{[\text{HONO}]_{\text{eq}}} = \tan \left\{ 2t \sqrt{k_f k_r [\text{NO}][\text{NO}_2][\text{H}_2\text{O}]} \right\} \quad (8.38)$$

Table 8.16 shows the approach of HONO to the equilibrium value as a function of time for representative values of the rate of reaction. The quantity of nitrous acid that forms in a chamber or atmosphere prior

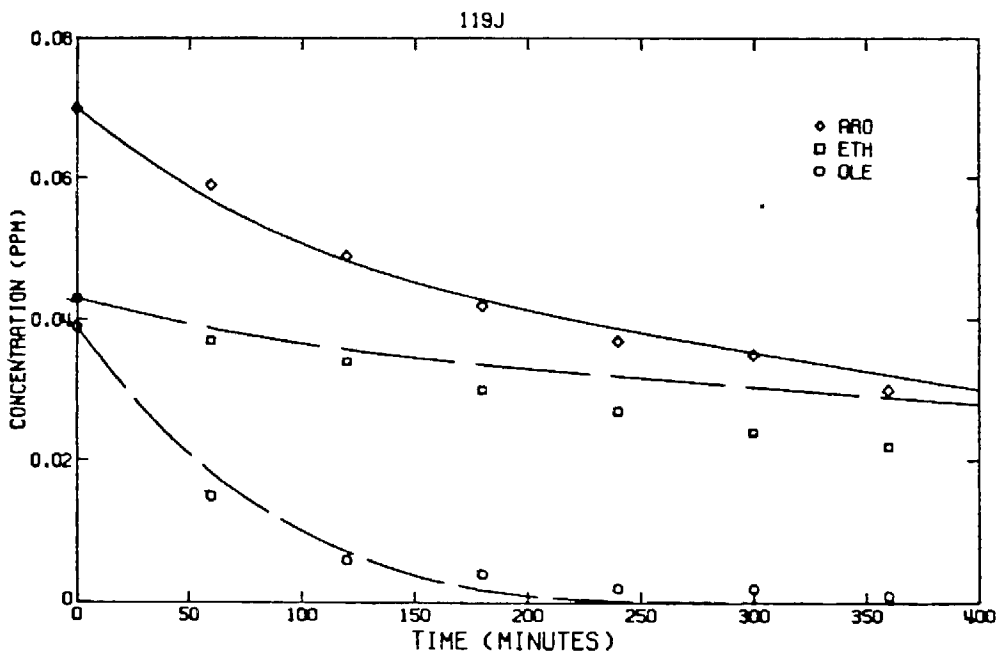
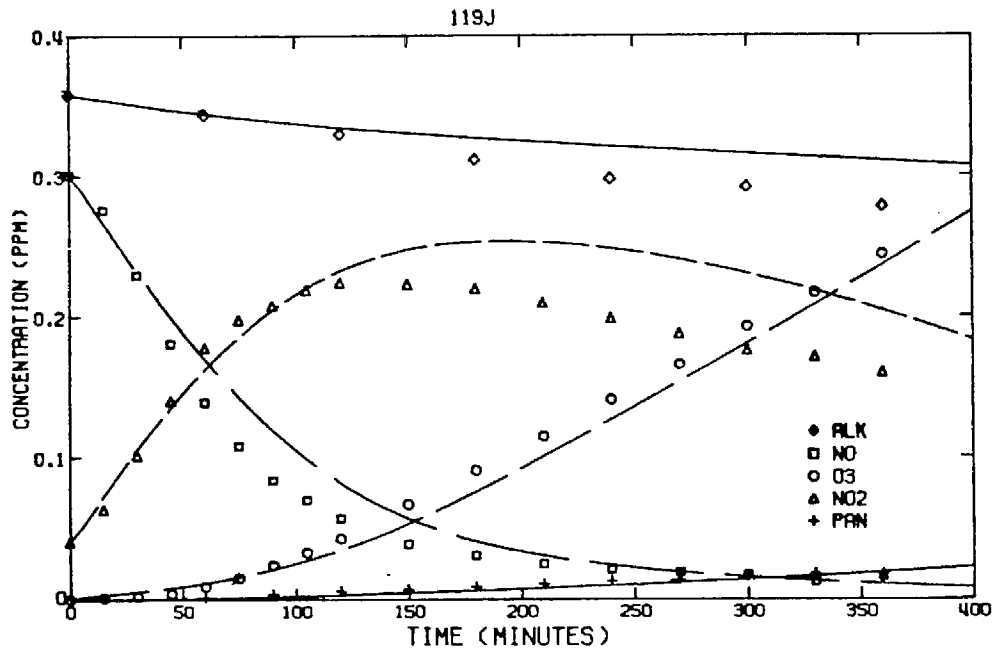


FIGURE 8.21

Predicted and Observed Concentration Profiles for Smog Chamber Experiment 119J

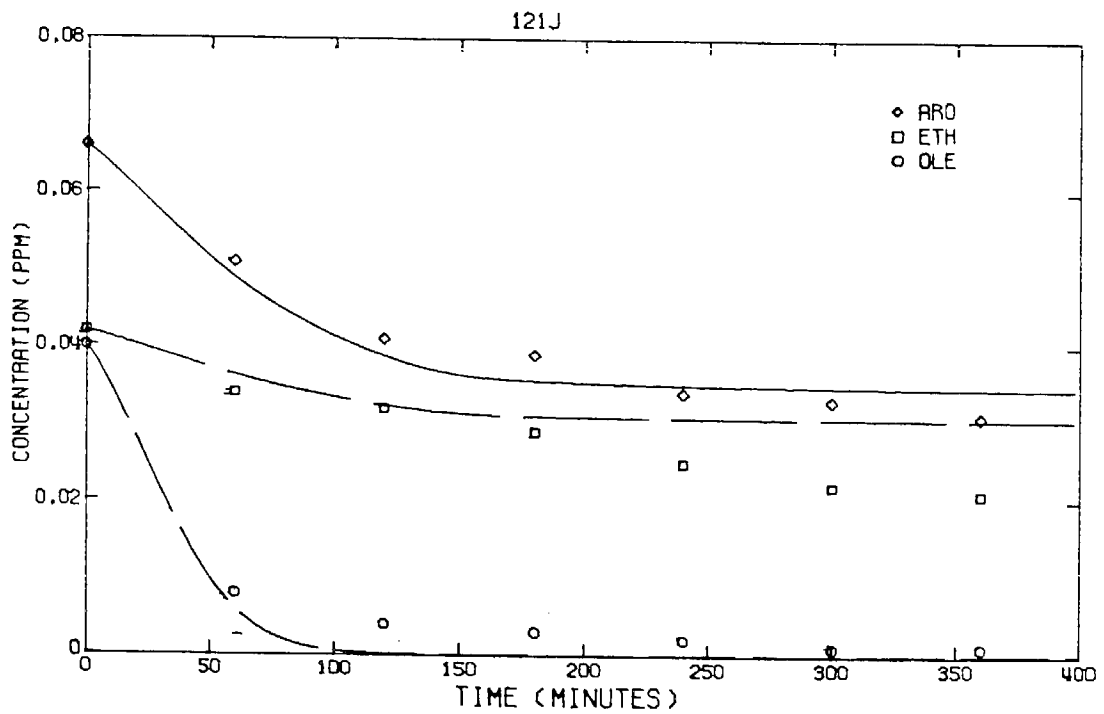
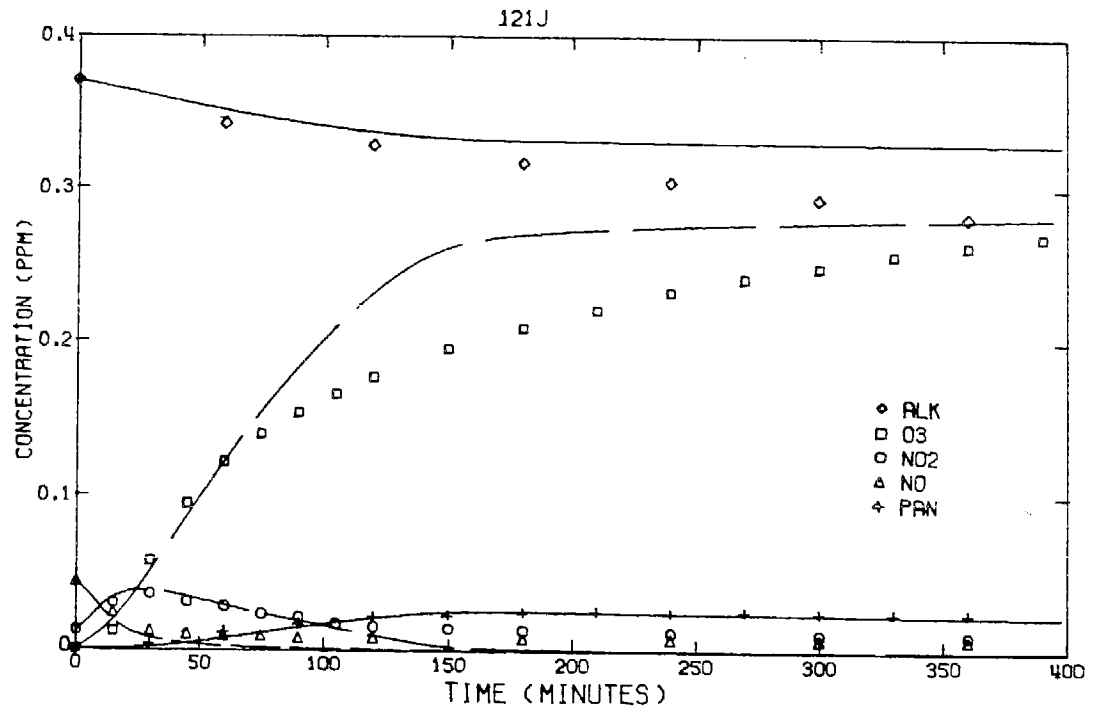


FIGURE 8.22

Predicted and Observed Concentration Profiles for Smog
Chamber Experiment 121J

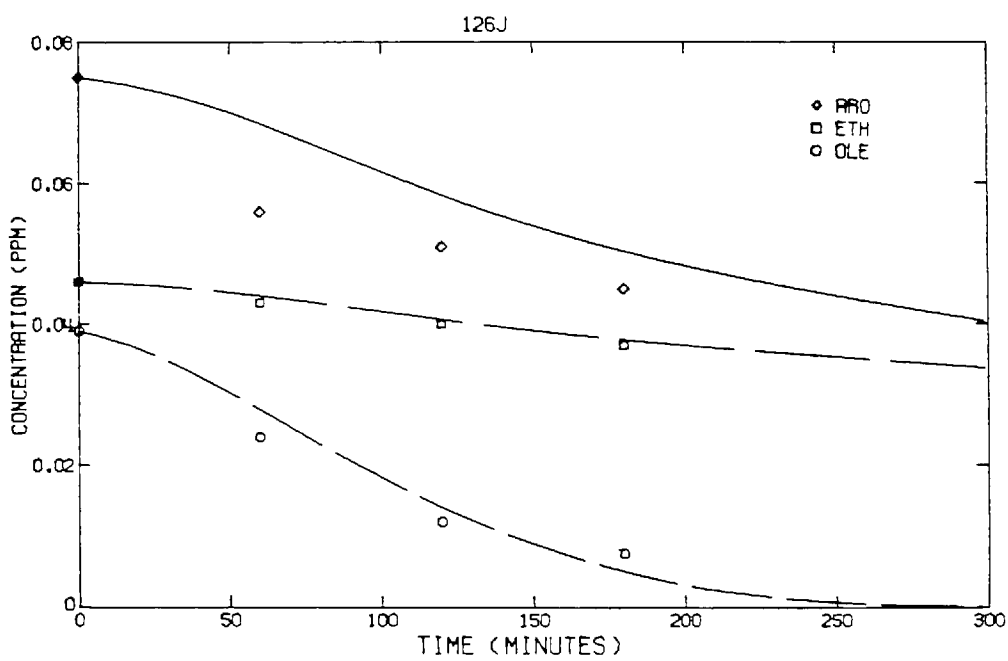
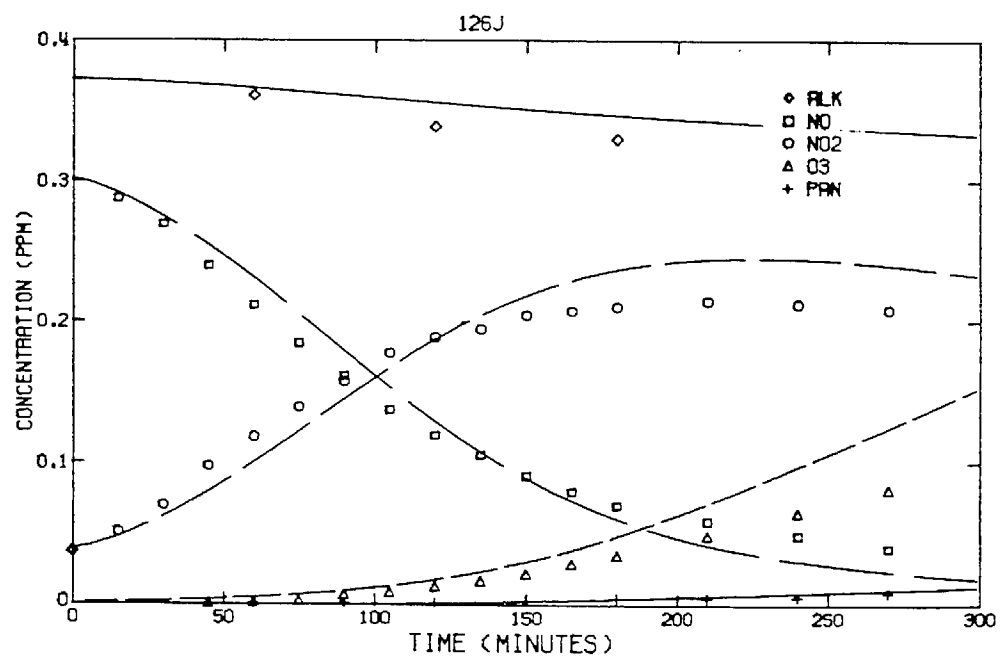


FIGURE 8.23

Predicted and Observed Concentration Profiles for Smog
Chamber Experiment 126J

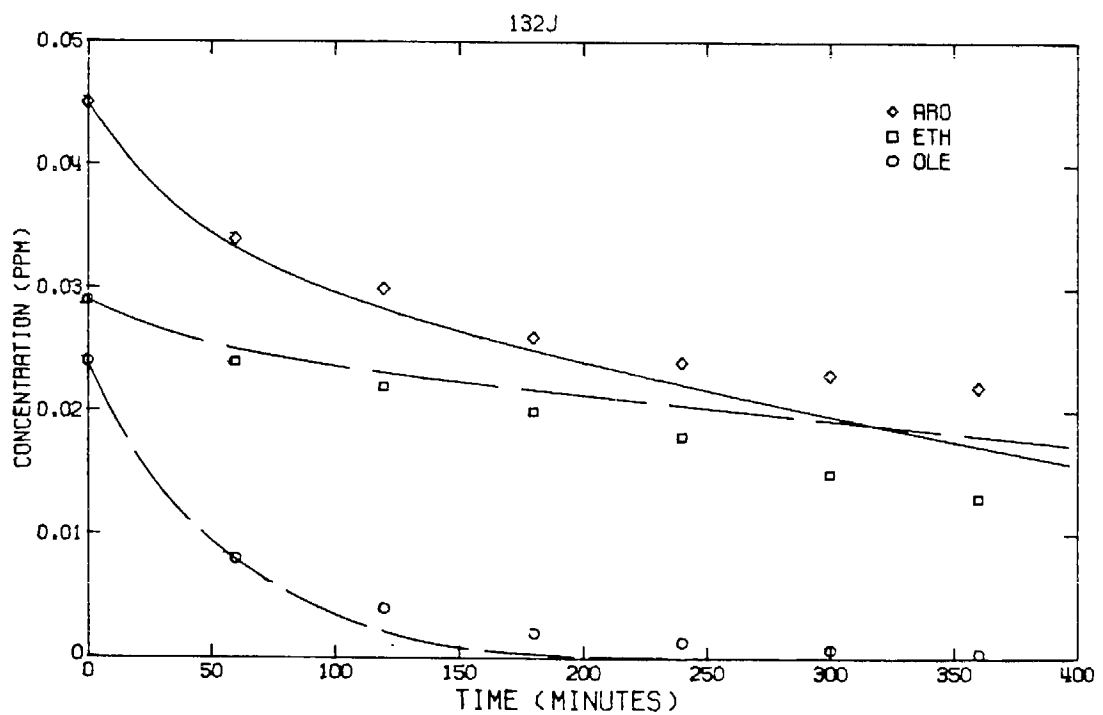
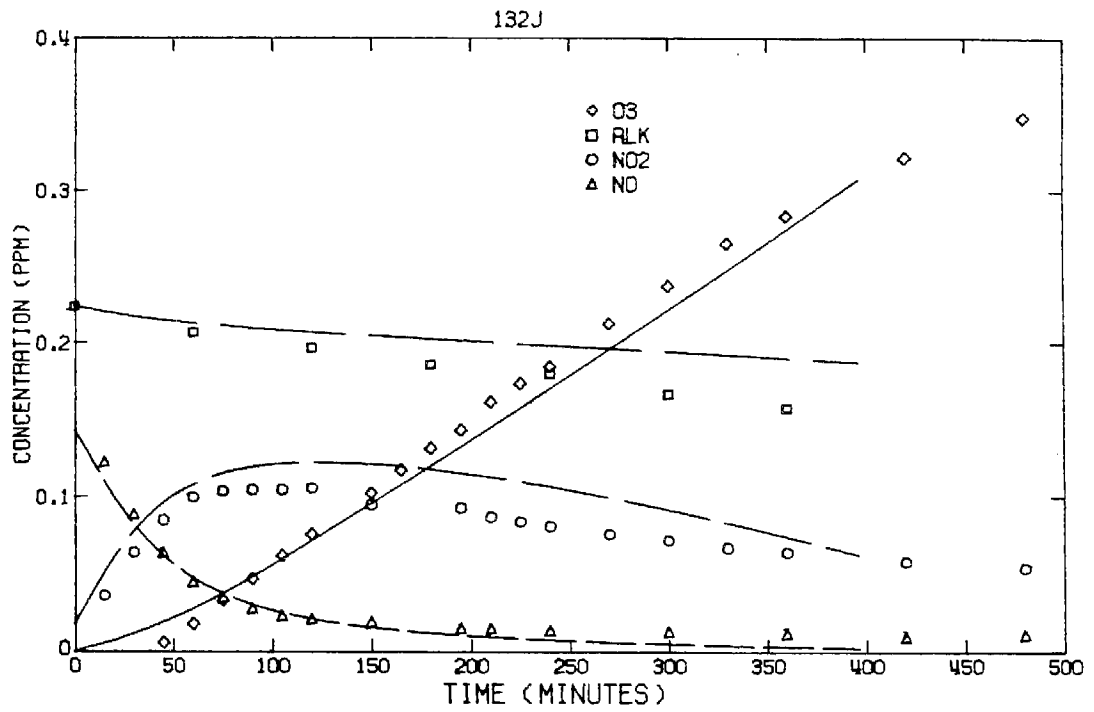


FIGURE 8.24

Predicted and Observed Concentration Profiles for Smog
Chamber Experiment 132J

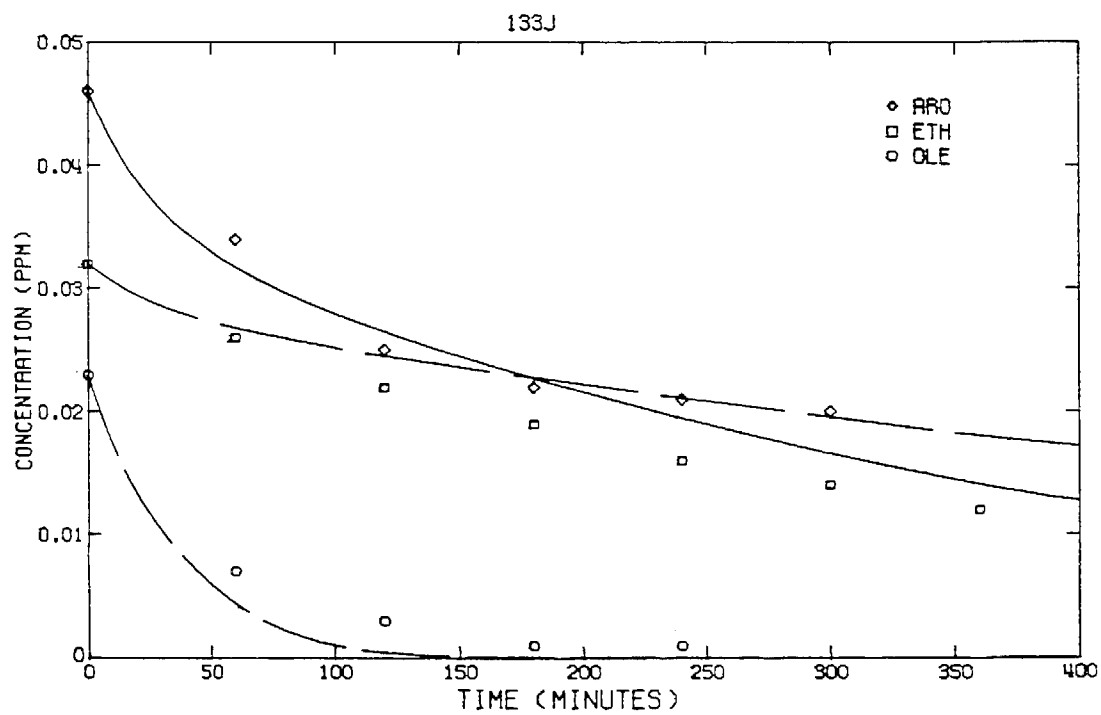
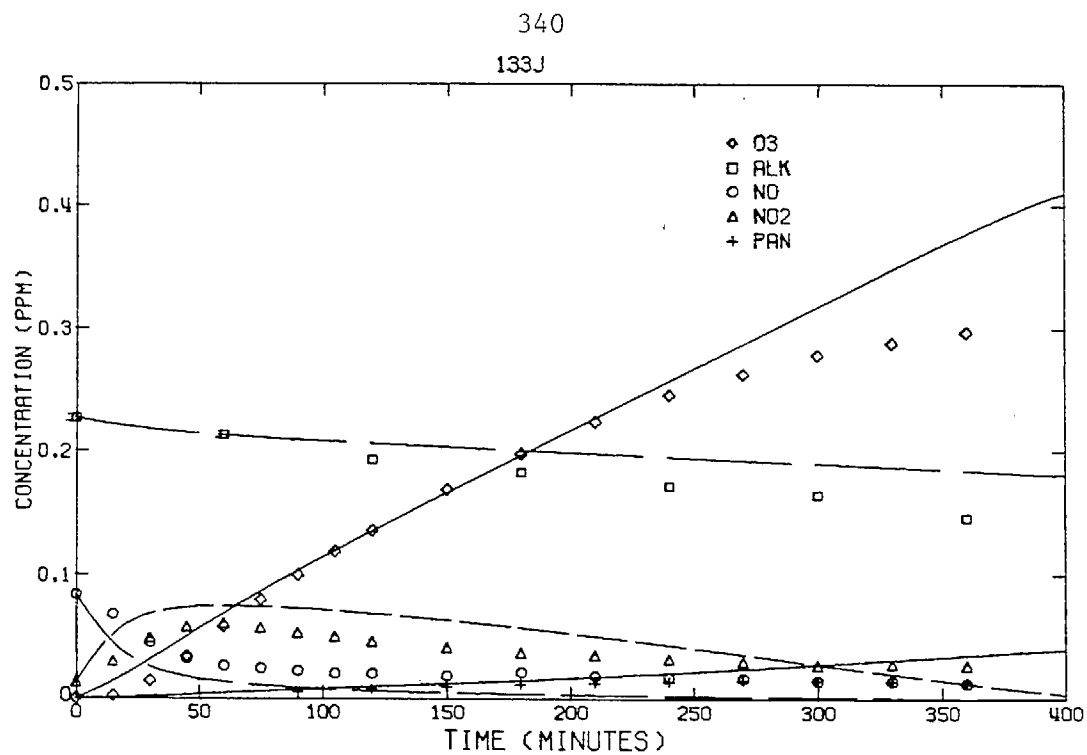


FIGURE 8.25
 Predicted and Observed Concentration Profiles for Smog
 Chamber Experiment 133J

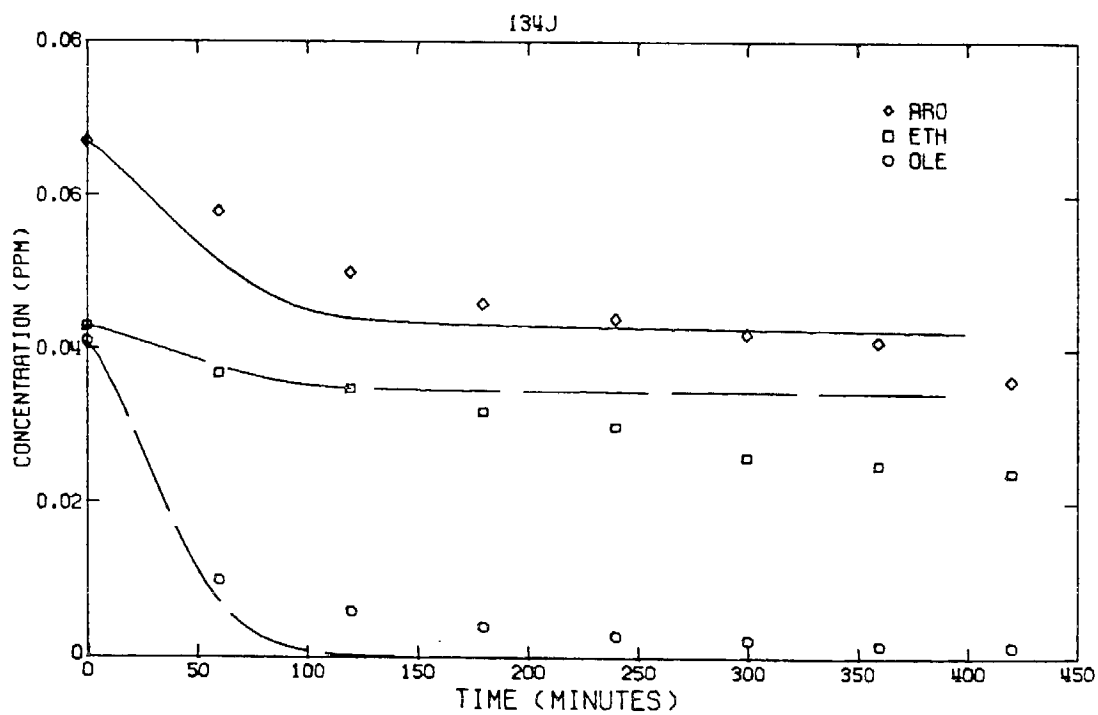
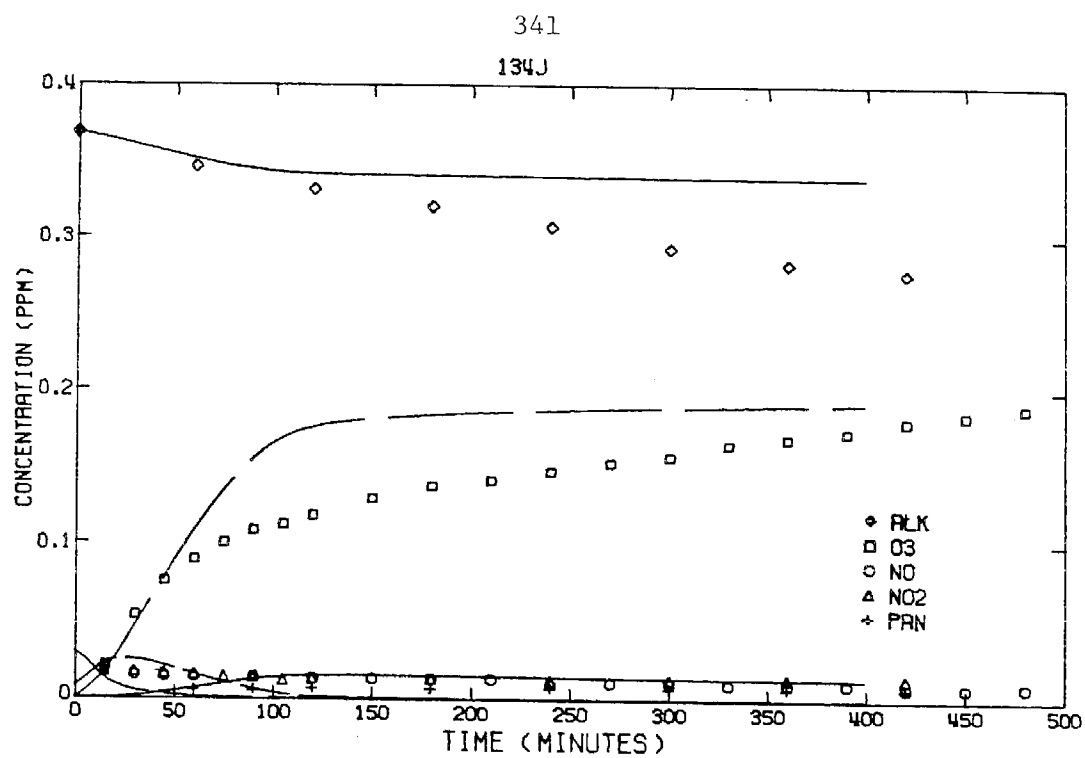


FIGURE 8.26

Predicted and Observed Concentration Profiles for Smog
Chamber Experiment 134J

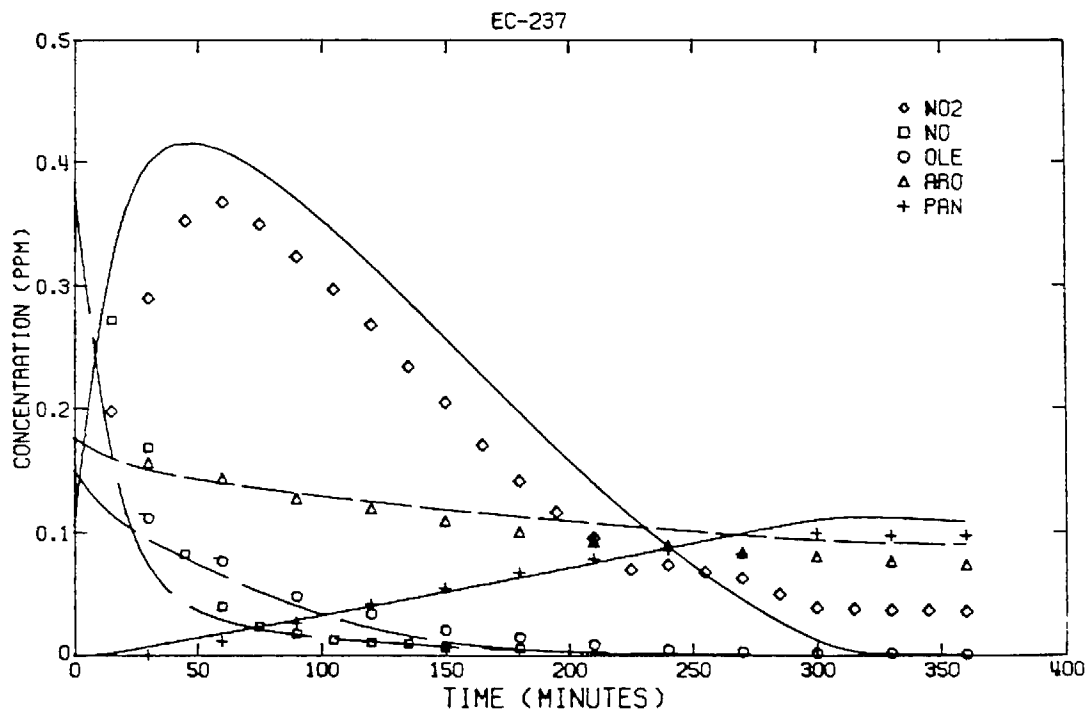
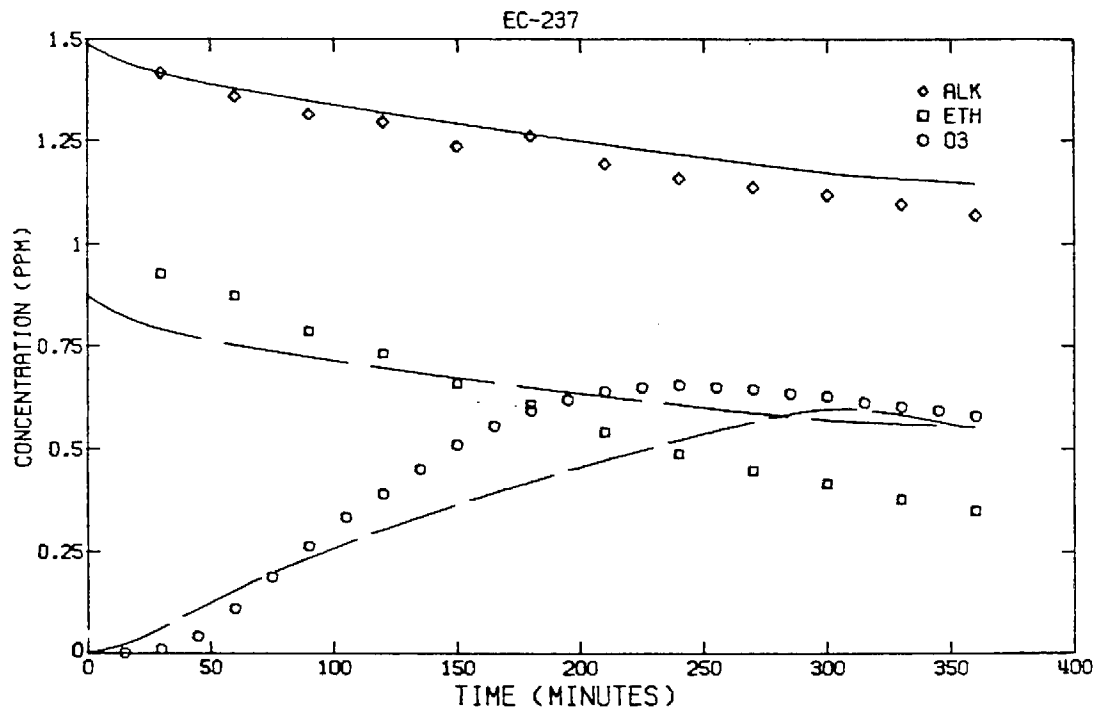


FIGURE 8.27

Predicted and Observed Concentration Profiles for Smog
Chamber Experiment EC-237

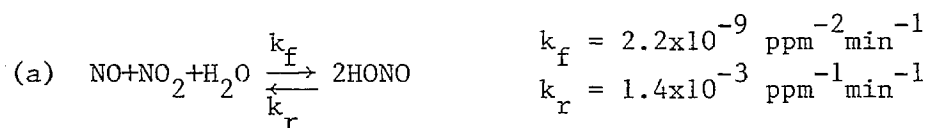
to irradiation can be estimated from equation (8.36). In their simulation of the SAPRC experiments, Whitten and Hogo (1976) found that about one-third of the equilibrium concentration of nitrous acid was required as an initial concentration. The results in Table 8.16, however, indicate that the time required to reach a substantial fraction of the equilibrium concentration is long compared to that characteristic of the loading and initial mixing in a smog chamber. The predicted values shown in Table 8.16 and 8.17 are also consistent with the recent atmospheric measurements of Platt et al. (1980). In some of the smog chamber experiments increasing the initial HONO concentration tends to decrease the time at which the NO_2 maximum occurs but does not influence the maximum concentration of NO_2 or O_3 . In atmospheric simulations it is usually unnecessary to assume an initial concentration of HONO since there is normally sufficient aldehydes present at sunrise to provide an initial radical flux.

TABLE 8.16

Approach to the Equilibrium Nitrous Acid (HONO) Concentration^(a)

<u>Case 1</u>	<u>Case 2</u>	<u>Case 3</u> ^(b)
(NO) = 0.1	(NO) = 1	(NO) = 0.301
(NO ₂) = 0.1	(NO ₂) = 1	(NO ₂) = 0.041
(H ₂ O) = 10000	(H ₂ O) = 10000	(H ₂ O) = 15000
(HONO) _{eq} = 0.0125	(HONO) _{eq} = 0.125	(HONO) _{eq} = 0.0171

Time (min)	Case 1	Case 2	Case 3
100	0.00004	0.0044	0.00008
300	0.00013	0.0132	0.00024
1000	0.00044	0.0423	0.00082
10000	0.00423	0.125	0.00758



(b) Initial conditions correspond to smog chamber experiment SUR-119J.

TABLE 8.17

Predicted Concentration of Nitrogen Containing Species for Smog
Chamber Experiment SUR-119J

SPECIES	CONCENTRATION (ppm)					
	0(min)	60(min)	120(min)	180(min)	240(min)	300(min)
NO_2	4.1×10^{-2}	1.6×10^{-1}	2.3×10^{-1}	2.5×10^{-1}	2.5×10^{-1}	2.3×10^{-1}
HNO_4	0	2.2×10^{-5}	4.6×10^{-5}	8.4×10^{-5}	1.3×10^{-4}	1.8×10^{-4}
NO	3.01×10^{-1}	1.7×10^{-1}	8.7×10^{-2}	4.4×10^{-2}	2.6×10^{-2}	1.6×10^{-2}
HNO_2	1.2×10^{-2}	6.9×10^{-3}	2.8×10^{-3}	1.1×10^{-3}	5.4×10^{-4}	3.3×10^{-4}
PAN	0	8.8×10^{-4}	3.1×10^{-3}	6.2×10^{-3}	1.0×10^{-2}	1.4×10^{-2}
RONO	0	1.0×10^{-3}	8.0×10^{-4}	4.6×10^{-4}	2.5×10^{-4}	1.3×10^{-4}
NO_3	0	2.3×10^{-8}	1.7×10^{-7}	7.8×10^{-7}	2.2×10^{-6}	4.6×10^{-6}
RNO_4	0	6.6×10^{-4}	1.4×10^{-3}	2.4×10^{-3}	3.6×10^{-3}	4.9×10^{-3}
$2\text{N}_2\text{O}_5$	0	2.3×10^{-6}	2.4×10^{-5}	1.2×10^{-4}	3.4×10^{-4}	6.6×10^{-4}
RNO_3	0	2.4×10^{-4}	5.7×10^{-4}	8.9×10^{-4}	1.2×10^{-3}	1.4×10^{-3}
HNO_3	0	1.2×10^{-2}	2.8×10^{-2}	4.5×10^{-2}	6.2×10^{-2}	8.0×10^{-2}
M [Nitrogen Balance]	0.3540	0.3539	0.3539	0.3539	0.3539	0.3539

8.11 Species Conservation Constraints

If a physical system satisfies one or more conservation laws, then a computational scheme which preserves the same constraint should be used to eliminate at least one source of potential numerical error. The use of numerical methods which do not preserve linear conservation laws can often lead to highly inaccurate solutions. For an initial value problem the basic constraint on conservation of mass can be expressed in the form

$$W^T C = M \quad (8.39)$$

or

$$W^T \frac{dC}{dt} = 0 \quad (8.40)$$

where $W = [w_1, w_2, \dots, w_n]^T$ is a vector of weights associated with each of the species, $C = [c_1, c_2, \dots, c_n]^T$ and M is a constant depending on the initial conditions. Constraints can be applied to the total mass within the system or to individual atomic components. In the airshed mechanism the presence of lumped reaction steps, unfortunately, precludes the use of total mass balance checks. The conservation constraint does however apply to atomic species such as nitrogen. For the mechanism shown in Table 8.1, M is given by

$$M = NO + NO_2 + NO_3 + HNO_2 + HNO_3 + HNO_4 + RNO_2 + RNO_3 + RNO_4 + 2N_2O_5 + PAN \quad (8.41)$$

The numerical method developed by Hindmarsh and Byrne (1975) and used in this chapter employs a variable step, variable order, backward

difference, multistep method of the form

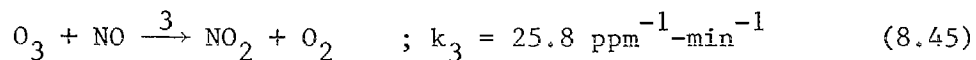
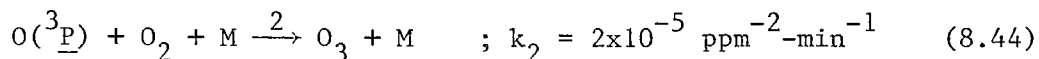
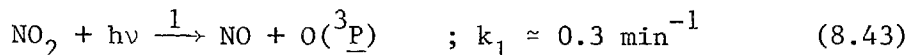
$$\sum_{j=0}^k \alpha_{k-j}^m c^{m-j} = h_m \sum_{j=0}^k \beta_{k-j}^m \frac{dc}{dt}^{m-j} \quad (8.42)$$

where $h_m = t_m - t_{m-1}$ is the step size for the m th step, $\{\alpha\}$ and $\{\beta\}$ are the coefficients for the m th step in the variable step method.

Rosenbaum (1977) has shown that such methods are conservative so that, M , defined by (8.41) should be constant. This is indeed the case as shown in Table 8.17 and Figure 8.19. While the use of linear constraints to check on numerical accuracy is often very useful, it is important to be aware of the limitations. In general, while a constant value for M implies that the roundoff errors are small, it gives little information about the magnitude of the truncation errors. Stated another way, it is possible to devise extremely poor numerical solution schemes that conserve mass.

8.12 Steady State Approximations for Ozone

The three principal reaction steps involved in the $\text{NO-NO}_2\text{-O}_3$ photolytic cycle are given by:



Under most conditions these three reactions proceed at a rate nearly two orders of magnitude faster than the kinetics of any of the other steps involving ozone. A sample calculation of the forward reaction

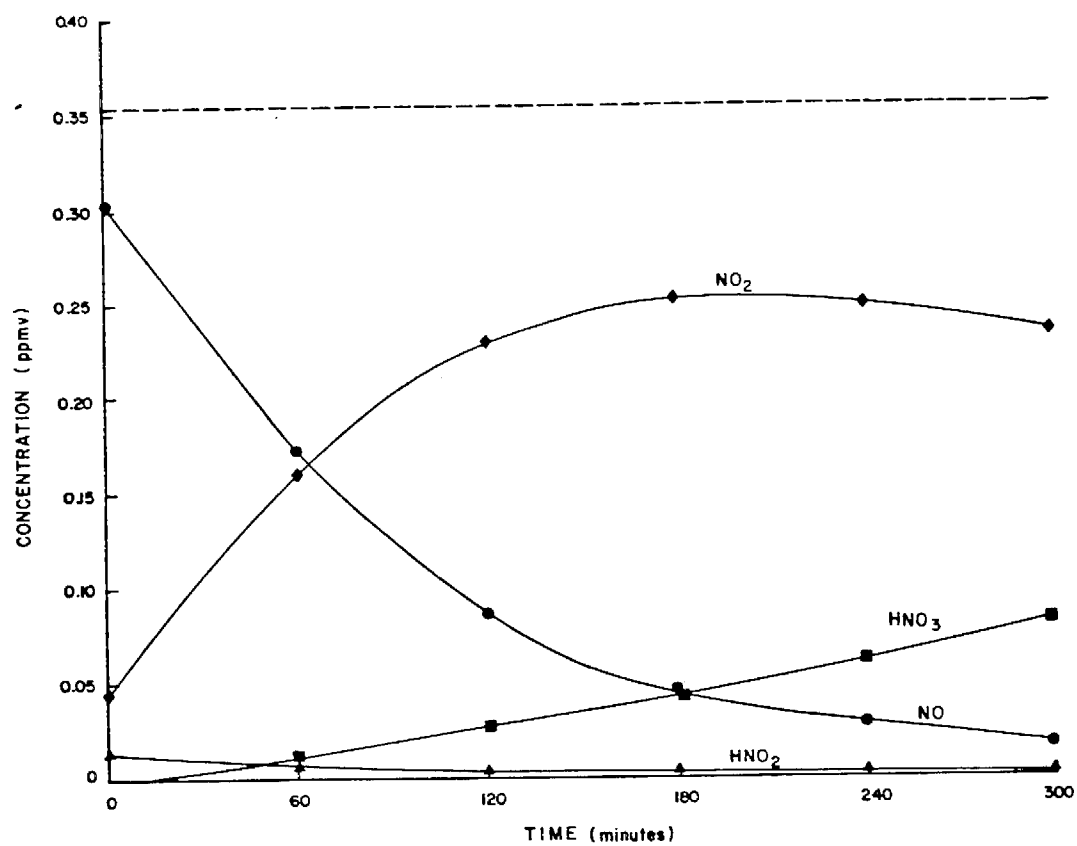


FIGURE 8.28

Concentration Profiles of Major Nitrogen Containing Species
for Smog Chamber Experiment 119J

rates is shown in Table 8.18. The main oxidizing reaction (8.45), for typical atmospheric concentrations, has a half life of approximately 30 seconds. Under these conditions many investigators have made the assumption that the ozone production and decay rates are in equilibrium and derived the photostationary state approximation (PSSA)

$$\frac{k_1(\text{NO}_2)}{k_3(\text{NO})(\text{O}_3)} = 1 \quad (8.46)$$

Since there is a recurring debate in the literature about the validity of the simple expression (8.46) this section presents a brief evaluation of its validity for smog chamber simulations.

Eschenroeder et al. (1972) and Calvert (1976) have examined experimental data collected in Los Angeles and concluded that time-averaged atmospheric measurements often do not obey the photostationary state approximation. Stedman and Jackson (1975) tested the hypothesis that $k_1(\text{NO}_2)/k_3(\text{NO})(\text{O}_3)=1$ in a set of carefully controlled measurements of ambient air quality. Using 400 data sets they found that the left-hand side was equal to 1.01 with a standard deviation of 0.2 and a standard error of the mean equal to 0.01. A variety of different explanations have been offered to explain the discrepancies. Eschenroeder et al. (1972), Seinfeld (1977) and Bilger (1977) postulated that inhomogeneities in atmospheric concentrations of NO and O₃ could reduce the effective reaction rates of the system (8.43-8.45). The basic problem is that when using time-averaged data in the photo stationary state equation the product of average concentrations is not equal to the average of the products. In general,

TABLE 8.18

Forward Reaction Rates for Smog Chamber Experiment SUR-119J^(a)

Mechanism Component	Reaction Rate (ppm/min)	
	t = 60 min	t = 300 min
dO_3/dt	3.070×10^{-4}	8.732×10^{-4}
$R_2 = k_2(O)(O_2)(M)$	5.43×10^{-2}	6.78×10^{-2}
$R_3 = k_3(NO)(O_3)$	5.36×10^{-2}	6.02×10^{-2}
$R_7 = k_7(NO_2)(O_3)$	1.24×10^{-4}	2.12×10^{-3}
$R_{20} = k_{20}(O_3)$	3.14×10^{-4}	4.61×10^{-3}
$R_{30} = k_{30}(OLE)(O_3)$	3.77×10^{-5}	2.63×10^{-6}
$R_{47} = k_{47}(OH)(O_3)$	1.34×10^{-7}	1.03×10^{-6}
$R_{48} = k_{48}(HO_2)(O_3)$	1.67×10^{-8}	1.63×10^{-6}
$R_1 = k_1(NO_2)$	5.41×10^{-2}	6.33×10^{-2}
(a) O_3	0.01364	0.2005
NO	0.1541	0.01178
NO_2	0.1690	0.1978
NO_2/NO	1.096	16.79

unless the atmosphere is well mixed or the averaging times are sufficiently short

$$\frac{k_1(\overline{\text{NO}_2})}{k_3(\overline{\text{NO}})(\overline{\text{O}_3})} \neq \frac{k_1}{k_3} \left[\frac{(\overline{\text{NO}_2})}{(\overline{\text{NO}})(\overline{\text{O}_3})} \right] \quad (8.47)$$

The basic problem with testing this explanation is that it is extremely difficult to perform the necessary experiments. Confirmation requires very accurate and rapid determinations of k_1 , temperature, (NO) , (NO_2) and (O_3) .

Part of the variation can be readily explained by considering the kinetics of ozone formation. In the airshed model the balance between ozone formation and decay rates is given by

$$\frac{d\text{O}_3}{dt} = R_2 - R_3 - R_7 - R_{20} - R_{30} - R_{47} - R_{48} - R_{49} \quad (8.48)$$

where

$$\begin{aligned} R_2 &= k_2(\text{O})(\text{O}_2)(\text{M}) \\ R_3 &= k_3(\text{NO})(\text{O}_3) \\ R_7 &= k_7(\text{NO}_2)(\text{O}_3) \\ R_{20} &= k_{20}(\text{O}_3) \\ R_{30} &= k_{30}(\text{OLE})(\text{O}_3) \\ R_{47} &= k_{47}(\text{OH})(\text{O}_3) \\ R_{48} &= k_{48}(\text{HO}_2)(\text{O}_3) \\ R_{49} &= k_{49}(\text{O}_3) \end{aligned} \quad (8.49)$$

So that the correct expression for the quasi steady state approximation (QSSA) is given by

$$\frac{k_2(O)(O_2)(M)}{[k_3(NO)+k_7(NO_2)+k_{20}+k_{30}(OLE)+k_{47}(OH)+k_{48}(HO_2)+k_{49}](O_3)} = 1 \quad (8.50)$$

Both (8.46) and (8.50) were tested using the concentrations predicted in a numerical solution of the smog chamber experiment SUR-119J (Pitts et al., 1976). At the end of a 400 minute simulation the error in the photo stationary state (PSSA) was approximately 5% whereas (8.50) was correct to within 1%. As shown in Table 8.18, early in the run, the ozone kinetics is dominated by the photolytic cycle (8.43-8.45) and as a result both (8.46) and (8.50) are of comparable accuracy. Later in the solution, when $NO_2 \gg NO$, the contributions from the terms R_7 and R_{20} become more apparent. These results indicate that in atmospheric applications there could be significant departures from the photo stationary state simply as a result of the chemistry. Future field measurements should be directed at separating the influences of turbulent inhomogeneities and chemistry when evaluating the validity of steady state approximations.

8.13 Conclusions

In this chapter the basic airshed mechanism has been presented together with sufficient information regarding initial conditions, rate constants and stoichiometry to allow an independent duplication of its performance. The mechanism incorporates recent information on rate

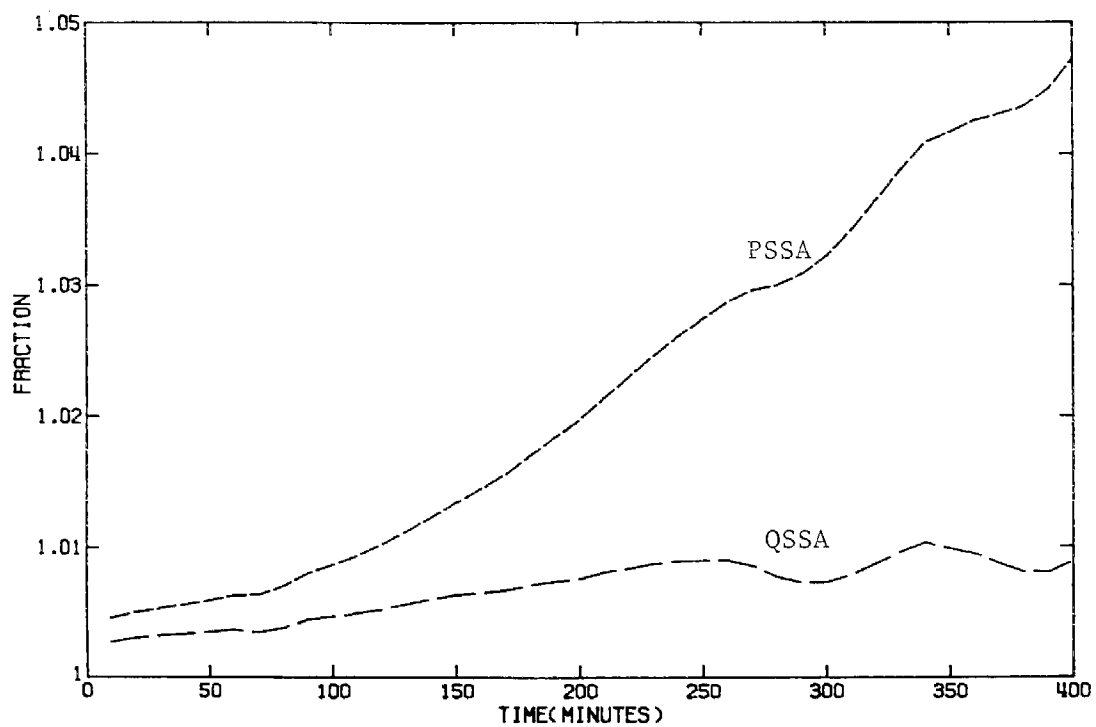


FIGURE 8.29

Errors in the Photo Stationary State (PSSA) and Quasi
Stationary State (QSSA) Approximations for Ozone in Smog
Chamber Experiment SUR-119J

constants, mechanistic structure and, in addition, has been successfully validated against a wide range of smog chamber experiments. Further discussion of the sensitivity of model predictions to changes in the various inputs is given in Chapter 12.

Note: Subsequent to the publication of the kinetic mechanisms in Falls and Seinfeld (1978) and McRae et al. (1981) a number of modifications were made to some of the reaction rate constants. These changes are documented in Tables 8.3, 8.8 and 8.12 and were made to reflect more recent determinations of the basic kinetic data. In section 8.10 Figures 8.21 and 8.27 show a comparison between observed and predicted concentration profiles for the two sets of rate constants.

CHAPTER 9

NUMERICAL SOLUTION OF THE ATMOSPHERIC DIFFUSION
EQUATION FOR CHEMICALLY REACTING FLOWS

(Reprinted from J. Computational Physics, 45, 1-42)

Review Article

Numerical Solution of the Atmospheric Diffusion Equation for Chemically Reacting Flows

GREGORY J. MCRAE, WILLIAM R. GOODIN,* AND JOHN H. SEINFELD[†]

*Environmental Quality Laboratory, California Institute of Technology,
Pasadena, California 91125*

Received May 15, 1981

A comprehensive study of numerical techniques for solving the atmospheric diffusion equation is reported. Operator splitting methods are examined in which the three-dimensional problem is converted into a sequence of one-dimensional problems. A Galerkin, linear finite element scheme with a nonlinear filter is found to be computationally superior to the other methods tested for the advection-diffusion components. The chemical reaction dynamics component, treated within the splitting scheme, is generally highly stiff. A second-order predictor, iterated corrector technique, in combination with an asymptotic treatment of the stiff components, is found to be computationally superior for the chemical kinetics. The validity of the pseudo steady state approximation for certain reactive species is also investigated.

1. INTRODUCTION

Many disciplines in engineering and science depend on the availability of predictive models of chemically reacting fluid flows. One area of considerable practical interest and a source of many challenging problems in numerical analysis is the construction of mathematical descriptions of the formation and transport of urban-scale air pollution. A complete treatment of atmospheric concentration dynamics and chemical interactions involves the full, three-dimensional turbulent planetary boundary layer equations for conservation of mass, momentum and energy. Unfortunately the routine solution of such a system is an enormous undertaking and not feasible on the present generation of computers since a typical calculation might involve $O(10^4)$ grid points, 20–50 chemical species and $O(10^6)$ computer storage locations. A somewhat more limited approach, and the focus of this work, is based on decoupling the mass conservation equations from the equations of motion of the air. This simplification results in a set of coupled parabolic partial differential equations that describe the combined

* *Present address:* Advanced Technology Group, Dames and Moore, 1100 Glendon Avenue, Los Angeles, CA 90024.

[†] Department of Chemical Engineering.

influences of advection, turbulent diffusion and chemistry within a prescribed flow field. The presence of nonlinearities and the existence of widely disparate temporal and spatial scales considerably complicate the selection and implementation of suitable solution techniques. In addition the availability and utilization of computational resources are practical considerations equally as important as the requirement for numerical accuracy.

This paper begins with a general statement of the atmospheric diffusion equation and proceeds to describe the use of coordinate transformations and operator splitting techniques for numerical solution. Once the equations have been decomposed into component parts by operator splitting, specially suited procedures for the components (advection, diffusion, and chemical reaction) can be applied. We then describe the choice and testing of appropriate techniques for solving the transport or advection-diffusion components of the equation. The final element involves numerical solution of the chemical kinetics. Although the numerical techniques described in this work have been specifically developed to solve the atmospheric diffusion equation, much of the material is applicable to other problems, particularly those that involve chemically reacting fluid flows.

2. GOVERNING DIFFERENTIAL EQUATIONS

Consider an arbitrary, time-varying, spatial domain Ω_t located in the Euclidean space E^3 and bounded by $\partial\Omega_t$. In this region, a spatial point is denoted $\mathbf{X} = \{X, Y, Z\} \in \Omega_t$. Within Ω_t the conservation of mass for each of p chemical species $c_i(\mathbf{X}, t)$; $i = 1, \dots, p$, can be expressed by the following set of coupled, nonlinear, parabolic, partial differential equations,

$$\frac{\partial c_i}{\partial t} + \nabla \cdot (\mathbf{u}c_i) = \nabla \cdot (\mathbf{K} \cdot \nabla c_i) + f_i(c_1, \dots, c_p), \quad (1)$$

with $(\mathbf{X}, t) \in \Omega_t \times [0, T]$. For this system \mathbf{u} is the prescribed advective velocity field $\mathbf{u}(\mathbf{X}, t) = (u, v, w)$, \mathbf{K} is a second-order, diagonal, eddy diffusivity tensor and f_i a temperature dependent chemical formation (or depletion) rate of species i . In meteorological applications (1) is frequently called the atmospheric diffusion equation [1].

To complete the problem formulation both the initial and boundary conditions need to be specified. For the system (1) the initial conditions $c_i(\mathbf{X}, 0)$, are given by

$$c_i(\mathbf{X}, 0) = c_i^0(\mathbf{X}); \quad i = 1, \dots, p; \quad \mathbf{X} \in \Omega_0. \quad (2)$$

The measured concentration data, from which the initial conditions are normally specified, are sparse, irregularly spaced, and generally limited to ground level values. Under these conditions, a representative initial field can be obtained by interpolation using the techniques described in Goodin *et al.* [2-4]. Boundary conditions simply represent statements of mass continuity across the enclosing surface $\partial\Omega_t$. For this

system most practical cases are described by the inhomogeneous mixed Neumann and Dirichlet boundary conditions

$$a(\mathbf{X}, t) c_i + b(\mathbf{X}, t) \frac{\partial c_i}{\partial \sigma} = g_i(\mathbf{X}, t); \quad (\mathbf{X}, t) \in \partial\Omega_i \times [0, T]. \quad (3)$$

In this equation σ indicates the normal direction to $\partial\Omega_i$, and the functions $a(\mathbf{X}, t)$, $b(\mathbf{X}, t)$ and $g_i(\mathbf{X}, t)$ describe particular cases, the explicit forms of which are presented in Reynolds *et al.* [5].

The difficulties that arise during numerical solution of (1)–(3) stem from the radically different character of the advection, $\nabla \cdot (\mathbf{u}c_i)$, turbulent diffusion, $\nabla \cdot (\mathbf{K} \cdot \nabla c_i)$, and chemical reaction, f_i , operators. Even though (1) is formally parabolic in most atmospheric flows, transport in the horizontal plane is dominated by advection, leading to hyperbolic like characteristics. One of the major sources of difficulty arises during numerical solution of the chemical reaction terms f_i . While complicating the numerical solution, the presence of the nonlinearities in f_i is not as much a problem as the potential for eigenvalues that span a wide range of time scales. In typical photochemical reaction mechanisms of the type described by Falls and Seinfeld [6], it is possible to encounter situations in which individual reaction times differ by $O(10^8)$ seconds. That, in turn, virtually dictates an implicit solution procedure for the chemical kinetics.

3. COORDINATE TRANSFORMATIONS

In typical applications the airshed domain Ω_i is defined by three bounding surfaces; the topography $Z = h(X, Y)$, vertical sides at the horizontal extremes, and a time varying upper boundary, $Z = H(X, Y, t)$. The presence of topographic relief can considerably complicate the numerical implementation of boundary conditions of the form (3). The problem can be avoided to a certain extent by transforming the spatial domain into one of simpler geometry. This can be accomplished by a mapping $\mathbf{F}: \Omega_i \rightarrow \Omega_c$, that transforms points in the physical domain Ω_i into the more convenient computational domain Ω_c . Points in Ω_c are denoted by $\mathbf{x} = (x, y, z, t)$.

A variety of functional forms for \mathbf{F} are used in practice; a common one in atmospheric modeling application is the terrain-following coordinate transformation [5, 7, 8],

$$\mathbf{x} = \mathbf{F}(\mathbf{X}) = \begin{bmatrix} X \\ Y \\ \frac{Z - h(X, Y)}{H(X, Y, t) - h(X, Y)} \end{bmatrix}, \quad (4)$$

that scales the vertical extent of the modeling region into the new domain $z \in [0, 1]$. So long as the time varying upper boundary H , does not intersect the terrain defined

by h , then a unique inverse for (4) exists. The general requirement for a nonzero Jacobian usually precludes the simultaneous use of these transformations in all three coordinate directions.

Once the form of the transformation has been established, the next step is to apply it to the atmospheric diffusion equation. An important characteristic of this equation is that it represents a differential statement of the conservation of mass for each species c_i . Roache [9] indicates that, with few exceptions, the most accurate numerical results are obtained using numerical approximations that are based on the flux or conservative form of the governing equations. With this in mind, it is desirable to preserve the conservative structure of (1) during the coordinate transformation. If this is done, then it is possible to consider each computational cell as a control volume and develop difference expressions that satisfy the physical conservation laws on a macroscopic level, not at the limit of small time steps and spatial dimensions. Methods for manipulating first and second-order partial differential equations that preserve the conservative properties are described in Anderson *et al.* [10], Oberkampf [11], and Vinokur [12]. Lapidus [13], in particular, has shown that with a nonsingular space transformation, the conservative form of the governing differential equations can be maintained. Using these procedures it is possible to develop the following conservative form of the atmospheric diffusion equation,

$$\frac{\partial \Delta H c_i}{\partial t} + \nabla \cdot (\mathbf{V} \Delta H c_i) = \nabla \cdot (\Delta H \mathbf{K}_c \cdot \nabla c_i) + \Delta H f_i, \quad (\mathbf{x}, t) \in \Omega_c \times [0, T], \quad (5)$$

where Ω_c is now the transformed domain and $\Delta H = H(x, y, t) - h(x, y)$. The components of the transformed velocity field are now $\mathbf{V} = (u, v, W)$, where the new vertical velocity W , is given by

$$W = \frac{1}{\Delta H} \left[w - u \left(\frac{\partial h}{\partial x} + z \frac{\partial \Delta H}{\partial x} \right) - v \left(\frac{\partial h}{\partial y} + z \frac{\partial \Delta H}{\partial y} \right) - z \frac{\partial \Delta H}{\partial t} \right]. \quad (6)$$

One problem arises as a result of the transformation. Initially the eddy diffusivity tensor \mathbf{K} was diagonal, however, the transformed form is given by

$$\mathbf{K}_c = \begin{bmatrix} K_{xx} & 0 & -\frac{K_{xx}}{\Delta H} \left(\frac{\partial h}{\partial x} + z \frac{\partial \Delta H}{\partial x} \right) \\ 0 & K_{yy} & -\frac{K_{yy}}{\Delta H} \left(\frac{\partial h}{\partial y} + z \frac{\partial \Delta H}{\partial y} \right) \\ -\frac{K_{xx}}{\Delta H} \left(\frac{\partial h}{\partial x} + z \frac{\partial \Delta H}{\partial x} \right) & -\frac{K_{yy}}{\Delta H} \left(\frac{\partial h}{\partial y} + z \frac{\partial \Delta H}{\partial y} \right) & \frac{K_{xx}}{\Delta H^2} \left(\frac{\partial h}{\partial x} + z \frac{\partial \Delta H}{\partial x} \right)^2 \\ & & + \frac{K_{yy}}{\Delta H^2} \left(\frac{\partial h}{\partial y} + z \frac{\partial \Delta H}{\partial y} \right)^2 \\ & & + \frac{K_{zz}}{\Delta H^2} \end{bmatrix}. \quad (7)$$

While the presence of off-diagonal terms can complicate the numerical solution, their contribution to turbulent transport in most urban scale flows is negligible since it is possible to show, that for all but the most rugged terrain,

$$\frac{1}{\Delta H} \left[\frac{\partial h}{\partial x} + z \frac{\partial \Delta H}{\partial x} \right] \ll 1; \quad \frac{1}{\Delta H} \left[\frac{\partial h}{\partial y} + z \frac{\partial \Delta H}{\partial y} \right] \ll 1. \quad (8)$$

4. GENERAL APPROACH TO THE NUMERICAL SOLUTION OF THE PROBLEM

Once the equations have been transformed, the next step is to formulate an approach for obtaining numerical solutions of the model system. Although the focus of the present work is the atmospheric diffusion equation, the problem can be stated in the more general form,

$$\frac{\partial c_i}{\partial t} = L(\mathbf{x}, t) c_i(\mathbf{x}, t) + f_i(c_1, \dots, c_p); \quad (\mathbf{x}, t) \in \Omega_c \times [0, T], \quad (9)$$

$$B(\mathbf{x}, t) c_i(\mathbf{x}, t) = g_i(\mathbf{x}, t); \quad (\mathbf{x}, t) \in \partial\Omega_c \times [0, T], \quad (10)$$

$$c_i(\mathbf{x}, 0) = c_i^0(\mathbf{x}); \quad (\mathbf{x}) \in \Omega_0, \quad (11)$$

where L is a multi-dimensional, semi-linear, elliptic differential operator containing first and second-order derivatives, with respect to x , y , and z , but no mixed derivatives, and B is a linear operator.

While there is an extensive literature relevant to obtaining solutions of the homogeneous system there are relatively few numerical treatments of problems that involve *both* chemical reactions and transport in three dimensions. Even though much of what is available is confined to one- and two-dimensional systems, many different techniques have been applied in practice. For example, Margolis [14] used the method of lines to examine the multi-component chemical dynamics of a premixed laminar flame. Chin and Braum [15] employed a discrete analog of the invariant embedding algorithm to solve the two-point boundary value problem associated with a model of oil shale retorting. A variety of schemes were used by Engquist *et al.* [16] to predict the performance of a catalytic converter; a fourth-order dissipative leap-frog difference method for the hyperbolic components, a Dufort–Frankel procedure for the parabolic elements and Newton iteration for the remaining nonlinear equations. Douglas *et al.* [17] utilized an extrapolated Crank–Nicholson–Galerkin procedure when solving a quasilinear parabolic problem. Kansa [18] used a block implicit scheme, modified to include the basic strategies of stiff ordinary differential equation solution algorithms, to model the combustion process in an axisymmetric wick.

There are two basic steps that must be undertaken as part of most approaches to obtaining numerical solutions of systems of the form (9)–(11). One is to identify the means for approximating the spatial derivatives and the other is to select the

procedure for time integration. Spatial discretization techniques are used to convert the system of time-varying partial differential equations into a set of ordinary differential equations. In most cases this can be accomplished by using either classical finite difference or finite element techniques to produce semi-discrete systems of the form

$$\mathbf{M} \frac{d\mathbf{c}_i}{dt} + \mathbf{S}\mathbf{c}_i = \mathbf{f}_i(c_1, \dots, c_p, t), \quad (12)$$

where the matrices \mathbf{M} and \mathbf{S} are typically large and sparse, especially for multi-dimensional problems, and \mathbf{c}_i is a vector-valued function representing the concentration distribution at r points in the computational domain. If \mathbf{M} is the identity matrix, as is often the case when finite difference techniques are used, then the system (12) can be solved using the method of lines. Further details of different parameterizations of the elements of \mathbf{M} and \mathbf{S} are discussed subsequently.

One of the major difficulties associated with a solution of (12) is that the set of equations is usually quite stiff. Consider for example, the case of $\mathbf{f} = \mathbf{f}(t)$ only and constant \mathbf{M} . Then the analytic solution of (12) is given by

$$\mathbf{c}_i(t) = \exp\{-\mathbf{M}^{-1}\mathbf{S}t\} \mathbf{c}_i(0) + \int_0^t \exp\{-(t-\tau)\mathbf{M}^{-1}\mathbf{S}\} \mathbf{S}^{-1}\mathbf{f}_i(\tau) d\tau. \quad (13)$$

If δ is the discretization parameter, either the computational cell size or finite element, then the condition number of $\mathbf{M}^{-1}\mathbf{S}$ is $O(\delta^{-2})$ [19, 20]. In fact, because of the unboundedness of the eigenvalue spectrum as $\delta \rightarrow 0$, increasing demands for accuracy simply exacerbate the stiffness problem. What is not often recognized is that the stiffness of the ordinary differential equations may be an artifact of the spatial discretization and, apart from the character of \mathbf{f} , is not a property of the governing differential equations. Because the equations are stiff this usually dictates that an implicit solution procedure must be used for the time integration. While not a major restriction for one-dimensional systems, this can create major computational and operational problems when extended to higher dimensions.

In many situations the practical aspects of implementing the computational procedures can impose another set of limitations. Often the number of previous results that can be held in fast core storage, during one solution step, constrains the choice of a time integration procedure. In addition, careful consideration must be given to the way in which arrays are indexed on computers that employ virtual memory systems otherwise the paging overheads can become very large. These issues, and the theoretical considerations discussed above, are some of the major motivations for the use of operator splitting techniques.

5. OPERATOR SPLITTING AND THE METHOD OF FRACTIONAL STEPS

If the spatial discretization procedures are directly applied to the three-dimensional operator L , the resulting matrices, while sparse, usually cannot be economically decomposed or inverted. One way to reduce the magnitude of the computational task is to employ operator splitting and reduce the multidimensional problem to a sequence of one-dimensional equations. If this is done then successive solutions to each component part can be combined to produce a "weak" approximation to the original operator. There are a number of significant advantages to be gained from this approach. Because the matrices arising from the one-dimensional spatial discretizations are usually tridiagonal, the cost of using stable implicit procedures is small. Perhaps the most important benefit is that the numerical solution techniques can be tailored to the physical behavior of each element, a feature that is particularly attractive in applications involving chemically reacting flows. For example, Rizzi and Bailey [21] used the space-marching procedure of Rizzi and Inouye [22], in combination with operator splitting, to examine the chemical dynamics occurring in supersonic flows over complex geometric shapes. Similar approaches were adopted by Kee and Miller [23] in a study of laminar diffusion flames and by Thomas and Wilson [24] for chemically reacting turbulent jets. In each case isolating the reaction kinetics removed the numerical time step restrictions on the transport operators imposed by the chemistry.

The initial step in operator splitting is to decompose L into a sum of simpler terms

$$L = \sum_{j=1}^3 L_j. \quad (14)$$

Although it is not strictly necessary, each L_j is usually associated with a particular coordinate direction. As an example (9) can be written in the form ($L_1 \equiv L_x$; $L_2 \equiv L_y$; $L_3 \equiv L_z$)

$$\frac{\partial c_i}{\partial t} = (L_x + L_y + L_z) c_i(\mathbf{x}, t) + f_i(c_1, \dots, c_p, \mathbf{x}, t). \quad (15)$$

Once the elemental components L_j have been identified, the next step is to determine their equivalent discrete representation in the computational domain. First, the continuously varying concentration field must be approximated at the r computational points by the values $\mathbf{c}_i = (c_i(\mathbf{x}_j, t); j = 1, 2, \dots, r)$. At each of the grid points, the spatial derivative L_j must be replaced by its discrete approximation. The net result is the replacement of the scalar operation, $L_j c_i$, distributed over the physical domain, by the matrix product $\mathbf{A}_j \mathbf{c}_i$. In this formulation the elements of \mathbf{A}_j depend on the particular discretization scheme and its coupling of adjacent grid point values. Given the numerical equivalents of each L_j , they then must be combined in a sequence that approximates the system as a whole. There are two common ways to accomplish this; one is to use Alternating Direction Implicit (ADI) schemes and the

other employs Locally One-Dimensional (LOD) or fractional step methods. The most widely known splitting procedure is the ADI algorithm which advances the concentration field a single time step Δt from the level n to time level $n+1$ using the sequence [25-27],

$$\mathbf{c}_i^* - \mathbf{c}_i^n = \frac{\Delta t}{2} \mathbf{A}_x \mathbf{c}_i^* + \Delta t \left[\frac{1}{2} \mathbf{A}_x + \mathbf{A}_y + \mathbf{A}_z \right] \mathbf{c}_i^n + \Delta t \mathbf{f}_i^n, \quad (16)$$

$$\mathbf{c}_i^{**} - \mathbf{c}_i^n = \frac{\Delta t}{2} [\mathbf{A}_x \mathbf{c}_i^* + \mathbf{A}_y \mathbf{c}_i^{**}] + \Delta t \left[\frac{1}{2} (\mathbf{A}_x + \mathbf{A}_y) + \mathbf{A}_z \right] \mathbf{c}_i^n, \quad (17)$$

$$\mathbf{c}_i^{***} - \mathbf{c}_i^n = \frac{\Delta t}{2} [\mathbf{A}_x \mathbf{c}_i^* + \mathbf{A}_y \mathbf{c}_i^{**} + \mathbf{A}_z \mathbf{c}_i^{***}] + \frac{\Delta t}{2} [\mathbf{A}_x + \mathbf{A}_y + \mathbf{A}_z] \mathbf{c}_i^n, \quad (18)$$

where \mathbf{c}_i^* , \mathbf{c}_i^{**} are the intermediate results and \mathbf{c}_i^{***} is an $O(\Delta t^3)$ approximation to \mathbf{c}_i^{n+1} . An alternate, but equivalent representation, that is more suited to practical problems, especially those involving steady state applications, is to solve for the concentration increment using

$$\left[\mathbf{I} - \frac{\Delta t}{2} \mathbf{A}_x \right] (\mathbf{c}_i^* - \mathbf{c}_i^n) = \Delta t [\mathbf{A}_x + \mathbf{A}_y + \mathbf{A}_z] \mathbf{c}_i^n + \Delta t \mathbf{f}_i^n, \quad (19)$$

$$\left[\mathbf{I} - \frac{\Delta t}{2} \mathbf{A}_y \right] (\mathbf{c}_i^{**} - \mathbf{c}_i^n) = \mathbf{c}_i^* - \mathbf{c}_i^n, \quad (20)$$

$$\left[\mathbf{I} - \frac{\Delta t}{2} \mathbf{A}_z \right] (\mathbf{c}_i^{***} - \mathbf{c}_i^n) = \mathbf{c}_i^{**} - \mathbf{c}_i^n. \quad (21)$$

By eliminating the intermediate results from (19)–(21) the ADI solution sequence can be written in the factored form [26]

$$\begin{aligned} & \left[\mathbf{I} - \frac{\Delta t}{2} \mathbf{A}_x \right] \left[\mathbf{I} - \frac{\Delta t}{2} \mathbf{A}_y \right] \left[\mathbf{I} - \frac{\Delta t}{2} \mathbf{A}_z \right] (\mathbf{c}_i^{n+1} - \mathbf{c}_i^n) \\ & = \Delta t [\mathbf{A}_x + \mathbf{A}_y + \mathbf{A}_z] \mathbf{c}_i^n + \Delta t \mathbf{f}_i^n. \end{aligned} \quad (22)$$

Briley and McDonald [27] discuss the computational implementation of these techniques and in particular the use of linearization procedures for solving nonlinear partial differential equations. Apart from accuracy considerations, implicit discretization procedures usually allow arbitrarily large integration steps. When splitting techniques are used to solve transient problems, the maximum allowable time step is often constrained by the treatment of intermediate level boundary conditions. Weare [28] and Briley and McDonald [27] present analyses of the errors arising from different formulations of the boundary conditions. Unfortunately, ADI procedures are not ideally suited to solving the atmospheric diffusion equation because the coupling between the chemistry and transport in (16) imposes unreasonable time step limitations. In addition, since each term of the governing

differential equation is represented in each fractional step the memory paging overheads can become excessive.

An alternative approach is to use the method of fractional steps introduced by Yanenko [29] and described in Marchuk [30, 31] and Yanenko *et al.* [32]. Only the homogeneous Cauchy problem will be considered here. We discuss how nonlinear reactions can be included later. For the transport alone, the locally one-dimensional approximations, using Crank–Nicholson time integration, are given by

$$\mathbf{c}_i^{n+1} = \prod_{j=1}^3 \left[\mathbf{I} - \frac{\Delta t}{2} \mathbf{A}_j \right]^{-1} \left[\mathbf{I} + \frac{\Delta t}{2} \mathbf{A}_j \right] \mathbf{c}_i^n \equiv \prod_{j=1}^3 \mathbf{T}_j^n \mathbf{c}_i^n \equiv \mathbf{T}^n \mathbf{c}_i^n. \quad (23)$$

The principal difference between this formulation and the ADI scheme (20)–(22) is that the solution is advanced only in one coordinate direction at a time. Detailed discussions of the relationships between the two approaches are presented in Morris [33], Gourlay and Mitchell [34], Gourlay [35], and Gottlieb [36]. One important observation that can be made is that there are two sources of error in the fully discrete fractional step algorithm—the intrinsic error involved with operator splitting and the discretization errors associated with the operator approximations. In general these errors interact in a complex fashion. Crandall and Majda [37] have analyzed the stability, accuracy, and convergence of the basic fractional step algorithm when used to obtain discontinuous solutions of scalar conservation equations.

The formal order of the temporal approximation (23) can be developed by expanding the operators \mathbf{T}_j^n in powers of Δt to give [31]

$$\mathbf{T}_j^n = \mathbf{I} - \Delta t \mathbf{A}_j^n + \frac{\Delta t^2}{2!} (\mathbf{A}_j^n)^2 - \frac{\Delta t^3}{3!} (\mathbf{A}_j^n)^3 + \dots \quad (24)$$

If $\mathbf{A}^n = \mathbf{A}_x^n + \mathbf{A}_y^n + \mathbf{A}_z^n$ then \mathbf{T}^n is given by

$$\mathbf{T}^n = \mathbf{I} - \Delta t \mathbf{A}^n + \frac{\Delta t^2}{2!} \left[(\mathbf{A}^n)^2 + \sum_{\alpha=1}^3 \sum_{\beta=\alpha+1}^3 (\mathbf{A}_\alpha^n \mathbf{A}_\beta^n - \mathbf{A}_\beta^n \mathbf{A}_\alpha^n) + \dots \right] + O(\Delta t^3). \quad (25)$$

Thus the split operator difference scheme will be second order accurate only if the split operators \mathbf{A}_α^n and \mathbf{A}_β^n commute; otherwise, it is only of first order. To obtain second order accuracy, it is necessary to reverse the order of the operators each alternate step to cancel the two noncommuting terms. The consecutive cycles are then

$$\mathbf{c}_i^n = \prod_{j=1}^3 \mathbf{T}_j^n \mathbf{c}_i^{n-1} \quad (26)$$

and

$$\mathbf{c}_i^{n+1} = \prod_{j=3}^1 \mathbf{T}_j^n \mathbf{c}_i^n. \quad (27)$$

The proof of the stability of these approximations is considerably simplified using the following lemmas [31].

LEMMA 1. Consider a positive semi-definite matrix \mathbf{A} , i.e., $\langle \mathbf{A}\mathbf{c}_i, \mathbf{c}_i \rangle \geq 0$, on the Euclidean space, then for any value of the parameter $\lambda \geq 0$,

$$\|(\mathbf{I} + \lambda\mathbf{A})^{-1}\| \leq 1, \quad (28)$$

where \mathbf{I} is the identity matrix and $\|\cdot\|$ is the appropriate norm.

LEMMA 2. For any positive semi-definite matrix \mathbf{A} and $\lambda \geq 0$ then

$$\|(\mathbf{I} - \lambda\mathbf{A})(\mathbf{I} + \lambda\mathbf{A})^{-1}\| \leq 1. \quad (29)$$

Using (28) and (29) it is possible to show that

$$\|\mathbf{c}_i^{n+1}\| \leq \|\mathbf{c}_i^n\| \leq \dots \leq \|\mathbf{c}_i^0\|. \quad (30)$$

These results ensure absolute stability and boundness of the solution provided that the discrete operator approximation \mathbf{A} is also positive semi-definite.

Implementation of operator splitting for the atmospheric diffusion equation (neglecting chemistry) can be accomplished by further separation of the material transport into advection $(\mathbf{T})_a$, and diffusive components $(\mathbf{T})_d$. If this is done, then a second-order accurate solution is given by

$$\mathbf{c}_i^{n+1} = (\mathbf{T}_x)_a(\mathbf{T}_x)_d(\mathbf{T}_y)_a(\mathbf{T}_y)_d(\mathbf{T}_z)_a(\mathbf{T}_z)_d(\mathbf{T}_z)_a(\mathbf{T}_y)_d(\mathbf{T}_y)_a(\mathbf{T}_x)_d(\mathbf{T}_x)_a \mathbf{c}_i^{n-1}. \quad (31)$$

Depending on the numerical scheme chosen, it is possible to combine the advection and diffusion into one transport step in each direction. For the remainder of this section and Sections 6 and 7 we focus on the atmospheric diffusion equation in the absence of chemistry to develop the solution procedure for the advection and diffusion components. Equation (31) indicates that the atmospheric diffusion equation can be decomposed, by operator splitting, into a series of simpler one-dimensional problems. Consequently, primary attention will be given to the one-dimensional transport problem (the subscript i denoting species i is dropped for convenience),

$$\frac{\partial c}{\partial t} = Lc = \frac{\partial}{\partial x} \left(K_{xx} \frac{\partial c}{\partial x} - uc \right) \quad (32)$$

and its component parts over the same domain

$$\text{Advection: } \frac{\partial c}{\partial t} = L_a c = - \frac{\partial uc}{\partial x} \quad (33)$$

and

$$\text{Diffusion: } \frac{\partial c}{\partial t} = L_d c = \frac{\partial}{\partial x} K_{xx} \frac{\partial c}{\partial x}. \quad (34)$$

The basic objective of the remainder of this work is to identify numerical solution techniques that are compatible with the characteristics of the physical problem, computationally efficient, stable, and accurate. In addition it is important, from a practical point of view, that the methods can be easily implemented and minimize core storage requirements.

6. FORMULATION OF THE NUMERICAL SOLUTION

A wide class of numerical approximations to the spatial derivatives in (32) can be expressed in the form $\mathbf{H}(\partial \mathbf{v} / \partial x) = \mathbf{B} \mathbf{v}$, where \mathbf{v} is the material flux at the r computational grid points. The matrices \mathbf{H} and \mathbf{B} are of dimensions $r \times r$ with elements set by the particular discretization scheme. For example, the standard second-order, centered difference formula would have $\mathbf{H} = \mathbf{I}$ and \mathbf{B} the tridiagonal form $[-1 \ 0 \ 1]$. Given the material flux

$$\mathbf{v} = \mathbf{K}_{xx} \frac{\partial \mathbf{c}}{\partial x} - \mathbf{U} \mathbf{c} \quad (35)$$

then (32) can be written as an equivalent set of first-order problems

$$\begin{aligned} \mathbf{H} \frac{\partial \mathbf{c}}{\partial x} &= \mathbf{B} \mathbf{c}, \\ \mathbf{P} \frac{\partial \mathbf{c}}{\partial t} &= \mathbf{Q} \mathbf{v}, \end{aligned} \quad (36)$$

where \mathbf{B} , \mathbf{H} , \mathbf{P} , \mathbf{Q} are large sparse matrices resulting from the particular discretization formulation and \mathbf{K}_{xx} and \mathbf{U} are diagonal matrices corresponding to the turbulent diffusion coefficients and advective velocity components at each grid point. Eliminating \mathbf{v} the system can be expressed in the partitioned matrix form,

$$\left(\begin{array}{c|c} \mathbf{H} & \mathbf{0} \\ \hline \mathbf{QK}_{xx} & -\mathbf{P} \end{array} \right) \left\{ \begin{array}{c} \frac{\partial \mathbf{c}}{\partial x} \\ \frac{\partial \mathbf{c}}{\partial t} \end{array} \right\} = \left\{ \begin{array}{c} \mathbf{B} \mathbf{c} \\ \mathbf{Q} \mathbf{U} \mathbf{c} \end{array} \right\}. \quad (37)$$

The relationship between this formulation and the operator splitting approach introduced in Section 5 can be seen in the explicit representations

$$\text{Advection: } \frac{\partial \mathbf{c}}{\partial t} = -\mathbf{P}^{-1} \mathbf{Q} \mathbf{U} \mathbf{c} \equiv (\mathbf{T}_x)_d \mathbf{c}, \quad (38)$$

$$\text{Diffusion: } \frac{\partial \mathbf{c}}{\partial t} = \mathbf{P}^{-1} \mathbf{Q} \mathbf{K}_{xx} \mathbf{H}^{-1} \mathbf{B} \mathbf{c} \equiv (\mathbf{T}_x)_d \mathbf{c}. \quad (39)$$

These two results can be combined to give the complete numerical approximation for $\partial \mathbf{c} / \partial t$,

$$\frac{\partial \mathbf{c}}{\partial t} = \mathbf{P}^{-1} \mathbf{Q} \{ \mathbf{K}_{xx} \mathbf{H}^{-1} \mathbf{B} - \mathbf{U} \} \mathbf{c} \equiv \mathbf{T}_x \mathbf{c}. \quad (40)$$

While easy to implement, a direct solution of (40) has a number of drawbacks, the most serious of which is the need to evaluate \mathbf{H}^{-1} and \mathbf{P}^{-1} . Normally both \mathbf{H} and \mathbf{B} are tridiagonal, unfortunately there is no guarantee that this property is preserved under the inverse transformation. If \mathbf{H}^{-1} and \mathbf{P}^{-1} are full matrices, then the operation count for evaluating the matrix products becomes quite large. The choice of whether to use a direct solution or a block tridiagonal LU decomposition depends to a large extent on the number of right-hand sides. A single evaluation of \mathbf{T}_x followed by many products of the form $\mathbf{T}_x \mathbf{c}_i$, $i = 1, 2, \dots, p$, may be more economical. The decision as to which is the more appropriate approach depends on the number of grid points, chemical species and a detailed operation count for each procedure. For the tests to be described in this paper block tridiagonal solution procedures were applied to the system (37). The resulting set of equations, subject to the appropriate boundary conditions, can be solved by standard methods. In subsequent sections the vector notation for \mathbf{c} , indicating the numerical approximations to $c(x, t)$ at the r grid points, will be omitted for clarity.

7. SOLUTION OF THE ADVECTIVE TRANSPORT STEP T_a

There is an extensive literature that describes techniques suitable for solving the hyperbolic problem (33) [9, 38–41]. Most of the approaches fall into five basic categories: finite difference, variational, particle-in-cell, spectral and special purpose procedures. On the basis of a preliminary survey, seven methods were identified for detailed evaluation. These schemes were: the flux corrected transport algorithm (SHASTA) [42–44], compact differencing methods [45–50], finite element methods [51–53], the zero-average phase-error technique [54], upwind differencing [9], the Crowley [55] technique and finally the scheme of Price *et al.* [56]. These methods were used as described in the literature except for the finite element scheme that was applied to the conservative formulation of the advection equation.

The particular finite element model used in this study employs a Galerkin formulation and linear basis functions. With this technique, approximations to the concentration and velocity fields are expressed in terms of time-varying coefficients $\alpha_j(t)$, $\beta_j(t)$ and piecewise continuous basis function $\phi_j(x)$,

$$c(x, t) = \sum_{j=1}^r \alpha_j(t) \phi_j(x), \quad (41)$$

$$u(x, t) = \sum_{j=1}^r \beta_j(t) \phi_j(x), \quad (42)$$

where

$$\begin{aligned}\phi_j(x) &= \frac{x - x_{j-1}}{x_j - x_{j-1}}; & x_{j-1} \leq x \leq x_j, \\ &= \frac{x_{j+1} - x}{x_{j+1} - x_j}; & x_j \leq x \leq x_{j+1}, \\ &= 0; & x < x_{j-1} \text{ or } x > x_{j+1}.\end{aligned}\quad (43)$$

Equation (43) describes a set of linear basis function that vanish outside the interval $[x_{j-1}, x_{j+1}]$. Using these functions, the Galerkin method requires that for all ϕ_j ,

$$\left\langle \phi_j, \left\{ \frac{\partial \alpha_q \phi_q}{\partial t} + \frac{\partial}{\partial x} (\beta_s \phi_s \alpha_q \phi_q) \right\} \right\rangle = 0. \quad (44)$$

By expanding the inner product (44), the following set of ordinary differential equations in the dependent variable $\alpha_q(t)$ can be derived*

$$M_{jq} \frac{d\alpha_q(t)}{dt} + \beta_s(t) N_{jq} \alpha_q(t) = 0, \quad (45)$$

where

$$M_{jq} = \int \phi_j(x) \phi_q(x) dx, \quad (46)$$

$$N_{jq} = \int \left[\phi_j(x) \phi_q(x) \frac{\partial \phi_s(x)}{\partial x} + \phi_j(x) \phi_s(x) \frac{\partial \phi_q(x)}{\partial x} \right] dx. \quad (47)$$

To compare the solution schemes, some idealized test problems with known solutions were selected. Particular attention was given to the harmonic content of each test case. A concentration distribution containing components with wavelengths shorter than the characteristic grid spacing represents a difficult test for any advection scheme. If little numerical or physical diffusion is present, an initial profile with sharp corners and steep sides should remain intact as it is transported by the velocity field. Test problems were also chosen to allow simultaneous and individual solutions of both transport components. In addition to the accuracy considerations judged by the important attributes of mass conservation, minimal dispersion and minimal pseudo-diffusion, additional constraints in choosing a numerical method arise as a result of the availability of computational resources. Execution time, storage requirements, ease of understanding, and implementation must also be considered since the most accurate scheme may also be the least efficient.

A series of test problems, listed in Table I was used to evaluate the schemes. The velocity was constant at 5 km/hr, the time step at 0.1 hours. The Courant number, C ,

* The algebraic details are contained in Appendix B.

TABLE I
Test Problems for Advection Equation

Wave form	Function	Fourier spectrum
Square	$c(x, 0) = \begin{cases} 1 & x \leq \frac{\theta}{2} \\ 0 & x > \frac{\theta}{2} \end{cases}$	$\frac{\sin \frac{\omega\theta}{2}}{\frac{\omega\theta}{2}}$
Triangle	$c(x, 0) = \begin{cases} 1 - x /\theta & x \leq \theta \\ 0 & x > \theta \end{cases}$	$\frac{\theta \sin\left(\frac{\omega\theta}{2}\right)}{\left(\frac{\omega\theta}{2}\right)^2}$
Gaussian	$c(x, 0) = \exp\left[-\pi\left(\frac{x}{\theta}\right)^2\right]$	$\theta \sqrt{\pi} \exp\left[-\frac{1}{2}(\theta\omega)^2\right]$

θ —Volume/unit width ratio for the wave form.

was 0.25, which is less than the stability limit for all schemes. These parameters were chosen to be representative of meteorological conditions over a typical urban airshed. The results of the tests are summarized in Table II and shown in Figs. 1–3. Further detailed testing with a range of sample problems narrowed the solution methods to the SHASTA technique and a class of techniques that use linear finite elements or compact differences together with Crank–Nicholson time integration.

7.1. Preservation of Positive Quantities and Filtering Schemes

During the course of the testing it became obvious that in order to develop a scheme that preserves peaks, retains positive quantities, and does not severely diffuse sharp gradients, an additional step must be performed to minimize the effect of dispersive waves. As noted by Kreiss and Oliger [57], the basic problem with conventional Galerkin formulations is that they result in nondissipative, discrete approximations when applied to hyperbolic equations. What is required is a procedure for damping out the small scale perturbations before they can corrupt the basic solution. There are several different filtering procedures that can be applied: (1) adding diffusions terms to the basic equation [58], (2) expansion of the concentration field in orthogonal functions with a recombination that omits high wave numbers [59], (3) numerical filtering where the grid point value is replaced by an average formed from surrounding values, (4) inclusion of a dissipative term in the problem formulation [60, 61].

At the simplest level, one approach is to set any negative concentration to zero or a very small positive number following each advection step. This procedure is demonstrated using the finite element method with a square wave in Fig. 4a. While trivial to implement, this correction scheme can induce violations of mass conser-

TABLE II
Summary of Results of Advection Tests for Different Initial Distributions*

Numerical scheme	Test Square (S) Gaussian (G) Triangle (T)	Extreme value		Change in mass (%)	Relative computational time
		Maximum	Minimum		
Upwind [9]	S	0.755	0.0	0.0	1.0
	T	0.693	0.0	-0.03	
	G	0.635	0.0	-0.01	
Price [56]	S	1.463	-0.390	-0.93	1.2
	T	0.971	-0.086	-0.50	
	G	1.108	-0.216	0.26	
Fromm [54]	S	1.084	-0.067	-0.05	1.8
	T	0.918	-0.015	0.28	
	G	0.964	-0.006	0.07	
Crowley [55]	S	1.219	-0.222	-2.02	2.0
	T	0.932	-0.017	0.28	
	G	0.990	-0.001	0.07	
Finite element [Text]	S	1.218	-0.382	-10.27	2.0
	T	0.953	-0.025	0.17	
	G	0.999	-0.001	0.16	
SHASTA [42-44]	S	0.997	0.0	0.0	5.2
	T	0.875	0.0	0.20	
	G	0.900	0.0	0.04	

* Results are at the end of 80 time steps.

vation. Mahlman and Sinclair [62] attempted to correct this problem by using a method called "downstream borrowing." In this scheme, implemented at the end of each time step, negative values are reset to zero by borrowing material from the downstream grid cell so that mass is conserved. In the event that the downstream cell does not contain an adequate amount of material to prevent both cell concentrations from becoming negative, the deficit is borrowed from the upstream cell. With higher-order schemes it is occasionally necessary to borrow mass from the second cells away from the one containing negative c . Although this filling procedure always acts to preserve the total mass in the system, it systematically acts to reduce the mean square concentration. Filling is thus equivalent to adding a nonlinear diffusion term. An example of the application of this procedure is shown in Fig. 4b again using the finite element method with a square wave initial condition.

Boris and Book [42,43] and van Leer [63] have introduced different approaches to the design of filtered second-order schemes. Their algorithms substantially inhibit

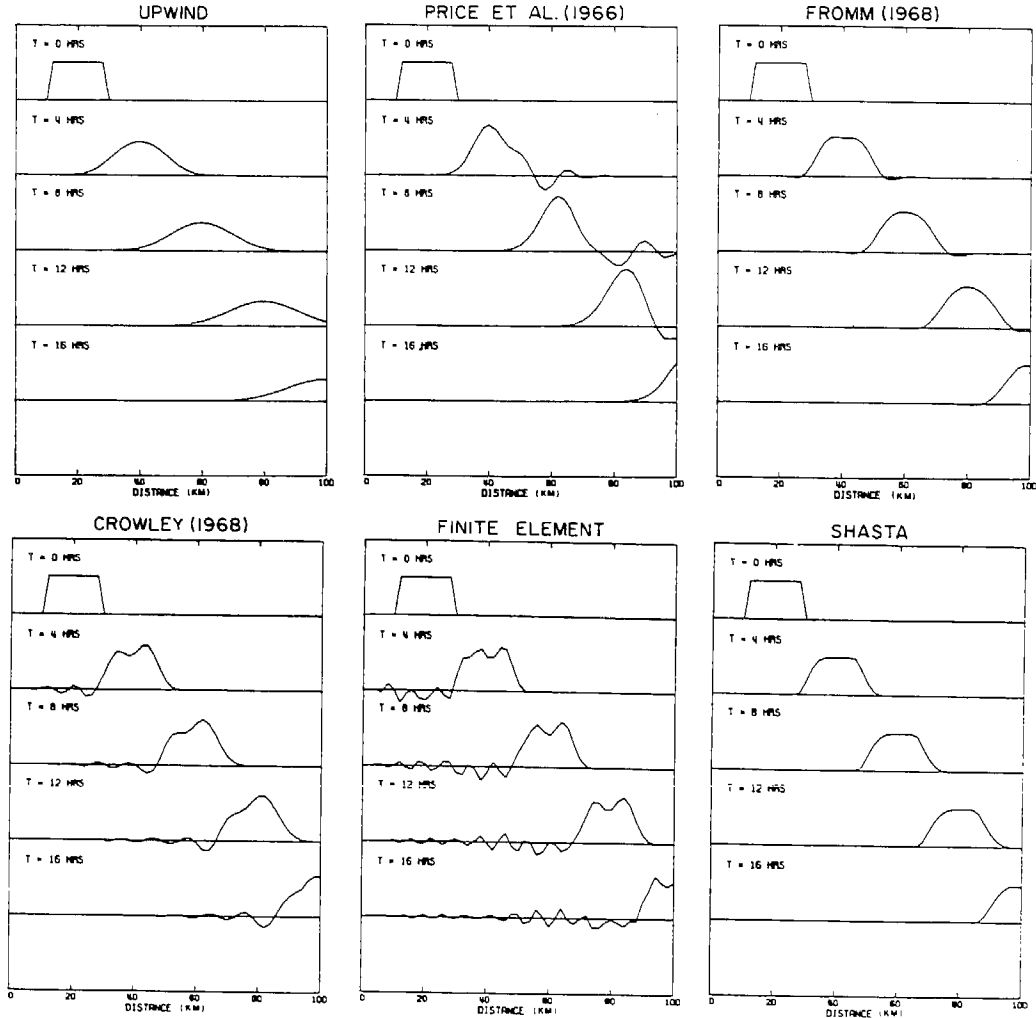


FIG. 1. Results of advection tests using square wave form.

or eliminate computational noise in regions of sharp gradients by using nonlinear smoothing techniques. The principal disadvantage of both methods is that there are substantial amplitude penalties associated with sharply peaked waves. When the SHASTA scheme of Boris and Book is used to advect a triangle, after a few steps the apex is typically severely truncated. However, once this has occurred, the distribution is transported with little change.

Recently Forester [64] introduced a very simple nonlinear filter designed to be used in conjunction with second and higher-order methods. Computational noise is

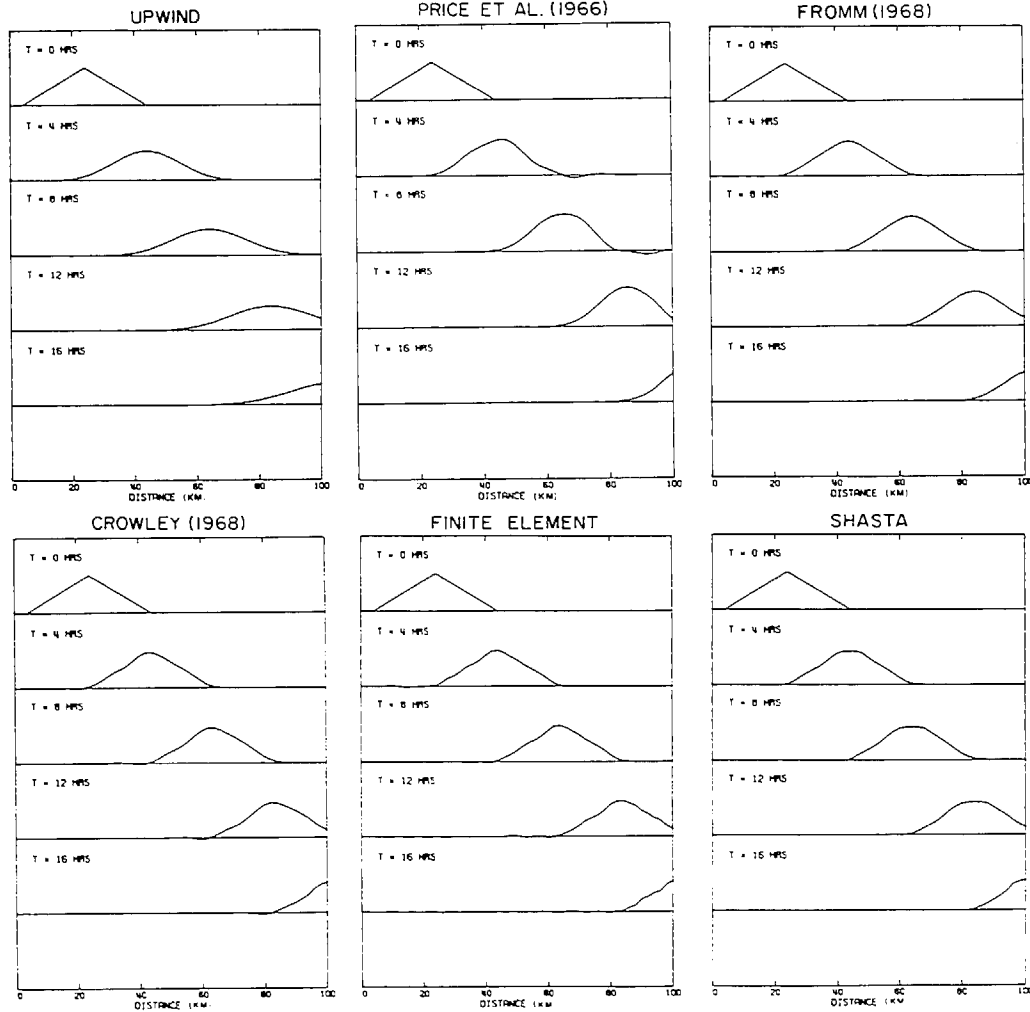


FIG. 2. Results of advection tests using triangular wave form.

minimized without incurring the amplitude penalty of either the SHASTA or van Leer techniques. When coupled with high-order schemes, the Forester method requires less than one-third of the mesh points of the SHASTA scheme to treat the extremes of sharply peaked waves. Positive concentrations are also preserved. The noise generated by the finite difference approximations of (33) is suppressed in the Forester method by a nonlinear filter that locally transforms (33) into

$$\frac{\partial c}{\partial t} + \frac{\partial uc}{\partial x} = \frac{\partial}{\partial x} K_n \frac{\partial c}{\partial x}, \quad (48)$$

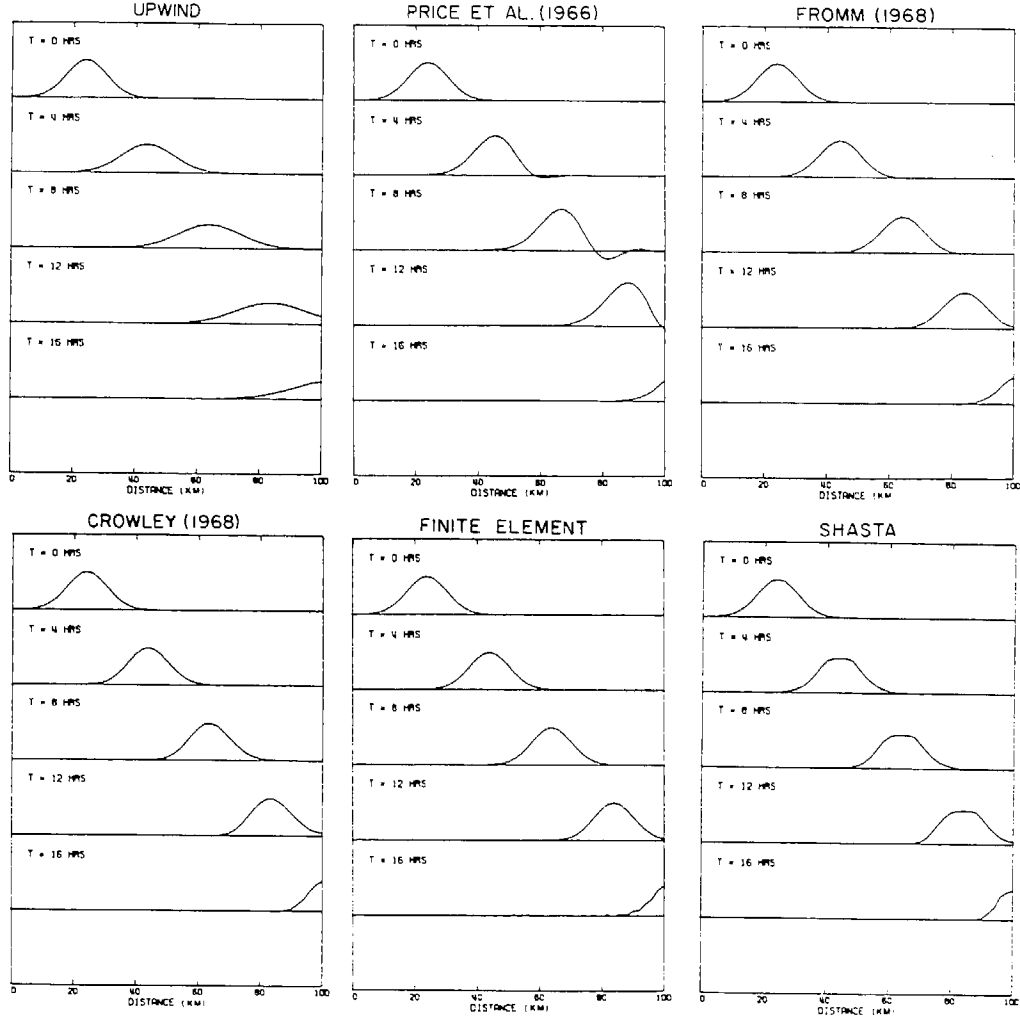


FIG. 3. Results of advection tests using Gaussian wave form.

where K_n is the diffusion coefficient associated with the filtering process. After the solution is advanced a time step, a set of empirically based criteria is used to decide if the term should remain or be removed. The filter for (33) is given by

$$c_j^{k+1} = c_j^k + \frac{K_f}{2} [(c_{j+1} - c_j)(\psi_j + \psi_{j+1}) - (c_j - c_{j-1})(\psi_j + \psi_{j-1})]^k, \quad (49)$$

where c_j^{k+1} is the value of c_j after k applications of the filter and K_f is the weighting coefficient associated with the filtering process. The ψ_j 's can only assume a value of 0

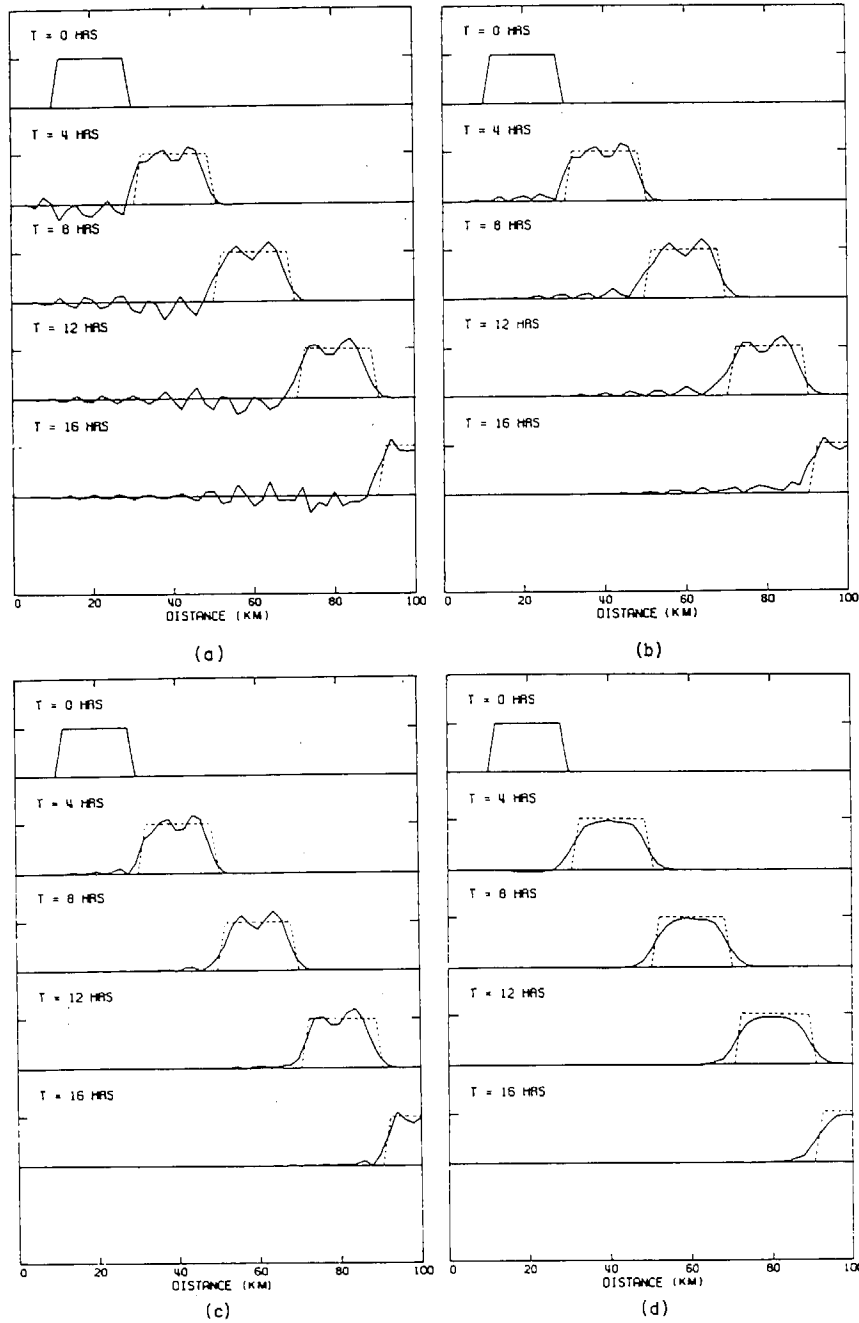


FIG. 4. Application of difference schemes to maintain concentration positivity. (a) Original linear finite element solution. (b) Absolute value $|c|$. (c) Downstream borrowing. (d) Nonlinear filter.

or 1 and determine the points at which smoothing occurs. Clearly if all are zero, no filtering takes place. For the condition $\psi_j = 1$, (51) takes a form that is analogous to the three-point difference expression for the diffusion term,

$$c_j^{k+1} = c_j^k + K_f [c_{j+1} - 2c_j + c_{j-1}]^k. \quad (50)$$

A key element of the filter application is the selection of the points in the grid mesh at which to set $\psi = 1$. Initially, all ψ are set to zero. Consider a point j and an interval $[j-m, j+m+1]$. On this interval the function S_e is evaluated using

$$S_e = \text{sgn}[c_e - c_{e-1}]; \quad e = j-m, j-m-1, \dots, j, j+1, \dots, j+m+1, \quad (51)$$

where

$$\begin{aligned} \text{sgn}(c) &= +1, & \frac{c}{|c|} &\geq 0, \\ &= -1, & \frac{c}{|c|} &< 0. \end{aligned} \quad (52)$$

At mesh point j there is an extremum of c_j if S_j and S_{j+1} are of opposite sign. The distribution of c on the interval $[j-m, j+m+1]$ is considered to be smooth if $S_{j+1}, \dots, S_{j+m+1}$ have the same sign and all S_{j-1}, \dots, S_{j-m} are of opposite sign to S_{j+1} . If this occurs, the values of ψ are left unchanged and no smoothing is applied to c_j . No tests for sign continuity of S_j, \dots, S_{j-m-1} are performed unless c_j is an extremum. These cases are illustrated in Fig. 5. If the slope or sign continuity does not hold for the m values of S on each side of the extremum in c_j , ψ is reset to 1 for the range of i from $i-l$ to $i+l$. To ensure that the mesh points at which ψ is nonzero in fact denote regions that contain computational noise, it is necessary to select the proper magnitudes for l and m . The value of m is chosen to be representative of one-half the wavelength of the lowest-frequency noise waves; l simply must be large enough to permit nonzero c values to be continuous.

For many high-order advective schemes nonlinear effects tend to drive the wavelength of the computational noise toward the limit of two mesh intervals, this can be seen in the results shown in Figs. 1-4. In general, the structure of the dispersive waves depends on the advection algorithm, its performance for different Courant numbers, and the nature of the concentration gradients. Values of m, l, K_f and the number of iterations required to satisfy the error tolerance must be determined empirically. For the above fourth-order schemes the values chosen were $m = 4$, $l = 2$, $K_f = 0.2$, and the number of iterations set to 2 and 3 for local Courant numbers less than 0.5 and greater than 0.5, respectively. An application of the filter, together with the finite element scheme, to the square-wave propagation problem is shown in Fig. 4d. There is clearly a significant improvement over the results displayed in Fig. 1.

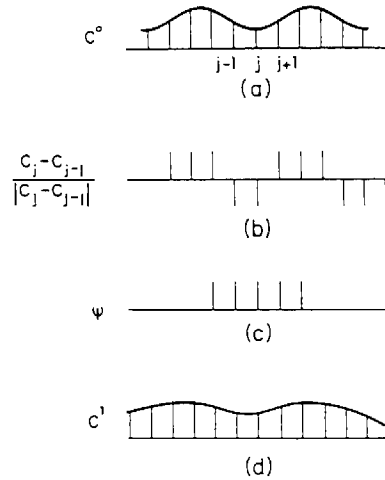


FIG. 5. Steps in the application of the discrete noise filter. (a) Initial distribution c^0 . (b) Evaluation of the normalized derivatives. (c) Establishment of ψ function. (d) Resulting distribution after one filter application c^1 .

7.2. Conservation Properties of Different Advection Methods

With the addition of the nonlinear filter, the performance of the finite element scheme improved to the point where it was useful to perform a quantitative comparison between it and the SHASTA method. In particular, it was important to assess the ability of each scheme to preserve mass, concentration gradients etc. A variety of initial distribution and velocity fields were used to test the techniques. The triangle test problem used in previous sections of this work has the property that

$$\frac{\partial}{\partial t} \int c \, dx = 0, \quad (53)$$

$$\frac{\partial}{\partial t} \int c^2 \, dx = 0, \quad (54)$$

$$\frac{\partial}{\partial t} \int c^4 \, dx = 0, \quad (55)$$

$$\frac{\partial}{\partial t} \int \left(\frac{\partial c}{\partial x} \right)^2 \, dx = 0, \quad (56)$$

$$\frac{\partial}{\partial t} \int \left(\frac{\partial^2 c}{\partial x^2} \right)^2 \, dx = 0. \quad (57)$$

Each of these integrals was evaluated numerically using, in the case of (56) and (57), standard finite difference approximations to the derivatives. While a numerical scheme should ideally conserve both mass (53) and mean square mass (54), diffusive

TABLE III
Results of Advection of Triangular Wave Form after 80 Time Steps

Numerical scheme	ERROR (%) = 100 (calculated/exact - 1)				
	$\int c \, dx$	$\int c^2 \, dx$	$\int c^4 \, dx$	$\int \left(\frac{\partial c}{\partial x}\right)^2 \, dx$	$\int \left(\frac{\partial^2 c}{\partial x^2}\right)^2 \, dx$
Fourth order	0.20	0.00	-0.44	-3.15	-28.17
SHASTA	0.20	-0.92	-5.51	-12.40	-97.75

effects tend to damp the latter quantity. The ability of a numerical scheme to maintain peak values is measured by (55), growth or decay of local gradients by (56) and change of profile curvature by (57). In a more general context, it should be noted that integrals (53) and (54) are analytically conserved in more complex source-free and nondiffusive flows. If gradient reducing diffusion terms are not included in calculations with more complicated flows, (56) and (57) tend to increase with time from either numerical distortion or from a physically real cascade to smaller spatial scales [62]. In practice, it is often difficult to establish which of these two effects is dominant. Since (56) and (57) are conserved in the test problem, any increase in their magnitude with time must be attributed to numerical errors. If this occurs, extra damping would be required to suppress the growth of the errors.

Errors in preserving the conservation properties for the SHASTA and fourth-order schemes are displayed in Table III. The SHASTA scheme performs poorly at maintaining peak values and, in addition, has the most diffusive effect on the profile. By comparison, the finite element method exhibits little diffusion.

A test of the capability of each scheme to handle variable velocity fields was also devised for the system

$$\frac{\partial c}{\partial t} + \frac{\partial uc}{\partial x} = 0; \quad x \in [0, 100], \quad (58)$$

where the velocity field $u(x)$ is given by

$$u(x) = \frac{x+1}{20}. \quad (59)$$

The exact solution, $c_e(x, t)$ of this system is

$$c_e(x, t) = 0.1(x+1) \exp \left[-\frac{t}{10} \right]. \quad (60)$$

Initial and boundary condition for the problem are $c(x, 0) = c_e(x, 0)$ and $c(0, t) = c_e(0, t)$. Each numerical scheme used a grid size $\Delta x = 2$ km, and a time step $\Delta t = 0.2$ hours. Under these conditions, the maximum Courant number is 0.5. After

TABLE IV
Errors in Concentration Predictions after 120 Time Steps
for a Spatially Varying Velocity Field

Numerical scheme	Error (%) at			
	$x = 24$	$x = 50$	$x = 76$	$x = 100$
Fourth order	0.87	-0.08	0.01	0.03
SHASTA	1.18	1.20	1.20	1.87
Exact solution	0.0338	0.0690	0.1042	0.1367

120 time steps (24 hours), the errors were calculated and the results are shown in Table IV. While each scheme performed reasonably well, the finite element method produced better predictions at all spatial locations.

A rather difficult advection calculation, in two dimensions, is the rotating cone problem introduced by Crowley [55] and Molenkamp [65]. The test consists of solving the axisymmetric advection problem

$$\frac{\partial c}{\partial t} + \omega \frac{\partial c}{\partial \theta} = 0, \quad (61)$$

where θ is the angular coordinate, and ω the angular velocity around the axis of rotation. The exact solution of (61) is given by $c(r, \theta, t) = c^0(r, \theta - \omega t)$, where c^0 is the initial distribution of c . Since there is no physical diffusion, the shape c^0 should remain unchanged upon rotation. The Crowley problem consists of solving (61) in rectangular coordinates where the rotation is anticlockwise about the origin.

TABLE V
Summary of Results of Two-Dimensional Cone in a Circular
Wind Field ($C_x = C_y = 0.5$)

Numerical scheme	1/4 Revolution		1 Revolution	
	Maximum value	Minimum value	Maximum value	Minimum value
Fromm	0.7400	-0.0218	0.5466	-0.0288
Crowley	0.8478	-0.0586	0.7283	-0.1279
Finite element	0.8731	-0.0335	0.8645	-0.0545
SHASTA	0.6670	0.0	0.5118	0.0
Exact solution	1.0000	0.0	1.000	0.0

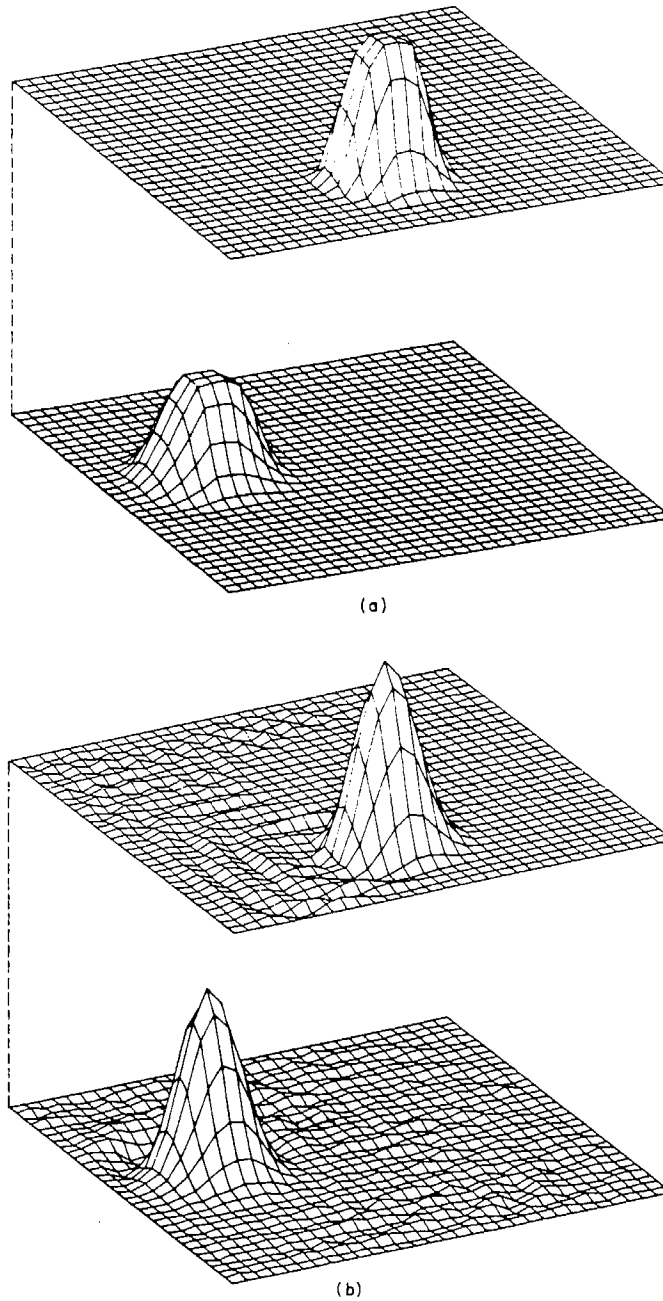


FIG. 6. Results of Crowley test problem for a quarter and complete revolution of a cone using (a) SHASTA method and (b) linear finite element scheme (without filtering step).

Under these conditions, the velocity components are given by $u = -y\omega$, $v = x\omega$ and

$$\frac{\partial c}{\partial t} - \frac{\partial \omega y c}{\partial x} + \frac{\partial \omega x c}{\partial y} = 0. \quad (62)$$

The method of fractional steps was used to solve the problem on a 32×32 grid with $\Delta x = \Delta y = 1$ km, $\Delta t = 0.5$ hrs and $\omega = 0.0626$ rad/hr. A conical distribution, centered initially at $(-8, 0)$, of base radius 4 and with $c_{\max} = 1$, $c_{\min} = 0$ was used to describe c^0 . The results of the experiment, summarized in Table V, are displayed in Fig. 6; the conclusions are similar to the last test case. The peak truncation problem, characteristic of SHASTA, is particularly apparent. From a practical point of view, it is encouraging to note that the amplitudes of the dispersive waves associated with unfiltered finite element scheme are quite small.

8. SOLUTION OF THE DIFFUSIVE TRANSPORT STEP T_d AND BOUNDARY CONDITION TREATMENT

Previous sections were devoted to the implementation and testing of a suitable scheme for the advection equation. The contribution to species transport from turbulent diffusion depends on the coordinate direction. In the horizontal plane, transport is dominated by advection and so a simple, explicit three-point finite difference form [9] can be adopted for $(T_x)_d$ and $(T_y)_d$. A linear finite element scheme, with Crank–Nicholson time differencing, was used for $(T_z)_d$. This removed the time step limitation of an explicit method and enabled the use of variable mesh spacing to resolve vertical concentration gradients.

The boundary of the grid is usually placed at the limits of the available data or far from the main calculation area. Boundary conditions are termed either inflow or outflow, depending on the direction of flow relative to the grid region. Often in fluid flow problems, the concentration at the inflow boundary is known and can be specified as a function of time. The outflow boundary is generally not known and therefore must be calculated. This boundary condition is sometimes called a “computational boundary condition” for this reason. Some helpful discussions of boundary conditions exist in the literature [66–73]. The boundary conditions used with (32) are

$$\text{inflow:} \quad uc - K_{xx} \frac{\partial c}{\partial x} = uc_{\text{in}}, \quad (63)$$

$$\text{outflow:} \quad -K_{xx} \frac{\partial c}{\partial x} = 0, \quad (64)$$

where c_{in} is the known concentration just outside of the inflow boundary. If it is assumed that advection is the dominant transport mechanism at the outflow

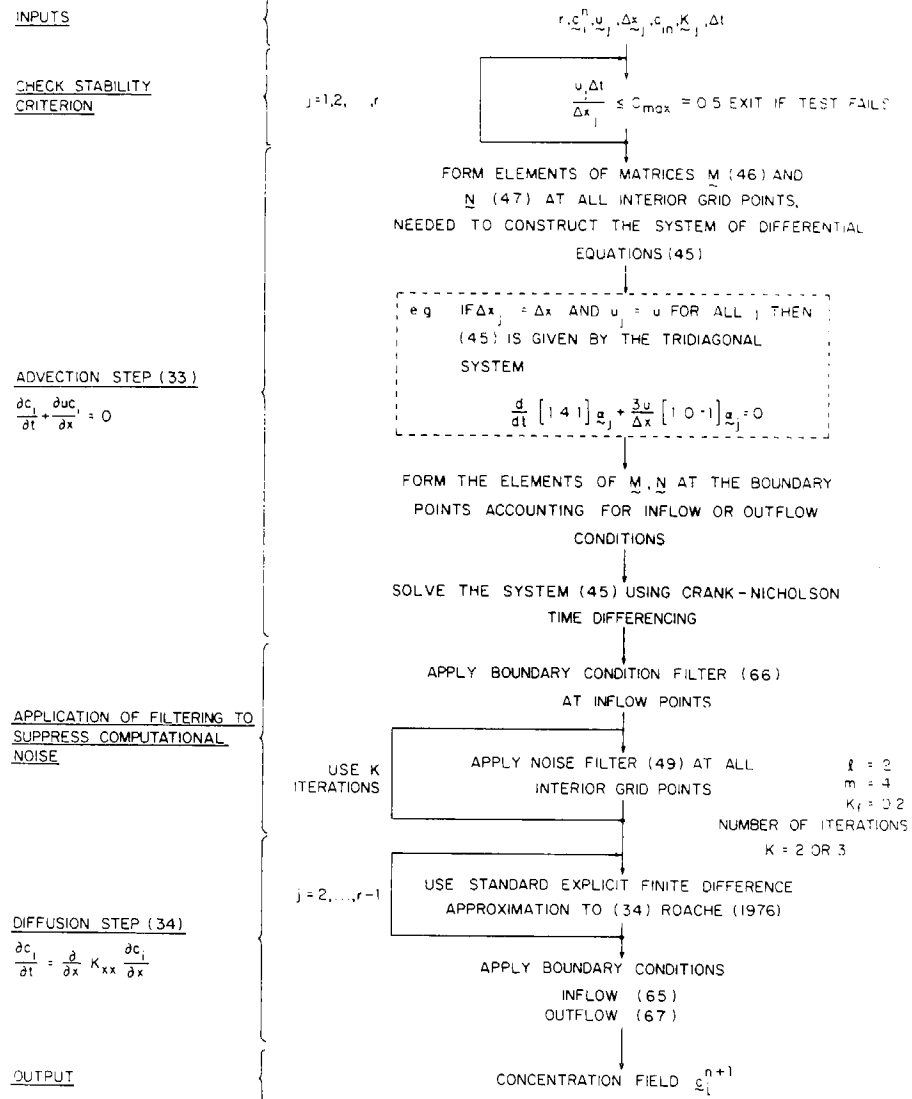


FIG. 7. Structure of the algorithm for solving the advection-diffusion equation for species transport in the x-direction.

boundary, then diffusive transport can be neglected. If the left end of the grid is an inflow boundary, then (63) can be represented as

$$u_1 c_1^{n+1} - \frac{1}{2}[(K_{xx})_1 + (K_{xx})_2] \frac{c_2^{n+1} - c_1^{n+1}}{\Delta x} = u_1 c_{in}^{n+1}, \quad (65)$$

which, in turn, can be solved explicitly for c_1^{n+1} since all other quantities are known. When using a multiple-step, advection-diffusion algorithm, (65) is used following the second (diffusion) step. A boundary value must also be set following the first (advection) step. The single condition $u_1 c_1 = u_1 c_{in}$ is used for this step in conjunction with a smoothing procedure at the point adjacent to the boundary point. This smoothing damps any waves that may be generated by the inflow boundary point. The simplest smoothing algorithm is

$$c_2^* = \frac{1}{2}c_2^{n+1} + \frac{1}{4}(c_1^{n+1} + c_3^{n+1}), \quad (66)$$

where c_2^* is the smoothed value of c^{n+1} at $j = 2$. A procedure analogous to the above can be applied to the right boundary. The concentration at an outflow boundary is influenced by information from the interior of the grid. Concentration gradients that are advected to the boundary must be preserved as they pass out of the grid. The simple choice of representing (64) by a zero gradient, i.e., $c_1 = c_2$ or $c_r = c_{r-1}$, where r is the right boundary point, was discarded due to its inability to preserve gradients. The approach adopted was to solve the advection equation (with zero diffusion) using a one-sided difference at the boundary:

$$\frac{c_r^{n+1} - c_r^n}{\Delta t} + \frac{u_r c_r^{n+1} - u_{r-1} c_{r-1}^{n+1}}{\Delta x} = 0. \quad (67)$$

This procedure preserves concentration gradients as they move out of the grid system as can be seen in the previous figures for the one dimensional test problems.

Figure 7 shows a flow diagram of the numerical solution of the advection and diffusion components of the atmospheric diffusion equation.

9. NUMERICAL SOLUTION OF THE CHEMICAL KINETICS

In the previous two sections primary emphasis was placed on the transport components of the atmospheric diffusion equation. Equation (1) contains terms, f_i , $i = 1, 2, \dots, p$, that describe the contributions to the rates of change of the p chemical species concentrations, c_1, c_2, \dots, c_p , due to chemical reactions. At any one spatial point the rate of change of each species concentration resulting only from the

chemical kinetics can be described by a set of coupled, nonlinear ordinary differential equations,

$$\frac{dc_i}{dt} = f_i(c_1, c_2, \dots, c_p, t); \quad i = 1, 2, \dots, p, \quad (68)$$

and associated initial conditions $c_i(0) = c_i^0$, $i = 1, 2, \dots, p$.

There are two sources of difficulty that arise during the numerical solution of (68). One is minor and caused by the nonlinearities resulting from the polynomial form of the mass action rate laws. The more serious problem, however, arises as a result of the fact that in atmospheric systems there are reactions whose characteristic time scales differ by orders of magnitude. Such systems are often referred to as being "stiff." There are various definitions of what constitutes stiffness, the most common is of the form:

DEFINITION. The system (68) is said to be *stiff* if

$$(a) \quad \operatorname{Re}(\lambda_i) < 0; \quad i = 1, 2, \dots, p,$$

and

$$(b) \quad (\max_i |\operatorname{Re} \lambda_i|) / (\min_i |\operatorname{Re} \lambda_i|) = R \gg 1,$$

where R is the stiffness ratio and λ_i are the eigenvalues of the Jacobian matrix $\mathbf{J} = \partial f / \partial c$. A way to view the problem of stiffness is to write (68) in the form

$$\frac{dc_i}{dt} = a_i - b_i c_i, \quad (69)$$

where a_i is the production rate for species c_i and $b_i c_i$ is the loss rate. The reciprocal of b_i can be interpreted as the characteristic time for decay of species i . If a_i and b_i are constants then (69) can be solved to give

$$c_i(t) = \frac{a_i}{b_i} + \left[c_i(0) - \frac{a_i}{b_i} \right] \exp(-b_i t). \quad (70)$$

Expressed in this way, it can be seen that $1/b_i$ describes how quickly species c_i reaches its equilibrium value. Figure 8 presents a typical eigenvalue spectrum for atmospheric reaction mechanisms together with the characteristic reaction times $1/b_i$. Two features are readily apparent: one is the close correspondence, for many species, between the eigenvalues and the characteristic reaction times and the other is the extreme range $O(10^{12} \text{ min})$ of the spectrum.

In passing it is worthwhile to comment on the reason why some of the eigenvalues are so closely matched to the corresponding reaction times. Consider atomic oxygen (O), which has the fastest reaction time of any species in the system. An examination

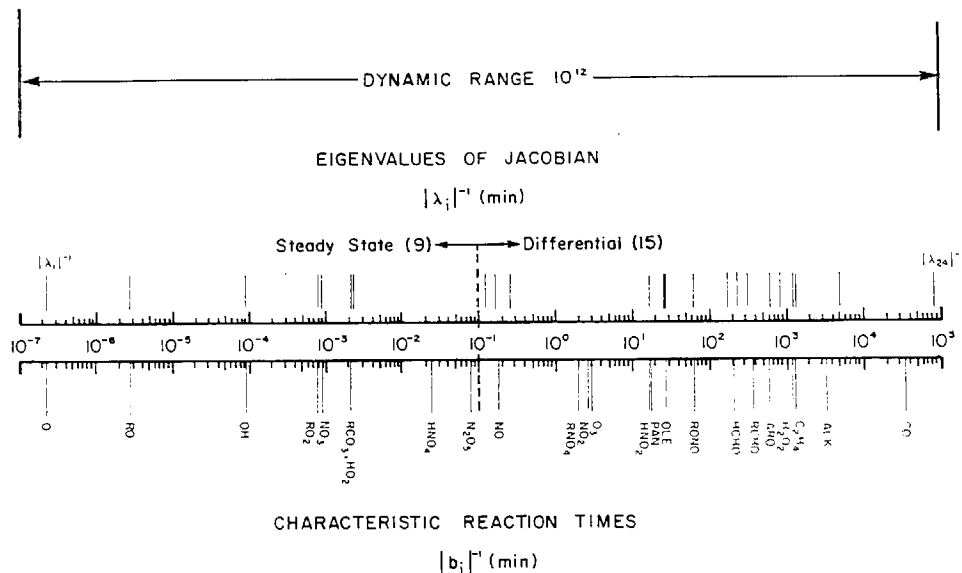


FIG. 8. Typical eigenvalue spectrum and characteristic reaction times for the photochemical mechanism of McRae *et al.* [89].

of O atom production and decay rates under typical conditions indicates that the predominant removal step (by four orders of magnitude) is reaction with molecular oxygen



Since the concentration of both molecular oxygen (O_2) and the third body (M), are fixed, the kinetics of O are described to a very good approximation by (69) with a_i and b_i constant. Under these conditions the eigenvalues and characteristic reaction times can be expected to be similar. This behavior was also observed for most of the free radicals: RO, OH, RO_2 , NO_3 , RCO_3 , and HO_2 . When there is coupling between species, and the rate terms are of comparable magnitude, the a_i 's and b_i 's are no longer constant and the analytic solution (70) is inappropriate.

9.1. Selection of a Suitable Solution Scheme

In the last few years considerable effort has been devoted to developing general purpose algorithms for solving stiff ordinary differential equations [74–79].

In applications involving simultaneous transport and chemistry such as that of interest here, the reaction rate equations must be integrated at a large number of grid points for relatively short periods of time between transport steps. As a consequence, self starting methods with low overheads are highly desirable. As mentioned earlier, the large size of the computational grid usually precludes storing more than the

results of the previous time step. From a pragmatic point of view it is important to recognize that errors associated with the transport steps are rarely smaller than a few percent so in general there is little to be gained by requiring highly accurate solutions of the kinetics. Summarizing, the desirable requirements of a solution scheme for the chemical kinetics are low start up costs, minimal computer memory requirements, and extreme computational speed.

Given the above considerations, two different solution schemes were sought; one capable of providing highly accurate benchmark standards of predictions and the other, an extremely fast algorithm for use in the airshed model. Since the factors influencing the choice of the method use in the model are discussed in Section 9.3 they will not be discussed here. The method chosen to establish the standard of accuracy for judging other methods was the implementation of the Gear technique by Hindmarsh and Byrne [80] and Byrne *et al.* [81]. Their program, called EPISODE, is extremely well documented and has been subjected to extensive testing by a number of different investigators [79, 81]. Unlike the original Gear method, the program employs a true variable step, variable order approximation that is ideally suited to problems with time varying parameters. Another reason for choosing this particular code was the ease with which different treatments of the Jacobian could be tested. In the version of EPISODE used in this study the Jacobian could be evaluated in either of four ways: functional iteration, analytic evaluation, finite differences, or diagonal approximations. The ability to exercise easily these options considerably simplified the task of identifying the most efficient means for solving the chemical kinetics.

9.2. Pseudo Steady State Approximation

Even with fast integration schemes the computational cost of solving the atmospheric diffusion equation is extremely high. There is a need to reduce both the number of active chemical species, to minimize storage requirements, and the stiffness, to lower the computational cost. One approach, commonly used in chemical kinetics, is to alleviate some of these difficulties by employing the pseudo steady state approximation [82, 83]. The basic idea behind this approximation is that the transients associated with the stiff variables decay very rapidly to their equilibrium values. If the concentrations are partitioned into two components, one associated with the nonstiff components \mathbf{c}_d and the other comprising the stiff species, \mathbf{c}_s , then if the pseudo steady state approximation is used, (68) is replaced by the systems

$$\dot{\mathbf{c}}_d = \mathbf{f}_d(\mathbf{c}_d, \mathbf{c}_s) \quad (72)$$

and

$$\mathbf{0} = \mathbf{f}_s(\mathbf{c}_d, \mathbf{c}_s). \quad (73)$$

The two main difficulties associated with the valid use of pseudo steady state approximations are the identification of those species that can be treated in this way and the determination of the time after which the approximation is valid. For simple systems there is an extensive literature that utilizes singular perturbation theory to establish

TABLE VI
Comparison between the Exact Calculation and the Pseudo Steady
State Approximation for Different Chemical Species

Time (min)	% Error									
	OH	O	CO ₃	RO ₂	RO	HO ₂	HNO ₄	NO ₃	N ₂ O ₃	
60	-2.5×10^{-3}	-4.3×10^{-6}	$+8.3 \times 10^{-3}$	-3.4×10^{-3}	-1.2×10^{-2}	$+8.6 \times 10^{-3}$	$+8.5 \times 10^{-2}$	-3.5×10^{-2}	-3.7×10^{-1}	
120	-2.7×10^{-3}	$+2.1 \times 10^{-6}$	-2.0×10^{-3}	-4.2×10^{-3}	$+8.6 \times 10^{-3}$	$+4.1 \times 10^{-3}$	$+3.8 \times 10^{-2}$	$+2.6 \times 10^{-2}$	$+3.3 \times 10^{-1}$	
180	$+2.6 \times 10^{-2}$	-5.6×10^{-6}	$+7.3 \times 10^{-3}$	-1.0×10^{-2}	$+1.5 \times 10^{-2}$	-1.1×10^{-2}	$+2.1 \times 10^{-2}$	-1.6×10^{-1}	$+1.6 \times 10^{-1}$	
240	$+7.0 \times 10^{-2}$	$+4.7 \times 10^{-6}$	-2.8×10^{-3}	-1.5×10^{-2}	$+1.8 \times 10^{-1}$	-4.5×10^{-2}	$+3.0 \times 10^{-3}$	$+9.1 \times 10^{-2}$	$+1.4 \times 10^{-1}$	
300	$+1.2 \times 10^{-1}$	$+3.2 \times 10^{-6}$	-2.0×10^{-2}	$+2.2 \times 10^{-3}$	$+4.3 \times 10^{-1}$	-7.3×10^{-2}	-3.0×10^{-2}	-2.1×10^{-1}	$+7.0 \times 10^{-2}$	
360	-8.8×10^{-2}	-1.9×10^{-5}	$+1.9 \times 10^{-3}$	-1.8×10^{-2}	-5.6×10^{-1}	$+7.9 \times 10^{-2}$	$+3.7 \times 10^{-2}$	$+1.7 \times 10^{-2}$	$+2.9 \times 10^{-2}$	

* Percentage Error = $100 |PSSA/EXACT - 1|$.

the appropriate bounds [78, 82–84]. Unfortunately, there is as yet no well-developed theory for systems as complex as the photochemical reaction mechanism utilized in this study. Thus, an approximate way to identify candidate species was developed.

The particular approach adopted in this study was to analyze the behavior of the kinetic equations by performing an eigenvalue–eigenvector analysis of the mechanism Jacobian under a wide variety of test conditions. The reason for doing this is that the eigenvalues all have negative real parts that can be ranked into two distinct subsets. The first set of largest negative eigenvalues generally have eigenvectors containing only one or two components. These elements as noted above usually correspond to those species that have very fast reaction times. These λ 's typically have magnitudes as large as 10^7 , corresponding to species half-lives as short as 10^{-6} seconds. The second set of eigenvalues has corresponding eigenvectors that each involve many, if not most, of the species in the reaction set. These represent the relatively slowly reacting species.

Using the eigenvalue analysis procedure, nine species were identified as candidates for the steady state approximation: O, RO, OH, RO₂, NO₃, RCO₃, HO₂, HNO₄, and N₂O₅. The solutions using the steady state approximation and one where all species were treated by differential equations were compared over a wide range of conditions. Typical examples of the results of these tests are shown in Tables VI and VII. Table VI is an assessment of the validity of each approximation. An inspection

TABLE VII
Comparison between Predictions of Complete System
and Kinetics Using Pseudo Steady State Approximations

Time (min)	Species	Concentration (parts-per-million by volume)		
		Complete system	Kinetics with 9 PSSA species	% Difference*
30	NO	0.0566	0.0567	0.18
	NO ₂	0.4034	0.4070	0.89
	O ₃	0.0830	0.0834	0.48
60	NO	0.0202	0.0202	0.00
	NO ₂	0.3869	0.3889	0.51
	O ₃	0.2189	0.2191	0.09
90	NO	0.0110	0.0110	0.00
	NO ₂	0.3338	0.3329	−0.27
	O ₃	0.3379	0.3383	0.12
120	NO	0.0066	0.0066	0.00
	NO ₂	0.2628	0.2652	0.91
	O ₃	0.4358	0.4391	0.75

* Percentage difference = 100 [PSSA/complete − 1].

of the results indicates that there are negligible differences between the species being treated by differential or algebraic equations. The most important comparison, however, is the influence of the use of the approximation on the predicted concentrations, c_d . Even after 120 minutes the maximum error shown in Table VII is less than 0.5%. The conclusion reached from an analysis of these and other test cases was that the species identified from the eigenvalue analysis could be treated in steady state with minimal effects on the predicted concentrations of the primary species, c_d .

Once the concentration vector has been partitioned into stiff and nonstiff components, there are a variety of algorithms that can take advantage of the problem structure. For example, Robertson [85] utilized the division in the iterations involved with the use of implicit multistep formulas. During any single step, by fixing the part of the iteration matrix corresponding to the nonstiff components and only updating the elements arising from the transients, significant computational economies were achieved. Techniques that achieve these efficiencies without prior knowledge about the problem structure are relatively rare. Enright and Kamel [86] have developed a general purpose computer code for systems where the stiffness is due to a few components of a large system.

One other approach for minimizing the influence of stiffness is to choose the initial conditions for c_s so that the complete system does not have the initial transient behavior. While it is extremely difficult to develop a general theory some initial steps in this direction have been made by Watkins [87] and Lambert [88]. The approach of Watkins [87] is particularly relevant because his algorithm has been developed to set initial conditions for transport problems. Unfortunately the cost of the proposed iteration scheme, when applied to systems of the size encountered in this study, is likely to be prohibitive. Kreiss [78] has addressed a similar situation in an attempt to set the initial conditions in a way that would eliminate the rapidly oscillating terms associated with large, purely imaginary eigenvalues. At this time there is no satisfactory means for a priori specification of the initial values for c_s that will remove or reduce the stiffness of systems of the type considered here.

9.3. *Asymptotic Integration Scheme*

In the previous section the size and stiffness of the reaction mechanism was reduced by employing the pseudo steady state approximation. Even with these changes it was still not feasible to economically use the EPISODE program in the solution of the full atmospheric diffusion equation. A variety of other alternatives were investigated in an attempt to significantly lower the computational cost but without substantially compromising the solution accuracy. The trapezoidal rule was rejected because of the overheads associated with the matrix decompositions. Even with the use of sparse matrix packages and infrequent Jacobian updating, the cost of Newton-type schemes was still excessive. The particular approach finally decided upon with the asymptotic integration method of Young and Boris [89, 90]. Designed to solve the reaction kinetics embedded in very large hydrodynamic problems, the method is self starting, extremely fast and requires minimal storage; as such, it satisfies most of the selection criteria discussed above.

A particularly attractive feature of the method is that it has a very low start up overhead because all that is required to begin a new integration step are the current values of the variables and the derivatives. A second-order predictor-corrector scheme that takes special notice of those equations determined at the beginning of the step to be stiff is employed to continue the integration process. When applied to stiff equations, the method is suited to situations where the solution is slowly changing or nearly asymptotic yet the time constants are prohibitively small. This occurs when the formation and loss rates are large, nearly equal, and there is strong coupling among the equations. Thus, the stiff equations are treated with a very stable method that damps out the small oscillations caused by the very small time constants.

The predictor-corrector algorithm provides enough information to choose the subsequent timestep size once convergence has been achieved. For efficiency, an initial timestep is chosen that approximates the timestep that will be determined after convergence of the predictor-corrector scheme. This initial trial timestep is chosen independently of the stiffness criterion and is determined such that none of the variables will change by more than a prescribed amount. If the formation rate is much larger than the loss rate, it is reasonable to assume that a_i and b_i will remain relatively constant for large changes in c_i . Often the initial change in c_i may be large enough to equilibrate the formation and loss rates. Thus the initial trial timestep $\Delta\tau$, is chosen in two ways:

$$\Delta\tau = \varepsilon \min_i \left[\frac{c_i}{f_i} \right] \quad (74)$$

or if $a_i \gg b_i c_i$ then

$$\Delta\tau = \varepsilon \min_i \left[\frac{1}{b_i} \right]. \quad (75)$$

The second criterion is needed when the initial conditions, for some species, are unknown or set to zero. Here ε is a scale factor, the selection of which is discussed shortly. The timestep dictated by (74) may be larger than some or all of the equilibrium times, in which case the corresponding equations would be classified as stiff. Nevertheless, when solved by the asymptotic method, this timestep ensures that accuracy can be maintained. When a stiff equation is close to equilibrium, the changes in the functional values over the timestep will be small even though the adjustment rate toward equilibrium can be very much shorter than the timestep. When the stiff equation is far from a dynamic equilibrium, the timestep should be scaled down proportionally to the equilibrium time to ensure that the transition to equilibrium will be followed accurately. This readjustment, because of the very fast rate, generally takes place rapidly after which much longer timesteps may be taken.

After a timestep has been chosen, all of the equations are separated into two classes, stiff and nonstiff, according to the values of the b_i . The two types of equations are then integrated by separate predictor-corrector schemes. A simple asymptotic formula is used for those equations determined to be stiff.

The predictor part of the step is performed as follows:

$$\text{Nonstiff: } c_i(1) = c_i(0) + \Delta\tau f_i(0), \quad (76)$$

$$\text{Stiff: } c_i(1) = c_i(0) + \frac{\Delta\tau f_i(0)}{1 + \Delta\tau f_i(0)}, \quad (77)$$

where $f_i(0) = f_i[t(0), c_i(0)]$ and $c_i(k)$ is the k th iterated value of c_i , or an approximation to $c_i[t(0) + \Delta\tau]$. The zeroth iteration, $c_i(0)$, is the initial value at $t(0)$ and $c_i(1)$ is the result of the predictor step. Also note that $f_i(k) = f_i[t(0) + \Delta\tau, c_i(k)]$. The corrector formulas are:

$$\text{Nonstiff: } c_i(k+1) = c_i(0) + \frac{\Delta\tau}{2} [f_i(0) + f_i(k)], \quad (78)$$

$$\text{Stiff: } c_i(k+1) = c_i(0) + \frac{2\Delta\tau[a_i(k) - b_i(0)c_i(0) + f_i(0)]}{4 + \Delta\tau[b_i(k) + b_i(0)]}. \quad (79)$$

By comparing $c_i(k+1)$ with $c_i(k)$ on successive iterations using the relative error criterion ε to satisfy

$$\max_i \left[\frac{|c_i(k+1) - c_i(k)|}{c_i(k+1)} \right] \leq \varepsilon \quad (80)$$

the convergence of each of the individual equations can be determined. As applied in the present application, ε is typically $O(10^{-3})$ and if the formation and loss rates are nearly equal ε is scaled down slightly, to allow quicker convergence for equations that are nearly in equilibrium.

In practice, c_i is constrained by a minimum value when c_i is decaying exponentially toward zero. This lower bound must be selected to insure that its value in no way affects the physics but yet decouples the equation from accurate integration. Decoupling is accomplished by avoiding applying (80) to all equations that have decayed to values corresponding to their lower bounds. Convergence for these equations is then trivial and the function no longer affects the size of the timestep. For equations that are decaying exponentially to zero, with time constants that are small enough to control the timestep, it is important for efficiency reasons to decouple these equations at the largest lower bound possible.

In practical application the maximum solution speed is realized by keeping the allowed number of corrector iterations small, typically one or two. If satisfactory convergence of all equations has not been obtained before or during the last iteration, the step is started over with a smaller timestep. By keeping the maximum number of iterations small, a minimum amount of time is wasted on an unstable or nonconvergent step. When nonconvergence is encountered, it is more efficient to reduce the timestep sharply (a factor of 2 or 3). On the other hand, when increasing the timestep, as, for example, when convergence is achieved on the first or second

iteration, it is best to increase only by 5–10% each step. The asymptotic integration scheme was compared against the program EPISODE [80,81] to evaluate the characteristics of the algorithm when applied to the photochemical reaction mechanism. For all EPISODE calculations semi-relative error control was used with a convergence tolerance of 0.0001. The starting and maximum step sizes were set to 10^{-5} and 10 minutes, respectively.

Both programs were exercised over a wide range of initial conditions, pseudo steady state approximations, photolysis rates and diurnal cycles. Two features were apparent in all the tests, and they are illustrated in Table VIII. First, and perhaps most important, is that there were negligible differences in the predictions of both schemes over solution steps comparable to the maximum expected transport times. For example, after 30 minutes the maximum discrepancy between the two schemes for the species NO, NO₂, and O₃ was $O(0.2\%)$.

The most striking difference between the two schemes is the high start up costs associated with the EPISODE algorithm. During the initial 30 minutes there is a factor of 7 difference in the computation time. Once started, however, the incremental cost, per time interval, of using EPISODE becomes successively smaller. From a

TABLE VIII
Comparison of Start Up Times for EPISODE and Hybrid Solution
Scheme for Typical Smog Chamber Experiment

Time (min)	Species	Concentration (parts-per-million by volume)		Computer time (ms) per 30 minute step	
		Episode	Hybrid solver	Episode	Hybrid
30	NO	0.0567	0.0567 (0.00)*	1014	152
	NO ₂	0.4070	0.4077 (0.17)		
	O ₃	0.0834	0.0832 (−0.24)		
60	NO	0.0202	0.0203 (0.50)	175	104
	NO ₂	0.3889	0.3914 (0.64)		
	O ₃	0.2191	0.2194 (0.14)		
90	NO	0.0110	0.0107 (−2.73)	79	81
	NO ₂	0.3329	0.3290 (−1.17)		
	O ₃	0.3383	0.3450 (1.98)		
120	NO	0.0066	0.0062 (−6.06)	47	70
	NO ₂	0.2652	0.2557 (−3.58)		
	O ₃	0.4391	0.4497 (2.41)		
				1315 ms	407 ms

* Percentage difference between EPISODE and Hybrid solution technique = 100 [Hybrid/EPISODE − 1].

practical point of view, considering the short integration intervals in an operator splitting solution, the asymptotic scheme is clearly preferable to the EPISODE algorithm for the present application.

9.4. Implementation of Asymptotic Integration Scheme

Using the operator splitting procedures described earlier, (9) can be written in the form

$$\text{Transport} \quad \frac{\partial c_i}{\partial t} = L(\mathbf{x}, t) c_i, \quad (81)$$

$$\text{Chemistry} \quad \frac{\partial c_i}{\partial t} = f_i(c_1, \dots, c_p, t). \quad (82)$$

If \mathbf{T}_x , \mathbf{T}_y , \mathbf{T}_z and \mathbf{C}_c are the numerical approximations to the transport and chemistry operators then a complete solution can be obtained from the sequence

$$\mathbf{c}_i^{n+1} = \mathbf{T}_x \mathbf{T}_y \mathbf{T}_z \mathbf{C}_c(2\Delta t) \mathbf{T}_z \mathbf{T}_y \mathbf{T}_x \mathbf{c}_i^{n-1}, \quad (83)$$

where \mathbf{C}_c symbolically denotes the means of solving (82) at each of the grid points given a set of initial conditions. Most of the computer time required for each cycle (83) is consumed by the chemical solution \mathbf{C}_c . Two advantages of operator splitting are apparent, the chemistry is decoupled from the transport and it can be solved for a period $2\Delta t$. This latter feature is particularly important because most of the overhead associated with solving (82) occurs at the start of each initial value problem; subsequent time increments can be obtained at minimal expense.

The actual sequence of operations used to obtain a solution of (83) is as follows. Solve

$$\frac{\partial c_i^*}{\partial t} = L_x c_i^*, \quad (84)$$

$$\frac{\partial c_i^{**}}{\partial t} = L_y c_i^{**}, \quad (85)$$

$$\frac{\partial c_i^{***}}{\partial t} = L_z c_i^{***}, \quad (86)$$

on the interval $t^{n-1} \leq t \leq t^n$,

$$\frac{\partial c_i}{\partial t} = f_i(c_1, \dots, c_p, t) \quad (87)$$

on the interval $t^{n-1} \leq t \leq t^{n+1}$, and then solve the system (84)–(86) in the reverse order, i.e., in z , y , and x directions. The initial conditions for each of the problems (84)–(86) are: $c_i^*(t^{n-1}) = c_i(t^{n-1})$, $c_i^{**}(t^{n-1}) = c_i^*(t^n)$, $c_i^{***}(t^{n-1}) = c_i^{**}(t^n)$ and for (87) $c_i(t^{n-1}) = c_i^{***}(t^n)$.

Unfortunately, there is little guidance in the literature relevant to establishing a priori bounds on the maximum value of Δt . Within the airshed model it has been observed that the convergence of the sequence (83), during the photochemically active daylight hours, is controlled more by the rate of vertical turbulent mixing than by the Courant limit of the horizontal advection schemes. As a result of considerable experimentation with successively smaller time steps it was found that if $2\Delta t$ was limited to be less than 10 minutes, the predicted results were comparable to cases in which the two-dimensional coupled problem (9) was solved directly. At night when there is little or no chemical activity, the chemical time steps are controlled by the stability limits of the advection schemes. The total computer time required to simulate the concentration dynamics of 15 species at 3000 grid points for a 24-hour period is $O(50 \text{ minutes})$ on an IBM 370/168. The interested reader is referred to McRae *et al.* [91] for a description of the air pollution model.

10. CONCLUSIONS

In this paper, a variety of numerical methods were studied in order to identify a solution scheme for the atmospheric diffusion equation. As a result of this investigation, a composite technique was developed in which operator-splitting was first used to segment the three-dimensional system of equations into a sequence of one-dimensional problems. Each transport step was further simplified to three basic components: an advection step, application of a nonlinear filter and finally a diffusion step. A Galerkin, linear finite element scheme was adopted for the critical advection step. The results of numerous numerical experiments indicate that this algorithm, together with the filter step, preserves extreme values, gradients, total mass and mean square concentration. The solution of the chemical kinetics component is carried out by a second-order predictor, iterated corrector technique, in combination with an asymptotic treatment of the stiff components of the problem [90, 91]. Computational economies are achieved by implementation of the pseudo steady state approximation.

APPENDIX: NOTATION

$a(\mathbf{X}, t), b(\mathbf{X}, t)$	Coefficients associated with boundary conditions (3)
a_i	Production rate for species i , $i = 1, 2, \dots, p$
\mathbf{A}	An $r \times r$ matrix representing the discrete approximation to L at r computational grid points. (\mathbf{A}_j is the discrete representation of L_j)
b_i	First-order coefficient for removal rate of species i , $i = 1, 2, \dots, p$
B	Linear boundary operator
$\mathbf{B}, \mathbf{H}, \mathbf{M}, \mathbf{P}, \mathbf{Q}, \mathbf{S}$	Matrices of dimension $r \times r$ associated with different spatial discretization techniques
\mathbf{c}_d	Concentration vector of nonstiff components
$c_i(k)$	k th iterate of c_i

$c_i(\mathbf{X}, t), c_i(\mathbf{x}, t)$	Concentrations of species i in the physical and computational domains; $i = 1, 2, \dots, p$
$\mathbf{c}_i(\mathbf{x}, t)$	Concentration vector of species i at r computational points $\mathbf{c}_i(\mathbf{x}, t) = (c_i(\mathbf{x}_j, t); j = 1, 2, \dots, r)$
\mathbf{c}_s	Concentration vector of stiff components
C	Courant number
\mathbf{C}_c	Symbol representing solution of the chemical kinetics
f_i	Chemical formation (or depletion) rate of species i $\mathbf{f}_i = (f_i(c_1(\mathbf{x}_j, t), \dots, c_p(\mathbf{x}_j, t))); j = 1, 2, \dots, r)$
\mathbf{F}	Mapping function that transforms points from \mathbf{X} into \mathbf{x}
$g_i(\mathbf{X}, t)$	Species specific boundary condition coefficient
$h(X, Y)$	Topographic surface (lower boundary of region)
$H(X, Y, t)$	Time varying upper surface of region
\mathbf{I}	Unit matrix of dimension $r \times r$
\mathbf{J}	Jacobian matrix with elements $\partial f_i / \partial c_j, i, j = 1, 2, \dots, p$
k_l	Rate constant for reaction l
K_f	Coefficient in noise filter
K_n	Diffusion coefficient associated with noise filter
\mathbf{K}	Second-order turbulent eddy diffusion tensor (usually a diagonal matrix with elements K_{xx}, K_{yy}, K_{zz}). In the computational domain \mathbf{K}_{xx} are the values of K_{xx} at each of the r grid points.
L	Three-dimensional, semi-linear, elliptic differential operator (L_x, L_y, L_z are the components in x, y and z directions).
R	Stiffness ratio
r	Radial coordinate for Crowley problem
t	Time
T	Extent of time interval for solution
\mathbf{T}	Composite transport operator (T_j is the transport operator for the j th direction)
$\mathbf{u}(\mathbf{X}, t)$	Velocity field in physical domain $\mathbf{u} = (u, v, w)$
\mathbf{U}	Velocity field in computational domain $\mathbf{U} = (u_j; j = 1, 2, \dots, r)$
$\mathbf{V}(\mathbf{x}, t)$	Velocity field in transformed domain $\mathbf{V} = (u, v, W)$
\mathbf{x}	Point in computational domain $\mathbf{x} = (x, y, z) \in \Omega_c$
\mathbf{X}	Point in physical domain $\mathbf{X} = (X, Y, Z) \in \Omega_t$

Greek Symbols

α, β	Time varying coefficients associated with the concentration and velocity distributions employed in the Galerkin formulation
δ	Discretization unit (either finite element or grid size)
ε	Relative error criterion
Δt	Basic time step of atmospheric diffusion equation
$\Delta \tau$	Time step for solution of the chemical kinetics
Δx	Size of computational grid element
ΔH	$= H(X, Y, t) - h(X, Y)$

θ	Volume to width ratio for test wave forms or angular coordinate
λ	An arbitrary parameter with $\lambda \geq 0$
λ_i	Eigenvalue of Jacobian matrix \mathbf{J} , $i = 1, 2, \dots, p$
σ	Normal direction to $\partial\Omega$
\mathbf{v}	Material flux = $\mathbf{K}_{xx}(\partial\mathbf{c}/\partial x) - \mathbf{U}\mathbf{c}$
ϕ_j	Basis functions for Galerkin formulation
ψ_j	Filter function variable (0, 1)
ω	Fourier frequency for test wave forms and angular velocity for Crowley problem
Ω_c	Time invariant computational domain
Ω_t	Time varying physical domain (Ω_0 initial extent)
$\partial\Omega$	Domain boundary

Sub- and Superscripts

a	Advective transport step
c	Indicates computational domain
d	Diffusive transport step or nonstiff component of concentration vector
e	Grid point subscript for testing sign changes during filter application
i	Species index
j	Index to denote coordinate direction ($x = 1, y = 2, z = 3$) or computational grid point ($j = 1, 2, \dots, r$)
k	Iteration counter during one time step
l	Domain of final filter application (number of grid points)
m	Half width of enveloping interval for testing slope change in filtering scheme
n	Time level
o	Initial conditions
p	Number of chemical species
q	Spatial integration index for Galerkin formulation
r	Number of computational grid points
s	Spatial integration index for Galerkin formulation or stiff component of concentration vector

ACKNOWLEDGMENTS

This work was supported by the State of California Air Resources Board under Contracts A5-046-87 and A7-187-30. Additional funding was provided by a Department of Energy Institutional Grant EY-76-G-03-1305. The assistance of Dr. T. R. Young of the Naval Research Laboratory, and Dr. J. W. Tilden of the Environmental Quality Laboratory is appreciated.

REFERENCES

1. J. H. SEINFELD, "Air Pollution: Physical and Chemical Fundamentals," McGraw-Hill, New York, 1975.
2. W. R. GOODIN, G. J. MCRAE, AND J. H. SEINFELD, *J. Appl. Meteorol.* 18 (1979a), 761.

3. W. R. GOODIN, G. J. MCRAE, AND J. H. SEINFELD, *J. Appl. Meteorol.* **19** (1979b), 98.
4. W. R. GOODIN, G. J. MCRAE, AND J. H. SEINFELD, *J. Appl. Meteorol.* **20** (1981), 92.
5. S. D. REYNOLDS, P. M. ROTH, AND J. H. SEINFELD, *Atmospheric Environment* **7** (1973), 1033.
6. A. H. FALLS AND J. H. SEINFELD, *Environ. Sci. Technol.* **12** (1978), 1398.
7. T. GAL-CHEN AND R. C. SOMERVILLE, *J. Comput. Phys.* **17** (1975), 209.
8. T. L. CLARK, *J. Comput. Phys.* **24** (1977), 186.
9. P. J. ROACHE, "Computational Fluid Dynamics," Second ed., Hermosa Publications, Albuquerque, 1976.
10. J. L. ANDERSON, S. PREISER, AND E. L. RUBIN, *J. Comput. Phys.* **2** (1968), 279.
11. W. L. OBERKAMPF, *Int. J. Numer. Methods Engrg.* **10** (1976), 211.
12. M. VINOKUR, *J. Comput. Phys.* **14** (1974), 105.
13. A. LAPIDUS, *J. Comput. Phys.* **2** (1967), 154.
14. S. B. MARGOLIS, *J. Comput. Phys.* **27** (1978), 410.
15. R. C. Y. CHIN AND R. L. BRAUN, *J. Comput. Phys.* **34** (1980), 74.
16. B. ENGQUIST, B. GUSTAFSSON, AND J. VREEBURG, *J. Comput. Phys.* **27** (1978), 295.
17. J. DOUGLAS, T. DUPONT, AND R. EWING, *SIAM J. Numer. Anal.* **16** (1979), 503.
18. E. J. KANSA, *J. Comput. Phys.* **42** (1981), 152.
19. J. DESCLOUX, *SIAM J. Numer. Anal.* **9** (1972), 260.
20. A. ISERLES, *SIAM J. Numer. Anal.* **18** (1981), 1.
21. A. W. RIZZI AND H. E. BAILEY, *AIAA J.* **14** (1976), 621.
22. A. W. RIZZI AND M. INOUE, *AIAA J.* **11** (1973), 1478.
23. R. J. KEE AND J. A. MILLER, *AIAA J.* **16** (1978), 169.
24. P. D. THOMAS AND K. H. WILSON, *AIAA J.* **14** (1976), 629.
25. J. DOUGLAS AND J. E. GUNN, *Numer. Math.* **6** (1964), 428.
26. J. E. DENDY, *SIAM J. Numer. Anal.* **14** (1977), 313.
27. W. R. BRILEY AND H. McDONALD, *J. Comput. Phys.* **34** (1980), 54.
28. T. J. WEARE, *Int. J. Numer. Methods Engrg.* **14** (1979), 921.
29. N. N. YANENKO, "The Method of Fractional Steps," Springer-Verlag, New York, 1971.
30. G. I. MARCHUK, in "Numerical Solution of Partial Differential Equations, II," Academic Press, New York, 1971.
31. G. I. MARCHUK, "Methods of Numerical Mathematics," Springer-Verlag, New York, 1975.
32. N. N. YANENKO, V. M. KOVENYA, V. D. LISEIKIN, V. M. FOMIN, AND E. V. VOROZHTSOV, *Comput. Methods Appl. Mech. Engrg.* **17** (1979), 659.
33. J. L. MORRIS, *J. Comput. Phys.* **5** (1970), 219.
34. A. R. GOURLAY AND A. R. MITCHELL, *SIAM J. Numer. Anal.* **6** (1969), 37.
35. A. R. GOURLAY, *Proc. Roy. Soc. London Ser. A* **323** (1971), 219.
36. D. GOTTLIEB, *SIAM J. Numer. Anal.* **9** (1972), 650.
37. M. CRANDALL AND A. MAJDA, *Numer. Math.* **34** (1980), 285.
38. E. S. ORAN AND J. P. BORIS, *Prog. Energy Combustion Sci.* **7** (1981), i.
39. D. ANDERSON AND B. FATAHI, *J. Atmospheric Sci.* **31** (1974), 1500.
40. C. Y. LIU, W. R. GOODIN, AND C. M. LAM, *Comput. Methods Appl. Mech. Engrg.* **9** (1976), 281.
41. G. R. CARMICHAEL, T. KITADA, AND L. K. PETERS, *Computers and Fluids* **8** (1980), 155.
42. J. P. BORIS AND D. L. BOOK, *J. Comput. Phys.* **11** (1973), 38.
43. J. P. BORIS AND D. L. BOOK, *J. Comput. Phys.* **20** (1976), 397.
44. D. L. BOOK, J. P. BORIS, AND K. HAIN, *J. Comput. Phys.* **18** (1975), 248.
45. Y. ADAM, *Comput. Math. Appl.* **1** (1975), 393.
46. Y. ADAM, *J. Comput. Phys.* **24** (1977), 24.
47. R. S. HIRSH, *J. Comput. Phys.* **19** (1975), 90.
48. F. THIELE, *J. Comput. Phys.* **27** (1978), 1.
49. M. CIMENT AND S. H. LEVENTHAL, *Math. Comp.* **32** (1978), 143.
50. M. CIMENT, S. H. LEVENTHAL, AND B. C. WEINBERG, *J. Comput. Phys.* **28** (1978), 135.
51. J. J. CONNOR AND C. A. BREBBIA, "Finite Element Techniques for Fluid Flow," Butterworth, London, 1976.

52. G. STRANG AND G. J. FIX, "An Analysis of the Finite Element Method," Prentice-Hall, Engelwood Cliffs, N.J.
53. K. W. MORTON AND A. K. PARROTT, *J. Comput. Phys.* **36** (1980), 249.
54. J. E. FROMM, *J. Comput. Phys.* **3** (1968), 176.
55. W. P. CROWLEY, *Monthly Weather Rev.* **96** (1968), 1.
56. H. S. PRICE, R. S. VARGA, AND J. E. WARREN, *J. Math. Phys.* **45** (1966), 301.
57. H. KREISS AND J. OLIGER, "Methods for the Approximation Solution of Time Dependent Problems," GARP Publication Series No. 10, World Meteorological Organization.
58. H. J. P. CULLEN, *Quart. J. Roy. Meteorol. Soc.* **102** (1976), 77.
59. H. STORCH, *Beiträge Phys. Atmosphäre* **51** (1978), 189.
60. W. H. RAYMOND AND A. GARDNER, *Monthly Weather Rev.* **104** (1976), 1583.
61. L. B. WAHLBIN, in "Mathematical Aspects of Finite Elements in Partial Differential Equations," Academic Press, New York, 1974.
62. J. D. MAHLMAN AND R. W. SINCLAIR, "Advances in Environmental Science and Technology," Vol. 8, Wiley, New York, 1977.
63. B. VAN LEER, *J. Comput. Phys.* **14** (1974), 361.
64. C. K. FORESTER, *J. Comput. Phys.* **23** (1977), 1.
65. C. R. MOLENKAMP, *J. Appl. Meteorol.* **7** (1968), 160.
66. T. NITTA, *J. Meteorol. Soc. Japan* **40** (1962), 13.
67. J. M. VARAH, *SIAM J. Numer. Anal.* **8** (1971), 569.
68. J. M. VARAH, *SIAM J. Numer. Anal.* **8** (1971), 598.
69. J. H. CHEN, *J. Comput. Phys.* **13** (1973), 522.
70. B. GUSTAFSSON, H. O. KREISS, AND A. SUNDSTROM, *Math. Comp.* **26** (1972), 649.
71. B. GUSTAFSSON, *J. Comput. Phys.* **34** (1980), 108.
72. D. GOTTLIEB AND E. TURKEL, *J. Comput. Phys.* **26** (1978), 181.
73. D. M. SLOAN, *Int. J. Numer. Methods Engrg.* **15** (1980), 1113.
74. R. A. WILLOUGHBY, "Stiff Differential Systems," Plenum, New York, 1974.
75. J. D. LAMBERT, in "Computational Techniques for Ordinary Differential Equations," Academic Press, London, 1976.
76. D. D. WARNER, *J. Phys. Chem.* **81** (1977), 2329.
77. A. R. CURTIS, in "Numerical Software—Needs and Availability," Academic Press, London, 1978.
78. H. O. KREISS, *SIAM J. Numer. Anal.* **16** (1979), 980.
79. L. F. SHAMPINE AND C. W. GEAR, *SIAM Rev.* **21** (1979), 1.
80. A. C. HINDMARSH AND G. D. BYRNE, "EPISODE: An Experimental Program for the Integration of Systems of Ordinary Differential Equation Systems," Lawrence Livermore Laboratory Report UCID-30112, 1975.
81. G. D. BYRNE, A. C. HINDMARSH, K. R. JACKSON, AND H. G. BROWN, *Comput. Chem. Engrng.* **1** (1977), 133.
82. R. C. AIKEN AND L. LAPIDUS, *AIChE J.* **21** (1975a), 817.
83. R. C. AIKEN AND L. LAPIDUS, *AIChE J.* **21** (1975b), 1227.
84. P. V. KOKOTOVIC, J. J. ALLEMONG, J. R. WINKELMAN, AND J. H. CHOW, *Automatica* **16** (1980), 23.
85. H. H. ROBERTSON, *J. Inst. Math. Appl.* **18** (1976), 249.
86. W. H. ENRIGHT AND M. S. KAMEL, *ACM Trans. Math. Software* **5** (1979), 374.
87. D. S. WATKINS, *SIAM J. Numer. Anal.* **18** (1981), 13.
88. J. D. LAMBERT, *SIAM J. Numer. Anal.* **18** (1981), 83.
89. T. R. YOUNG, "CHEMEQ—A Subroutine for Solving Stiff Ordinary Differential Equations," NRL Memorandum Report 4091, Naval Research Laboratory, Washington, D.C. (1980).
90. T. R. YOUNG AND J. P. BORIS, *J. Phys. Chem.* **81** (1977), 2424.
91. G. J. MCRAE, W. R. GOODIN, AND J. H. SEINFELD, *Atmospheric Environment*, in press.

CHAPTER 10
SENSITIVITY AND UNCERTAINTY ANALYSIS OF
URBAN SCALE AIR POLLUTION MODELS

10.1 Introduction

When complex systems are described by mathematical models a natural question arises: what are the influences of uncertainties in the characterization of physical processes? While a variety of means can be employed to answer the question considerable insight can often be gained from formal studies of the effects of parameter variations. Such sensitivity analyses can provide a direct means for revealing how the predictions vary as a result of changes in model or input variables. Information derived from these investigations is useful for defining limits of valid applications and identifying those areas which might require additional development work.

This chapter presents a technique, the Fourier Amplitude Sensitivity Test (FAST), which can be used to assess the relative influence of parameter variations on the model predictions. A major advantage of this procedure is that, unlike conventional methods, it readily accommodates arbitrarily large variations in the parameters. This feature is exploited in two practical applications. One example involves a combined sensitivity/uncertainty analysis of a photochemical reaction mechanism for the polluted troposphere and the other, a study of a simplified form of the atmospheric diffusion equation. Both cases, and a description of the computational procedure, have been previously published as Koda et al. (1979b), Falls et al. (1979) and McRae and Tilden (1980); these articles form sections of this chapter.

10.2 Methods for Sensitivity Analysis of Mathematical Models

An inevitable consequence of using mathematical models to describe complex systems is that some approximations are involved. These uncertainties arise either from the characterization of the physical processes or from the measurement errors inherent in model input variables. Leaving aside the conceptual question of model validity, the essential problem in sensitivity analysis is to examine the changes in system outputs which result from variations in either the input or structural parameters. This section presents a brief literature survey of different sensitivity analysis methods. While some of the techniques are well known in control theory (Cruz, 1973; Tomovic, 1963; Tomovic and Vucobratovic, 1972; and Frank, 1978) they have not, as yet, been extensively employed in atmospheric modeling. Gelinas and Vajk (1978) have, however, examined the suitability of some methods for air quality applications.

In order to provide a framework for the survey consider a general system of the form

$$F(\underline{u}, \underline{k}) = 0 \quad (10.1)$$

where F is a general algebraic or differential operator, \underline{u} is a vector of n output variables and \underline{k} a set of m parameters. Given such a model there are four basic factors which need to be considered when selecting a method or an approach for performing a sensitivity analysis of a model system. The issues are: the extent of the parameter domain, the sensitivity measure or criterion, the combined roles of parameter sensitivity and uncertainty, and finally, the computational cost.

From a practical point of view a dominant consideration in selecting a sensitivity analysis method is the computational cost. When comparing different techniques it is important to keep in mind two basic considerations: one is simply the number of times that the model must be solved to obtain the desired sensitivity information. The second factor is the amount of time required to implement the particular technique. In many situations it is this latter factor which has a major influence on the selection process. For example some techniques do not require extensive programming beyond that needed to solve the basic model while others can require considerable additional effort on the part of the investigator. While the cost of each method can be expressed in terms of the number of required solutions the final choice will often be dictated by the complexity of the basic system being analysed. Gelinas and Vajk (1978) have carried out an extensive study of the expected cost of applying different sensitivity analysis methods to some different mathematical models of environmental processes.

Perhaps the most fundamental constraint which dictates the choice of a sensitivity analysis method is the extent of parameter variations to be considered. All the feasible values of the parameter vector \underline{k} define the parameter space. Varying the parameters over their full domain produces the m -dimensional surface $\underline{u}(\underline{k})$. A typical example is depicted in Figure 10.1 where the response of one model output, $u_i(t)$, to variations in \underline{k} , is shown. In this case the extent of parameter space is defined by the upper and lower limits for each of the variables k_1 and k_2 . The point Q on the solution surface represents the magnitude of u_i

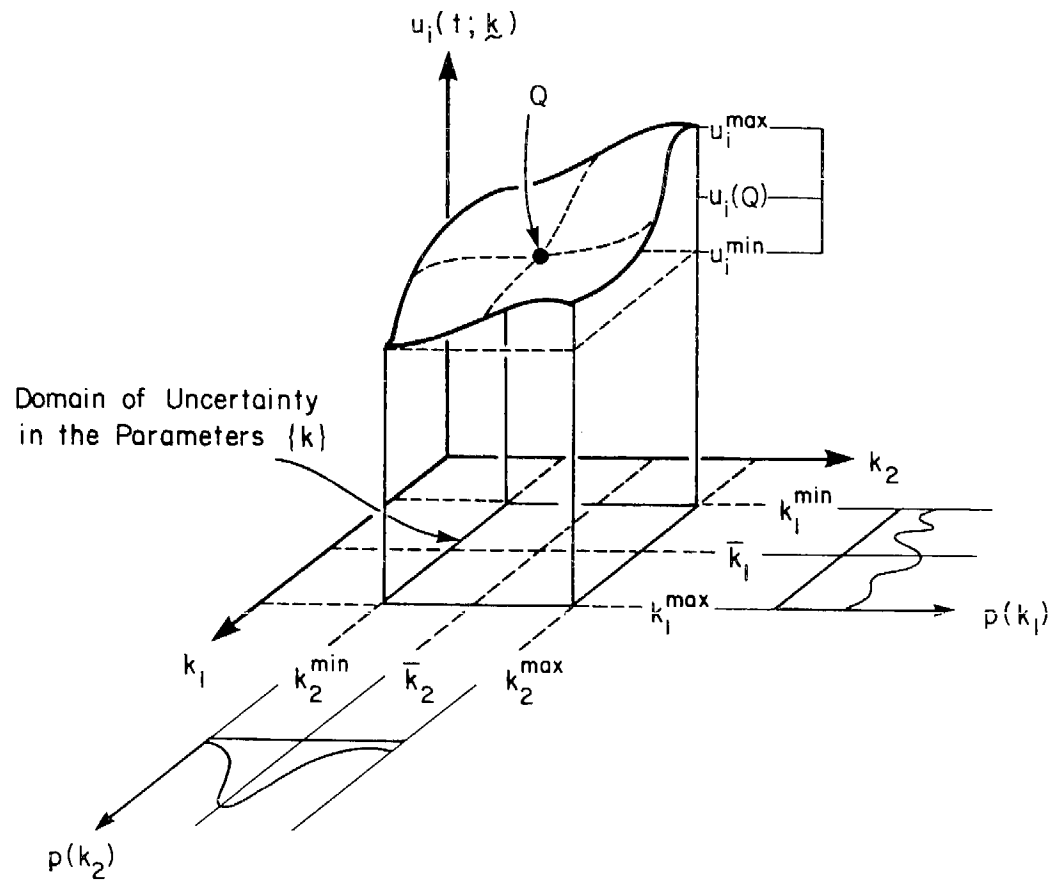


FIGURE 10.1

Schematic Representation of the Parameter Space k and the Response Surface for State Variable $u_i(t; \tilde{k})$

resulting from the parameter combination (\bar{k}_1, \bar{k}_2) . These nominal values typically represent the best a priori estimates of the parameters.

The ultimate goal of any sensitivity analysis is to determine the form of the system output resulting from the parameter variations. Since most models will require numerical solution, the outputs needed to define the response surface will only be available for a finite set of parameter combinations. Given this situation the basic problem then becomes how to sample the parameter space with sufficient regularity to adequately characterize $u(\underline{k})$. An analysis which accounts for simultaneous variations in all the parameters over their full range of uncertainties is called a global method. Conversely, local analyses attempt to infer the shape or value of the response surface at a particular point. The limitations of local approaches are readily apparent, particularly if the model is highly nonlinear or the range of parameter variations is large. A typical case is shown in Figure 10.2. For small variations in \bar{k} the tangent plane approximation differs from the actual surface by only a small amount. Unfortunately this simplification does not contain useful information on the behavior of a u away from \bar{k} . This example highlights a critical limitation of local methods when they are applied to problems which involve large uncertainties in the parameters. For example, a variable to which the model predictions are not especially sensitive at say \bar{k} , may have such a large range of uncertainty that, when all possible variations are considered, its influence on the results may be quite large. Information of this type is very useful in the design of experimental programs because more effort can be devoted to elucidating

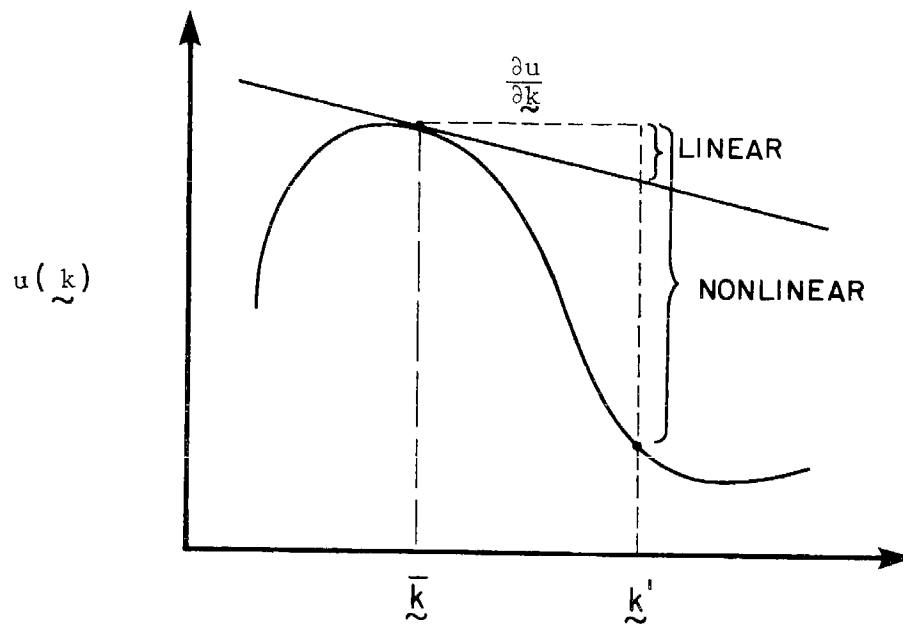


FIGURE 10.2
Linear and Nonlinear Sensitivity Analysis

the important phenomena and eliminating potentially unproductive measurements.

So far in the discussion all values of \underline{k} have been considered to be equally likely; however, in practice, the parameters often have non-uniform probability distributions. While the response surface, $u(\underline{k})$, is independent of all assumptions about the likely parameter combinations, the expected value or mean sensitivity, $\langle u(\underline{k}) \rangle$, depends on both the probability distribution for \underline{k} and the form of the model. A sensitivity analysis then refers to the influence of parameter variations on the model predictions whereas a combined sensitivity/uncertainty analysis considers the additional factor of the parameter distributions. Regardless of refinements in knowledge of parameter accuracy the global sensitivity of the model remains the same. In Figure 10.1 the probability distributions associated with k_1 and k_2 are independent and denoted by $p(k_1)$ and $p(k_2)$. By considering \underline{k} to be a random vector with probability density $P(\underline{k})$ the ensemble mean sensitivity can be expressed in the form

$$\langle u_i(\underline{k}) \rangle = \int \dots \int u_i(k_1, \dots, k_m) P(k_1, \dots, k_m) dk_1, \dots, dk_m \quad (10.2)$$

\underline{k}

In general (12.2) does not correspond to the solution obtained when the parameters are set to their nominal values $\bar{\underline{k}}$. A variety of other sensitivity measures are available for assessing the system performance. Some of the more common criteria are listed below and in Table 10.1; further details can be found in Frank (1978). Perhaps the most elementary criterion is the change in system output, $\delta \underline{u}$, which results from an arbitrary variation, $\delta \underline{k}$, in the parameters away from some nominal value $\bar{\underline{k}}$ i.e.

TABLE 10.1
Summary of Sensitivity Measures

SENSITIVITY MEASURE	DEFINITION
Response from arbitrary parameter variation \underline{k}	$\underline{u} = \underline{u}(\underline{\bar{k}} + \delta \underline{k}) - \underline{u}(\underline{k})$
Normalized Response	$D_i = \frac{\delta u_i}{u_i(\underline{\bar{k}})} ; \quad i=1,2,\dots,n$
Local Gradient Approximation	$\delta \underline{u} \approx [S] \delta \underline{k} ; \quad S_{ij} = \frac{\partial u_i}{\partial k_j}$
Normalized Gradient	$S_{ij}^n = \frac{\bar{k}_j}{u_i(\underline{\bar{k}})} \frac{\partial u_i}{\partial k_j}$
Average Response	$\underline{u}_i(\underline{\bar{k}}) = \frac{\int \dots \int u_i(\underline{\bar{k}}) d\underline{k}}{\int \dots \int d\underline{k}}$
Expected Value	$\langle u_i(\underline{k}) \rangle = \int \dots \int u_i(\underline{k}) P(\underline{k}) d\underline{k}$
Variance	$\delta_i^2(\underline{k}) = \langle u_i(\underline{k})^2 \rangle - \langle u_i(\underline{k}) \rangle^2$
Extrema	$\max [u_i(\underline{k})], \quad \min [u_i(\underline{k})]$

$$\delta \underline{u} = \underline{u}(\underline{\bar{k}} + \delta \underline{k}) - \underline{u}(\underline{\bar{k}}) \quad (10.3)$$

This difference measure is often expressed in the normalized form

$$D_i = \frac{\delta u_i}{u_i(\underline{\bar{k}})} = \frac{u_i(\underline{\bar{k}} + \delta \underline{k})}{u_i(\underline{\bar{k}})} - 1 \quad (10.4)$$

If the parameters are varied one at a time then (10.4) is given by

$$D_{ij} = D_i(\delta k_j) = \frac{u_i(\underline{\bar{k}} + \delta k_j)}{u_i(\underline{\bar{k}})} - 1 \quad (10.5)$$

Both of these criteria are essentially point estimates. If a sufficiently large number of \underline{k} combinations are considered then it is possible to develop estimates of some of the important response statistics, namely: the mean, variance and extrema of $\underline{u}(\underline{k})$. The extreme values are often of critical importance in environmental applications. In the interests of computational economy it is desirable to obtain as much information as possible from each parameter combination. One means is to extrapolate the results away from the nominal solution $\underline{u}(\underline{\bar{k}})$. A wide class of methods can be represented by the form

$$\delta \underline{u} \approx [\underline{S}] \delta \underline{k} \quad (10.6)$$

The most simple case corresponds to the well known Taylor series expansion for which the elements of the matrix $[\underline{S}]$ are given by

$$S_{ij} = \frac{\partial u_i}{\partial k_j} \quad ; \quad i=1,2,\dots,n \quad j=1,2,\dots,m \quad (10.7)$$

Equation (10.7) is often written in the normalized form

$$S_{ij}^n = \frac{\partial \ln(u_i)}{\partial \ln(k_j)} = \frac{\bar{k}_j}{u_i(\bar{k})} \frac{\partial u_i}{\partial k_j} \quad (10.8)$$

Methods which neglect the higher order terms in the expansion are referred to as first order or linear techniques. In space and time dependent models the linear sensitivities are more appropriately defined in terms of operator or Frechet derivatives.* These derivatives are linear continuous and have the usual properties of the classical differentials of functions of one or more variables. In particular the chain rule holds (Nashed, 1971). This latter result is extremely useful in practical applications.

Once the basic model has been formulated and an appropriate sensitivity measure identified the next step is to actually solve the sensitivity problem. As noted previously there are two basic approaches: local or global techniques. In order to illustrate how local methods

* Consider a mapping $F:X \rightarrow Y$ where both X and Y are complete, normed linear spaces. Given that $x \in X$, then if a bounded linear map, F' , exists such that

$$\lim_{\|h\| \rightarrow 0} \frac{\|F(x+h) - F(x) - F'(x)h\|_Y}{\|h\|_X} = 0$$

then F is said to be Frechet differentiable at \underline{x} and $F'(\underline{x})$ is the Frechet derivative of F at \underline{x} . Under certain conditions the continuous, linear operator $F'(\underline{x})$ is represented by the Jacobian matrix at \underline{x} (Dieudonné, 1960; Tapia, 1971).

are applied, consider the following set of ordinary differential equations and initial conditions.

$$F(\underline{u}, \underline{k}) \equiv \frac{d\underline{u}}{dt} - \underline{f}(\underline{u}, \underline{k}) = 0 \quad (10.9)$$

$$\underline{u}(0) = \underline{u}^0 \quad (10.10)$$

A very wide class of practical problems can be described by systems of the form (10.9-10). The change in \underline{u} away from some nominal parameter values $\bar{\underline{k}}$ can be expressed, using operator derivatives in the form

$$\frac{d}{dt} \left(\frac{\partial \underline{u}}{\partial \underline{k}} \right) - \frac{\partial \underline{f}}{\partial \underline{u}} \left(\frac{\partial \underline{u}}{\partial \underline{k}} \right) - \frac{\partial \underline{f}}{\partial \underline{k}} = 0 \quad (10.11)$$

or more compactly as the matrix differential equation

$$\dot{[Z]} = [J][Z] + [B] \quad (10.12)$$

where

$$Z_{ij} = \frac{\partial u_i}{\partial k_j} \quad \begin{array}{l} i=1,2,\dots,n \\ j=1,2,\dots,m \end{array} \quad (10.13)$$

$$J_{ij} = \frac{\partial f_i}{\partial u_j} \bigg|_{f_i[\underline{u}(\bar{\underline{k}}), \bar{\underline{k}}]} \quad \begin{array}{l} i=1,2,\dots,n \\ j=1,2,\dots,n \end{array} \quad (10.14)$$

$$B_{ij} = \frac{\partial f_i}{\partial k_j} \bigg|_{f_i[\underline{u}(\bar{\underline{k}}), \bar{\underline{k}}]} \quad \begin{array}{l} i=1,2,\dots,n \\ j=1,2,\dots,m \end{array} \quad (10.15)$$

A typical column of $[Z]$, defined by $\partial u_i / \partial k_j$; $i=1,2,\dots,n$, denotes the sensitivity of \underline{u} with respect to the j th parameter. The initial conditions for (10.12) are given by $[Z(0)] = [0]$ unless any $u_i(0)$ are included in $\bar{\underline{k}}$

in which case the appropriate elements of $[Z]$ are set to one. Because there is no direct coupling in (10.12) each of the m vector differential equations can be solved independently.

There is a variety of ways to obtain the desired sensitivity information. The simplest involves a direct solution of the coupled systems of $n(m+1)$ ordinary differential equations (10.9-10 and 10.12). This method was used by Dickinson and Gelinas (1976) and Atherton et al. (1975). Operationally it is sometimes more convenient to consider the parameters one at a time; if this is done then the number of required solutions increases to $2nm$. This number can be reduced, at some loss of numerical accuracy, to $n(m+1)$ if the nominal solution $u(\bar{k}, t_p)$, $p=1,2,\dots$ are retained and used for constructing interpolated approximations to the $u(k, t)$ needed in the evaluation of (10.14 and 10.15). While the three approaches produce similar results they can involve considerably different computational costs: $O[n^3(m+1)^3]$ for the coupled system, $O[m(2n)^3]$ for the one parameter at a time case and $O[(m+1)n^3]$ for the interpolated solution. Since the equations of interest are usually stiff, and $m(>n)$ is in general quite large, the above procedures can be quite expensive. Another approach, which is the focus of work by Hwang et al. (1978), Dougherty et al. (1979) and Hwang and Rabitz (1979), is to make use of the associated Green's function matrix.

An $n \times n$ Green's function matrix $[K(t, \tau)]$ can be constructed which satisfies

$$\frac{d}{dt} [K(t, \tau)] - [J][K(t, \tau)] = [0] \quad ; \quad t > \tau \quad (10.16)$$

with

$$[K(t,t)] = I \quad (10.17)$$

The sensitivity information is then given by the following set of integrals (Hwang et al., 1978)

$$[Z(t)] = [K(t,0)][Z(0)] + \int_0^t [K(t,\tau)][B(\tau)]d\tau \quad (10.18)$$

In practice $[K]$ is determined by first solving (10.9-10) to obtain $\underline{u}(\underline{k}, t_p)$ $p=1,2,\dots$, at an adequate number of grid points so that $[J(t)]$ can be determined by interpolation. Operationally it is more convenient to solve the adjoint system (10.19-20) backwards in time.

$$\frac{d[K^*(\tau,t)]}{d\tau} + [K^*(\tau,t)][J(\tau)] = [0] ; \tau < t \quad (10.19)$$

$$[K^*(\tau,\tau)] = I \quad (10.20)$$

with

$$[K^*(\tau,t)] = [K(t,\tau)] \quad (10.21)$$

The major advantage of the adjoint formulation is that the sensitivity integrals (10.18) can be more easily evaluated row by row as functions of τ at a fixed time t . Another good feature of the Green's function approach is that the calculations needed to evaluate $\underline{u}(\underline{k}, t_p)$ and $[K^*(\tau,t)]$ are independent of the number of parameters m . If $m > n$ this can result in a very large savings in computational time over the direct methods.

In passing it is important to emphasize that the procedure produces a local approximation to the system sensitivity $\underline{u}(\underline{k})$. Section 10.3 presents a procedure valid for global analyses.

The remaining class of methods are global sensitivity analysis techniques in which the major concern is to characterize the response surface $\underline{u}(\underline{k})$ over the full range of parameter variations. In carrying out such analyses, the basic consideration to keep in mind is to minimize the number of model solutions. Conceptually the simplest approach is to solve the system repeatedly, varying one parameter at a time. Without careful prescreening this "brute force" approach can become prohibitively expensive. For example consider a model system of m parameters and r different values for each k_j . The systematic evaluation would require $O(m^r)$ solutions and even relatively small values of m could render the procedure impractical. The key to a successful global sensitivity method is then to devise an economical means for sampling the parameter space. Similar problems arise in locating starting points for optimization algorithms or in the evaluation of multi-dimensional integrals.

Perhaps the most well known sampling procedure is the Monte-Carlo method. In this procedure the parameter combinations are selected at random. A random number generator is used to select values of the parameters from the \underline{k} space which are then used to evaluate $\underline{u}(\underline{k})$. What is often not realized is that the value of Monte-Carlo methods is not the randomness of the sampling but the resulting equidistribution properties of the sets of points in the parameter space. Once it is recognized that the main goal of a Monte-Carlo procedure is to produce a uniform distribution of points in the parameter space, then pattern search methods

become a viable global sensitivity method. The brute force method for distributing points is far from optimal. Consider the two-dimensional cases shown in Figure 10.3 which correspond to $N=16$, $r=4$, and $m=2$. If $u(k_1, k_2)$ depends strongly on one of the variables the first distribution (Figure 10.3a) yields only 4 essentially different values each repeated four times while the second set produces 16 values of either $u_i(k_1)$ or $u_i(k_2)$. An algorithm which generates sequences of points that uniformly fill the parameter space is described in Sobol (1979). Aird and Rice (1977) compared two systematic search procedures with the standard random assignment technique and found that the pattern methods consistently performed better than the Monte-Carlo procedure. Unfortunately pattern and Monte-Carlo methods are not well suited to non-rectangular parameter spaces because of difficulties associated with locating points inside the boundaries.

One major advantage of the Monte-Carlo procedure is that it can be readily adapted to situations in which one or more of the parameters have known distributions. Stolarski et al. (1978) used a Monte-Carlo procedure to study the propagation of reaction rate uncertainties in the stratospheric ozone depletion model of Rundel et al. (1978). The uncertain rate constants were assumed to be lognormally distributed about the mean measured values. The computational procedure adopted in their work was to continue to sample from the parameter space until the model output statistics stabilized. For the criteria established by Stolarski et al. (1978) 2000 separate combinations were required to assess the effects of fifty-five parameters. Freeze (1975) used a similar approach in a study of two ground water flow problems and in addition considered the

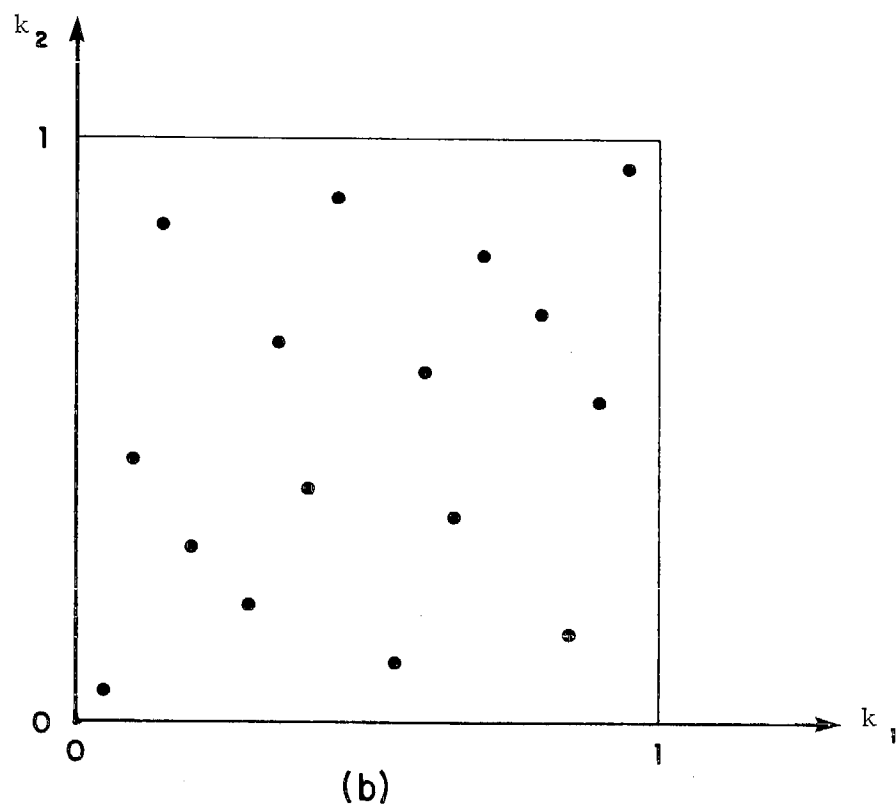
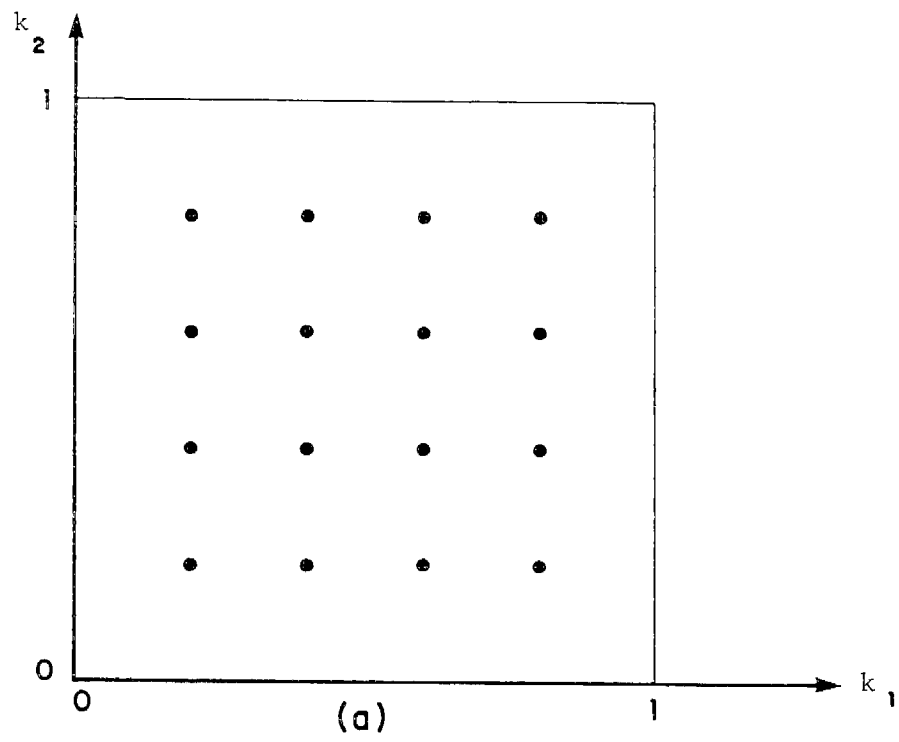


FIGURE 10.3

Systematic Search Patterns of Parameter Space

effects of parameter coupling by using multivariate distributions. Both studies encountered the problem of developing a priori estimates of the number of trials required to produce stable results.

An alternative method for global sensitivity analyses, and the focus of Section 10.3, is the Fourier Amplitude Sensitivity Test (FAST) introduced by Cukier et al. (1973). The essence of this procedure is to assign periodic functions of a new variable, s , to each of the parameters. Under certain conditions each new value of s defines a unique parameter combination $\underline{k}(s)$, along a search curve which can be made to pass arbitrarily close to any point in the \underline{k} space (Weyl, 1938). By sampling $\underline{u}(\underline{k})$ along the search curve and performing a discrete Fourier analysis it is possible to determine the contribution of individual parameters to the global sensitivity of the model (Beauchamp and Yuen, 1979).

In this section the basic issues involved in selecting sensitivity analysis methods have been discussed. Since for some of the techniques there is an extensive literature Figures 10.4 and 10.5 summarize the results of a survey directed at identifying representative treatments of local and global methods. For details of particular applications the reader is referred to the original papers. Subsequent sections of this chapter are directed at developing and applying global methods to components of the atmospheric diffusion equation.

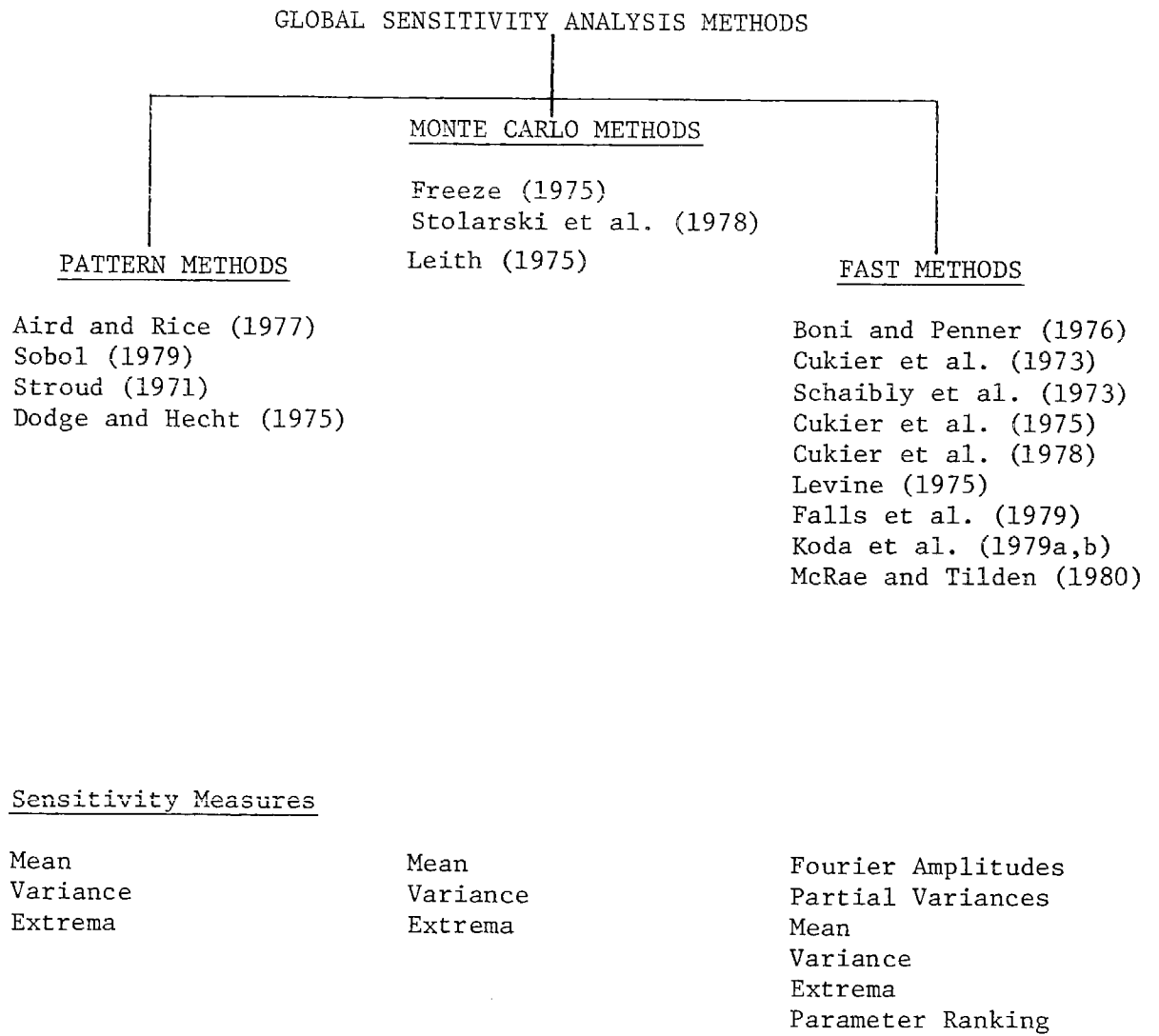


FIGURE 10.4
Survey of Global Sensitivity Analysis Methods

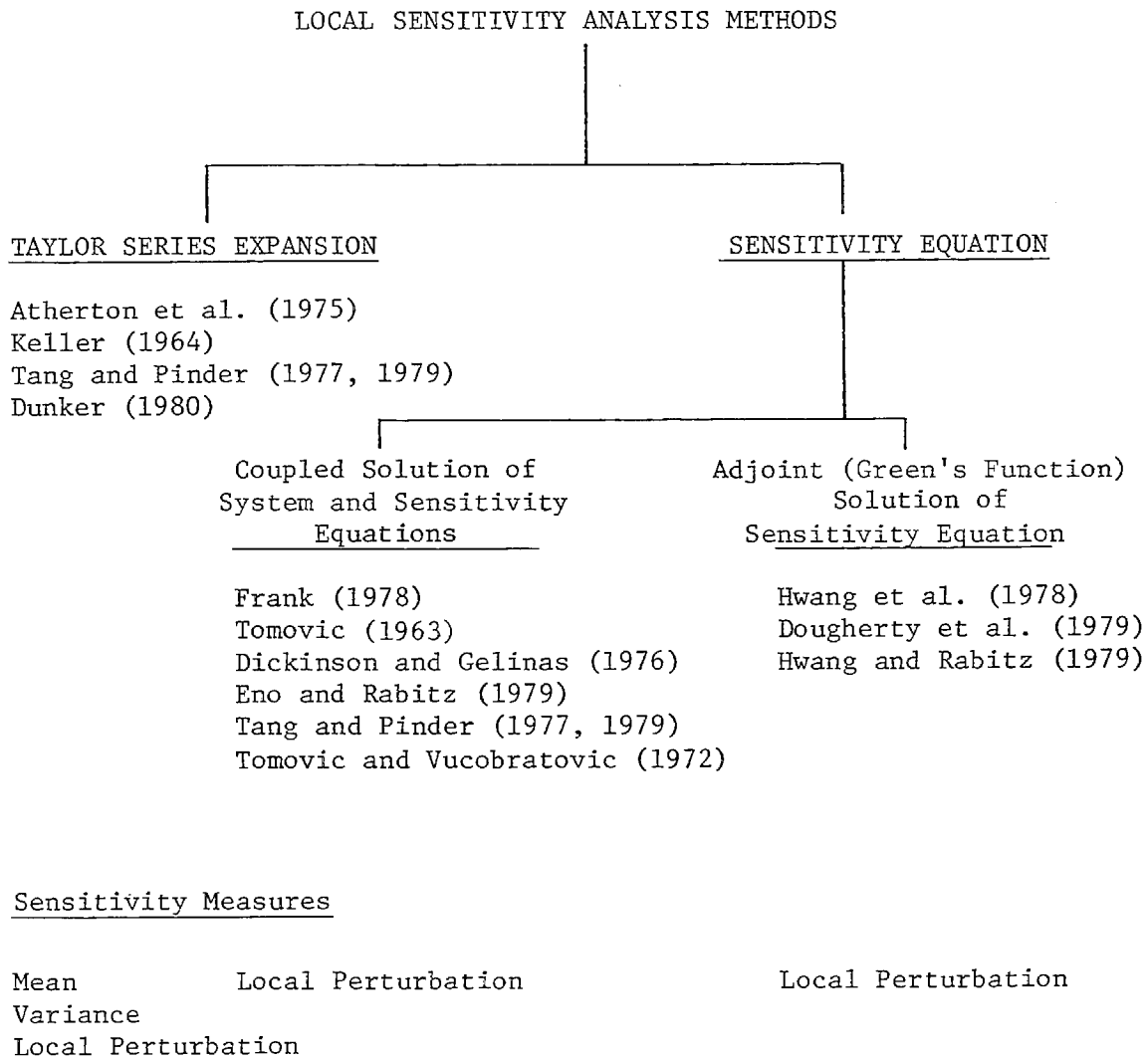


FIGURE 10.5
Survey of Local Sensitivity Analysis Methods

10.3 Automatic Sensitivity Analysis of Kinetic Mechanisms

(Reprinted from Int. Journal of Chemical Kinetics, 11, 427-444.)

Automatic Sensitivity Analysis of Kinetic Mechanisms

MASATO KODA, GREGORY J. MCRAE, and JOHN H. SEINFELD

Department of Chemical Engineering, California Institute of Technology, Pasadena, California 91125

Abstract

An algorithm for the automatic sensitivity analysis of kinetic mechanisms based on the Fourier amplitude sensitivity test (FAST) method of Shuler and co-workers is reported. The algorithm computes a measure of the relative sensitivity of each concentration to each parameter of interest, such as rate constants, Arrhenius parameters, stoichiometric coefficients, and initial concentrations. Arbitrary variations in the magnitude of the parameters are allowable. The algorithm is illustrated for the simple example of computing the sensitivity of the concentration of species A to variation of the two Arrhenius parameters for the hypothetical reaction $A + A \rightarrow$.

Introduction

A variety of chemical phenomena are described by lengthy and complex reaction mechanisms. It is often desirable to determine the effect of uncertainties in rate constants and other parameters on the predictions of the mechanism and to ascertain which parameters are most influential. When a measure of the sensitivity of the concentrations to variations of a parameter is combined in an appropriate manner with a measure of the degree of uncertainty in the parameter's value, one may then determine which parameters, through both their sensitivity and uncertainty, have the most influence on the predicted concentrations.

Conceptually the simplest approach to a sensitivity analysis is to solve the system repeatedly while varying one parameter at a time and holding the others fixed. This type of analysis soon becomes impractical as the number of parameters subject to variation increases. Most of the theories for sensitivity analysis of sets of differential equations containing parameters are linearized ones, valid strictly only for small variations of the parameter value [1]. Recently a new sensitivity analysis method has been developed by Shuler and co-workers [2-5] that is not restricted to small parameter variations. The method is particularly attractive for chemical kinetics applications because order of magnitude uncertainties in rate constant values are not uncommon.

The object of this paper is to report a computational method for the automatic sensitivity analysis of systems of differential equations based on the Fourier amplitude sensitivity test (FAST) method of Shuler and co-workers [2-5]. The computational method processes the concentration-time histories from integration of the system to produce a measure of the sensitivity of each concentration to each parameter. An arbitrary choice of the range of variation of each parameter is possible. The mathematical foundation of the FAST method has been described in detail previously [5]. Thus we present here only a concise discussion of those elements of the method necessary for the understanding and implementation of the computational algorithm. We have extended the basis of the FAST method in one respect; that is, we have developed a way to treat parameters that are constrained by a relationship of the form $H(k_1, k_2, \dots, k_m) \leq 0$. Such a constraint is important in chemical kinetics applications. Parameters in a chemical reaction mechanism are frequently related to each other. For example, the ratio of two rate constants k_i/k_j may be fixed with k_i or k_j subject to individual uncertainty. Also, if a species may decompose by two paths, the fractional occurrences of which are k_1 and k_2 , one may wish to examine the sensitivity of the mechanism's predictions to k_1 and k_2 , subject to the constraint that $k_1 + k_2 = 1$.

In the next section we summarize the key elements of the FAST method. The computation of the partial variances, the basic sensitivity measure, is then outlined, followed by a description of the practical implementation of the method. Finally, we illustrate its application in the case of a single reaction.

Mathematical Basis of the FAST Method

We consider a system described by the set of ordinary differential equations

$$(1) \quad \frac{d\mathbf{u}(t)}{dt} = \mathbf{F}(\mathbf{u}, \mathbf{k})$$

$$(2) \quad \mathbf{u}(0) = \mathbf{u}_0$$

where $\mathbf{u}(t)$ is the n -dimensional vector of state variables (concentrations) and \mathbf{k} is the m -dimensional vector of parameters (rate constants, Arrhenius parameters, stoichiometric coefficients, etc.) We assume that eq. (1) can be solved numerically subject to the initial condition of eq. (2) to give $\mathbf{u}(t)$ for any choice of \mathbf{k} .

We are interested in determining the sensitivity of each concentration u_i , $i = 1, 2, \dots, n$, to variation of each parameter k_j , $j = 1, 2, \dots, m$. We consider the parameter vector \mathbf{k} to be a random vector with probability density function $P(\mathbf{k})$. In reality the k_j are not, of course, random variables. However, their precise values are uncertain and it is advantageous to treat

them as if they were random variables with a presumed distribution for the purpose of computing the sensitivities. If the k_j are random variables, then the u_i resulting from the solution of eq. (1) are also random variables. The (ensemble) mean value of the concentration of species i at any time t is then given by

$$(3) \quad \langle u_i(t) \rangle = \int \cdots \int u_i(t; k_1, \cdots, k_m) P(k_1, \cdots, k_m) dk_1 \cdots dk_m$$

where $u_i(t; k_1, \cdots, k_m)$ denotes the solution of eq. (1). The key concept of the FAST method is to convert the m -dimensional integral of eq. (3) into an equivalent one-dimensional integral.

The method uses the transformations

$$(4) \quad k_l = G_l(\sin \omega_l s), \quad l = 1, 2, \cdots, m$$

where G_l , $l = 1, 2, \cdots, m$, are a set of known functions, ω_l , $l = 1, 2, \cdots, m$, are a set of frequencies, and s is a scalar variable. By means of this transformation variations of the m parameters are transformed into variations of the single scalar variable s . By variation of s over the range $-\infty \leq s \leq \infty$, eq. (4) traces out a space-filling curve in the m -dimensional parameter space. For a suitable choice of the G_l , which transforms the probability density $P(\mathbf{k})$ into s space, Weyl [6] demonstrated that

$$(5) \quad \bar{u}_i(t) = \lim_{T \rightarrow \infty} \frac{1}{2T} \int_{-T}^T u_i(t; k_1(s), \cdots, k_m(s)) ds$$

is identically equal to $\langle u_i(t) \rangle$ from eq. (3). Equation (5) is the fundamental expression in the FAST method for computing the mean value, variance, and other properties of the concentration u_i .

The set of frequencies $\{\omega_l\}$ should be incommensurate, in that

$$(6) \quad \sum_{l=1}^m \gamma_l \omega_l = 0$$

for an integer set $\{\gamma_l\}$ if and only if $\gamma_l = 0$, $l = 1, 2, \cdots, m$. If the frequencies $\{\omega_l\}$ are, in fact, incommensurate, the search curve in s space is space-filling in that it passes arbitrarily close to any point in the m -dimensional parameter space of \mathbf{k} . Unfortunately the set of $\{\omega_l\}$ used in actual computation cannot be truly incommensurate. As discussed by Shuler and co-workers [3-5], we select $\{\omega_l\}$ as an appropriate set of integer frequencies. The use of integer frequencies in eq. (4) implies that the parameters k_l , $l = 1, 2, \cdots, m$, are periodic in s on the finite interval $(-\pi, \pi)$, in which case eq. (5) becomes

$$(7) \quad \bar{u}_i(t) = \frac{1}{2\pi} \int_{-\pi}^{\pi} u_i(t; k_1(s), \cdots, k_m(s)) ds$$

The variance of concentration i is then

$$(8) \quad \sigma_i^2(t) = \frac{1}{2\pi} \int_{-\pi}^{\pi} u_i^2(t; k_1(s), \cdots, k_m(s)) ds - \bar{u}_i^2$$

Henceforth we will replace $\bar{u}_i(t)$ by $\langle u_i(t) \rangle$, representing the s -space average. Then $\bar{u}_i = \langle u_i \rangle$ and $\sigma_i^2 = \langle u_i^2 \rangle - \langle u_i \rangle^2$. In addition, for convenience, we will denote $u_i(t; k_1(s), \dots, k_m(s))$ by $u_i(t; s)$.

The evaluation of σ_i^2 can be carried out by using the s -space Fourier coefficients of u_i . From Parseval's theorem we have

$$(9) \quad \langle u_i^2(t) \rangle = \frac{1}{2\pi} \int_{-\pi}^{\pi} u_i^2(t; s) ds = \sum_{j=-\infty}^{\infty} \{A_j^{(i)}(t)^2 + B_j^{(i)}(t)^2\}$$

where the Fourier coefficients $A_j^{(i)}$ and $B_j^{(i)}$ are defined as

$$(10) \quad A_j^{(i)}(t) = \frac{1}{2\pi} \int_{-\pi}^{\pi} u_i(t; s) \cos js ds$$

$$(11) \quad B_j^{(i)}(t) = \frac{1}{2\pi} \int_{-\pi}^{\pi} u_i(t; s) \sin js ds$$

Thus, from eqs. (10) and (11),

$$(12) \quad \langle u_i(t) \rangle^2 = A_0^{(i)2} + B_0^{(i)2} = A_0^{(i)2}$$

Using eqs. (9)–(12) we can express the variance $\sigma_i^2(t)$ in terms of the Fourier coefficients as

$$(13) \quad \sigma_i^2(t) = 2 \sum_{j=1}^{\infty} (A_j^{(i)}(t)^2 + B_j^{(i)}(t)^2)$$

If the Fourier coefficients (10) and (11) are evaluated for the fundamental frequencies of the transformation (4) or its harmonics, that is, $j = p\omega_l$, $p = 1, 2, \dots$, the variance

$$(14) \quad \sigma_{\omega_l}(t)^2 = 2 \sum_{p=1}^{\infty} (A_{p\omega_l}^{(i)}(t)^2 + B_{p\omega_l}^{(i)}(t)^2)$$

is the part of the total variance σ_i^2 that corresponds to the variance of u_i arising from the uncertainty in the l th parameter. The ratio $S_{\omega_l}^{(i)} = \sigma_{\omega_l}^2 / \sigma_i^2$ is the so-called partial variance, which serves as the basic measure of sensitivity for the FAST method. We note that $S_{\omega_l}^{(i)}$ is a normalized sensitivity measure, so that the $S_{\omega_l}^{(i)}$ may be ordered with respect to l to indicate to which parameters concentration u_i is most sensitive.

We can now summarize the essential elements of the FAST method. The sensitivity measures are the partial variances $S_{\omega_l}^{(i)}$, $i = 1, 2, \dots, n$, $l = 1, 2, \dots, m$. The relative magnitudes of the m partial variances for each concentration reflect the relative influence of each of the m parameters on that concentration. The partial variances are calculated from the ratio of eqs. (14) and (13), the main computation involved being the evaluation of the integrals (10) and (11). To evaluate the Fourier coefficients from eqs. (10) and (11) requires that the solution of the system of eq. (1) be obtained for enough values of s so that the integrals in eqs. (10) and (11) can be calculated with sufficient accuracy. Thus, with the parameter values being

determined by eq. (4), the system of differential equations, eq. (1), is solved repeatedly for each value of s needed to calculate the Fourier coefficients in eqs. (10) and (11). Therefore the FAST method only requires that the set of eq. (1) be solved numerically a certain number of times to produce the concentrations $u_i(t; s)$ needed to determine the Fourier coefficients and subsequently the partial variances. By contrast, the common linearized methods frequently require that eqs. (1) be differentiated with respect to the k_l to produce an auxiliary set of nm differential equations for the sensitivity coefficients $\partial u_i / \partial k_l$, $i = 1, 2, \dots, n$, $l = 1, 2, \dots, m$. Thus whereas the linearized methods require the one-time solution of nm differential equations (in addition to the original n differential equations), the FAST method requires a certain number, N_s , solutions of the original set of n differential equations. The relative solution times depend, of course, on the values of n , m , and N_s . The choice of N_s for the FAST method will be discussed shortly.

The basic sensitivity measure in the FAST method is the partial variance $S_{\omega_l}^{(i)}$, whereas in the direct, linearized methods the measure is the sensitivity coefficient $\partial u_i / \partial k_l$. The relation between these two measures is developed in Appendix A. Appendix B indicates how the case of correlated parameters can be treated.

Exploitation of Symmetry Properties

Before describing the practical implementation of the FAST method it is worthwhile to reexamine the search curves and the Fourier integrals, eqs. (10) and (11). As discussed in the previous section, the FAST method requires the repeated evaluation of the model system for each parameter combination. As this generally represents the major component of the computational cost, it is clearly desirable to minimize the required number of model solutions. One way to do this is to exploit the symmetry properties of the search curves. As defined by eq. (4) the search curves have a period of 2π . By choosing the frequency set $\{\omega_l\}$ so that it is composed entirely of odd integers, the functions $G_l(\sin \omega_l s)$, $l = 1, 2, \dots, m$, become symmetric about $\pm\pi/2$. Consequently the following symmetry properties hold:

$$u(t; \pi - s) = u(t; s)$$

$$u(t; -\pi + s) = u(t; -s)$$

$$u(t; \pi/2 + s) = u(t; \pi/2 - s)$$

$$u(t; -\pi/2 + s) = u(t; -\pi/2 - s)$$

Thus eqs. (10) and (11) become

$$(15) \quad A_j^{(i)}(t) = \begin{cases} 0, & j \text{ odd} \\ \frac{1}{\pi} \int_0^{\pi/2} [u_i(t; s) + u_i(t; -s)] \cos js \, ds, & j \text{ even} \end{cases}$$

$$(16) \quad B_j^{(i)}(t) = \begin{cases} 0, & j \text{ even} \\ \frac{1}{\pi} \int_0^{\pi/2} [u_i(t; s) - u_i(t; -s)] \sin js \, ds, & j \text{ odd} \end{cases}$$

Exploitation of the symmetry properties has therefore reduced the range of integration and, more importantly, the required number of solutions of the differential equations by one half.

Computation of the Partial Variances

The key sensitivity measure in the FAST method is the partial variance which, suppressing the dependence on t , can be written in the form

$$(17) \quad S_{\omega_l}^{(i)} = \frac{2}{\sigma_i^2} \sum_{p=1}^{\infty} [|A_{p\omega_l}^{(i)}|^2 + |B_{p\omega_l}^{(i)}|^2]$$

where the amplitudes $A_{p\omega_l}^{(i)}$, $B_{p\omega_l}^{(i)}$ are now determined by the integrals, eqs. (15) and (16). The principal idea behind the partial variance concept of sensitivity is to examine the output $u_i(t; s)$ and isolate the effects of variations in parameter k_l from the influence of changes in all the other parameters. When evaluating eq. (17) it is important to recognize, however, the limitations imposed by the use of integers to define the frequency set $\{\omega_l\}$. In the summation, interferences from the effects of parameters other than ω_l can lead to meaningless situations in which $S_{\omega_l}^{(i)} > 1$. The interference problem is readily illustrated by selecting two arbitrary parameters k_l , k_j and their associated frequencies ω_l , ω_j . In evaluating the terms contributing to $S_{\omega_l}^{(i)}$ two or more values, say r and q , of the harmonic index p will be encountered such that $r\omega_l = q\omega_j$, which in turn implies that

$$(18) \quad |A_{r\omega_l}^{(i)}|^2 + |B_{r\omega_l}^{(i)}|^2 = |A_{q\omega_j}^{(i)}|^2 + |B_{q\omega_j}^{(i)}|^2$$

This result indicates that the calculation of $S_{\omega_l}^{(i)}$ is being influenced by terms arising from variations in the other parameter, ω_j . A similar problem arises when the FAST method is applied numerically. In most circumstances algebraic complexities or computational costs restrict the availability of the output $u_i(t; s)$ to discrete values of s in the range $\pm\pi/2$. Unless the integration points are chosen carefully, aliasing errors can cause interferences similar to eq. (18). Ordinarily the Fourier amplitudes decrease as p increases. We expect, therefore, that most of the contributions to the

summation in eq. (17) should occur with the first few values of p . At this point the key question to address is simply: how many harmonics can be included in the summation without causing interference problems.

To answer this question we start by considering the choice of the frequency set $\{\omega_l\}$ and the number N_s of sample points in the s domain used to approximate the integrals, eqs. (15) and (16). We note first of all that if we select $\omega_l = 1$, eq. (17) yields $S_{\omega_l}^{(i)} = 1$, which yields no information. The frequency set $\{\omega_l\}$ used in this paper is developed recursively using

$$(19) \quad \begin{aligned} \omega_1 &= \Omega_n \\ \omega_i &= \omega_{i-1} + d_{n+1-i}, \quad i = 2, 3, \dots, n \end{aligned}$$

The Ω_n and d_n , tabulated in Cukier and co-workers [4] for n varying from 3 to 50, have been augmented for the two-parameter case with $\{\omega_l\} = 3, 5$ ($\Omega_2 = 3, d_1 = 2$), and for $n = 6$, ω_1 has been reset to 13. The maximum frequency ω_{\max} is given by ω_n if eq. (19) is used to generate the set $\{\omega_l\}$. Also, then the minimum frequency ω_{\min} is ω_1 . If the amplitudes A, B could be determined exactly, the maximum number of terms that can be included in the summation without the possibility of interferences is simply $\omega_{\min} - 1$. This is another reason for avoiding the choice $\omega_l = 1$. The simplest numerical integration procedure for evaluating the amplitudes, which exploits the symmetry properties of $u_i(t; s)$, requires $N_s = N\omega_{\max} + 1$ ($N \geq 2$) uniformly spaced points in the interval $\pm\pi/2$. Several factors influence the choice of N . The lower limit, $N = 2$, is imposed by the Nyquist criterion [7, 5], which indicates that the output $u_i(s)$ needs to be sampled at least twice as often as the highest frequency ω_{\max} . For convenience, it is useful to choose N to be divisible by 2, and so the minimum number of integration points is $2\omega_{\max} + 1$. The numerical approximation of the Fourier integrals can be improved by using $N > 2$ at the expense of increasing the computational cost. As mentioned above, the numerical approximation of the Fourier integrals leads to another type of interference problem commonly called aliasing. These interferences occur when

$$(20) \quad q\omega_n \equiv p\omega_l \pmod{N\omega_{\max} + 1}$$

This generally imposes a lower limit to the number of terms that can be included before interferences occur. The aliasing problem in the computation of $S_{\omega_l}^{(i)}$ can be minimized if, using the previous example, we restrict the higher harmonics to satisfy the conditions $r\omega_l < N\omega_{\max} + 1$. The natural choice for r is N , in which case eq. (17) can be rewritten as

$$(21) \quad S_{\omega_l}^{(i)} = \frac{2}{\sigma_i^2} \sum_{p=1}^N [|A_{p\omega_l}^{(i)}|^2 + |B_{p\omega_l}^{(i)}|^2]$$

If N is chosen to be 2, then, since $B_{2\omega_l}^{(i)} = 0$, eq. (21), with eq. (12), can be written as

$$(22) \quad S_{\omega_l}^{(i)} = \frac{2}{\sigma_i^2} [|B_{1\omega_l}^{(i)}|^2 + |A_{2\omega_l}^{(i)}|^2]$$

The variance σ_i^2 is given by eq. (13).

Practical Implementation of the FAST Method

While applicable to any problems that are described by a set of differential equations, the FAST method is particularly useful in the analysis of chemical kinetics. The parameters k_j may include rate constants, Arrhenius parameters, stoichiometric coefficients, branching ratios, and initial conditions u_0 . Application of the FAST method to the sensitivity analysis of reaction mechanisms is illustrated in Figure 1.

Several steps are involved. First the rate laws must be specified. Having established the basic set of differential equations, the next step is to select the parameters to be varied. For each parameter that is to be studied a range of uncertainty must be established and a search curve selected from the options presented in Table I. Given this information and the times

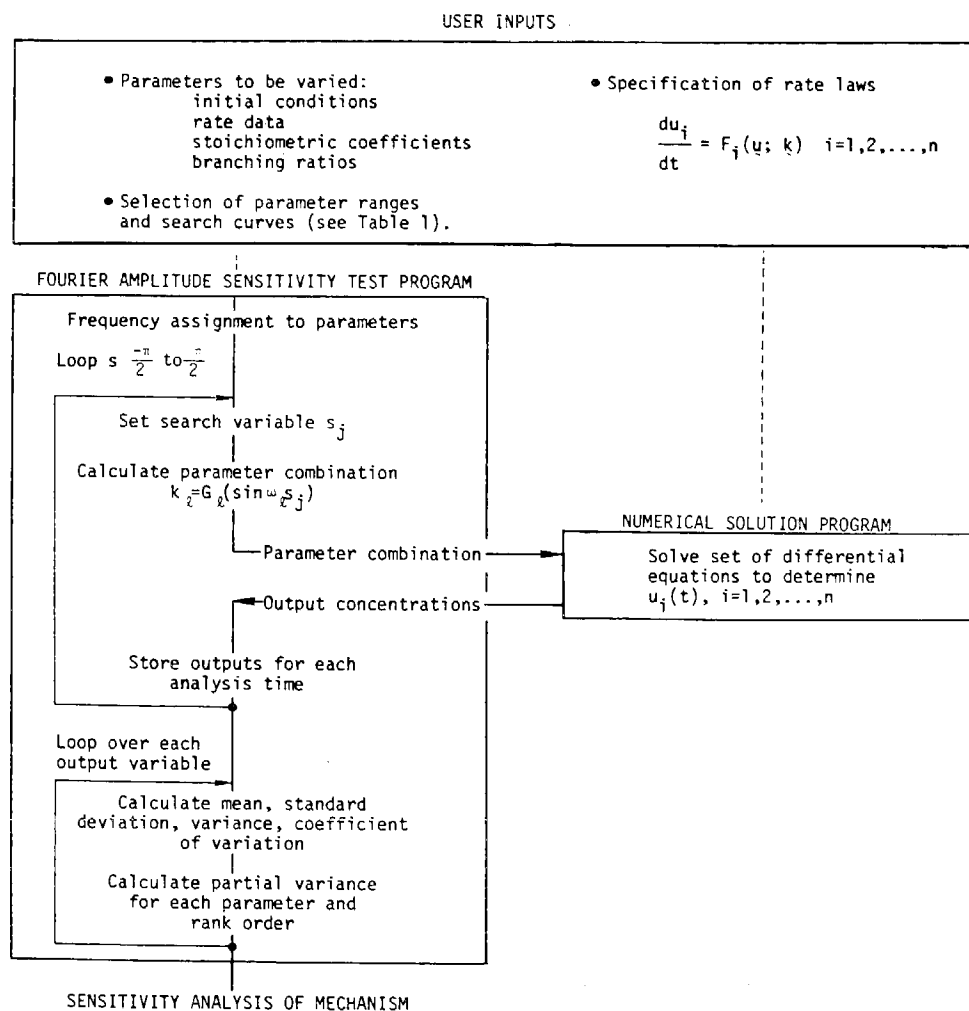


Figure 1. Application of the FAST method to chemical kinetics.

TABLE I. Search curves for different parameter variations.

Application	$k_j(s)$	Mean Value \bar{k}_j	Nominal Value \bar{v}_j
Additive variation	$k_j(s) = \bar{k}_j [1 + \bar{v}_j \sin \omega_j s]$	$\frac{k_j^u + k_j^l}{2}$	$\frac{k_j^u - k_j^l}{k_j^u + k_j^l}$
Exponential variation	$k_j(s) = \bar{k}_j \exp [\bar{v}_j \sin \omega_j s]$	$\sqrt{k_j^u k_j^l}$	$\frac{1}{2} \ln \left(\frac{k_j^u}{k_j^l} \right)$
Proportional variation	$k_j(s) = \bar{k}_j \exp [\bar{v}_j \sin \omega_j s]$	\bar{k}_j	$\ln(a)$
Skewed variation	$k_j(s) = v_j \left[\frac{\alpha_j + \beta_j \sin \omega_j s - 1}{\alpha_j + \beta_j} \right]$	$v_j \left(\frac{\alpha_j - 1}{\alpha_j} \right)$	$\alpha_j = \frac{1}{2} \left[\frac{r^u}{r^u - 1} + \frac{r^l}{r^l - 1} \right]^b$ $\beta_j = - \frac{\alpha_j (r^u + r^l - 2)}{(r^u - r^l)}$ $v_j = - \bar{k}_j \left[\frac{r^u + r^l - 2r^u r^l}{r^u + r^l - 2} \right]$

^a k_j^u —upper limit for parameter; k_j^l —lower limit for parameter.

^b $r^u = k_j^u/\bar{k}_j$, $r^l = k_j^l/\bar{k}_j$.

for the analysis of the concentrations, the FAST program automatically evaluates the model system for each parameter combination. The concentration outputs at each time are then processed to determine the partial variances and sensitivity ranking for each of the parameters. The detailed computational procedure is as follows:

(a) Assign to each of the m parameters a different frequency ω_l , $l = 1, 2, \dots, m$.

(b) Based on some knowledge of the expected range of variation for each parameter, select appropriate search curves from Table I.

(c) Select the number of parameter combinations to be evaluated. For N_s points, a symmetric and uniform spacing in s , including $s = 0$, is given by

$$(23) \quad s_j = \frac{\pi}{2} \left[\frac{2j - N_s - 1}{N_s} \right], \quad j = 1, 2, \dots, N_s$$

(d) Solve the set of differential equations, eq. (1), for each parameter combination s_j defined by $k = \bar{k}_l G_l(\sin \omega_l s_j)$, $j = 1, 2, \dots, N_s$. In many applications, particularly in chemical kinetics, where stiffness is a problem, the computation time per solution can be minimized by using a variable-order method, such as the well-known Gear algorithm [8].

Once the model system has been evaluated for each parameter combi-

nation, the influence of the l th parameter k_l on the i th concentration at time t can be examined by calculating the partial variance $S_{\omega_l}^{(i)}(t)$,

$$(24) \quad S_{\omega_l}^{(i)}(t) = \frac{2 \sum_{p=1}^N [|A_{p\omega_l}^{(i)}(t)|^2 + |B_{p\omega_l}^{(i)}(t)|^2]}{\sigma_i^2(t)}$$

The variance $\sigma_i^2(t)$ can be approximated numerically by

$$(25) \quad \frac{1}{N_s} \sum_{j=1}^{N_s} \{u_i(t; s_j) - \langle u_i(t) \rangle\}^2$$

and the mean value $\langle u_i(t) \rangle$ by

$$(26) \quad \langle u_i(t) \rangle = \frac{1}{N_s} \sum_{j=1}^{N_s} u_i(t; s_j)$$

Simple quadrature formulas can be used to evaluate the amplitudes $A_{p\omega_l}^{(i)}(t)$ and $B_{p\omega_l}^{(i)}(t)$. The following expressions were derived directly from eqs. (15) and (16):

$$(27) \quad A_{p\omega_l}^{(i)}(t) = \begin{cases} 0, & p\omega_l \text{ odd} \\ \frac{1}{N_s} \left\{ u_i(t; N_0) + \sum_{q=1}^{N_q} [u_i(t; N_0 + q) + u_i(t; N_0 - q)] \right. \\ \quad \left. \times \cos \frac{p\omega_l q \pi}{N_s} \right\}, & p\omega_l \text{ even} \end{cases}$$

$$(28) \quad B_{p\omega_l}^{(i)}(t) = \begin{cases} 0, & p\omega_l \text{ even} \\ \frac{1}{N_s} \left\{ \sum_{q=1}^{N_q} [u_i(t; N_0 + q) - u_i(t; N_0 - q)] \sin \frac{p\omega_l q \pi}{N_s} \right\}, & p\omega_l \text{ odd} \end{cases}$$

where $N_q = (N_s - 1)/2$ and $N_0 = N_q + 1$. (The index notation in eqs. (26) and (27) has been chosen to simplify the computer implementation using programming languages such as FORTRAN that do not allow negative or zero indices.)

Figure 2 with $\{\omega_l\} = [3, 5]$ and Figure 3 with $\{\omega_l\} = [11, 13]$ illustrate the two basic approximations involved in the FAST method. The first is that the frequency sets $\{\omega_l\}$ are commensurate, that is, the search curves do not completely cover the parameter space. The second approximation involves the use of a finite number of points in the numerical quadrature. Both of these considerations have been quantitatively examined by Cukier and co-workers [4] and for this reason will not be repeated here.

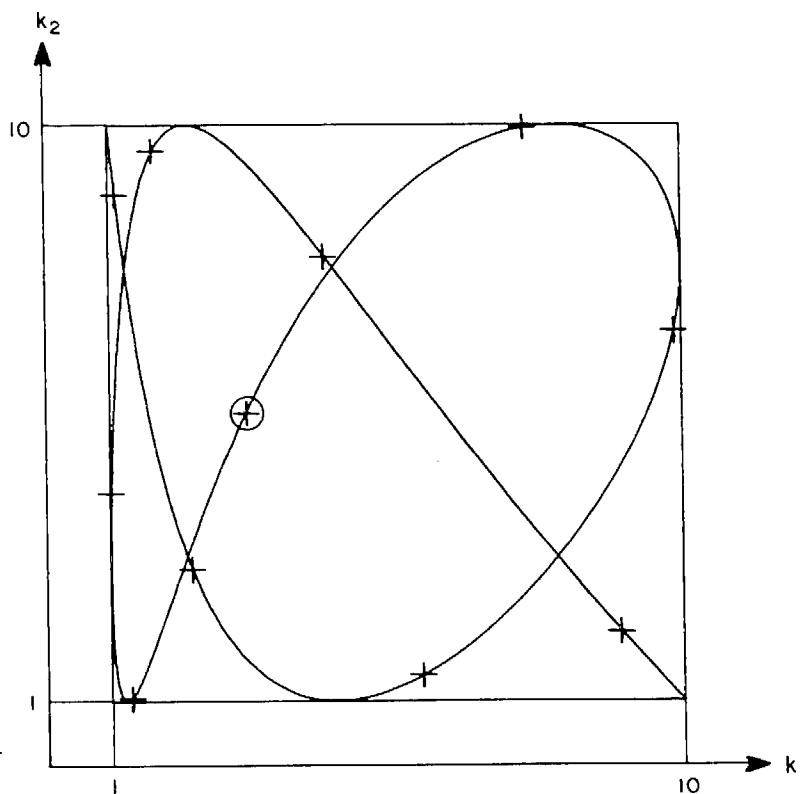
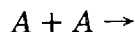


Figure 2. Space-filling search curve for case $\{\omega_i\} = [3, 5]$ where $k_1 = \bar{k}_1 \exp(\bar{\nu}_1 \sin \omega_1 s)$ and $k_2 = \bar{k}_2 [1 + \bar{\nu}_2 \sin \omega_2 s]$. +—integration points for $N_s = 2\omega_{\max} + 1$; \oplus —nominal value of k_1 and k_2 .

Example—Application to a Single Reaction

In this section we wish to present an example of the use of the FAST method. We have purposely chosen a very simple system so that the interpretation of the results can be easily discussed; an application involving a larger number of parameters is described in Boni and Penner [9]. Consider a hypothetical recombination reaction



with rate constant $\kappa = k_1 \exp(-k_2/T)$. We wish to examine the sensitivity of the concentration of A to variations in the Arrhenius parameters k_1 and k_2 at $T = 298^\circ\text{K}$. We let $u = [A]/[A_0]$, the normalized concentration. The nominal values of k_1 and k_2 are chosen as 1.79×10^{10} l/mol-sec and 500°K , respectively. The (arbitrary) ranges of uncertainty and initial concentration were chosen as $8.97 \times 10^9 \leq k_1 \leq 3.59 \times 10^{10}$, $0 \leq k_2 \leq 1000$, $[A_0] = 1$ mol/l.

We use the transformations (see Table I) $k_1 = \bar{k}_1 \exp \nu_1$ and $k_2 = \bar{k}_2 (1 + \nu_2)$, where $\nu_1 = (\ln 2) \sin \omega_1 s$ and $\nu_2 = \sin \omega_2 s$. For this particular problem the sensitivity coefficients can be calculated analytically, $\partial u / \partial k_1 = -2[A_0] \kappa t u^2 / \bar{k}_1$ and $\partial u / \partial k_2 = 2[A_0] \kappa t u^2 / T$. The FAST method essentially

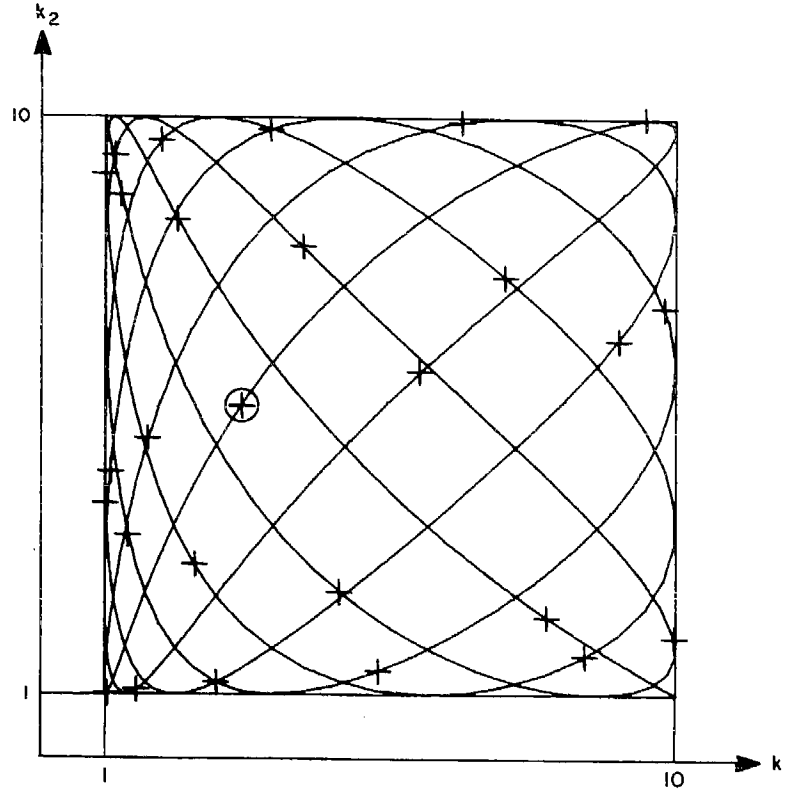


Figure 3. Space-filling search curve for case $\{\omega_l\} = [11, 13]$ where $k_1 = \bar{k}_1 \exp(\bar{\nu}_1 \sin \omega_1 s)$ and $k_2 = \bar{k}_2 [1 + \bar{\nu}_2 \sin \omega_2 s]$. $+—$ integration points for $N_s = 2\omega_{\max} + 1$; \oplus —nominal value of k_1 and k_2 .

calculates the Fourier amplitude B_{ω_l} which is proportional to $\langle \partial u / \partial \nu_l \rangle$, which is the relative sensitivity with respect to the nondimensional ν_l for the transformations $\exp \nu_l = k_l / \bar{k}_l$ or $1 + \nu_l = k_l / \bar{k}_l$ (see Appendix A).

In Figure 4 the concentration u , partial variances S_{ω_1} and S_{ω_2} , fundamental Fourier coefficients B_{ω_1} and B_{ω_2} , and the relative sensitivity coefficients $\bar{k}_1 \partial u / \partial k_1$ and $\bar{k}_2 \partial u / \partial k_2$ are plotted for $\{\omega_1, \omega_2\} = (3, 5)$ and $N_s = 21$. (The results were found to be insensitive to the choice of the frequency set and number of dividing points.) The fundamental Fourier coefficients B_{ω_1} and B_{ω_2} follow quite well the general trends of the relative sensitivity coefficients $\bar{k}_1 \partial u / \partial k_1$ and $\bar{k}_2 \partial u / \partial k_2$, demonstrating the fundamental relationship in the FAST method, $B_{\omega_l} \propto \langle \partial u / \partial \nu_l \rangle$. The partial variance S_{ω_2} follows the trends of B_{ω_2} and $\bar{k}_2 \partial u / \partial k_2$. On the other hand, the partial variance S_{ω_1} does not follow the trends of B_{ω_1} or $\bar{k}_1 \partial u / \partial k_1$. It decreases when the absolute values of B_{ω_1} and $\bar{k}_1 \partial u / \partial k_1$ increase and increases when the absolute values of B_{ω_1} and $\bar{k}_1 \partial u / \partial k_1$ decrease. We observe the following relationship between the partial variances;

$$(29) \quad S_{\omega_1} + S_{\omega_2} \simeq 0.96 \pm 0.03$$

This implies that if the relative importance of the effects of the parameter

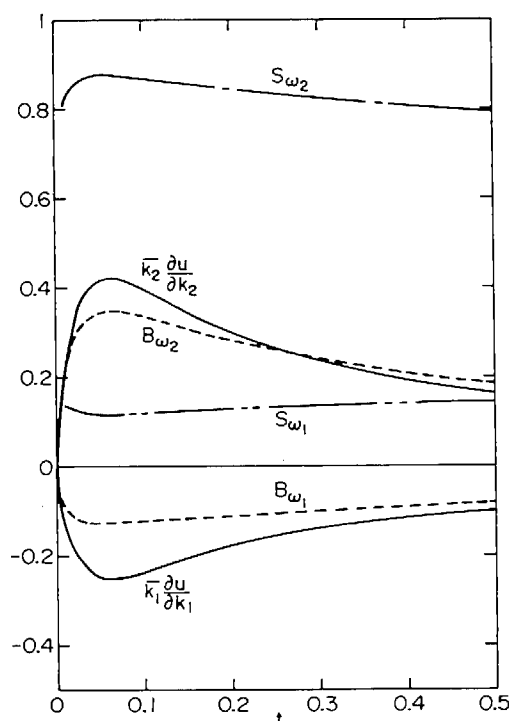


Figure 4. Comparison of the analytical sensitivity coefficients $\bar{k}_i \partial u / \partial k_i$ and the fundamental Fourier coefficients B_{ω_i} and partial variance S_{ω_i} as calculated by the FAST method ($i = 1, 2$). Plots are based on the normalized concentration, that is, $u = [A]/[A_0]$. The parameters used are $\omega_1 = 3$, $\omega_2 = 5$, and $N_s = 4\omega_{\max} + 1 = 21$.

uncertainty in k_1 , that is, the partial variance S_{ω_1} increases, then S_{ω_2} , the measure of relative importance for k_2 , automatically decreases. For the more general multiparameter examples studied by Cukier and co-workers [5], we can observe the same relationship, namely, $\sum_{i=1}^m S_{\omega_i} \simeq \text{constant}$ when the coupling terms like $S_{\omega_i + \omega_j}$ are small. For the parameter range we have studied, all the sensitivity measures including the analytical sensitivity coefficients agreed and gave consistent results, indicating that the concentration of A is more sensitive to changes in k_2 than to changes in k_1 .

To test the FAST method further, we increased the range of uncertainty for the parameter k_1 as follows: $0 \leq k_1 \leq 3.59 \times 10^{10}$.¹ To take account of this range of uncertainty we use the transformation (see Table I) $k_1 = \bar{k}_1 (1 + \sin \omega_1 s)$. The range of uncertainty of k_2 is held fixed.

The results of calculations are plotted in Figure 5. Since the parameter uncertainty for k_1 is increased, we observe that the relative importance of the parameter uncertainty in k_1 is increased and $S_{\omega_1} > S_{\omega_2}$ for $t > 0.08$. This fact, is also reflected in the fundamental Fourier coefficients B_{ω_1} and B_{ω_2} . The fundamental Fourier coefficient B_{ω_1} does not agree with the trend

¹ Such a range of variation is, of course, physically implausible. We have chosen it only to illustrate the ability of the method to handle extreme limits of variation.

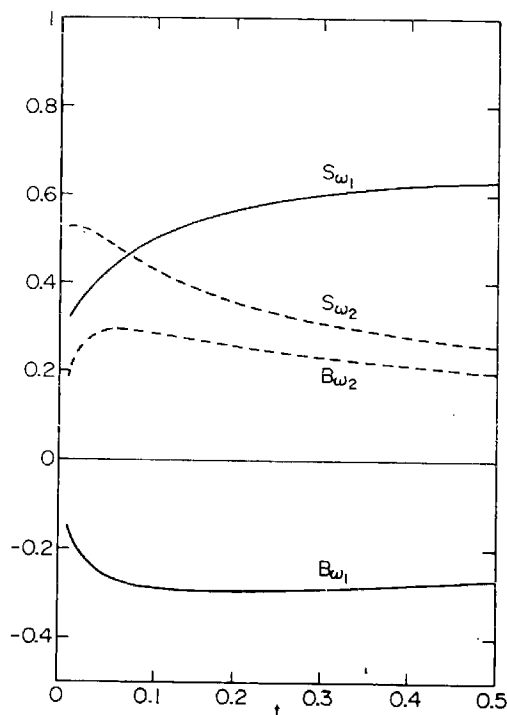


Figure 5. Fundamental Fourier coefficients B_{ω_i} and partial variances S_{ω_i} ($i = 1, 2$) for the case of increased range of uncertainties in the parameter k_1 . The parameters used in the FAST method are $\omega_1 = 3$, $\omega_2 = 5$, and $N_s = 4\omega_{\max} + 1 = 21$.

of the analytical sensitivity solution of $\bar{k}_1 \partial u / \partial k_1$. This behavior is due to the characteristics of the Fourier amplitude sensitivity test and the sensitivity coefficient. The FAST method takes account of the very large variations about the nominal values, while the sensitivity coefficient $\bar{k}_1 \partial u / \partial k_1$ is computed at the nominal values for infinitesimal variations. Thus for the case of the increased range of uncertainty of k_1 , we conclude that the concentrations of A is more sensitive to k_1 than to k_2 . We observe from this example that the partial variances essentially propagate the uncertainties in the parameters.

Summary

An algorithm for the automatic sensitivity analysis of kinetic mechanisms based on the FAST method of Shuler and co-workers [2-5] has been described, and a simple example illustrating its use has been given. With this method assessment of the relative influence of kinetic parameters on the predicted concentrations from a chemical mechanism becomes a relatively routine undertaking. A complete code for the sensitivity analysis of mechanisms includes three routines: 1) one that forms the kinetic rate equations based on the set of chemical reactions, 2) one that integrates the ordinary differential (ODE) rate equations, and 3) one that processes the

concentrations to produce the partial variances of the FAST method. This paper has focused on the third routine. The authors have prepared a complete code consisting of an algebraic manipulation routine to form the rate equations for any set of chemical reactions, the ODE solver EPISODE [10, 11], and the FAST method described here. Interested readers may contact the authors to obtain a copy of the code.

Acknowledgment

This work was supported by the Environmental Protection Agency under Grant No. R805537.

Appendix A

Relation of the FAST Method to Sensitivity Coefficients

In this appendix we summarize the relationship of the FAST method to the generalized sensitivity coefficients $\langle \partial u_i / \partial k_l \rangle$ and to the customary linear sensitivity measures $\partial u_i / \partial k_l|_{\bar{k}}$, $i = 1, 2, \dots, n$ and $l = 1, 2, \dots, m$. Cukier and co-workers [4, 5] have considered the problem in somewhat more detail. Here we illustrate the results, using as an example the parameter representation.

$$(30) \quad k_l = G_l(\sin \omega_l s) = \bar{k}_l \exp v_l$$

$$(31) \quad v_l = g_l(\sin \omega_l s)$$

where \bar{k}_l is the nominal value for the parameter k_l . The function g_l is determined to satisfy

$$(32) \quad \cos^2 \theta_l \frac{\partial g_l(\sin \theta_l)}{\partial \sin \theta_l} = \frac{1}{a_l}$$

where $\theta_l = \omega_l s \pmod{2\pi}$ and a_l is a constant parameter. From eq. (3) and Weyl's theorem, we can write

$$(33) \quad B_{\omega_l}^{(i)}(t) = \langle u_i(t; s) \sin \theta_l \rangle \\ = \int_0^{2\pi} \dots \int_0^{2\pi} u_i(t; \theta_1, \dots, \theta_m) \sin \theta_l P(\theta_1, \dots, \theta_m) d\theta_1 \dots d\theta_m$$

where $P(\theta_1, \dots, \theta_m) = (2\pi)^{-m}$. Then using eqs. (30)–(33) and integrating by parts, we obtain the desired relationship between $B_{\omega_l}^{(i)}$ and $\langle \partial u_i / \partial v_l \rangle$,

$$(34) \quad B_{\omega_l}^{(i)} = \frac{1}{a_l} \left\langle \frac{\partial u_i}{\partial v_l} \right\rangle$$

where

$$(35) \quad \left\langle \frac{\partial u_i}{\partial v_l} \right\rangle = \frac{\int_{-\infty}^{\infty} \dots \int_{-\infty}^{\infty} \frac{\partial u_i}{\partial v_l} \prod_{j=1}^m p(v_j, a_j) dv_j}{\int_{-\infty}^{\infty} \dots \int_{-\infty}^{\infty} \prod_{j=1}^m p(v_j, a_j) dv_j}$$

and where $p(\nu_j, a_j) = a_j / \cosh a_j \nu_j$. The function

$$(36) \quad P(\nu_1, \dots, \nu_m) = \prod_{j=1}^m p(\nu_j, a_j)$$

can be interpreted as a probability density in ν space. Thus the Fourier coefficient $B_{\omega_l}^{(i)}$ is related to a generalized average of the sensitivity $\langle \partial u_i / \partial \nu_l \rangle$. (For an alternative transformation, $G_l(\sin \omega_l s) = \bar{k}_l(1 + \nu_l)$, the same result is obtained.) The relationship of eq. (34) to the linear sensitivity measure can be seen by expanding $\partial u_i / \partial \nu_l$ in a MacLaurin series about $\nu = 0$ and substituting the results into eq. (35) to give

$$(37) \quad \left\langle \frac{\partial u_i}{\partial \nu_l} \right\rangle = \frac{\partial u_i}{\partial \nu_l} \Big|_{\nu=0} + \frac{\int_{-\infty}^{\infty} \dots \int_{-\infty}^{\infty} \prod_{j=1}^m p(\nu_j, a_j) \sum_{r=1}^{\infty} \frac{\nu_l^r}{r!} \left[\frac{\partial^r}{\partial \nu_l^r} \left(\frac{\partial u_i}{\partial \nu_l} \right) \right]_{\nu=0} d\nu_1 \dots d\nu_m}{\int_{-\infty}^{\infty} \dots \int_{-\infty}^{\infty} \prod_{j=1}^m p(\nu_j, a_j) d\nu_1 \dots d\nu_m}$$

From eq. (37) it is clear that unless the $u_i(t; s)$ are linear functions of the parameters k_1, \dots, k_m , the generalized form eq. (34) is not equivalent to $\partial u_i / \partial \nu_l|_{\nu=0}$. If the second and higher order terms can be neglected, then the following approximate relationship holds:

$$(38) \quad B_{\omega_l}^{(i)} \simeq \frac{1}{a_l} \frac{\partial u_i}{\partial \nu_l} \Big|_{\nu=0}$$

Appendix B

Extension to Correlated Parameters

In the preceding development the parameters k_l , $l = 1, 2, \dots, m$, have been assumed to be uncorrelated. Thus a range of uncertainty can be assigned to each parameter independent of the uncertainty range assigned to the other parameters. Relationships may exist, however, among two or more parameters. For example, if k_1 and k_2 represent fractional paths for a single reaction, then $k_1 + k_2 = 1$.

We assume that the parameters are subject to the following constraint:

$$(39) \quad H(k_1, k_2, \dots, k_m) \leq 0$$

To employ the FAST method it is necessary to find a set of transformations $k_l = h_l(\alpha_1, \alpha_2, \dots, \alpha_m)$ such that eq. (39) is satisfied for a set of independent α_l . The fundamental Fourier coefficient for α can be called B_{ω_α} . We need

to relate B_{ω_α} to the Fourier coefficients B_{α_1} and B_{ω_2} . This can be done by considering the sensitivity coefficients

$$(40) \quad \frac{\partial u_i}{\partial k_j} = \sum_{l=1}^m \frac{\partial \alpha_l}{\partial k_j} \frac{\partial u_i}{\partial \alpha_l}$$

where $\partial \alpha_l / \partial k_j$ is evaluated at the nominal values \bar{k}_j . The material in Appendix A is now needed. By using the ν -space average, eq. (35), we can approximate eq. (40) by

$$(41) \quad \frac{\partial u_i}{\partial k_j} \cong \sum_{l=1}^m \frac{1}{a_l} \frac{\partial \alpha_l}{\partial k_j} \left\langle \frac{\partial u_i}{\partial \nu_l} \right\rangle$$

Then, from eq. (41),

$$(42) \quad B_{\omega_j}^{(i)} \cong \sum_{l=1}^m \frac{\partial \alpha_l}{\partial k_j} B_{\omega_{\alpha l}}^{(i)}$$

To illustrate the approach consider, for example, the case of the constraint

$$(43) \quad \frac{k_2}{a} + \frac{k_1}{b} = 1$$

where $0 < k_1 < b$, $0 < k_2 < a$, and $\bar{k}_1 = b/2$ and $\bar{k}_2 = a/2$. To apply the FAST method to k_1 and k_2 we represent k_1 and k_2 by

$$(44) \quad k_1 = b - \frac{b}{\sqrt{a^2 + b^2}} \alpha$$

$$(45) \quad k_2 = \frac{a}{\sqrt{a^2 + b^2}} \alpha$$

Thus for $0 < \alpha < \sqrt{a^2 + b^2}$, the constraint eq. (43) is satisfied. The search for α is chosen as

$$(46) \quad \alpha = \frac{\sqrt{a^2 + b^2}}{2} (1 + \sin \omega_\alpha s)$$

and the FAST method is applied to α rather than to k_1 and k_2 . For example, the constraint (44) becomes

$$(47) \quad \begin{aligned} B_{\omega_1} &\cong \frac{\partial \alpha}{\partial k_1} \left\langle \frac{\partial u}{\partial k_1} \right\rangle \cong \frac{\sqrt{a^2 + b^2}}{b} B_{\omega_\alpha} \\ B_{\omega_2} &\cong \frac{\partial \alpha}{\partial k_2} \left\langle \frac{\partial u}{\partial k_2} \right\rangle \cong \frac{\sqrt{a^2 + b^2}}{a} B_{\omega_\alpha} \end{aligned}$$

We note that $-bB_{\omega_1} \cong aB_{\omega_2}$, which is consistent with the relationship between the sensitivity coefficients $\partial u / \partial k_1$ and $\partial u / \partial k_2$.

Bibliography

- [1] J. H. Seinfeld and L. Lapidus, "Mathematical Methods in Chemical Engineering," vol. III, Process Modeling, Estimation and Identification, Prentice-Hall, Englewood Cliffs, NJ, 1974.
- [2] R. I. Cukier, C. M. Fortuin, K. E. Shuler, A. G. Petschek, and J. H. Schaibly, *J. Chem. Phys.*, **59**, 3873 (1973).
- [3] J. H. Schaibly and K. E. Shuler, *J. Chem. Phys.*, **59**, 3879 (1973).
- [4] R. I. Cukier, J. H. Schaibly, and K. E. Shuler, *J. Chem. Phys.*, **63**, 1140 (1975).
- [5] R. I. Cukier, H. B. Levine, and K. E. Shuler, *J. Comp. Phys.*, **26**, 1 (1978).
- [6] H. Weyl, *Am. J. Math.*, **60**, 889 (1938).
- [7] R. A. Cadzow, "Discrete Time Systems," Prentice-Hall, Englewood Cliffs, NJ, 1973.
- [8] C. W. Gear, "Numerical Initial Value Problems in Ordinary Differential Equations," Prentice-Hall, Englewood Cliffs, NJ, 1971.
- [9] A. A. Boni and R. C. Penner, *Combust. Sci. Technol.*, **15**, 99 (1976).
- [10] A. C. Hindmarsh and G. D. Byrne, "EPISODE: An Experimental Package for the Integration of Systems of Ordinary Differential Equations," Lawrence Livermore Laboratory Rep. UCID-30112, May 1975.
- [11] G. D. Byrne, A. C. Hindmarsh, K. R. Jackson, and H. G. Brown, *Computers and Chem. Eng.*, **1**, 133 (1977).

Received June 30, 1978

Revised August 28, 1978

10.4 Global Sensitivity Analysis - A Computational Implementation
of the Fourier Amplitude Sensitivity Test (FAST)

(Reprinted from Computers and Chemical Engineering, 6, 15-25.)

GLOBAL SENSITIVITY ANALYSIS—A COMPUTATIONAL IMPLEMENTATION OF THE FOURIER AMPLITUDE SENSITIVITY TEST (FAST)

GREGORY J. MCRAE, JAMES W. TILDEN and JOHN H. SEINFELD*

Environmental Quality Laboratory, California Institute of Technology, Pasadena, CA 91125, U.S.A.

(Received August 18, 1980; received for publication 6 January 1981)

Abstract—This paper describes a computational implementation of the Fourier Amplitude Sensitivity Test (FAST) and illustrates its use with a sample problem. The FAST procedure is ideally suited to the task of determining the global sensitivity of nonlinear mathematical models subjected to variations of arbitrary size in either the system parameters or initial conditions. A FORTRAN computer program, capable of performing sensitivity analyses of either algebraic or differential equation systems is described.

Scope—In virtually all branches of science and engineering, descriptions of phenomena lead to differential equations of substantial complexity. The complexity of such models makes it difficult to determine the effect uncertainties in physical parameters have on their solutions. Traditionally, the analysis of the sensitivity of models to small perturbations in parameters is called *local sensitivity analysis*. When a measure of the sensitivity of the solution to variations of a parameter is combined in an appropriate manner with a measure of the actual degree of uncertainty in the parameter's value, it may then be determined which parameters, through both their sensitivity and uncertainty, have the most influence on the solution. Such a procedure can be called a *global sensitivity analysis*.

Conventional global sensitivity analysis techniques have generally been based on either a pattern search or Monte Carlo technique. Pattern search and Monte Carlo approaches can become extremely time consuming and expensive as the number of parameters become large.

The Fourier Amplitude Sensitivity Test (FAST) technique associates each uncertain parameter with a specific frequency in the Fourier transform space of the system. The system sensitivities are then determined by solving the system equations for discrete values of the Fourier transform variable and then computing the Fourier coefficients associated with each parameter frequency. This approach allows nonlinear global sensitivities of systems subjected to large parameter variations to be determined in a practical and efficient manner.

Conclusions and Significance—Because of the complex nature of many physical and chemical systems, an integral element of any modeling study should be a formal assessment of the effects of uncertainties in the parameterization of the physical processes. In this paper particular attention is given to the Fourier Amplitude Sensitivity Test (FAST) for examining the global sensitivity of nonlinear mathematical models. The FAST technique allows arbitrarily large variations in either system parameters or initial conditions.

The computer program presented here provides a general framework for implementation of the FAST method. When combined with a user supplied subroutine for the specific system of interest, the FAST program computes the sensitivities of the system outputs to the parameter variations specified by the user. The method is illustrated on an example involving a simple autocatalytic reaction mechanism.

1. INTRODUCTION

A variety of chemical engineering phenomena are described by lengthy and complex mathematical models. It is often desirable to determine the effect of uncertainties in system parameters on the system behavior and to determine which parameters are most influential. The complexity of many models makes it difficult to determine the effect uncertainties in physical and chemical parameters have on solutions. When a measure of the sensitivity of the solution to variations of a parameter is combined in an appropriate manner with a measure of the degree of uncertainty in the parameter's value, one may then determine which parameters, through both their sensitivity and uncertainty, have the most influence

on predicted system behavior. Such a study can be termed a *sensitivity/uncertainty analysis* or a *global sensitivity analysis*.

Consider a system that is described by a set of n coupled ordinary differential equations containing m parameters, k_1, k_2, \dots, k_m ,

$$\frac{dx}{dt} = f(x; k) \quad (1)$$

where x is the n -dimensional vector of the system state and k is the m -dimensional parameter vector. A basic measure of the effect of uncertainties in k on $x(t)$ is the deviation in x caused by a variation in k , $\Delta x(t; k) = x(t; \bar{k} + \Delta k) - x(t; \bar{k})$, where $x(t; \bar{k})$ denotes the solution of (1) at time t with $k = \bar{k}$. Taylor's theorem can be invoked

*Author whom correspondence should be addressed.

to express the deviation in state variable i as

$$x_i(t; \bar{\mathbf{k}} + \Delta \mathbf{k}) = x_i(t; \bar{\mathbf{k}}) + \sum_{j=1}^m \frac{\partial x_i}{\partial k_j} \Delta k_j + O((\max \Delta k_j)^2). \quad (2)$$

The partial derivatives $\partial x_i(t)/\partial k_j$, $i = 1, 2, \dots, n$, $j = 1, 2, \dots, m$ are the so-called *sensitivity coefficients*. Much of the work on sensitivity analysis has been concerned with calculation of these sensitivity coefficients. Sensitivity analysis techniques that rely on calculation of the sensitivity coefficients are strictly applicable only to small parameter variations since the higher order terms in (2) are neglected.

Although the sensitivity coefficients $\partial x_i/\partial k_j$ provide direct information on the effect of a small variation in each parameter about its nominal value \bar{k}_j on each state variable, they do not indicate the effect of simultaneous, large variations in all parameters on the state variables. An analysis that accounts for simultaneous parameter variations of arbitrary magnitude can be termed a global sensitivity analysis. The sensitivity coefficients are local gradients in the multidimensional parameter space at the nominal value $\bar{\mathbf{k}}$. A technique that considers the effect of simultaneous parameter variations over their actual expected ranges of uncertainty produces an average measure of sensitivity over the entire admissible region of variation and thus provides an essentially different measure of sensitivity than that of the sensitivity coefficients. Therefore, both types of analysis are useful in studying the behavior of a system.

Figure 1 shows schematically a hypothetical solution surface $x_i(t; \mathbf{k})$ over the domain of uncertainty of two parameters, k_1 and k_2 . The nominal parameter values are \bar{k}_1 and \bar{k}_2 , and the assumed upper and lower limits of variation are indicated producing the domain of uncertainty in the k_1 - k_2 plane. The resulting range of uncertainty in x_i is also indicated. The surface shown in Fig. 1 is that at a certain time t . Generally the variations in the solutions $x_i(t)$, $i = 1, 2, \dots, n$ must be considered as a function of time. The point Q on the solution surface represents the magnitude of the solution x_i at time t with both parameters at their nominal, or best guess, values. Varying both parameters over the full domain of uncertainty generates the two-dimensional solution surface that changes as t changes. The sensitivity coefficients, $\partial x_i/\partial k_1$ and $\partial x_i/\partial k_2$, evaluated at \bar{k}_1 and \bar{k}_2 represent the slopes of the surface in the two

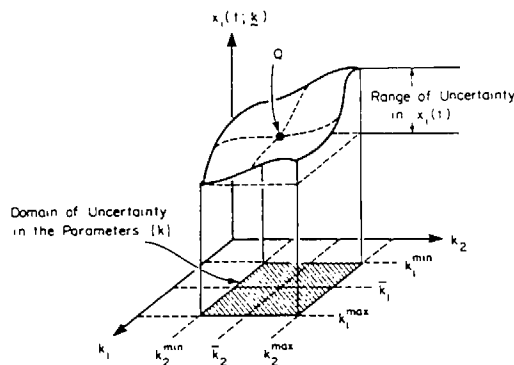


Fig. 1. Hypothetical solution surface over the domain of uncertainty of two parameters (after Gelinis and Vajk[8]).

coordinate directions at point Q . A local sensitivity analysis would focus on calculation of these two derivatives and their time variation. For small displacements about the nominal values, the tangent plane at Q differs from the actual solution surface only by a small amount. In this regime the sensitivity coefficients indicate to which parameter the solution is most sensitive. The sensitivity coefficients at point Q do not contain information on the behavior of the surface away from Q nor do they indicate the full range of variation of x_i in the domain of uncertainty of the parameters. The global sensitivity analysis is concerned with assessing the behavior of the entire solution surface of x_i over the domain of uncertainty of the two parameters.

If we have some knowledge of the probability distributions of the two parameters, $p_1(k_1)$ and $p_2(k_2)$, the probability distribution for x_i can in principle be computed. From the probability distribution of x_i , certain statistical properties such as the expected value,

$$\langle x_i(t) \rangle = \int_{k_2^{\min}}^{k_2^{\max}} \int_{k_1^{\min}}^{k_1^{\max}} x_i(t; k_1, k_2) p_1(k_1) p_2(k_2) dk_1 dk_2 \quad (3)$$

and the variance,

$$\sigma_i^2(t) = \langle x_i(t)^2 \rangle - \langle x_i(t) \rangle^2 \quad (4)$$

where

$$\langle x_i(t) \rangle^2 = \int_{k_2^{\min}}^{k_2^{\max}} \int_{k_1^{\min}}^{k_1^{\max}} x_i(t; k_1, k_2)^2 p_1(k_1) p_2(k_2) dk_1 dk_2 \quad (5)$$

can be computed.

In Fig. 2 given assumed probability distributions for each parameter, a hypothetical probability distribution for the solution is shown. Note that the best value of each parameter, the nominal value, may differ in general from either the most likely value or the mean value. Likewise, the mean value of the solution, $\langle x_i(t) \rangle$ may not correspond to the value at the nominal parameter values, i.e. point Q .

Whether or not the probability distributions for k_1 and k_2 are given, the solution surface for x_i can be determined by systematically selecting points in the domain of uncertainty of k_1 and k_2 and solving the system to

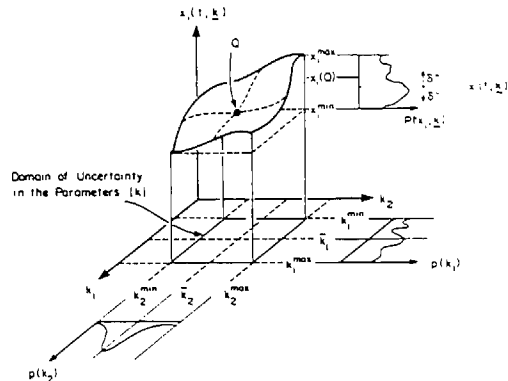


Fig. 2. Hypothetical probability distribution of solution surface corresponding to the probability distributions of the two parameters (after Gelinis and Vajk[8]).

determine $x_i(t; k_1, k_2)$. This approach is indicated in Fig. 3. A sensitivity/uncertainty analysis necessitates some form of sampling over the domain of uncertainty of the parameters.

Figure 3 is a schematic illustration of the Monte Carlo method of sensitivity analysis. A random number generator is used to select values of the uncertain parameters within the domain of uncertainty. The system is then solved for each of the parameter combinations randomly selected. The values of $x_i(t; k)$ thus computed are analyzed by standard statistical methods. The distribution of values obtained is shown in Fig. 3 as a histogram with mean value $\langle x_i \rangle$. The randomly selected points in the domain of uncertainty of the parameters can be chosen according to any prescribed probability density functions for the parameters. No special programming is required, only that needed to select the parameter values and analyze the solutions statistically.

This paper is devoted to a pattern search procedure for global sensitivity analysis that is an alternative to the Monte Carlo method illustrated in Fig. 3. The method is called the Fourier Amplitude sensitivity Test (FAST) and was originally developed by Shuler *et al.* [1-4].

In the next section the mathematical basis of the FAST method is outlined. Then in Section 3 its computational implementation is described. Section 4 contains the description of the computer program and its operation. An example drawn from chemical kinetics is given in Section 5 to illustrate the use of the program.

2. MATHEMATICAL BASIS OF THE FAST METHOD

The basic problem is to determine the sensitivity of each x_i to simultaneous variations in all the parameters $\{k_j\}$. This is done by considering that the $\{k_j\}$ have a distribution of values resulting from either imprecision or uncertainty in their definition. Under these conditions, the ensemble mean for x_i is given by the generalization of (3),

$$\langle x_i \rangle = \int \cdots \int x_i(k_1, k_2, \dots, k_m) p(k_1, k_2, \dots, k_m) dk_1 dk_2, \dots, dk_m \quad (6)$$

where p is the m -dimensional probability density for k .

The central idea of the FAST method is to convert the m -dimensional integral (6) into a one dimensional form

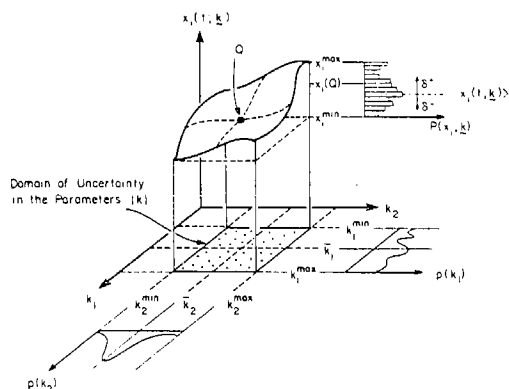


Fig. 3. Monte Carlo approach to generating the solution surface (after Gelinis and Vajk[8]).

by using the transformation,

$$k_l = G_l[\sin(\omega_l s)]; \quad l = 1, 2, \dots, m. \quad (7)$$

For an appropriate set of functions $\{G_l\}$, it can be shown that [5]

$$\bar{x}_i = \langle x_i \rangle = \lim_{T \rightarrow \infty} \frac{1}{2T} \int_{-T}^T x_i[k_1(s), k_2(s), \dots, k_m(s)] ds. \quad (8)$$

This relationship will hold only if the frequency set, $\{\omega_l\}$, is incommensurate, i.e.

$$\sum_{i=1}^m \gamma_i \omega_i = 0. \quad (9)$$

for an integer set of $\{\gamma_i\}$ if and only if $\gamma_i = 0$ for every i . The functions $\{G_l\}$ need to be chosen so that the arc length, ds , is proportional to $p(k_1, k_2, \dots, k_m) dk_1$ for all l . The transformation then results in a search curve that samples the parameter space in a manner consistent with the statistics described by $p(k_1, k_2, \dots, k_m)$.

The parametric curve defined by (7) is termed a search curve, and s is termed the search variable. As s is varied, (7) traces out a space filling curve in the parameter space. If it were possible to use an incommensurate frequency set, the curve would never close upon itself and would pass arbitrarily close to every point in the parameter space. This result is a consequence of Weyl's theorem. When integer frequencies are used, it is not possible to obtain a truly incommensurate frequency set and the search curves take on the appearance of multi-dimensional Lissajous curves. The use of higher frequencies results in successively longer search curves. Two examples are shown in Fig. 4 and 5. The length of the search curve and the density of sample points is considerably greater in the second case.

Practical considerations dictate that an integer rather than an incommensurate frequency set must be used. This introduces two types of error. First, the search curve is no longer space-filling, i.e. it does not pass

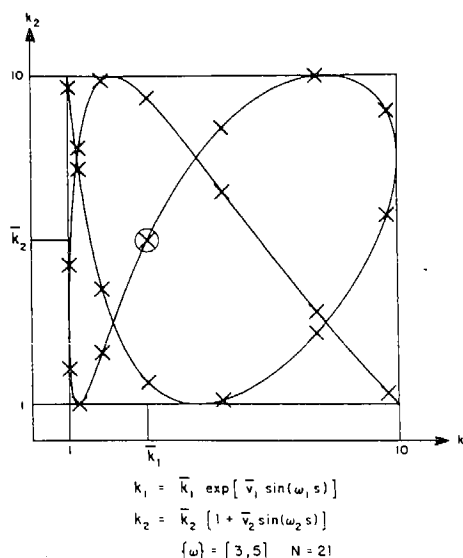
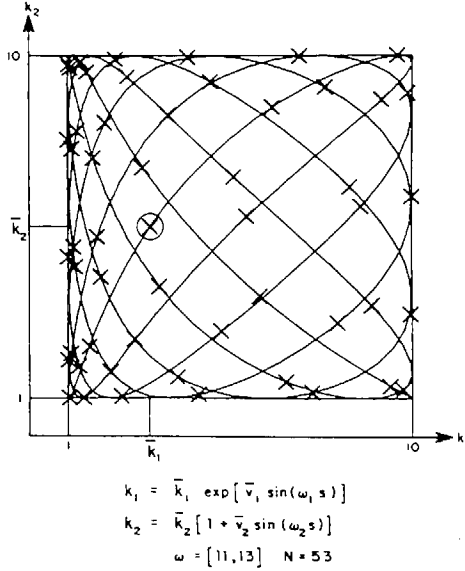


Fig. 4. Search curve with frequencies $\omega_1 = 3$, $\omega_2 = 5$.

Fig. 5. Search curve with frequencies $\omega_1 = 11$, $\omega_2 = 13$.

arbitrarily close to any point in the k -space; secondly, the fundamental frequencies used to describe the set $\{k_i\}$ will have harmonics that interfere with one another. However, the differences between \bar{x} and $\langle x \rangle$ for a well chosen integer frequency set can be made arbitrarily small [2, 3].

An integer frequency set results in a periodic search curve that becomes a closed path in the s -space. When s is varied between $-\pi$ and $+\pi$, the entire search curve is traversed. The periodicity of the $\{k_i\}$ then implies that the Fourier coefficients

$$A_{p\omega_i}^{(i)} = \frac{1}{2\pi} \int_{-\pi}^{\pi} x_i[k_1(s), \dots, k_m(s)] \cos(p\omega_i s) ds$$

$$B_{p\omega_i}^{(i)} = \frac{1}{2\pi} \int_{-\pi}^{\pi} x_i[k_1(s), \dots, k_m(s)] \sin(p\omega_i s) ds$$

$p = 0, 1, 2, \dots$ (10)

$p = 1, 2, \dots$ (11)

are a measure of the sensitivity of the x_i output function to the k th uncertain parameter. For instance, in the case where x_i is totally insensitive to a given parameter, the coefficients corresponding to that parameter would be zero.

The ensemble average,

$$\langle x_i \rangle = \frac{1}{2\pi} \int_{-\pi}^{\pi} x_i[k_1(s), \dots, k_m(s)] ds \quad (12)$$

can be expressed in terms of the Fourier coefficients as

$$\langle x_i \rangle^2 = A_0^{(i)2} + B_0^{(i)2} = A_0^{(i)2}. \quad (13)$$

The variance of x_i is then

$$\sigma_i^2 = \frac{1}{2\pi} \int_{-\pi}^{\pi} x_i^2 ds - \langle x_i \rangle^2. \quad (14)$$

Parseval's theorem can then be used to determine the

variance of x_i , i.e.

$$\langle x_i^2 \rangle = \frac{1}{2\pi} \int_{-\pi}^{\pi} x_i^2(s) ds = \sum_{j=-\infty}^{\infty} \{A_j^{(i)2} + B_j^{(i)2}\}. \quad (15)$$

The variance and harmonics due to ω_i are expressed by

$$\sigma_{\omega_i}^{(i)2} = 2 \sum_{p=1}^{\infty} [A_{p\omega_i}^{(i)2} + B_{p\omega_i}^{(i)2}]. \quad (16)$$

The normalized sensitivity measure, the partial variance, $S_{\omega_i}^{(i)}$, is then defined by the ratio of the variance due to frequency ω_i to the total variance,

$$S_{\omega_i}^{(i)} = \frac{(\sigma_{\omega_i}^{(i)})^2}{(\sigma^{(i)})^2}. \quad (17)$$

Thus the $\{S_{\omega_i}^{(i)}\}$ represent an ordered measure of the sensitivity of the system to each of the $\{k_i\}$ parameters.

The FAST method requires that the system be solved to produce the output state variable values, the Fourier coefficients and subsequently the partial variances.

3. COMPUTATIONAL IMPLEMENTATION OF THE FAST ALGORITHM

Application of the FAST method requires the numerical evaluation of the Fourier coefficients, $A_{p\omega_i}^{(i)}$ and $B_{p\omega_i}^{(i)}$. This in turn requires the x_i be evaluated as s ranges over $[-\pi, \pi]$. Restricting the frequency set to odd integers reduces the range of s to $[-\pi/2, \pi/2]$. In this case

$$x(\pi - s) = x(s)$$

$$x(-\pi + s) = x(-s)$$

$$x\left(\frac{\pi}{2} + s\right) = x\left(\frac{\pi}{2} - s\right)$$

$$x\left(-\frac{\pi}{2} + s\right) = x\left(-\frac{\pi}{2} - s\right) \quad (18)$$

and the Fourier coefficients can be expressed as:

$$A_j^{(i)} = \begin{cases} 0 & ; j \text{ odd} \\ \frac{1}{\pi} \int_0^{\pi/2} [x_i(s) + x_i(-s)] \cos js ds & ; j \text{ even} \end{cases} \quad (19)$$

and

$$B_j^{(i)} = \begin{cases} 0 & ; j \text{ even} \\ \frac{1}{\pi} \int_0^{\pi/2} [x_i(s) - x_i(-s)] \sin js ds & ; j \text{ odd} \end{cases} \quad (20)$$

The actual number of points at which the system must be evaluated can be derived from the Nyquist criterion [6], and is found to be

$$r \geq N\omega_{\max} + 1. \quad (21)$$

Where r is the number of solution points and N an even integer. For convenience in calculating the Fourier coefficients, the additional condition

$$2r = 4q + 2 \quad (22)$$

where q is an integer is also imposed. The values of s are taken to be equally spaced throughout the range $[-\pi/2, \pi/2]$.

$\pi/2$], and the discrete points at which x_i is calculated in the Fourier space are given by

$$s_j = \frac{\pi}{2} \left[\frac{2j-r-1}{r} \right] \quad j = 1, 2, \dots, r. \quad (23)$$

The following difference expressions for Fourier coefficients can be derived by a simple numerical quadrature technique [4, 7],

$$A_j^i = 0 \quad (j \text{ odd}) \quad (24)$$

$$B_j^i = 0 \quad (j \text{ even}) \quad (25)$$

$$A_j^i = \frac{1}{2q+1} \left[x_0^i + \sum_{k=1}^q (x_k^i + x_{-k}^i) \cos \left(\frac{\pi j k}{2q+1} \right) \right]; \quad (j \text{ even}) \quad (26)$$

$$B_j^i = \frac{1}{2q+1} \left[\sum_{k=1}^q (x_k^i - x_{-k}^i) \sin \left(\frac{\pi j k}{2q+1} \right) \right]; \quad (j \text{ odd}) \quad (27)$$

where x^i replaces x_i for notational purposes.

Interference between the frequencies will occur as a result of this numerical evaluation when

$$q\omega_j = p\omega_l [\text{Mod}(N\omega_{\max} + 1)] \quad (28)$$

which results in

$$|A_{p\omega_l}^{(i)}|^2 + |B_{p\omega_l}^{(i)}|^2 = |A_{q\omega_j}^{(i)}|^2 + |B_{q\omega_j}^{(i)}|^2 \quad (29)$$

since

$$\sin \left[\frac{\pi q\omega_j}{N\omega_{\max} + 1} \right] = \pm \sin \left[\frac{\pi p\omega_l}{N\omega_{\max} + 1} \right] \quad (30)$$

and

$$\cos \left[\frac{\pi q\omega_j}{N\omega_{\max} + 1} \right] = \pm \cos \left[\frac{\pi p\omega_l}{N\omega_{\max} + 1} \right]. \quad (31)$$

This interference, called aliasing, is eliminating when

$$r\omega_l \leq N\omega_{\max} + 1. \quad (32)$$

N is therefore the maximum number of Fourier coefficients that may be retained in calculating the partial variances without interferences between the assigned frequencies. The expression for $S_{\omega_l}^{(i)}$ then becomes

$$S_{\omega_l}^{(i)} = \frac{2}{\sigma_i^2} \sum_{j=1}^N \left[|A_{j\omega_l}^{(i)}|^2 + |B_{j\omega_l}^{(i)}|^2 \right]. \quad (33)$$

Interference will also result from the use of an integer frequency set if the number of Fourier coefficients N used in the summation (33) is greater than or equal to the smallest frequency. To illustrate this consider (33) for the frequencies ω_l and $\omega_{l'}$,

$$S_{\omega_l}^{(i)} = A_{\omega_l}^{(i)2} + B_{\omega_l}^{(i)2} + \dots + A_{N\omega_l}^{(i)2} + B_{N\omega_l}^{(i)2}$$

$$S_{\omega_{l'}}^{(i)} = A_{\omega_{l'}}^{(i)2} + B_{\omega_{l'}}^{(i)2} + \dots + A_{N\omega_{l'}}^{(i)2} + B_{N\omega_{l'}}^{(i)2}.$$

If $N \geq \omega_1$, terms in the series for $S_{\omega_l}^{(i)}$ and $S_{\omega_{l'}}^{(i)}$ become identical. For example, if $N = \omega_1$, and if $\omega_{l'} > \omega_l$, there will be a term in the $S_{\omega_{l'}}^{(i)}$ series for which

$$A_{\omega_l \omega_{l'}}^{(i)} = A_{j\omega_{l'}}^{(i)}.$$

In such a case, the effect of the variation of parameter l enters spuriously into the partial variance for the variation of parameter l' .

In general, the interference between the higher harmonics will be eliminated when

$$N < \omega_{\min} - 1. \quad (37)$$

N is also related to the number of function evaluations required by (21), so it is desirable to use the minimum possible value, which is $N = 2$. Then a minimum frequency of at least three is sufficient to remove any harmonic interference effects from the partial variances. The final expression for the partial variances then becomes

$$S_{\omega_l}^{(i)} = \frac{2}{\sigma_i^2} \{ |B_{1\omega_l}^{(i)}|^2 + |A_{2\omega_l}^{(i)}|^2 \}. \quad (38)$$

The choice of $N = 2$ restricts the number of terms in the series to two. This is generally sufficient because the magnitude of the higher order terms in the Fourier series tend to decrease rapidly.

Implementation of the FAST technique also requires the selection of a frequency set, which can be done recursively using

$$\omega_1 = \Omega_n \quad (39)$$

$$\omega_i = \omega_{i-1} + d_{n+i-1} \quad (40)$$

as described in Cukier *et al.* [4]. The Ω_n and d_n we have used are tabulated in Table 1.

The final step in the FAST implementation is the determination of the transformation function $\{G_i\}$ that determine the actual search curve traversed in s -space. If the probabilities of occurrence for the parameters $\{k_i\}$ are independent, the probability density describing their effects has the form,

$$P(k_1, k_2, \dots, k_m) = P_1(k_1)P_2(k_2) \dots P_m(k_m). \quad (41)$$

In this case it can be shown that the transformation functions must obey the relation [5]

$$\pi(1-x^2)^{1/2} P_i(G_i) \frac{dG_i(x)}{dx} = 1 \quad (42)$$

with the initial conditions $G_i(0) = 0$. A tabulation of four different search curve formulations and their transformation functions is given in Table 2.

The parameter probability distributions used to derive these curves are described in Cukier *et al.* [3]. The first search curve is suitable for cases with small variations in the uncertain parameters while the second and third are applicable to cases with large variations.

4. PROGRAM DESCRIPTION AND OPERATION

A flowchart of the FAST program is shown in Fig. 6. There are two user interfaces with the program. One is the input data set which contains the following information; program description cards, control cards, analysis times (optional), and parameter cards. The second interface is a user supplied subroutine, called F , that calculates the state variable values for a given parameter combination. When the state variables must

Table 1. Parameters used in calculating frequency sets free of interferences to fourth order

N	Ω_n	d_n	N	Ω_n	d_n
1	0	4	26	385*	416
2	3	8	27	157	106
3	1	6	28	215	208
4	5	10	29	449	328
5	11	20	30	163	198
6	1	22	31	337	382
7	17	32	32	253	88
8	23	40	33	375	348
9	19	38	34	441	186
10	25	26	35	673	140
11	41	56	36	773	170
12	31	62	37	875	284
13	23	46	38	873	568
14	87	76	39	587	302
15	67	96	40	849	438
16	73	60	41	623	410
17	85	86	42	637	248
18	143	126	43	891	448
19	149	134	44	943	388
20	99	112	45	1171	596
21	119	92	46	1225	216
22	237	128	47	1335	100
23	267	154	48	1725	488
24	283	196	49	1663	166
25	151	34	50	2019	0

Table 2. Search curves for Fourier Amplitude Sensitivity Test computer program

APPLICATION	$k_j(s)$	MEAN VALUE \bar{k}_j	NOMINAL VALUE \bar{k}_j
ADDITIVE VARIATION	$k_j(s) = \bar{k}_j [1 + \bar{v}_j \sin \omega_j s]$	$\frac{k_j^u + k_j^l}{2}$	$\frac{k_j - k_j^l}{k_j + k_j^l}$
EXPONENTIAL VARIATION	$k_j(s) = \bar{k}_j \exp [\bar{v}_j \sin \omega_j s]$	$\sqrt{k_j^u k_j^l}$	$\frac{1}{2} \ln \left(\frac{k_j^u}{k_j^l} \right)$
PROPORTIONAL VARIATION	$k_j(s) = \bar{k}_j \exp [v_j \sin \omega_j s]$ $k_j^u = \alpha \bar{k}_j, k_j^l = \left(\frac{\bar{k}_j}{\alpha} \right)$	\bar{k}_j	$\ln(\alpha)$
SKewed VARIATION	$k_j(s) = v_j \left[\frac{a_j + \beta_j \sin \omega_j s - 1}{a_j + \beta_j \sin \omega_j s} \right]$ $k_j > \left(\frac{k_j^u + k_j^l}{2} \right)$	$v_j \left(\frac{a_j - 1}{a_j} \right)$	$\alpha_j = \frac{1}{2} \left[\frac{r^u}{r^u - 1} + \frac{r^l}{r^l - 1} \right]^b$ $\beta_j = \frac{-a_j (r^u + r^l - 2)}{(r^u - r^l)}$ $v_j = -\bar{k}_j \left[\frac{r^u + r^l - 2r^u r^l}{r^u + r^l - 2} \right]$

^a k_j^u = upper limit for parameter, k_j^l = lower limit for parameter

^b $r^u = k_j^u / \bar{k}_j, r^l = k_j^l / \bar{k}_j$

be calculated numerically, the user must also provide a subroutine to perform this function. For chemical kinetic applications several existing differential equation solvers can be easily adopted.

The input information is stored in an array called *P*. Subroutine *F* must access *P* in the same sequence that the parameters were specified on the input cards. The state variables calculated in the *F* subroutine are returned in an array named *C*. The structure of this array is shown in Fig. 7. An example of subroutine *F* for the sample problem in Section 5 is given in Fig. 8. The detailed fields and formats for the input file are shown in Table 3.

The default for the number of analysis times is one, and the default for the number of terms in the partial variance series is two. If this latter default is to be changed, care must be exercised to be sure that the

number of points at which *x* and the Fourier coefficients are evaluated is also modified so that interferences between the parameters will not occur.

Five files can be accessed during execution of the program. These are described in Table 4. Whenever the option to save the results is used, both file IDOUT and file IDISC must be allocated. IDOUT must be allocated when the reanalysis option is specified, and IDPLT must be allocated when the option to plot the partial variances is used. ICARD and IPRIN must be allocated at all times.

Several of the arrays used in the FAST program can become quite large for problems involving several parameters, output state variables and/or analysis times. The default sizes for the program arrays are given in Table 5. The program tests the input requests to determine if the fault storage is sufficient, if not, the program

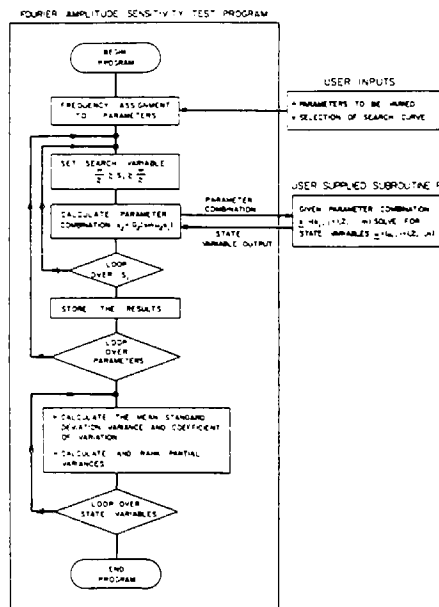


Fig. 6. Fourier Amplitude Sensitivity Test program.

SUBROUTINE F(NT,TIME,NPC,NP,PM,P,NSTAT,C)

INPUT VARIABLE	DESCRIPTION	VARIABLE TYPE
NT	NUMBER OF ANALYSIS TIMES	INTEGER
TIME	ARRAY OF ANALYSIS TIMES	REAL ARRAY
NPC	CURRENT PARAMETER COMBINATION NUMBER	INTEGER
NP	NUMBER OF PARAMETERS	INTEGER
P	ARRAY OF PARAMETER VALUES	REAL ARRAY
NSTAT	NUMBER OF OUTPUT VARIABLES	INTEGER

OUTPUT VARIABLE	DESCRIPTION	VARIABLE TYPE
C	ARRAY OF STATE VARIABLE VALUES FOR EACH ANALYSIS TIME	REAL ARRAY

DIMENSION TIME(NT), P(NP), C(NSTAT)

F FOR TEST PROBLEM A + X = 2X

UNLOAD THE PARAMETERS

```

    XD=P(1)
    AD=P(2)
    A=P(3)
    B=P(4)
    TA=P(5)

    SOLVE THE SYSTEM
    DO 10 J=1,NT
      T=TIME(J)
      RATE = A*EXP(-B/TA)
      S = 1.0 / (1.0 + (1.0 - AD)*EXP(-RATE * AD * T / TA))
      STORE THE SOLUTION IN THE OUTPUT ARRAY
      INT=(J-1)*NSTAT
      C(INT+1)=S
    10 CONTINUE
    RETURN
    END
  
```

Fig. 8. Description of subroutine F.

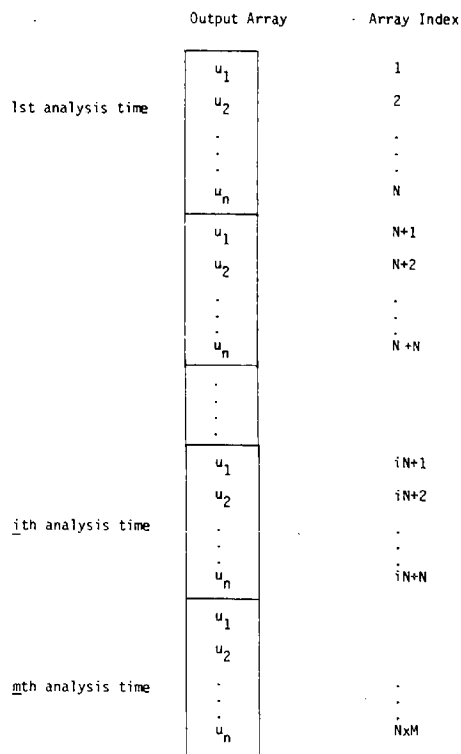
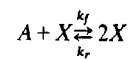


Fig. 7. Structure of the output array C

will terminate and write an error message describing which arrays require enlargement.

5. SAMPLE PROBLEM

To illustrate the use of the FAST program, a simple example consisting of a single, autocatalytic reaction,



is considered. The concentration of X is governed by

$$\frac{d[X]}{dt} = k_f[A][X] - k_r[X]^2$$

$$[X(0)] = [X]_0$$

If we assume that $[A]$ is constant, the dimensionless concentration

$$[\hat{X}] = \frac{k_f[X]}{k_r[A]}$$

can be defined, and the differential equation solved to yield

$$[\hat{X}] = [1 - (1 - [\hat{X}]_0^{-1})^{-k_f[A]t}]^{-1}$$

For the purposes of sensitivity analysis, we express k_f in the Arrhenius form,

$$k_f = B_f e^{-C_f/T}$$

72A1

Control Card

							1515						
1							75						

Col.	Description
1-5	number of analysis times
6-10	number of input parameters
11-15	number of output state variables
16-20	number of terms in the partial variance sum (default 2)
21-25	option to print amplitudes
26-30	option to print parameter combinations
31-35	option to print state variable outputs
36-40	multiplier N in $N=N_{max}+1$ (default 2)
41-45	option to print unsorted partial variances
46-50	option to save state variable outputs on disc file
51-55	option to reanalyze state variable outputs
56-60	option to plot partial variances
61-65	option to renormalize partial variances for plotting
66-70	option to print partial variances during reanalysis
71-75	option to print sorted partial variances during plotting

F10.0

Col	Description
1-10	Analysis time. Number of cards required is determined by the number of analysis times entered in the control card. (These cards may be omitted if the number of analysis times entered on the control card is zero.)

I5	I5	F10.0	F10.0	50A1
1	6	11		80

Col	Description
1-5	Parameter number. This number is the array index used for the P array in Subroutine F. The frequency assignment is done in the order in which the parameter cards are input. If an alternative frequency assignment is desired, the order in which the parameter cards are input should be changed, but <u>not</u> the parameter number.
6-10	Search curve type 0 = Fixed Parameter 1 = Small Parameter Variation 2 = Large Parameter Variation 3 = Parameter Variation Expressed as Fractional Change
11-20	Lower parameter limit or fixed parameter value
21-30	Upper parameter limit (type 1) or scale factor (types 2 and 3).
31-80	Parameter Description.

Table 4. Files used by FAST program

Name	Unit Number	Description
IDOUT	1	Reanalysis file. When the option to save the results is used, the output values are stored on this file. When the reanalysis option is used, the state values from this file are read as input.
IDISC	2	Save file. When the save option is on, all other program information including the partial variances is written to this file for later use.
IDPLT	3	Plot file. All information required for plotting is stored on this file during program execution and read back during the execution of the plot routine.
ICARD	5	User's input file.
IPRIN	6	Output print file.

Table 5. FAST program array default sizes

Array	Description	Default Size	Size Variable
IVARB	Variable Numbers	100	NVMAX
ITYPE	Variable Types	100	NVMAX
UBAR	Nominal Values	100	NVMAX
PBAR	Mean Values	100	NVMAX
PV	Variances	100	NVMAX
INDEX	Sort Array	100	NVMAX
PARM	Parameter Combinations	100	NVMAX
DESC	Parameter Descriptions	(48,100)	NVMAX
IW	Frequency Set	50	NPMAX
TIME	Analysis Times	50	NTMAX
OUTPT	Parameter Output	200	NOMAX
FI	Output for All Parameter Combinations	2000	NSMAX
NVMAX	Max Number of Input Parameters		100
NPMAX	Max Number of Variable Parameters		50
NTMAX	Max Number of Analysis Times		50
NOMAX	Max Storage for Each Parameter Combination		200
NSMAX	Max Storage for All Parameter Combinations		2000
NEQN	Number of Solutions for Each Combination		no limit
NSTAT	Number of State Variable Outputs		no limit

We wish to examine the sensitivity of $[\hat{X}]$ to $[\hat{X}]_0$, $[A]$, B , C , and T from $t = 0$ to $t = 2$. The nominal values and ranges of variation of these five parameters are given in Table 6.

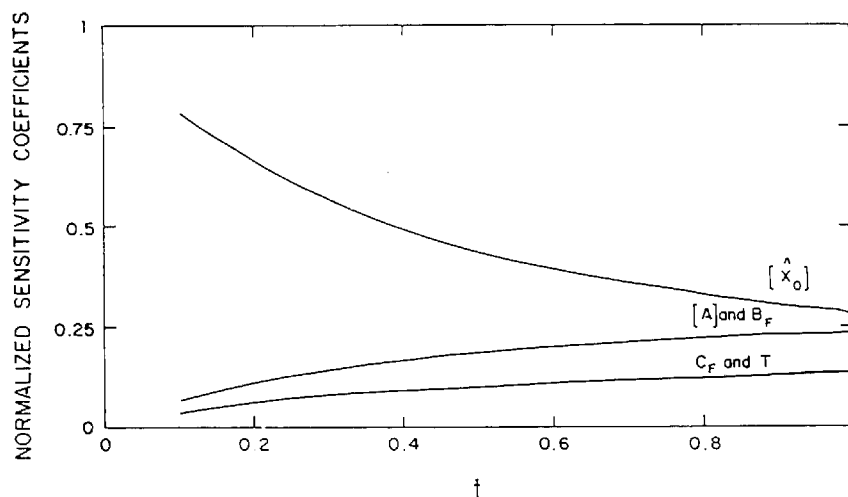
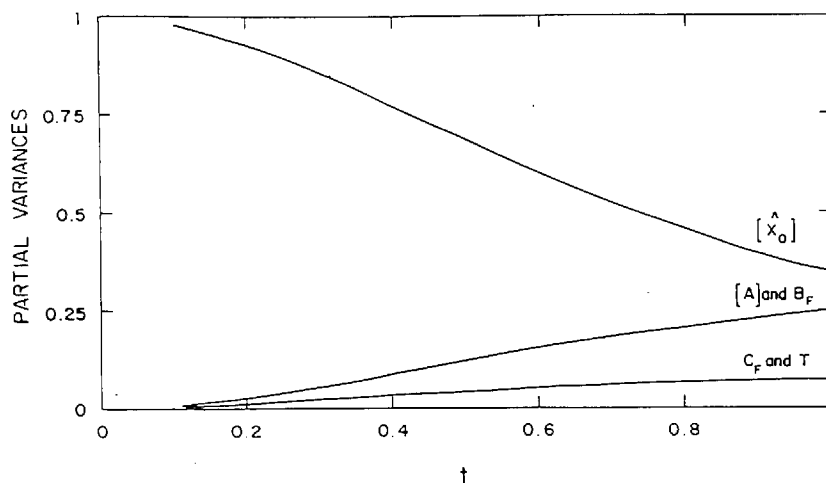
Figure 9 shows the first-order normalized sensitivity coefficients as a function of time evaluated at the nominal values of Table 6. These are defined by

$$\rho_i(t) = \frac{\left| \frac{\partial \hat{x}}{\partial k_i} \Delta k_i \right|}{\sum_{j=1}^m \left| \frac{\partial \hat{x}}{\partial k_j} \Delta k_j \right|}$$

Figure 10 presents the partial variances for the 5 parameters as determined by the FAST method with the

Table 6. Parameter variations for autocatalytic system

Parameter	Nominal Value	Range of Uncertainty ($\pm 5\%$)
\hat{X}_0	0.15	0.1425 - 0.1575
$[A]$	1.73	1.644 - 1.817
B_f	1.0	0.95 - 1.05
C_f	165.0	156.8 - 173.3
T	300.0	285.0 - 315.0

Fig. 9. First-order sensitivity coefficients for the reaction $A + X \rightleftharpoons 2X$.Fig. 10. Partial variances from the FAST method for the reaction $A + X \rightleftharpoons 2X$.

$\pm 5\%$ variations of Table 6 using search curve 1 of Table 2. We note first that the first-order sensitivities of $[\hat{X}]$ to variations in $[A]$ and B_f are identical because these two parameters appear as a product in $[\hat{X}]$. The same behavior is noted for C_f and T . As long as the uncertainty ranges chosen for these two sets of parameters

are the same, the partial variances of $[A]$ and B_f and C_f and T are identical, as seen in Fig. 10. The qualitative results of both the first-order sensitivity coefficients and the FAST partial variances are the same, although the relative magnitudes differ somewhat. A difference in relative magnitudes is expected since the first-order sen-

sitivity coefficients are computed at the nominal values, whereas the FAST partial variances involve simultaneous variation of all five parameters over their range of uncertainty, in this case $\pm 5\%$. Both sets of calculations show that $[\dot{X}]$ is most sensitive to $[A]$ and B_f . Note that the FAST method shows that the sensitivity of $[\dot{X}]$ to $[\dot{X}]_0$ close to $t=0$ is larger than indicated by the first order sensitivity coefficient.

Acknowledgement—This work was supported by U.S. Environmental Protection Agency grant R805537.

NOMENCLATURE

A	constant chemical species
$A_j^{(i)}$	j th Fourier cosine coefficient for the i th state variable
B_f	pre-Arrhenius rate term
$B_j^{(i)}$	j th Fourier sine coefficient for the i th state variable
C_f	activation energy term
d_n	frequency set generation parameter
$f(\mathbf{x}; \mathbf{k})$	general system function
G_t	transformation function
k_f	forward rate constant
k_i	i th uncertain parameter
k_i^l	lower limit of i th uncertain parameter
k_i^u	upper limit of i th uncertain parameter
k_r	reverse rate constant
m	number of uncertain parameters
n	number of state variables
N	number of Fourier coefficients
$p(\mathbf{k})$	probability distribution of the uncertain parameters \mathbf{k}
q	quadrature index
r	number of numerical solution points
r^l	ratio of parameter lower limit and mean value
r^u	ratio of parameter upper limit and mean value
s	Fourier space variable

s_j	discrete Fourier space variable
$S_j^{(i)}$	partial sensitivity of the i th state variable to the j th uncertain parameter
T	temperature
x	state variable
x_k^i	the value of the i th state variable at the k th numerical solution point
X	chemical species
\bar{X}	normalized chemical species
α_j	search curve parameter
β_j	search curve parameter
σ_i^2	partial variance of the i th state variable
ρ_i	normalized linear sensitivity coefficient for the i th state variable
ω_j	Fourier frequency assigned to the j th parameter
$\bar{\nu}_j$	nominal value of the j th uncertain parameter
Ω_n	frequency set generation parameter
$\langle \rangle$	ensemble average quantity
$-$	time average quantity

REFERENCES

1. R. I. Cukier, C. M. Fortuin, K. E. Shuler, A. G. Petschek & J. H. Schaibly, *J. Chem. Phys.* **59**(8), 3873 (1973).
2. J. H. Schaibly & K. E. Shuler, *J. Chem. Phys.* **59**(8), 3879 (1973).
3. R. I. Cukier, J. H. Schaibly & K. E. Shuler, *J. Chem. Phys.* **63**(3), 1140 (1975).
4. R. I. Cukier, H. B. Levine & K. E. Shuler, *J. Comp. Phys.* **26**(1), 1 (1978).
5. H. Weyl, *Amer. J. Math.* **60**, 889 (1938).
6. K. G. Beauchamp & C. K. Yuen, *Digital Methods for Signal Analysis*. George Allen and Unwin, London (1979).
7. M. Koda, G. J. McRae & J. H. Seinfeld, *Int. J. Chem. Kinetics* **11**, 427 (1979).
8. R. J. Gelinas & J. P. Vajk, *Systematic Sensitivity Analysis of Air Quality Simulation Models*, Final Report to U.S. Environmental Protection Agency under Contract No. 68-02-2942, Science Applications, Inc., Pleasanton, California (1978).

10.5 Application of the Fourier Amplitude Sensitivity Test to Atmospheric Dispersion Problems

A major advantage of the Fourier Amplitude Sensitivity Test (FAST), introduced in the previous section, is that it enables a formal study of the relative influences of large parameter variations in nonlinear systems. As such the method is ideally suited for examining the effects of parameter uncertainties on the predictions of atmospheric dispersion models. In this research the system of most interest is the atmospheric diffusion equation.

$$\frac{\partial c}{\partial t} + \nabla \cdot (\underline{u}c) = \nabla \cdot (\underline{K}\nabla c) + R(c) \quad (10.22)$$

This equation describes the formation and transport of photochemical air pollution. The parameters and processes of most importance are: advective transport by the flow field, \underline{u} , turbulent diffusion characterized by the eddy diffusivities, \underline{K} , and the chemical reactions $R(c)$. In addition the source emissions, which enter the system (10.22) through the boundary conditions, have a major impact on the calculated results. This section discusses the application of two sensitivity analysis methods to a simplified representation of the full, three-dimensional airshed model.

While a complete sensitivity analysis of (10.22) has not as yet been undertaken, some preliminary steps have been made by studying individual elements of the basic model. For example, Falls et al. (1979)

investigated the influence of parameter variations on the predictions of a photochemical reaction mechanism. The results of that study are presented in Section 10.6. Koda et al. (1979a) used the FAST method to examine the effects of uncertainties in specification of the vertical turbulent transport. The system considered in their work was the one-dimensional form of (10.22)

$$\frac{\partial c}{\partial t} = \frac{\partial}{\partial z} K_{zz} \frac{\partial c}{\partial z} \quad (10.23)$$

with the boundary and initial conditions given by

$$K_{zz} \frac{\partial c}{\partial z} \bigg|_{z=0} = Q \quad (10.24)$$

$$\frac{\partial c}{\partial z} \bigg|_{z=Z_i} = 0 \quad (10.25)$$

$$c(z,0) = 0 \quad (10.26)$$

The principal finding from their study was that the concentration predictions were most sensitive to variations of the turbulent diffusivity, $K(z)$, close to the surface. In passing it is worthwhile to mention that this physically realistic result was also found when the direct and variational sensitivity analysis methods were applied to the problem.

Perhaps the most commonly employed form of (10.22) is the simple Gaussian plume approximation introduced by Pasquill (1961) and implemented in the well known workbook of Turner (1970). This formulation

is a good example to illustrate an application of the FAST method because the model can be solved analytically, it is widely used in practice and has not been subjected to extensive sensitivity analyses. The model can be derived from (10.22) by invoking the following assumptions: steady conditions, a uniform wind speed, u , in the x -direction, constant diffusivities, no chemical reaction and that transport in the flow direction is dominated by advection. Under these restrictions (10.22) can be written in the form

$$u \frac{\partial c}{\partial x} = K_{yy} \frac{\partial^2 c}{\partial y^2} + K_{zz} \frac{\partial^2 c}{\partial z^2} \quad (10.27)$$

A suitable set of boundary conditions for an initially pollutant free, unbounded atmosphere with no absorption at the ground is given by

$$-K_{zz} \left. \frac{\partial c}{\partial z} \right|_{z=0} = 0 \quad (10.28)$$

$$c(x, y, z) = 0; \quad x, y \rightarrow \pm \infty \quad (10.29)$$

If a single source of strength Q is located at an elevation H above the surface then the solution of the system (10.27- 10.29) is given by

$$c(x, y, z) = \frac{Q}{4\pi x \sqrt{K_{yy} K_{zz}}} \exp \left\{ -\frac{uy^2}{4xK_{yy}} \right\} \left[\exp \left\{ -\frac{u(z-H)^2}{4xK_{zz}} \right\} + \exp \left\{ -\frac{u(z+H)^2}{4xK_{zz}} \right\} \right] \quad (10.30)$$

In most applications the plume spreading is characterized in terms of the distance downwind from the source and as a result the diffusivities employed in (10.30) are often replaced by expressions of the form

$$\sigma_y^2 = 2K_{yy}t \quad (10.31)$$

$$\sigma_z^2 = 2K_{zz}t \quad (10.32)$$

The basic Gaussian plume model for the ground level concentration is then given by

$$c(x,y) = \frac{Q}{\pi u \sigma_y \sigma_z} \exp \left\{ -\frac{1}{2} \left(\frac{y}{\sigma_y} \right)^2 \right\} \exp \left\{ -\frac{1}{2} \left(\frac{H}{\sigma_z} \right)^2 \right\} \quad (10.33)$$

The dispersion coefficients σ_y and σ_z are determined from field experiments and are typically expressed in the form (Gifford, 1976)

$$\sigma = ax^b \quad (10.34)$$

where a and b are constants which depend on the atmospheric stability.

The coefficients used in the Turner Workbook are based on the initial work of Pasquill (1961) and Gifford (1961). While the values are often applied to a large range of stability and wind speed conditions, they were originally intended for use only under rather limited conditions: wind speeds greater than 2 m/s, nonbuoyant plumes, flow over open country and downwind distances of only a few kilometers (Gifford, 1976; Pasquill, 1976). In a study of the Gaussian model, Weber (1976) has

shown that the dispersion coefficients and the release height are some of the most critical parameters. Miller et al. (1979) reached a similar conclusion after an examination of field measurements. In an attempt to improve the predictions Lamb (1979) used Lagrangian similarity theory to describe the dispersion under unstable conditions. So far relatively few systematic studies have been made of the influence of parameter uncertainties on the predictions of the Gaussian model.

Because of the simple form of (10.33) it allows a straightforward evaluation of the partial derivatives of the concentration with respect to the different model parameters. These expressions are given by:

$$\frac{\partial c}{\partial Q} = \frac{c}{Q} \quad (10.35)$$

$$\frac{\partial c}{\partial u} = \frac{c}{u} \quad (10.36)$$

$$\frac{\partial c}{\partial H} = \frac{cH}{Z^2} \quad (10.37)$$

$$\frac{\partial c}{\partial \sigma_y} = \frac{c}{\sigma_y} \left[\left(\frac{y}{\sigma_y} \right)^2 - 1 \right] \quad (10.38)$$

$$\frac{\partial c}{\partial \sigma_z} = \frac{c}{\sigma_z} \left[\left(\frac{H}{\sigma_z} \right)^2 - 1 \right] \quad (10.39)$$

If $f(x) = ax^b$ then

$$\frac{\partial c}{\partial a} = \left(\frac{\partial c}{\partial \sigma} \right) x^b \quad (10.40)$$

$$\frac{\partial c}{\partial b} = \left(\frac{\partial c}{\partial \sigma}\right) abx^{b-1} \quad (10.41)$$

where σ can be either σ_y or σ_z . Given the system (10.35 - 10.41) it is possible to define a set of normalized sensitivities at each downwind distance.

$$\rho_i(x) = \frac{\left| \frac{\partial c(x)}{\partial k_i} \Delta k_i \right|}{\sum_{j=1}^m \left| \frac{\partial c(x)}{\partial k_j} \Delta k_j \right|} ; i=1,2,\dots,m \quad (10.42)$$

The expressions, $\rho_i(x)$, are analogous to the partial variances associated with the FAST method, however it is important to note that the partial derivatives are a local representation of the model sensitivity. The conditions chosen for the study are shown in Table 10.2.

Figures 10.6-10.8 depict the results of three calculations, two involve small perturbations and the other large variations in the model parameters. The first two cases were chosen to provide a means of comparing the FAST method with the linearized approximation (10.35 - 10.41). As expected both approaches produced similar results. Close to the source the major influence on the ground level concentration is from the vertical dispersion and in particular the coefficient $b(\sigma_z)$. Further downwind, at the location of maximum impact, the model predictions are most influenced by the horizontal dispersion and the source height.

TABLE 10.2
Parameters Studied in Gaussian Plume Model

PARAMETER (k)	NOMINAL VALUE k(0)	LARGE PARAMETER RANGE
Source Strength (g/s)	100	50 - 200
Wind Speed (m/s)	5	2.5 - 10
Release Height (m)	10	5 - 20
$\sigma_z(m) = ax^b$ $\left\{ \begin{array}{l} a \\ b \end{array} \right.$	32.0	16 - 64
	0.84	0.42- 1.68
$\sigma_y(m) = ax^b$ $\left\{ \begin{array}{l} a \\ b \end{array} \right.$	67.9	34 - 136
	0.93	0.47- 1.86

Note: the σ_z and σ_y values correspond to Pasquill-Gifford stability class D and have been extrapolated from Turner (1970).

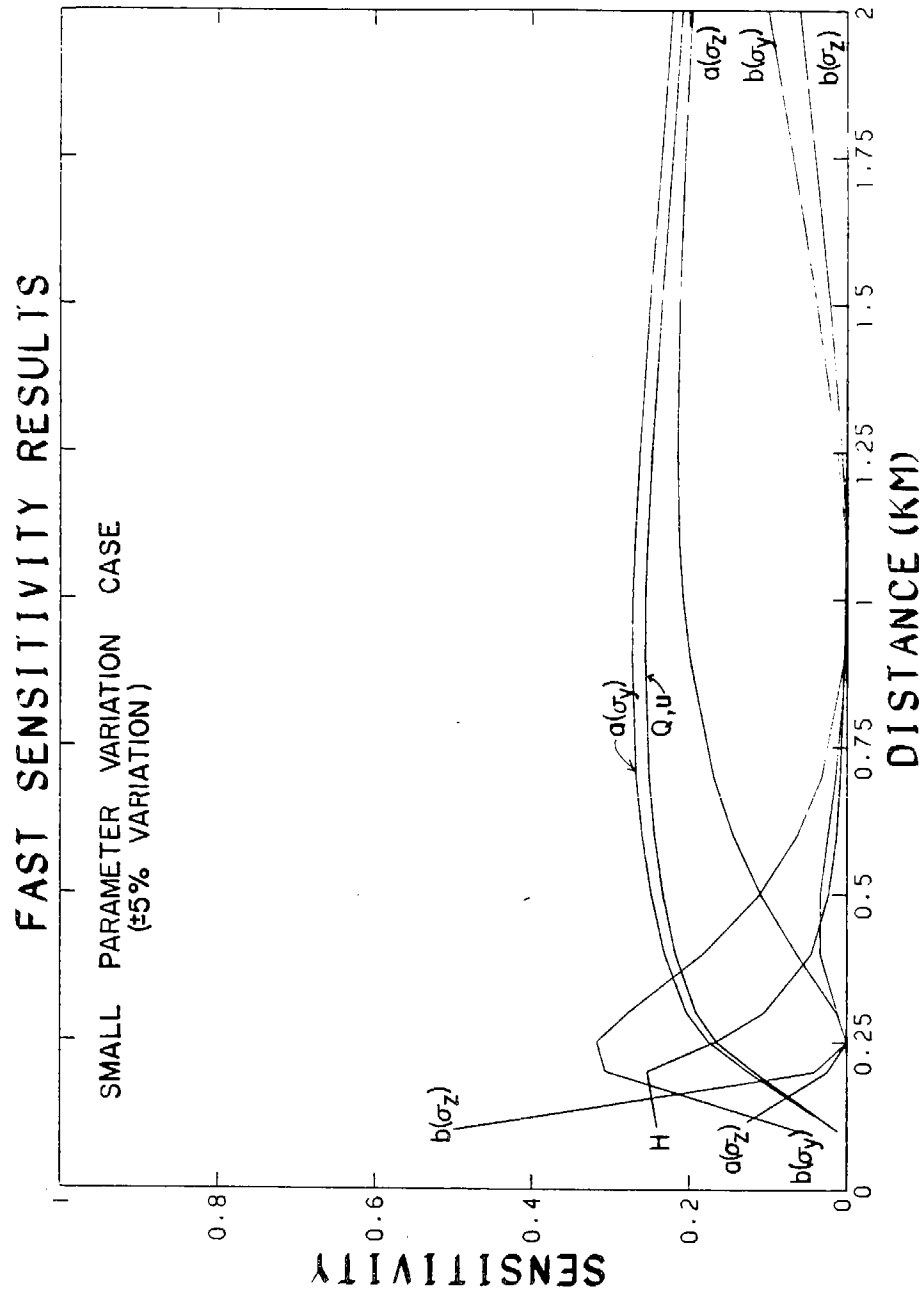


FIGURE 10.6

Linearized Sensitivity Analysis of a Gaussian Plume Model
($\pm 5\%$ Parameter Variation)

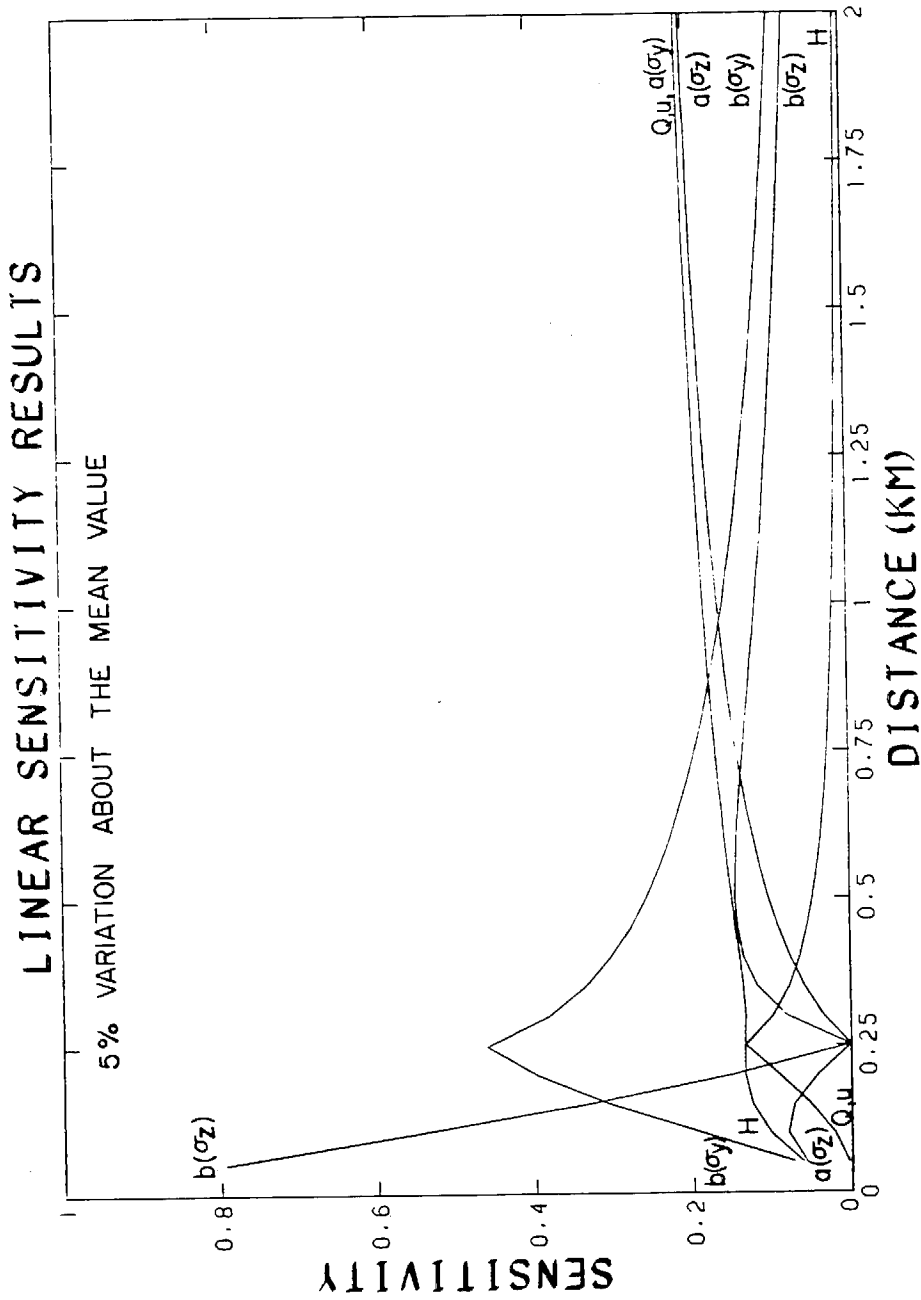


FIGURE 10.7

Fourier Amplitude Sensitivity Test (FAST) Analysis of a Gaussian Plume Model
(+ 5% Parameter Variation)

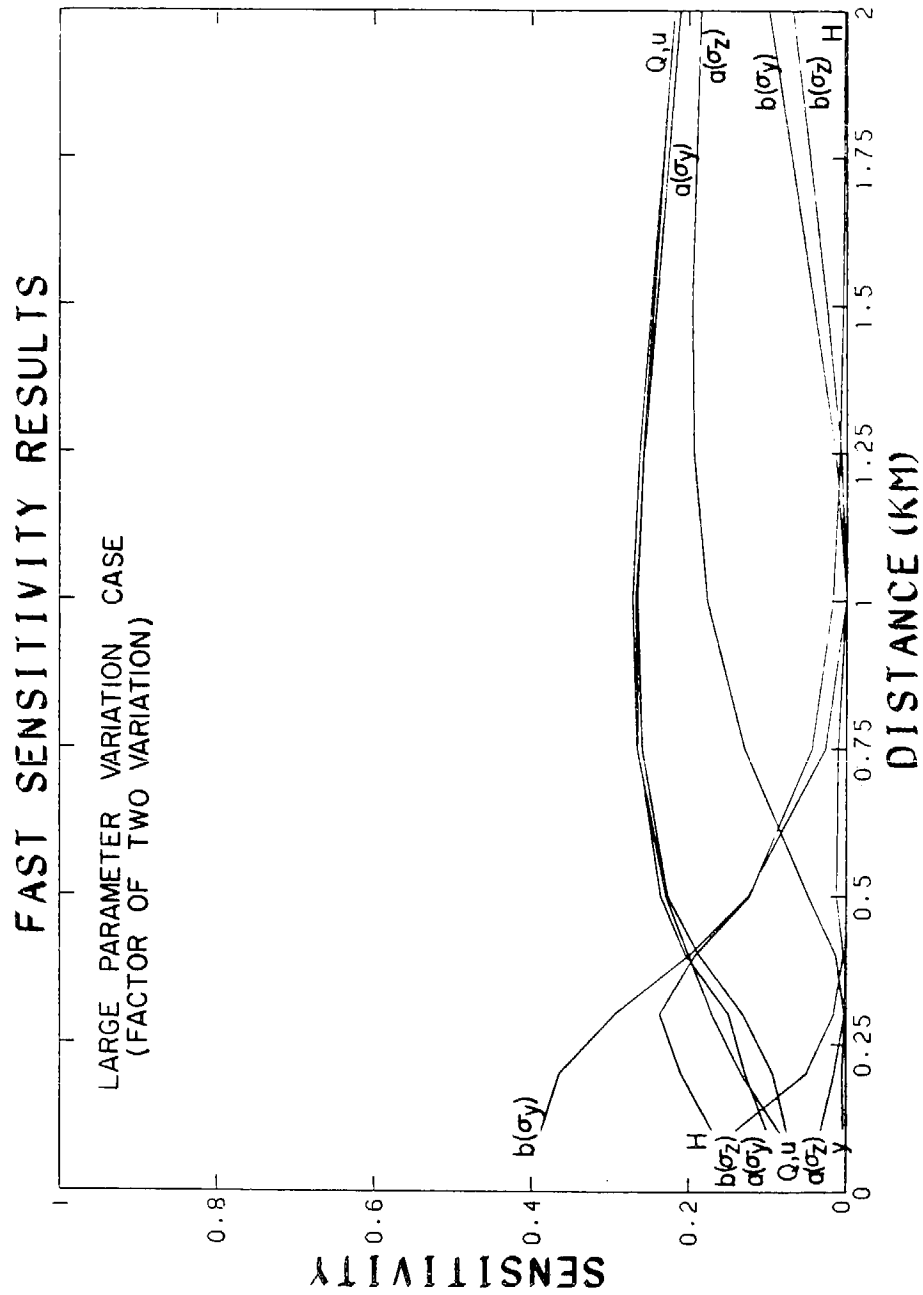


FIGURE 10.8

Fourier Amplitude Sensitivity Test (FAST) Analysis of a Gaussian Plume Model
(Factor of Two Parameter Variation)

In the far field, dispersion still dominates the concentration levels however the effects of wind speed and source strength are more apparent. The oscillation in the sensitivity coefficients associated with σ_z arise from the sign change which occurs in (10.42) when the downwind distance, x , exceeds the value $(H/a)^{1/b}$. The only major difference between the small and large variation cases is that the relative roles of σ_y and σ_z are reversed.

The results of the sensitivity analyses have important practical consequences. For the chosen condition both the effective release height and the dispersion coefficients have a major impact on the ground level concentration. Each of these parameters is strongly influenced by the vertical temperature structure. As a result the parameters, and in turn the model prediction, are quite dependent on the accuracy of the procedures adopted to characterize the atmospheric stability. Considering the known limitations of the Pasquill-Gifford stability classification scheme the findings of this study suggest that more attention needs to be given to developing better estimates of the plume rise and turbulent dispersion coefficients. Additional work is required to analyze the sensitivity of the complete atmospheric diffusion equation. The following section presents a detailed evaluation of the chemical reactions embedded in the airshed model.

10.6 Sensitivity and Uncertainty of Reaction Mechanism for
Photochemical Air Pollution

(Reprinted from Int. Journal of Chemical Kinetics, 11, 1137-1162.)

Sensitivity and Uncertainty of Reaction Mechanisms for Photochemical Air Pollution

ANDREW H. FALLS, GREGORY J. McRAE, and JOHN H. SEINFELD

Department of Chemical Engineering, California Institute of Technology, Pasadena, California 91125

Abstract

A sensitivity/uncertainty analysis is performed on a mechanism describing the chemistry of the polluted troposphere. General features of the photochemical reaction system are outlined together with an assessment of the uncertainties associated with the formulations of mechanistic details and rate data. The combined effects of sensitivity and uncertainty are determined using the Fourier amplitude sensitivity test (FAST) method. The results of this analysis identify the key parameters influencing the chemistry of NO_2 , O_3 , and PAN. Based on these findings, a series of recommendations are made for future experimental kinetic studies.

Introduction

A key problem underlying the development and evaluation of kinetic mechanisms for atmospheric chemistry is determining the sensitivity of the concentration predictions to those uncertain aspects of the reaction scheme. Such a determination can serve as a valuable guide for future experimental studies and for identifying those parameters that, when varied within accepted bounds, will be most influential on the predictions of the mechanism.

Although the qualitative aspects of the chemistry of the polluted troposphere appear to be reasonably well understood, there are many important details that still need to be investigated before a complete quantitative understanding of the photochemical smog system is possible. Several groups [1-7] have formulated chemical reaction mechanisms for polluted tropospheric chemistry. Some of these are based on specific surrogate hydrocarbon chemistries [1-4]. In others, attempts have been made to simulate the complex ambient atmospheric system by representing the general features of the hydrocarbon chemistry [2,5-7]. All mechanisms contain aspects of uncertainty, whether in unknown rate constants, in the importance of competing reaction paths, or in the manner of representing

the reaction of a generalized species. The measure of the accuracy of a mechanism is usually based on the extent of agreement between predicted concentration profiles and those generated experimentally in smog chambers.

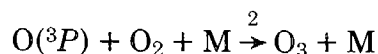
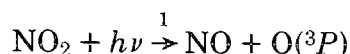
Even though the mechanisms [1-7] currently under study differ in details, the basic structure and qualitative behavior of each is similar. Thus, a separate study of the sensitivity of each of the mechanisms is unnecessary.

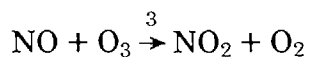
The object of this work is to examine closely the sensitivity of mechanisms for photochemical smog to those aspects of the chemistry that are currently uncertain. In doing so, it is hoped that certain general features of the photochemical system will emerge; features that are common to all mechanisms and for which estimates of the effect of uncertain parameters will be valuable. A similar study was carried out by Dodge and Hecht [8] in 1975 using the Hecht-Seinfeld-Dodge mechanism [9]. The mechanism of Falls and Seinfeld [7], which includes the latest available information on rate constants, reactions, and has all of the major features present in the lumped mechanisms of Whitten and Hogo [2], Gelinas and Skewes-Cox [5], and Martinez et al. [6] is used in this work. Sensitivity analyses are carried out using the Fourier amplitude sensitivity test (FAST) method of Shuler et al. [10], as described by Koda et al. [11]. Only a brief discussion of the method is given here; extensive details are available in the cited references.

This work begins with a brief discussion of the chemistry of photochemical smog, aimed at elucidating the general structure of the system within which mechanistic and kinetic uncertainties will be evaluated. Next, based on published reports of measured rate constants and product distributions for individual reactions, the uncertainty associated with each element of the Falls and Seinfeld mechanism [7] is estimated. The sensitivity analysis method is then described briefly, with emphasis on the implementation of the parameter uncertainty bounds and interpretation of the results. Finally, the results of the sensitivity analysis are presented and discussed in detail, leading to a ranking of the most influential elements of the mechanism based on the combined effects of uncertainty and sensitivity.

Photochemical Smog Chemistry

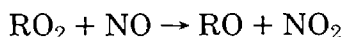
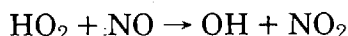
NO_2 , NO , and O_3 participate in the well-known cyclic set of reactions





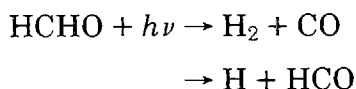
In the absence of significant competing reactions, a photostationary state is reached among reactions (1)–(3) in which the steady-state ozone concentration is given by $[\text{O}_3]_{\text{ss}} = k_1[\text{NO}_2]/k_3[\text{NO}]$. However, if a process other than that in reaction (3) can convert NO to NO_2 without consuming a molecule of O_3 , the ozone concentration will increase due to the increase in the NO_2/NO concentration ratio.

The two main processes by which NO is converted to NO_2 , without the loss of ozone, involve the hydroperoxy radical HO_2 and peroxyalkyl radicals RO_2 via

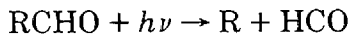


Hydroperoxy and peroxyalkyl radicals arise in the photochemical smog system from the photolysis and oxidation of hydrocarbon species.

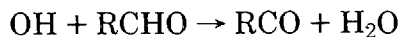
One source of peroxy radicals is from the photolysis of aldehydes that originate in the atmosphere both from emissions and as the products of chemical reactions. Formaldehyde photolysis, at wavelengths less than 370 nm, proceeds by either a molecular or a radical path:



Both hydrogen atoms and formyl radicals react rapidly with O_2 to produce HO_2 and $\text{HO}_2 + \text{CO}$, respectively. (There is still some disagreement concerning the $\text{HCO}-\text{O}_2$ reaction products; however, most evidence indicates that the products are HO_2 and CO .) Higher aldehydes also photodissociate to give alkyl and formyl radicals:

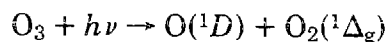
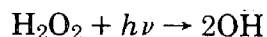
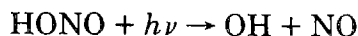


In addition to their photolysis, the reaction of aldehydes with OH serves as an important radical source and chain carrier. Hydroxyl radicals are generally thought to abstract the aldehydic H atom from aldehydes:



Oxidation of hydrocarbon species provides another source of hydroperoxy and peroxyalkyl radicals in the atmospheric system. The key species in the initial oxidation of hydrocarbons is the hydroxyl radical, the major sources of which are indirect chain-related processes such as the photolysis of aldehydes and the reaction of O_3 with olefins which lead to OH radicals through the reaction of HO_2 with NO. Minor sources of the hydroxyl radical include the photolysis of nitrous acid, the photolysis of hydrogen

peroxide, and the reaction of water with singlet oxygen atoms ($O(^1D)$) which originate from the photolysis of ozone:



Hydroxyl radical attack on hydrocarbons leads eventually to a variety of peroxy radicals, such as peroxyalkyl, peroxyacyl, and hydroxy-peroxy-alkyl radicals. These radical species convert NO to NO_2 , thereby producing ozone, and also serve as sources of alkoxy, acyl, hydroxy-alkoxy, and hydroperoxy radicals.

Major Uncertainties in Photochemical Smog Chemistry

With the recent elucidation of the chemistry of the reactions of OH and HO_2 with NO and NO_2 [12,14,15], the inorganic portion of the photochemical smog mechanism is now, by and large, well understood. Table I lists the mechanism under study along with its associated uncertainties. Figure 1 shows the structure and species interaction within the reaction mechanism. Uncertainties to be discussed here include:

- (a) Photolysis rates
- (b) Alkane-OH product distributions
- (c) Olefin-OH and olefin- O_3 product distributions
- (d) Aromatic chemistry
- (e) Alkoxy radical reactions
- (f) RO_x/NO_x reactions

A major uncertainty in the mechanism lies in the values of the photolysis rate constants. For analyzing smog chamber data, photolysis rate constants relative to the reported value for NO_2 are frequently used. Photolysis rate constants as a function of wavelength can be calculated from

$$k_j = \int_0^\infty \sigma_j(\lambda) \phi_j(\lambda) I(\lambda) d\lambda$$

where

- k_j = photolysis rate constant for species j
- $\sigma_j(\lambda)$ = absorption cross section of species j
- $\phi_j(\lambda)$ = quantum yield for the photolysis of species j
- $I(\lambda)$ = actinic irradiance

Data applicable to some atmospheric systems have been compiled by Schere and Demerjian [26]. For species such as NO_2 , HONO, and O_3 , for which extensive experimental determinations of absorption cross sections

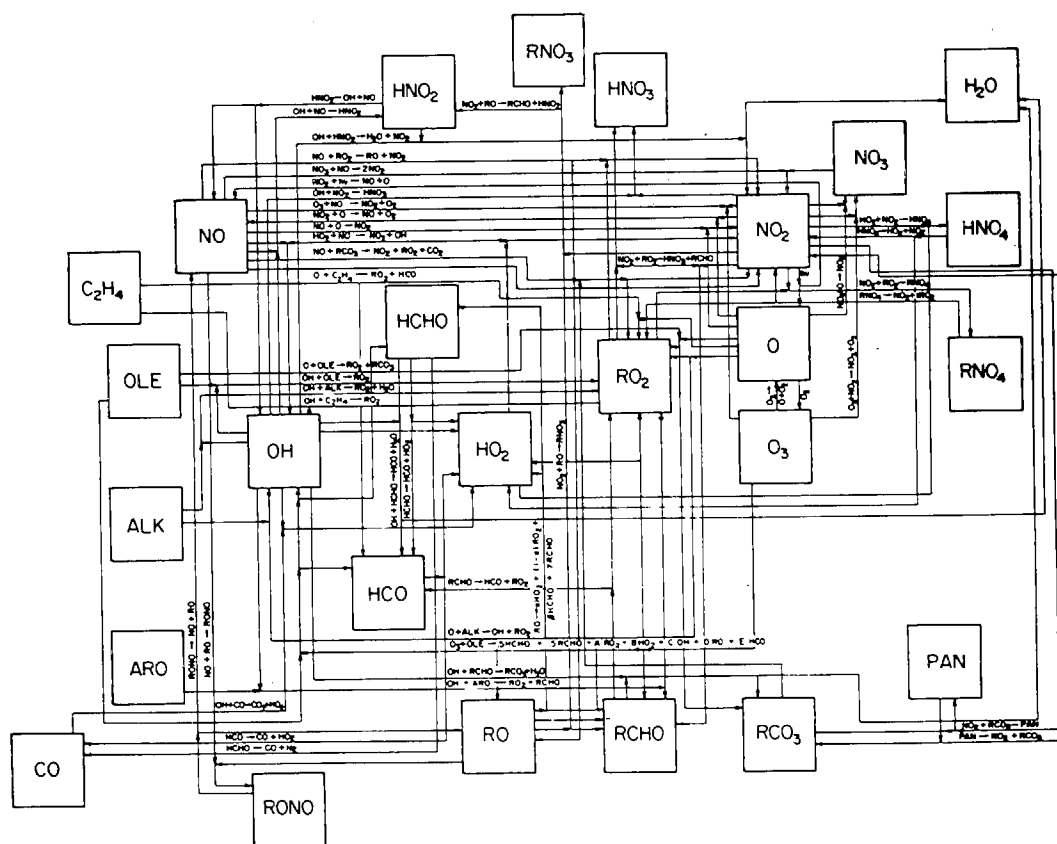
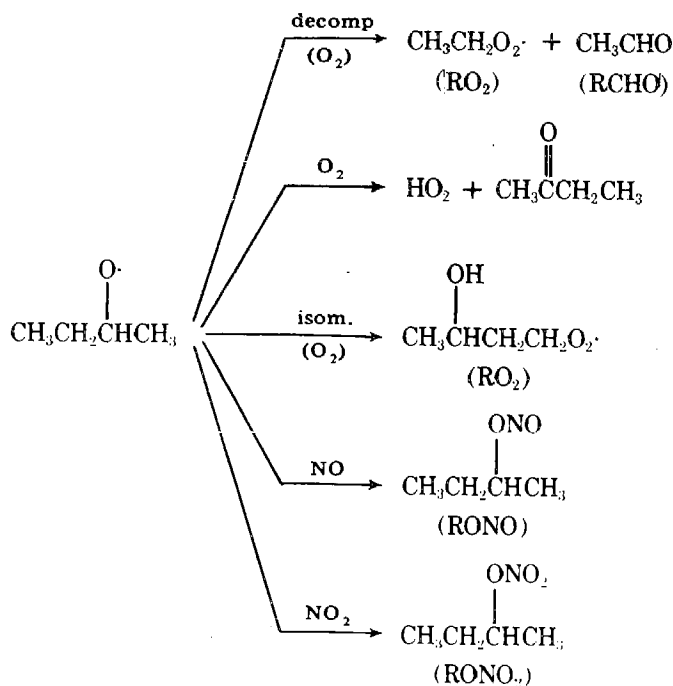


Figure 1. Flow diagram of Falls and Seinfeld reaction mechanism.

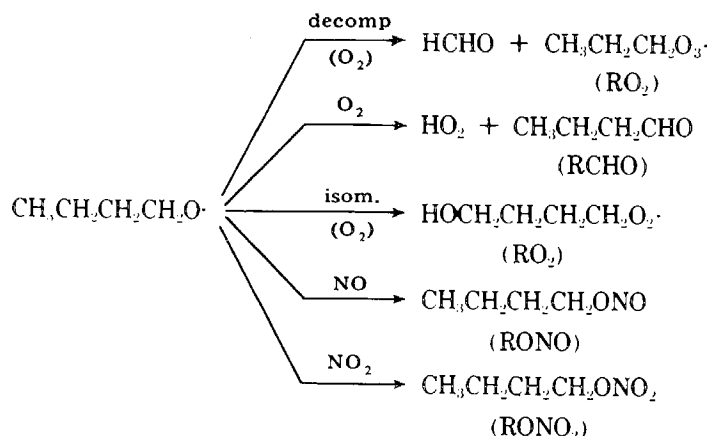
and quantum yields have been accomplished, photolysis rate constants are thought to be fairly reliable. However, since cross section and quantum yield data for formaldehyde, higher aldehydes, and alkyl nitrites are much less well characterized, many photolysis rate constants are subjected to large uncertainty. Of course, even if absorption cross sections and quantum yields could be determined accurately for all photosensitive species, uncertainties in atmospheric photolysis rate constants would still exist, as meteorological conditions, clouds, dust, and aerosols cause unknown variances in actinic irradiance.

Whereas rate constants in the inorganic portion of the mechanism are known fairly well, many more uncertainties, both in reaction rate constants and products, are associated with the organic reaction steps. Still to be determined are product distributions and reaction rate constants for the initial steps of the reactions of OH and hydrocarbon species, the largest uncertainties lying in the routes of the various radical species produced. For example, although rate constants for alkane-OH reactions are well established, the ratio of internal to external abstraction for all alkanes is not known. Addition to O₂ to form peroxyalkyl (RO₂) radicals can be

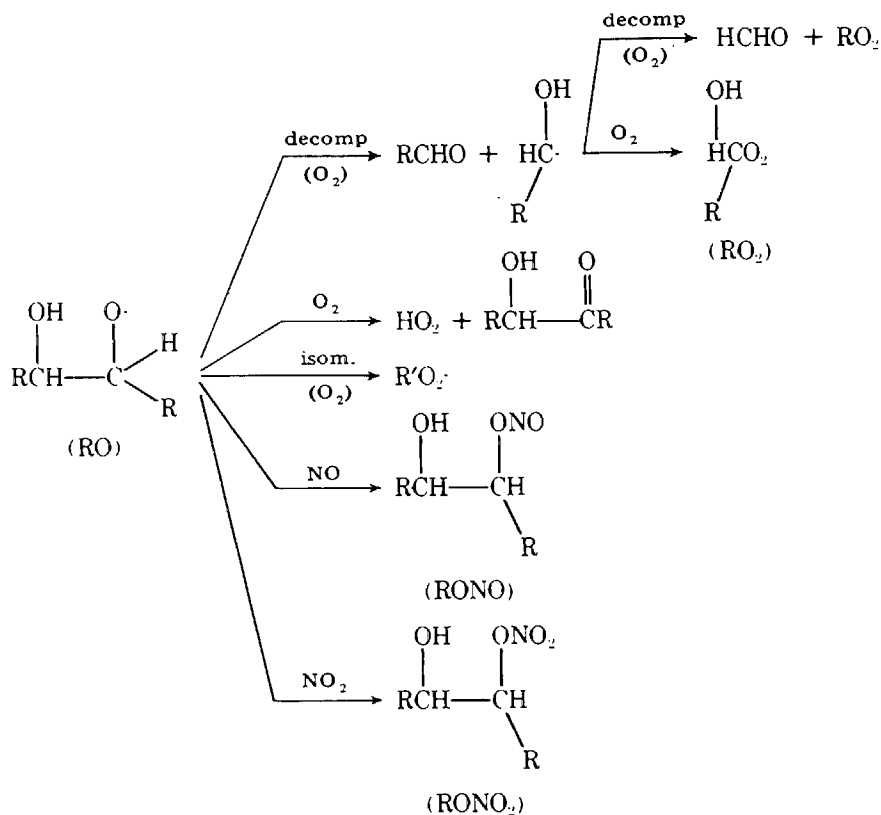
considered as the sole fate of the alkyl radicals first produced in alkane-OH reactions, but after the formation of alkoxy radicals through the conversion of NO to NO₂, the reaction mechanism becomes uncertain. Alkoxy radicals can decompose, react with O₂, isomerize, or react with NO or NO₂, with the importance and rate of each reaction path depending on the nature of the alkoxy group. Even for the most studied of the alkane-OH reactions, the relative rates between decomposition, isomerization, and reaction with O₂, NO, and NO₂ for alkoxy radicals have not been measured, but must be estimated [3]. The *n*-butane-OH reaction mechanism, for which the ratio of internal to external abstraction is known to be about 86-14 [3], gives rise to *sec*-butoxy and *n*-butoxy radicals. Various possible reaction pathways for these two radicals are:



and



Less well understood than alkane reaction mechanisms are olefin oxidation processes. Whereas reactions of alkanes with O_3 could be neglected, both olefin-OH and olefin- O_3 reactions occur to a significant extent. Olefin-OH reactions may proceed by addition or abstraction [35]. For smaller olefins, the addition path predominates. However, the abstraction fraction increases with the size of the olefin. Along the addition path for terminally bonded olefins, there is uncertainty as to the ratio of internal-to-external addition. Similar to alkyl radicals, the hydroxy-alkyl radicals formed in the initial OH addition to olefins are thought to immediately add O_2 to form hydroxy-peroxyalkyl radicals and thereafter react with NO to give NO_2 and hydroxy-alkoxyl species. The fate of the hydroxy-alkoxyl radicals is subject to speculation, although the analogous alkoxyl reaction paths of decomposition, isomerization, and reaction with NO, NO_2 , and O_2 are the most likely possibilities:



Of some importance in the photochemical smog system is the oxidation of olefins by ozone. The initial rate-determining step in the attack of ozone on the double bond of olefins is the formation of a molozonide, which, as the ring opens, results in a rapid equilibrium between the two possible forms of the oxy-peroxy biradical. The primary uncertainty in the olefin-ozone reaction mechanism lies in the fate of the oxy-peroxy biradical. Currently

it is thought that for lower olefins the biradical decomposes according to the Criegee mechanism of solution phase ozonolysis. However, α - and β -hydrogen abstraction mechanisms have also been proposed [27]. Figure 2 depicts the Criegee mechanism for the gas-phase ozonolysis of a general olefin, with reaction products analogous to those proposed by Dodge [28] for the propylene- O_3 mechanism.

Although much work has been devoted to the understanding of alkane and olefin systems, comparatively little research has been devoted to the study of atmospheric aromatic mechanisms. Recently, absolute rate constants have been determined for the reaction of OH with a series of aromatic hydrocarbons over a range of temperatures [29]. The initial aromatic-OH reaction step can be either abstraction or addition to the ring. At room temperature, the percentage of reaction proceeding by abstraction is on the order of 2–20%, depending on the individual hydrocarbon [29]. The aromatic-OH adduct presumably reacts with other atmospheric species such as O_2 , NO, or NO_2 . In addition, opening of the aromatic ring presumably occurs at some point in the atmospheric chemistry. Hendry [30] has postulated an aromatic mechanism that accounts for ring cleavage as well as for the formation of oxygenated species such as glyoxal, $H_2C_2O_2$, seen in smog chambers.

The aromatic-OH reaction products in Table I have been represented simply as RO_2 and an oxygenated species that is lumped with the aldehydes. Because the atmospheric chemistry of aromatics is poorly understood, little can be accomplished by speculating on reaction products and mechanisms at this point. For this reason, a sensitivity/uncertainty analysis associated with aromatic species has not been incorporated into this study.

The inherent uncertainty of the decomposition, reaction with O_2 , and isomerization of the alkoxyl and hydroxy-alkoxyl radical class in the present mechanism [7] has been concentrated into one reaction step:



As seen from the earlier discussions of alkoxyl radical behavior, RO always gives rise to either HO_2 or RO_2 in any of the decomposition, isomerization, or O_2 reaction pathways. Hence, the stoichiometric coefficients representing the fraction of HO_2 and RO_2 found in the lumped RO reaction should add to 1. Since the RO lumped species represents a large class of different-sized radicals and because splits between reaction paths for even specific radicals are unknown, α can have a value in the range 0 to 1. Many RO reaction routes produce aldehydes with some yielding two, as the one suggested by Martinez et al. [6]. Thus, $0 \leq \beta \leq 1$ and $0 \leq \gamma \leq 1$. Since the composition of the RO radical pool is continually changing during the course of a photooxidation, the actual values of α , β , and γ are functions of time. Thus, the selection of constant values of these coefficients introduces uncertainty.

TABLE I. Uncertainties associated with reaction rate constants in the Falls and Seinfeld mechanism [7].

Reaction	Nominal rate constant ppm-min units (30°C)	Uncertainty Range ^a	Refer- ence	Sensi- tivity Uncer- tainty Analys
1. $\text{NO}_2 + h\nu \rightarrow \text{NO} + \text{O}(^3\text{P})$	variable	$k_1 = \pm 20\%$	(est.)	*
2. $\text{O}(^3\text{P}) + \text{O}_2 + \text{M} \rightarrow \text{O}_3 + \text{M}$	2.03×10^{-5b}	$1.72 \times 10^{-5} \leq k_2 \leq 2.38 \times 10^{-5}$	12	
3. $\text{O}_3 + \text{NO} \rightarrow \text{NO}_2 + \text{O}_2$	2.55×10^1	$1.80 \times 10^1 \leq k_3 \leq 3.60 \times 10^1$	12	
4. $\text{NO}_2 + \text{O}(^3\text{P}) \rightarrow \text{NO} + \text{O}_2$	1.32×10^4	$1.15 \times 10^4 \leq k_4 \leq 1.52 \times 10^4$	12	
5. $\text{NO}_2 + \text{O}(^3\text{P}) \rightarrow \text{NO}_3$	3.52×10^3c	$2.22 \times 10^2 \leq k_5 \leq 5.58 \times 10^3$	12	
6. $\text{NO} + \text{O}(^3\text{P}) \rightarrow \text{NO}_2$	3.87×10^3	$2.45 \times 10^3 \leq k_6 \leq 6.13 \times 10^3$	12	
7. $\text{NO}_2 + \text{O}_3 \rightarrow \text{NO}_3 + \text{O}_2$	5.37×10^{-2}	$4.26 \times 10^{-2} \leq k_7 \leq 6.76 \times 10^{-2}$	12	
8. $\text{NO}_3 + \text{NO} \rightarrow 2\text{NO}_2$	2.72×10^4	$2.12 \times 10^4 \leq k_8 \leq 3.31 \times 10^4$	13	
9. $\text{NO}_3 + \text{NO}_2 \rightarrow \text{N}_2\text{O}_5$	3.69×10^3c	$1.06 \times 10^3 \leq k_9 \leq 1.21 \times 10^4$	13	
10. $\text{N}_2\text{O}_5 \rightarrow \text{NO}_3 + \text{NO}_2$	1.21×10^1	-	13	
11. $\text{N}_2\text{O}_5 + \text{H}_2\text{O} \rightarrow 2\text{HONO}_2$	$< 1.45 \times 10^{-5}$	-	12	
12. $\text{NO} + \text{NO}_2 + \text{H}_2\text{O} \rightarrow 2\text{HONO}$	2.11×10^{-9b}	-	12	
13. $\text{HONO} + \text{HONO} \rightarrow \text{NO} + \text{NO}_2 + \text{H}_2\text{O}$	1.38×10^{-3}	-	12	
14. $\text{O}_3 + h\nu \rightarrow \text{O}_2 + \text{O}(^1\text{D})$	variable	$k_{14} = \pm 30\%$	(est.)	
15. $\text{O}_3 + h\nu \rightarrow \text{O}_2 + \text{O}(^3\text{P})$	variable	$k_{15} = \pm 30\%$	(est.)	*
16. $\text{O}(^1\text{D}) + \text{M} \rightarrow \text{O}(^3\text{P}) + \text{M}$	4.14×10^4	$3.29 \times 10^4 \leq k_{16} \leq 5.21 \times 10^4$	12	
17. $\text{O}(^1\text{D}) + \text{H}_2\text{O} \rightarrow 2\text{OH}$	3.34×10^5	$2.65 \times 10^5 \leq k_{17} \leq 4.21 \times 10^5$	12	
18. $\text{HO}_2 + \text{NO}_2 \rightarrow \text{HONO} + \text{O}_2$	$< 10^{-3} k_{19}$	-	14	
19. $\text{HO}_2 + \text{NO}_2 \rightarrow \text{HO}_2\text{NO}_2$	1.58×10^3	-	15	
20. $\text{HO}_2\text{NO}_2 \rightarrow \text{HO}_2 + \text{NO}_2$	7.5	$3.3 \leq k_{20} \leq 17.1$	15	
21. $\text{HO}_2 + \text{NO} \rightarrow \text{NO}_2 + \text{OH}$	1.18×10^4	$9.59 \times 10^3 \leq k_{21} \leq 1.39 \times 10^4$	12	
22. $\text{OH} + \text{NO} \rightarrow \text{HONO}$	1.74×10^4c	-	12	
23. $\text{OH} + \text{NO}_2 \rightarrow \text{HONO}_2$	1.5×10^4c	$1.31 \times 10^4 \leq k_{23} \leq 2.07 \times 10^4$	12	*
24. $\text{HONO} + h\nu \rightarrow \text{OH} + \text{NO}$	variable	$k_{24} = \pm 30\%$	(est.)	*
25. $\text{CO} + \text{OH} \rightarrow \text{CO}_2 + \text{H}_2\text{O}$	4.36×10^2	$3.46 \times 10^2 \leq k_{25} \leq 5.49 \times 10^2$	12	
26. $\text{OH} + \text{HONO} \rightarrow \text{H}_2\text{O} + \text{NO}_2$	9.59×10^3	$9.15 \times 10^2 \leq k_{26} \leq 1.00 \times 10^4$	12	
27. $\text{HO}_2 + \text{HO}_2 \rightarrow \text{H}_2\text{O}_2 + \text{O}_2$	3.63×10^3	$1.82 \times 10^3 \leq k_{27} \leq 7.26 \times 10^3$	12	
28. $\text{H}_2\text{O}_2 + h\nu \rightarrow 2\text{OH}$	variable	$k_{28} = \pm 30\%$	(est.)	
29. $\text{OH} + \text{O}_3 \rightarrow \text{HO}_2 + \text{O}_2$	8.04×10^1	$4.03 \times 10^1 \leq k_{29} \leq 1.6 \times 10^2$	12	
30. $\text{HO}_2 + \text{O}_3 \rightarrow \text{OH} + 2\text{O}_2$	3.04	$1.52 \leq k_{30} \leq 6.08$	12	
31. $\text{HCHO} + h\nu \rightarrow 2\text{HO}_2 + \text{CO}$	variable	$k_{31} = \pm 30\%$	(est.)	*
32. $\text{HCHO} + h\nu \rightarrow \text{H}_2 + \text{CO}$	variable	$k_{32} = \pm 30\%$	(est.)	*
33. $\text{HCHO} + \text{OH} \rightarrow \text{HO}_2 + \text{CO}$	2.03×10^4	$1.62 \times 10^4 \leq k_{33} \leq 2.56 \times 10^4$	12	

TABLE I. (Continued)

Reaction	Nominal rate constant ppm-min units (30°C)	Uncertainty Range ^a	Refer- ence	Sensi- tivity/ Uncer- tainty Analysis
34. $\text{RCHO} + \text{hv} \rightarrow \text{RO}_2 + \text{HO}_2 + \text{CO}$	variable	$k_{34} = \pm 50\%$	(est.)	*
35. $\text{RCHO} + \text{OH} \rightarrow \text{RCO}_3$	2.1×10^4	-	16	
36. $\text{OLE} + \text{OH} \rightarrow \text{RO}_2$	variable ^d	-	17	
37. $\text{OLE} + \text{O} \rightarrow \text{RO}_2 + \text{RCO}_3$	variable ^d	-	17	
38. $\text{OLE} + \text{O}_3 \rightarrow 0.5\epsilon\text{RCHO} + (1-0.5\epsilon)\text{HCHO} + [0.5\epsilon(1-0.5\epsilon)(\xi+2\eta)+\rho\delta]\text{HO}_2 + 0.5\epsilon(2\xi+\eta)(1-0.5\delta)\text{RO}_2 + 0.5\epsilon\xi(1-0.5\delta)\text{OH} + 0.5\epsilon\eta(1-0.5\delta)\text{RO}$	variable ^d	$0 \leq \epsilon \leq 1, 0 \leq \xi \leq 1, 0 \leq \eta \leq 1, 0 \leq \rho \leq 1, 0 \leq \delta \leq 1$ Nominal values $\epsilon = 0.8, \xi = 0.68, \eta = 0.17, \delta = 1.0, \rho = 0.1$	17	*
39. $\text{ALK} + \text{OH} \rightarrow \text{RO}_2$	variable ^d	-	17	
40. $\text{ALK} + \text{O} \rightarrow \text{RO}_2 + \text{OH}$	variable ^d	-	17	
41. $\text{C}_2\text{H}_4 + \text{OH} \rightarrow \text{RO}_2$	1.14×10^4	$7.06 \times 10^3 \leq k_{41} \leq 1.87 \times 10^4$	12	
42. $\text{C}_2\text{H}_4 + \text{O} \rightarrow \text{RO}_2 + \text{HCO}$	1.24×10^3	$1.03 \times 10^3 \leq k_{42} \leq 1.49 \times 10^3$	12	
43. $\text{ARO} + \text{OH} \rightarrow \text{RO}_2 + \text{RCHO}$	variable ^d	-		
44. $\text{RO} \rightarrow \alpha\text{HO}_2 + (1-\alpha)\text{RO}_2 + \beta\text{HCHO} + \gamma\text{RCHO}$	3.6×10^5	$0 \leq \alpha \leq 1, 0 \leq \beta \leq 1, 0 \leq \gamma \leq 1$ Nominal Values $\alpha=1, \beta=1, \gamma=0$	3	*
45. $\text{NO} + \text{RO} \rightarrow \text{RONO}$	4.9×10^4	$k_{45} = (3.1 \times 10^4 - 1.55 \times 10^5)$	18-20	*
46. $\text{RONO} + \text{hv} \rightarrow \text{RO} + \text{NO}$	variable	$k_{46} = \pm 30\%$	(est.)	*
47. $\text{NO}_2 + \text{RO} \rightarrow \text{RONO}_2$	1.55×10^4	$k_{45}/(k_{47}+k_{48}) = (1.2-2.7)$	21-23	*
48. $\text{NO}_2 + \text{RO} \rightarrow \text{RCHO} + \text{HONO}$	1.35×10^3	$k_{47}/k_{48} = (0.08-0.23)$	21-23	*
49. $\text{NO}_2 + \text{RO}_2 \rightarrow \text{RO}_2\text{NO}_2$	5.5×10^3	$k_{49} = (1600-5500)$	(est.)	*
50. $\text{NO}_2 + \text{RO}_2 \rightarrow \text{RCHO} + \text{HONO}_2$	5.5 (est.)	-		
51. $\text{RO}_2\text{NO}_2 \rightarrow \text{NO}_2 + \text{RO}_2$	0.5 (est.)	$0.55 \leq k_{51} \leq 40.0$	37	*
52. $\text{NO} + \text{RO}_2 \rightarrow \text{NO}_2 + \text{RO}$	1.18×10^4 (est.)	$3000 \leq k_{52} \leq 12000$	(est.)	*
53. $\text{NO} + \text{RCO}_3 \rightarrow \text{NO}_2 + \text{RO}_2$	3.77×10^3	$k_{54}/k_{53} = 0.54 \pm 0.17$	25	
54. $\text{NO}_2 + \text{RCO}_3 \rightarrow \text{PAN}$	2.03×10^3		25	
55. $\text{PAN} \rightarrow \text{NO}_2 + \text{RCO}_3$	0.055	$0.0039 \leq k_{55} \leq 0.78$	25	
56. $\text{O}_3 \rightarrow \text{wall loss}$	variable ^e			
57. $\text{RO}_2 + \text{RO}_2 \rightarrow 2\text{RO} + \text{O}_2$	196.0	$50.0 \leq k_{57} \leq 600.0$	38	*

^a Uncertainties determined from reliabilities in rate constant measurements given in original references. Where no uncertainty was reported, either an estimate was made or the uncertainty neglected.

^b Units of rate constant are $\text{ppm}^{-2}\text{min}^{-1}$.

^c Pseudo-second-order rate constant for 1 atm air.

^d Rate constants for the reactions of lumped olefins, alkanes, and aromatics with OH, O, and O₃ were taken to be average mole-weighted ratio, based on initial compositions of each hydrocarbon class. Thus $k_1 = \sum_i k_i n_i / \sum_i n_i$ where k_1 is the lumped hydrocarbon rate constant, k_i the individual rate constant for hydrocarbon i , and n_i the number of moles of hydrocarbon i in the initial lumped mix.

^e Depends on smog chamber experiment, Winer [36].

TABLE II. Reactions in the RO_x-NO_x system.

	NO	NO ₂
RO	$\text{RO} + \text{NO} \rightarrow \text{RONO}^{\text{a}}$ $\xrightarrow{h\nu}$ $\rightarrow \text{RCHO} + \text{HNO}$	$\text{RO} + \text{NO}_2 \rightarrow \text{RONO}_2^{\text{b}}$ $\rightarrow \text{RCHO} + \text{HONO}$
RO ₂	$\text{RO}_2 + \text{NO} \rightarrow \text{NO}_2 + \text{RO}^{\text{c}}$ $\rightarrow \text{RONO}_2$	$\text{RO}_2 + \text{NO}_2 \rightleftharpoons \text{RO}_2\text{NO}_2^{\text{d}}$ $\rightarrow \text{RCHO} + \text{HONO}_2$
RCO ₃	$\text{RCO}_3 + \text{NO} \xrightarrow{\text{O}_2} \text{NO}_2 + \text{RO}_2 + \text{CO}_2^{\text{e}}$	$\text{RCO}_3 + \text{NO}_2 \rightleftharpoons \text{PAN}^{\text{f}}$

^a The primary pathway for the alkoxy-NO reaction is $\text{RO} + \text{NO} \rightarrow \text{RONO}$. Rate constants for this series of reactions have not been measured directly, but have been calculated from measured rates of the reverse reaction and thermodynamic estimates. Batt and co-workers [18] obtained rate constants for several of the above reactions that fall in the range of $3.1\text{--}6.2 \times 10^4 \text{ ppm}^{-1}\text{min}^{-1}$. Both Mendenhall and co-workers [19] and Batt and Milne [20] determined the rate constant for *t*-butoxyl + NO, obtaining 1.55×10^5 and $6.2 \times 10^4 \text{ ppm}^{-1}\text{min}^{-1}$, respectively. Thus the probable uncertainty in an estimated value of a particular RO-NO rate constant is a factor of 2-4. In addition to the path shown above there is an abstraction reaction, the fractional occurrence of which depends on the alkyl group. The abstraction fraction can be estimated based on the data of Batt and co-workers [18].

^b Two reaction paths for alkoxy-NO₂ reactions exist, addition and abstraction. For methoxyl + NO₂ the abstraction fraction has been estimated by Weibe and co-workers [21] to be 0.08 and by Barker and co-workers [23] to be 0.23. Rate constants for alkoxy-NO₂ reactions have been inferred from measured values of the ratio of the rate constants of alkoxy-NO to alkoxy-NO₂ reactions. Wiebe and co-workers [21] reported that for methoxyl radicals this ratio is 1.2, whereas Baker and Shaw [22] obtained 2.7 for the same ratio. Baker and Shaw [22] determined a ratio of 1.7 for *t*-butoxyl radicals. Absolute rate constants for RO-NO₂ reactions are then obtained on the basis of RO-NO rate constants.

^c The peroxyalkyl radical-NO reaction may proceed as shown. Conversion to NO to NO₂ occurs primarily by the first reaction. It has been postulated that the second reaction will occur a fraction of the time for longer chain peroxyalkyl radicals [$n > 4$]. Darnall and co-workers [32] estimated the ratio k_2/k_1 to be 0.09 and 0.16 for $n = 4$ and 5, respectively. Aside from the HO₂-NO reaction, rate constant values have not been measured for RO₂-NO reactions. A lower limit for the rate constants for these reactions can be estimated as $3 \times 10^3 \text{ ppm}^{-1}\text{min}^{-1}$ based on theoretical considerations.

^d Rate constants for the RO₂-NO₂ reaction and the RO₂NO₂ decomposition must be estimated.

^e Hendry and Kenley [31] report a value of $4900 \text{ ppm}^{-1}\text{min}^{-1}$ for $\text{CH}_3\text{C}(\text{O})\text{O}_2 + \text{NO}$, whereas Cox and Roffey [25] found $3800 \text{ ppm}^{-1}\text{min}^{-1}$.

^f The rate constant for the PAN formation step is determined by Hendry and Kenley [31] to be $1500 \text{ ppm}^{-1}\text{min}^{-1}$ and by Cox and Roffey [25] to be $2070 \text{ ppm}^{-1}\text{min}^{-1}$. PAN thermal decomposition rates are also reported by the two investigators.

Reactions in the RO_x/NO_x subsystem (Table II) are subject to degrees of uncertainty for two reasons. First, the rate constants reported for spe-

cific reactions in each lumped group differ among investigators. For instance, different PAN formation and decomposition rates have been determined by Cox and Roffey [25] and Hendry and Kenley [31]. Second, since the composition of the lumped radical classes changes throughout the degradation process of the different atmospheric hydrocarbon species, it is difficult to select accurate rate constants for reactions of the RO_x/NO_x system. The uncertainties associated with each reaction in the RO_x/NO_x network are summarized in Table II.

Sensitivity/Uncertainty Analysis

A sensitivity/uncertainty analysis can provide two different but related types of information. By individually perturbing parameters a small amount from their nominal values, say $\pm 5\%$, the absolute sensitivity of the predictions of the mechanism can be ascertained. A sensitivity/uncertainty analysis incorporates the same information and, in addition, takes into account the degree of uncertainty associated with each parameter, thereby generating a combined measure of sensitivity and uncertainty. Both types of analyses are important. For example, a parameter to which the predictions of the mechanism are not especially sensitive may have such a large range of uncertainty that, when all possible variations are considered, its influence on the predictions is rather substantial. On the other hand, a very sensitive parameter may have a small range of uncertainty, and therefore its overall influence on the mechanism, considering both sensitivity and uncertainty, may be lower than that of other parameters.

In many problems the uncertainties are such that linearized methods are no longer applicable. The FAST method, which overcomes this restriction, has been developed by Shuler et al. [10]. The particular advantage of this approach is that order of magnitude changes in parameter values can be easily accommodated. Basically the procedure involves a simultaneous variation of all the parameters over their individual ranges of estimated uncertainty. Formally the parameters are ranked in the order of importance by using normalized statistical measures called partial variances. These variances indicate the relative contribution of individual parameters to uncertainties in model predictions. The FAST analysis identifies the contribution of individual parameters to the total variance in each predicted species concentration. To determine the sensitivity of the mechanism, the method can be used with each parameter varied a small amount from its nominal value. Detailed descriptions of the technique are available elsewhere [10,11] and will not be repeated here.

Discussion of Results

Two types of the sensitivity/uncertainty analysis were performed on simulations of three different surrogate hydrocarbon smog chamber experiments carried out at the Statewide Air Pollution Research Center at the University of California, Riverside [33,34]. First, in order to ascertain the absolute sensitivity of the predictions of the mechanism to each of the reaction parameters being studied, runs were made in which all parameters of interest were perturbed from their nominal values by $\pm 5\%$. In a second set of cases, the parameters were permitted to vary over their entire uncertainty range, thus providing combined sensitivity and uncertainty information. The parameter values for these two cases are shown in columns 2 and 3 of Table I. Many of the reactions have been shown to have relatively little influence on concentration behavior [8]. Thus, only those rate constants of reactions for which an asterisk(*) exists in column 4 of Table I were subject to variation in the studies to be described.

Effects of the parameter variations on predictions of NO_2 , O_3 , and PAN were monitored. These output variables were chosen because air quality standards exist for NO_2 and O_3 , and because NO_2 and O_3 reflect the major features of the chemistry. To explore the effects of varying initial hydrocarbon- NO_x mixtures on the results of the study, smog chamber simulations with a wide range of initial conditions were examined. Tables III-VIII list the parameters and their partial variances, ranked according to their effect on each of the output variables, for each of the analyses performed.

TABLE III. Parameter rankings for case 1,^a small parameter variations.

Time	60 min.		120 min.		180 min.		240 min.		300 min.	
Rank	Parameter	Partial Variance	Parameter	Partial Variance	Parameter	Partial Variance	Parameter	Partial Variance	Parameter	Partial Variance
OUTPUT VARIABLE: NO_2										
1	α	0.310	k_{23}	0.472	k_{23}	0.583	k_{31}	0.354	α	0.320
2	k_{23}	0.309	α	0.310	k_1	0.310	α	0.233	k_{31}	0.286
3	k_{24}	0.193	k_{31}	0.080	α	0.073	β	0.200	β	0.203
4	k_{31}	0.111	β	0.051	k_{31}	0.026	k_1	0.077	k_{23}	0.074
5	β	0.030	k_1	0.025	k_{34}	0.017	k_{34}	0.056	k_{34}	0.051
OUTPUT VARIABLE: O_3										
1	k_1	0.363	k_{23}	0.317	α	0.328	α	0.340	α	0.345
2	α	0.196	α	0.297	k_{23}	0.305	k_{23}	0.278	k_{23}	0.254
3	k_{23}	0.181	k_{31}	0.130	k_{31}	0.148	k_{31}	0.159	k_{31}	0.163
4	k_{24}	0.120	k_1	0.102	β	0.106	β	0.131	β	0.150
5	k_{31}	0.083	β	0.071	k_1	0.038	k_{34}	0.032	k_{34}	0.035
OUTPUT VARIABLE: PAN										
1	k_{23}	0.391	k_{23}	0.485	k_{23}	0.432	k_{23}	0.386	k_{23}	0.350
2	k_{24}	0.212	α	0.187	α	0.213	α	0.230	α	0.245
3	k_{31}	0.153	k_{31}	0.161	k_{31}	0.171	k_{31}	0.181	k_{31}	0.183
4	α	0.128	β	0.078	β	0.110	β	0.135	β	0.153
5	β	0.035	β	0.026	β	0.025	k_{34}	0.019	k_{34}	0.020

^a Simulation: UCR 119J [32]. Initial conditions: $[\text{NO}_2] = 0.041$; $[\text{NO}] = 0.301$; $[\text{OLE}] = 0.039$; $[\text{ALK}] = 0.358$; $[\text{ARG}] = 0.070$; $[\text{ETH}] = 0.043$; $[\text{HCHO}] = 0.038$; $[\text{RCHO}] = 0.023$; $[\text{HONO}]$ (assumed) = 0.0; $k_1 = 0.32$; simulated NO_2 peak time = 200 min; $[\text{HC}/\text{NO}_x]_0 = 1.7$

TABLE IV. Parameter rankings for case 2,^a small parameter variations.

Time	60 min.		120 min.		180 min.		240 min.		300 min.	
Rank	Parameter	Partial Variance	Parameter	Partial Variance	Parameter	Partial Variance	Parameter	Partial Variance	Parameter	Partial Variance
OUTPUT VARIABLE: NO ₂										
1	k ₃₁	0.264	k ₃₁	0.378	k ₃₁	0.377	a	0.459	a	0.575
2	k ₁	0.191	a	0.194	a	0.321	k ₃₁	0.338	k ₃₁	0.265
3	s	0.139	k ₁	0.112	s	0.104	s	0.105	s	0.095
4	k ₂₃	0.128	s	0.091	k ₁	0.054	s	0.023	k ₃₄	0.015
5	c	0.086	k ₂₃	0.066	s	0.039	k ₂₃	0.020	s	0.013
OUTPUT VARIABLE: O ₃										
1	k ₁	0.473	k ₁	0.584	k ₁	0.696	k ₁	0.778	k ₁	0.839
2	a	0.274	a	0.243	a	0.187	a	0.134	a	0.086
3	k ₂₃	0.086	k ₂₃	0.072	k ₂₃	0.071	k ₂₃	0.069	k ₂₃	0.068
4	k ₃₁	0.056	k ₃₁	0.043	s	0.021	s	0.009	k ₅₂	0.003
5	s	0.032	s	0.035	k ₃₁	0.016	k ₃₁	0.003	s	0.002
OUTPUT VARIABLE: PAN										
1	k ₂₃	0.270	k ₃₁	0.290	k ₂₃	0.334	k ₂₃	0.380	k ₂₃	0.404
2	k ₁	0.216	k ₂₃	0.284	k ₃₁	0.306	k ₃₁	0.320	k ₃₁	0.344
3	k ₃₁	0.186	k ₁	0.219	k ₁	0.199	k ₁	0.145	k ₁	0.082
4	s	0.184	s	0.112	s	0.091	s	0.084	s	0.082
5	c	0.062	s	0.043	s	0.043	s	0.046	s	0.018

^a Simulation: UCR-121J [32]. Initial conditions: [NO₂] = 0.012; [NO] = 0.044; [OLE] = 0.04; [ALK] = 0.37; [ARO] = 0.066; [ETH] = 0.042; [RCHO] = 0.06; [HCHO] = 0.011; [HONO] (assumed) = 0.0; k₁ = 0.32; simulated NO₂ peak time = 30 min; [HC/NO_x]₀ = 10.5.

TABLE V. Parameter rankings for case 3,^a small parameter variations.

Time	60 min.		120 min.		180 min.		240 min.		300 min.	
Rank	Parameter	Partial Variance	Parameter	Partial Variance	Parameter	Partial Variance	Parameter	Partial Variance	Parameter	Partial Variance
OUTPUT VARIABLE: NO ₂										
1	a	0.289	a	0.423	a	0.433	a	0.441	a	0.445
2	k ₃₁	0.167	s	0.226	s	0.238	s	0.240	s	0.232
3	s	0.164	k ₃₁	0.197	k ₃₁	0.198	k ₃₁	0.198	k ₃₁	0.200
4	s	0.112	k ₂₃	0.035	k ₂₃	0.051	k ₂₃	0.048	k ₂₃	0.040
5	c	0.084	s	0.031	s	0.015	c	0.096	s	0.009
OUTPUT VARIABLE: O ₃										
1	a	0.464	a	0.463	a	0.458	a	0.448	a	0.401
2	k ₂₃	0.295	k ₂₃	0.210	s	0.190	s	0.189	k ₁	0.205
3	s	0.083	s	0.155	k ₂₃	0.165	k ₂₃	0.136	s	0.149
4	k ₃₁	0.042	k ₃₁	0.094	k ₃₁	0.120	k ₃₁	0.120	k ₂₃	0.117
5	s	0.027	k ₁	0.025	k ₁	0.034	k ₁	0.075	k ₃₁	0.088
OUTPUT VARIABLE: PAN										
1	k ₂₃	0.521	k ₂₃	0.348	a	0.287	a	0.297	a	0.284
2	a	0.169	a	0.249	k ₂₃	0.263	k ₂₃	0.227	k ₃₁	0.225
3	s	0.084	s	0.160	s	0.203	s	0.214	k ₂₃	0.224
4	s	0.074	k ₃₁	0.148	k ₃₁	0.188	k ₃₁	0.209	s	0.207
5	k ₃₁	0.070	s	0.042	s	0.026	s	0.021	s	0.021

^a Simulation: EC-237s [32]. Initial conditions: [NO₂] = 0.021; [NO] = 0.075; [OLE] = 0.030; [ALK] = 0.298; [ARO] = 0.035; [ETH] = 0.175; [HCHO] = 0.0; [RCHO] = 0.001; [HONO] (assumed) = 0.020; k₁ = 0.30; simulated NO₂ peak time = 30 min; [HC/NO_x]₀ = 5.57.

TABLE VI. Parameter rankings for case 4,^a large parameter variations.

Time	60 min.		120 min.		180 min.		240 min.		300 min.	
Rank	Parameter	Partial Variance	Parameter	Partial Variance	Parameter	Partial Variance	Parameter	Partial Variance	Parameter	Partial Variance
OUTPUT VARIABLE: NO ₂										
1	a	0.933	a	0.831	a	0.854	a	0.846	a	0.826
2	k ₂₃	0.018	b	0.055	a	0.091	b	0.105	b	0.122
3	k ₂₄	0.011	k ₅₁	0.031	k ₅₁	0.018	k ₅₁	0.009	k ₃₂	0.013
4	b	0.010	k ₂₃	0.019	b	0.008	k ₃₁	0.009	k ₃₁	0.010
5	k ₃₁	0.005	c	0.010	k ₃₁	0.006	k ₃₂	0.008	b	0.007
OUTPUT VARIABLE: O ₃										
1	a	0.861	a	0.861	a	0.855	a	0.849	a	0.834
2	b	0.033	b	0.065	b	0.086	b	0.097	b	0.106
3	k ₅₁	0.029	k ₅₁	0.023	k ₅₁	0.015	k ₅₁	0.010	k ₃₂	0.013
4	k ₅₁	0.015	b	0.011	b	0.008	k ₂₃	0.008	k ₂₃	0.009
5	c	0.009	k ₃₁	0.007	k ₂₃	0.007	b	0.006	k ₅₁	0.006
OUTPUT VARIABLE: PAN										
1	a	0.643	a	0.624	a	0.634	a	0.633	a	0.618
2	b	0.112	b	0.203	b	0.243	b	0.265	b	0.286
3	k ₅₁	0.061	a	0.048	b	0.031	k ₃₁	0.027	k ₃₁	0.027
4	k ₅₁	0.031	k ₃₁	0.030	k ₃₁	0.028	b	0.023	k ₂₃	0.020
5	k ₂₃	0.028	k ₂₃	0.027	k ₂₃	0.022	k ₂₃	0.020	b	0.018

^a Simulation: UCR 119J [32]. Initial conditions: [NO₂] = 0.041; [NO] = 0.301; [OLE] = 0.039; [ALK] = 0.358; [ARO] = 0.070; [ETH] = 0.043; [HCHO] = 0.038; [RCHO] = 0.023; [HONO] (assumed) = 0.0; k₁ = 0.32; simulated NO₂ real time = 200 min; [HC/NO_x]₀ = 1.7.

TABLE VII. Parameter rankings for case 5,^a large parameter variations.

Time	60 min.		120 min.		180 min.		240 min.		300 min.	
Rank	Parameter	Partial Variance	Parameter	Partial Variance	Parameter	Partial Variance	Parameter	Partial Variance	Parameter	Partial Variance
OUTPUT VARIABLE: NO ₂										
1	a	0.535	a	0.677	a	0.695	a	0.685	a	0.665
2	b	0.223	b	0.139	b	0.158	b	0.169	b	0.173
3	b	0.085	b	0.085	b	0.052	k ₅₁	0.037	k ₅₁	0.030
4	c	0.046	k ₃₁	0.038	k ₃₁	0.036	b	0.037	k ₃₁	0.030
5	b	0.041	b	0.015	k ₅₁	0.019	k ₃₁	0.033	b	0.028
OUTPUT VARIABLE: O ₃										
1	a	0.453	a	0.523	a	0.466	a	0.394	a	0.417
2	k ₅₁	0.298	k ₅₁	0.219	k ₅₁	0.198	k ₁	0.256	k ₁	0.269
3	k ₅₂	0.066	k ₁	0.097	k ₁	0.169	k ₅₁	0.150	k ₅₂	0.142
4	k ₁	0.064	k ₅₂	0.078	k ₅₂	0.112	k ₅₂	0.149	k ₅₁	0.073
5	b	0.032	b	0.037	b	0.015	k ₂₃	0.017	b	0.035
OUTPUT VARIABLE: PAN										
1	a	0.454	a	0.505	a	0.568	a	0.644	a	0.699
2	b	0.229	b	0.165	b	0.123	b	0.116	b	0.111
3	k ₅₁	0.144	k ₅₁	0.105	b	0.122	b	0.097	b	0.084
4	b	0.035	b	0.104	k ₅₁	0.083	k ₅₁	0.053	k ₃₁	0.035
5	b	0.031	k ₃₁	0.040	k ₃₁	0.042	k ₃₁	0.038	k ₅₁	0.027

^a Simulation: UCR-121J [32]. Initial conditions: [NO₂] = 0.012; [NO] = 0.044; [OLE] = 0.04; [ALK] = 0.37; [ARO] = 0.066; [ETH] = 0.042; [HCHO] = 0.06; [RCHO] = 0.011; [HONO] (assumed) = 0.0; k₁ = 0.32; simulated NO₂ peak time = 30 min; [HC/NO_x]₀ = 10.5.

TABLE VIII. Parameter rankings for case 6,^a large parameter variations.

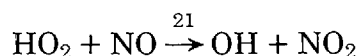
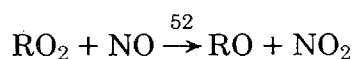
Time	60 min.		120 min.		180 min.		240 min.		300 min.	
	Parameter	Partial Variance	Parameter	Partial Variance	Parameter	Partial Variance	Parameter	Partial Variance	Parameter	Partial Variance
OUTPUT VARIABLE: NO ₂										
1	α	0.697	α	0.691	α	0.649	α	0.237	α	0.240
2	β	0.161	β	0.207	β	0.267	k_{51}	0.205	k_{51}	0.200
3	λ	0.074	k_{51}	0.047	k_{51}	0.031	k_{23}	0.119	k_{23}	0.120
4	k_{51}	0.041	λ	0.028	k_{31}	0.021	k_{31}	0.109	k_{31}	0.110
5	k_{31}	0.125	k_{31}	0.016	λ	0.020	λ	0.098	λ	0.090
OUTPUT VARIABLE: O ₃										
1	α	0.718	α	0.742	α	0.716	α	0.650	α	0.589
2	k_{51}	0.161	β	0.098	β	0.149	β	0.227	β	0.285
3	β	0.043	k_{51}	0.092	k_{51}	0.061	k_{51}	0.044	k_1	0.040
4	k_{52}	0.035	k_{52}	0.025	k_{52}	0.022	k_1	0.028	k_{51}	0.034
5	λ	0.018	k_1	0.013	k_1	0.016	k_{52}	0.019	k_{52}	0.020
OUTPUT VARIABLE: PAN										
1	k_{51}	0.280	β	0.417	β	0.495	α	0.239	α	0.230
2	λ	0.259	α	0.212	α	0.230	k_{51}	0.204	k_{51}	0.119
3	β	0.224	k_{51}	0.144	k_{51}	0.101	k_{23}	0.121	k_{23}	0.118
4	α	0.107	λ	0.130	λ	0.081	k_{31}	0.105	k_{31}	0.100
5	k_{23}	0.080	k_{23}	0.046	k_{31}	0.051	λ	0.091	λ	0.090

^a Simulation: EC-237s [32]. Initial conditions: [NO₂] = 0.021; [NO] = 0.075; [OLE] = 0.030; [ALK] = 0.298; [ARO] = 0.035; [ETH] = 0.175; [HCHO] = 0.0; [RCHO] = 0.001; [HONO] (assumed) = 0.020; k_1 = 0.30; simulated NO₂ peak time = 30 min; [HC/NO_x]₀ = 5.57.

NO₂ Behavior

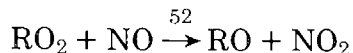
The results of the FAST sensitivity/uncertainty analyses help to point out and affirm observations about the qualitative aspects of the chemical mechanism and also provide some new insight into the essential features of the system. The ranking of those parameters to which the predictions of NO₂ behavior are most sensitive highlights the most important of the many mechanisms by which NO₂ is produced. In all the small parameter variation cases, the parameters dominating NO₂ behavior around the time of the NO₂ peak are the photolysis rate, k_1 , and the nitric acid formation step. Before and after the predicted peak time, variations in the rates of those reactions forming peroxy radicals, especially the aldehyde photolysis rates, have the most marked effect. In the simulation with the high hydrocarbon to NO_x ratio (case 2), the production of RO₂ and HO₂ from the ozone-olefin reaction is also important.

As discussed earlier, peroxy radicals act to convert NO to NO₂ by



Hence, the rate constants associated with the above reactions, as well as the quantities of RO_2 and HO_2 available, should have a distinct effect on NO_2 concentration levels. The fact that aldehyde photolysis, alkoxyl radical decomposition, and ozone-olefin reactions all produce peroxy radicals explains the large partial variances associated with these parameters. Relative to competing reactions, small variations in k_{52} , the RO_2 -NO rate constant, do not produce a large effect on NO_2 predictions. The reason for this is that the RO_2 -NO rate constant is so large that other reactions cannot effectively compete for RO_2 .

The differences in chemistry brought about by changes in initial conditions are evident from a close examination of the outcome of the larger parameter variation studies, cases 4-6. When the initial hydrocarbon to NO_x ratio is low (case 4), α , the fraction of times that HO_2 is produced from RO, makes the largest contribution to variations in NO_2 predictions. Where initial HC/NO_x levels were higher (case 5), uncertainties in ozone-olefin product distribution and in the production of aldehydes from alkoxyl radicals also contributed significant variances. In systems where initial HC/NO_x ratios are small, or in which fairly unreactive species comprise the hydrocarbon mix, there are not enough radicals present to convert all the available NO to NO_2 . As a result, in smog chamber experiments of these systems NO_2 peaks are broad and occur later in the test. For those initial mixtures which are richer in hydrocarbons, or contain very reactive species, there are a larger number of peroxy radicals for the NO_x in the chamber. As the fraction of time that RO_2 is produced from alkoxyl radical reactions is increased (represented by decreasing α), the number of peroxy radicals in the simulation increases. This occurs as a result of the cyclic effect of producing RO_2 from alkoxyl radical reactions and subsequent reconversion to RO through reaction with NO:



Since simulations with low initial HC/NO_x levels can be thought to be radical deficient, α varied over its entire range of uncertainty has a large influence on NO_x predictions. However, α has much less effect on cases in which the initial HC/NO_x ratio is large than when it is small, as other modes of radical production besides RO reactions occur to a significant extent in the high HC/NO_x situation.

O₃ Behavior

Much of the interest in mechanisms for photochemical smog is focused on understanding the avenues for the production of ozone. The results

of the sensitivity analyses are extremely pertinent to this understanding.

Time-varying plots of the partial variances of the major parameters affecting the production of ozone are given in Figures 3-8. As was the case for NO_2 behavior, the results are substantially different for the various initial conditions. For the higher $[\text{HC}]/[\text{NO}_x]_0$ simulations of cases 2 and 3, small variations in the NO_2 photolysis rate have the biggest impact on ozone formation. On the other hand, at times in the analysis of the low $[\text{HC}]/[\text{NO}_x]_0$ run (case 1), ozone concentrations are more influenced by peroxy radical production routes. In the large parameter variation cases α dominates the ranked list for low initial HC/NO_x ratios, whereas the other parameters in the alkoxy radical reaction and the decomposition of the peroxy nitrates are also important for high initial HC/NO_x ratios.

The effects of the parameter variations on ozone behavior can be ex-

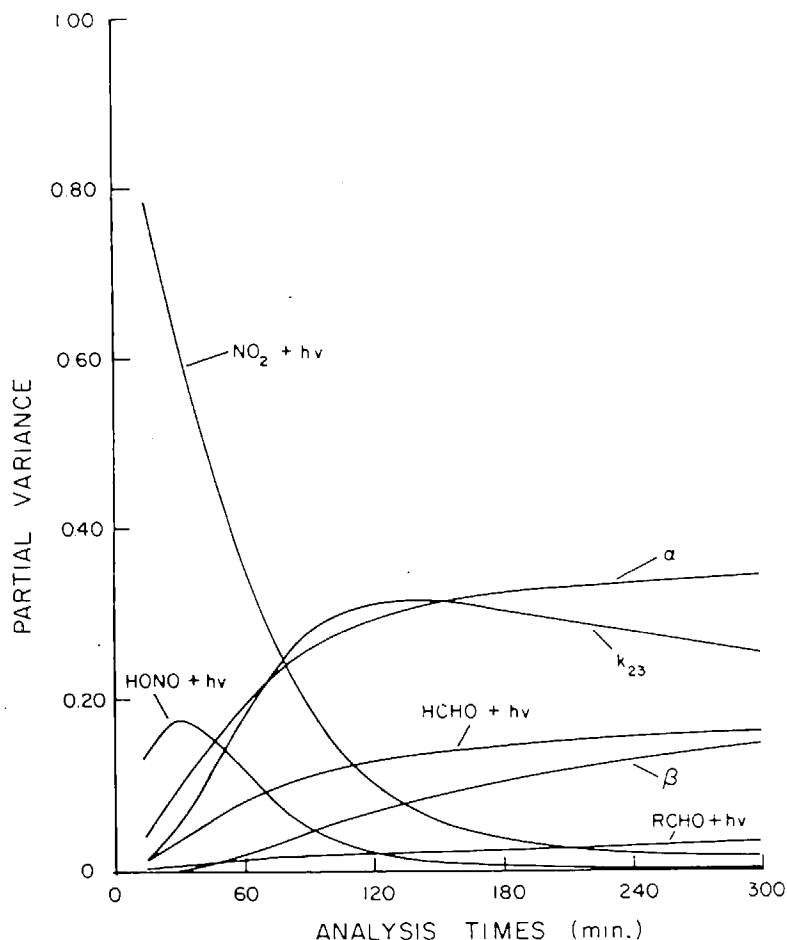


Figure 3. Time-varying partial variances of the major parameters affecting ozone for case 1 (small parameter variation).

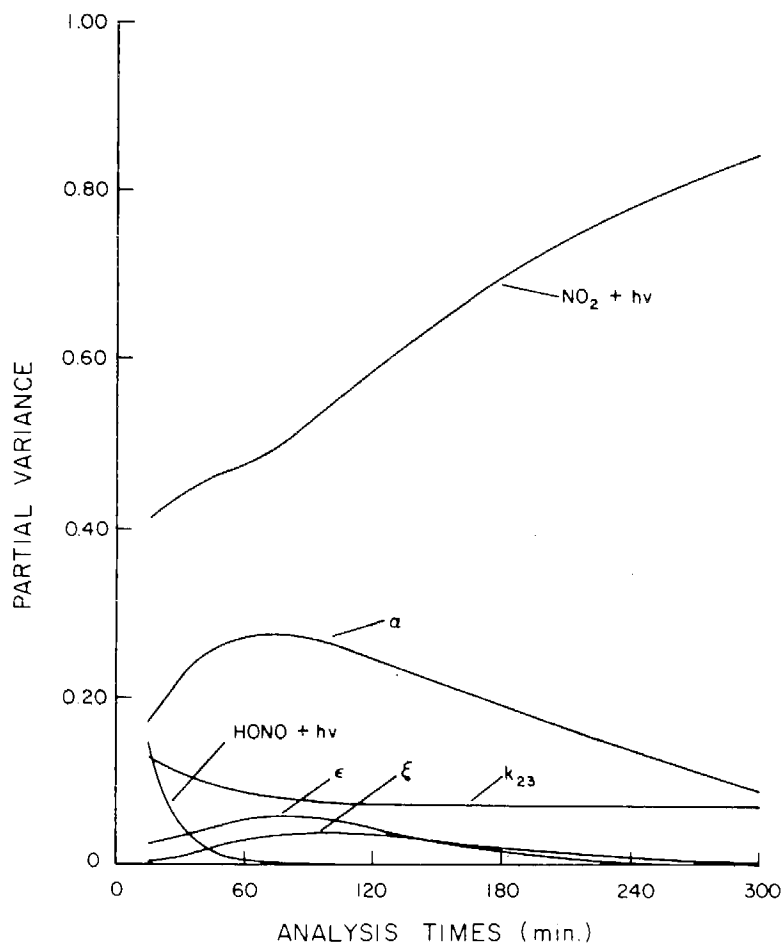


Figure 4. Time-varying partial variances of the major parameters affecting ozone for case 2 (small parameter variation).

plained in much the same fashion as the NO_2 discussion earlier. As can be seen from Figure 1, the ozone level at any time is the result of the complex interplay between NO and NO_2 , peroxy radicals, and ozone. Ozone builds up as NO is converted to NO_2 without consuming O_3 . When concentration levels of peroxy radicals are low, as in simulations with a lean initial hydrocarbon mix, reactions (1)–(3) exist in a photostationary state. As peroxy radical levels rise, however, the rates of reactions that convert NO to NO_2 without consuming O_3 become comparable to or surpass the rate of reaction (3), modifying the equilibrium set up by reactions (1)–(3). Simulations with low peroxy radical levels will therefore show a much larger sensitivity to those parameters, such as α , which substantially affect the concentrations of the peroxy radicals. When RO_2 levels are higher, as in simulations of high initial HC/NO_x mixtures, there already exists an adequate number of free radicals present to convert NO to NO_2 . Hence, the sensitivity of

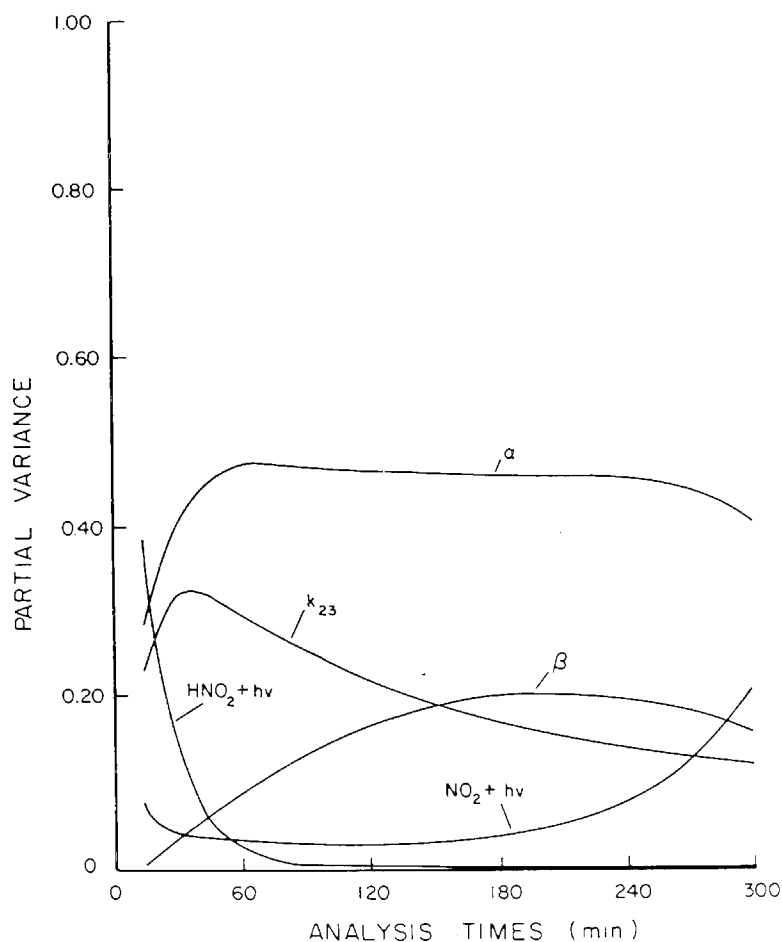


Figure 5. Time-varying partial variances of the major parameters affecting ozone for case 3 (small parameter variation).

the system lies in NO_2 photolysis rates. Moreover, in these systems, the effects of the large variation cases are divided between other parameters which affect the levels of both peroxy radicals and NO_2 .

PAN Behavior

PAN predictions are influenced by both NO_2 and RCO_3 concentration levels. Results of the sensitivity/uncertainty analysis can be explained in this light. For case 1, the parameters which highly influence the rate of PAN formation are the nitric acid formation rate constant k_{23} which directly affects the NO_2 level, and the two coefficients α and γ associated with RO decomposition which influences the concentration of RCHO. PAN is affected by RCHO levels because peroxyacyl radicals RCO_3 are formed primarily through the reaction of OH with aldehydes. RCO_3 then

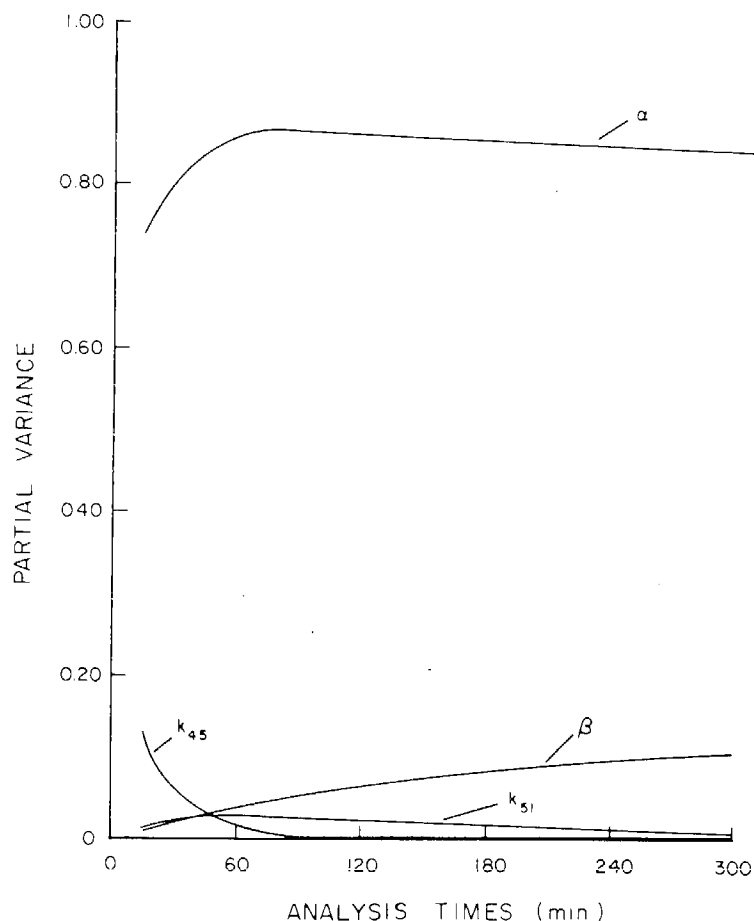


Figure 6. Time-varying partial variances of the major parameters affecting ozone for case 4 (large parameter variation).

reacts with NO_2 to form PAN through a competing reaction with NO . Thus, those parameters that affect RCO_3 production and the availability of OH radicals in the mechanism will subsequently influence PAN levels. For the small parameter variation cases 2 and 3, in which the initial HC/NO_x ratios are higher, parameters perturbing NO_2 levels are much more important in PAN production.

These results are seen even more clearly in the combined sensitivity/uncertainty analyses in cases 4–6. For the low HC/NO_x simulation, the parameters k_{23} and α have large partial variances. The same results are observed in the higher HC/NO_x cases.

Conclusions and Recommendations

Sensitivity and sensitivity/uncertainty analyses have been performed on a representative photochemical smog reaction mechanism. These

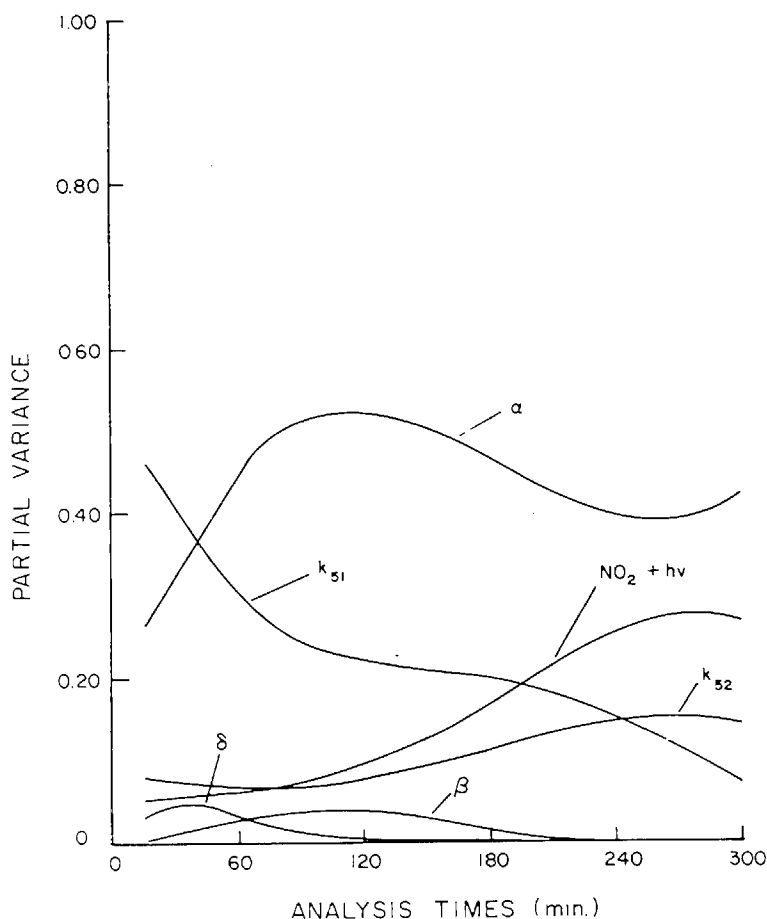


Figure 7. Time-varying partial variances of the major parameters affecting ozone for case 5 (large parameter variation).

studies have shown that the major sensitivity of the NO_2 , $\dot{\text{O}}_3$, and PAN concentrations lies in photolysis rates for NO_2 and aldehydes. On the other hand, when all parameters studied are allowed to vary over their entire ranges of uncertainty, generalized stoichiometric coefficients and certain rate constants have been shown to exert the most influence on the predictions of the mechanism.

Within present experimental uncertainties, the current mechanism for photochemical smog provides a good representation of the chemistry of the major species in the polluted troposphere as evidenced by comparisons of predicted and observed concentrations in smog chamber studies [7]. Based on the sensitivity studies presented here, the level of detail in the treatment of free radical and hydrocarbon chemistry in the mechanism seems to be consistent with the current level of understanding of these processes. However, as additional fundamental studies of alkoxy radical chemistry, shown by the sensitivity/uncertainty portion of this study to

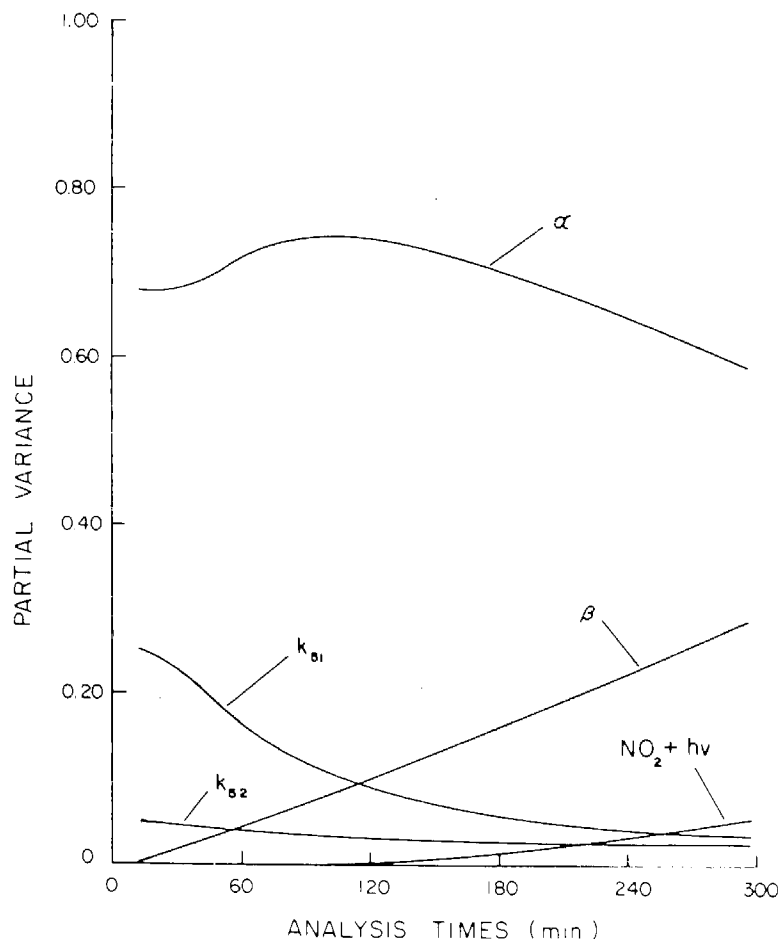


Figure 8. Time-varying partial variances of the major parameters affecting ozone for case 6 (large parameter variation).

be highly important in the reaction network, are carried out, a more highly resolved radical lumping procedure than is used here may be necessary to improve the accuracy of the mechanism. In addition, when a detailed reaction mechanism for aromatic compounds becomes available, lumped aromatic reaction steps will undoubtedly need to be refined. Because no investigation into the role of aromatics has been attempted in this work, little can be said about the effects such improvements would have on the overall predictions.

In summary, based on these findings, we recommend that experimental work in atmospheric chemistry be concentrated in the following areas:

- (a) Studies of decomposition, isomerization, and O_2 reaction pathways of alkoxy and hydroxyalkoxy radicals
- (b) Improvements in knowledge of the spectral distribution and level

of actinic irradiance for both atmospheric studies and smog chamber experiments

(c) Better measurements of quantum yields and absorption cross sections for aldehydes

and, less importantly, that work be done on:

(d) Olefin-ozone product distributions, needed for accurately modeling systems in which olefins comprise a large fraction of the hydrocarbon mix

(e) Determination of rate parameters associated with the formation and decomposition of peroxy nitrates

(f) Determination of emission levels and routine atmospheric measurements of aldehydes, because of their pronounced influence on radical concentrations.

Acknowledgment

This work was supported by the Environmental Protection Agency under grant R805537. Computational resources were provided by the California Air Resources Board under contract A7-187-30. Comments and assistance by Dr. Marcia Dodge and Dr. James Tilden are gratefully appreciated.

Bibliography

- [1] T. E. Graedel, L. A. Farrow, and T. A. Weber, *Atmos. Environ.*, **10**, 1095 (1976).
- [2] G. Z. Whitten and H. Hogo, "Mathematical Modeling of Simulated Photochemical Smog," Environmental Protection Agency Rep. EPA-600/3-77-011, 1977.
- [3] A. C. Baldwin, J. R. Barker, D. M. Golden, and D. G. Hendry, *J. Phys. Chem.*, **81**, 2483 (1977).
- [4] W. P. Carter, A. C. Lloyd, J. L. Sprung, and J. N. Pitts, Jr., *Int. J. Chem. Kinet.*, **11**, 45 (1979).
- [5] R. J. Gelinas and P. D. Skewes-Cox, *J. Phys. Chem.*, **81**, 2468 (1977).
- [6] J. R. Martinez, K. T. Tran, A. C. Lloyd, and G. M. Hidy, "Development of an Atmospheric Model for Sulphate Formation," Environmental Research and Technology, Inc., 1977, Doc. P-1534.
- [7] A. H. Falls and J. H. Seinfeld, *Environ. Sci. Technol.*, **12**, 1398 (1978).
- [8] M. C. Dodge and T. A. Hecht, *Int. J. Chem. Kinet.*, **1**, 155 (1975).
- [9] T. A. Hecht, J. H. Seinfeld, and M. C. Dodge, *Environ. Sci. Technol.*, **8**, 327 (1974).
- [10] R. I. Cukier, H. B. Levine, and K. E. Shuler, *J. Comp. Phys.*, **26**, 1 (1978).
- [11] M. Koda, G. J. McRae, and J. H. Seinfeld, *Int. J. Chem. Kinet.*, **11**, 427 (1979).
- [12] R. J. Hampson, Jr., and D. Garvin, "Reaction Rate and Photochemical Data for Atmospheric Chemistry—1977," NBS Special Rep. Publ. 513, National Bureau of Standards, Washington, DC, 1978.
- [13] R. A. Graham and H. S. Johnston, *J. Phys. Chem.*, **82**, 254 (1978).
- [14] R. A. Graham, A. M. Winer, and J. N. Pitts, Jr., *Chem. Phys. Lett.*, **51**, 215 (1977).
- [15] R. A. Graham, A. M. Winer, and J. N. Pitts, Jr., *J. Chem. Phys.*, **68**, 4505 (1978).
- [16] A. C. Lloyd, Workshop on Chemical Kinetic Data Needs for Modeling the Lower Troposphere, Environmental Protection Agency and National Bureau of Standards, Reston, VA, May 15–17, 1978.

- [17] G. J. McRae, W. R. Goodin, and J. H. Seinfeld, "Development of a Second Generation Mathematical Model of Photochemical Air Pollution," California Air Resources Board, contract A5-046-87, Final Rep. 1979.
- [18] L. Batt, R. D. McCulloch, and R. T. Milne, *Int. J. Chem. Kinet.*, **S1**, 441 (1975).
- [19] G. Mendenhall, D. M. Golden, and S. W. Benson, *Int. J. Chem. Kinet.*, **7**, 725 (1975).
- [20] L. Batt and R. T. Milne, *Int. J. Chem. Kinet.*, **8**, 59 (1976).
- [21] H. A. Wiebe, A. Villa, T. M. Hillman, and J. Hecklen, *J. Am. Chem. Soc.*, **95**, 7 (1975).
- [22] G. Baker and R. Shaw, *J. Chem. Soc. (London)*, 6965 (1965).
- [23] J. R. Barker, S. W. Benson, and D. M. Golden, *Int. J. Chem. Kinet.*, **9**, 31 (1977).
- [24] R. Simonaitis and J. Hecklen, *J. Phys. Chem.*, **78**, 2417 (1974).
- [25] R. A. Cox and M. J. Roffey, *Environ. Sci. Technol.*, **11**, 382 (1977).
- [26] K. L. Schere and K. L. Demerjian, "Calculation of Selected Photolytic Rate Constants over a Diurnal Range," Environmental Protection Agency Rep. EPA-600/4-77-015, 1977.
- [27] H. E. O'Neal and C. Blumstein, *Int. J. Chem. Kinet.*, **5**, 397 (1973).
- [28] M. C. Dodge, Workshop on Chemical Kinetic Data Needs for Modeling the Lower Troposphere, Environmental Protection Agency and National Bureau of Standards, Reston, VA, May 15-17, 1978.
- [29] R. A. Perry, R. Atkinson, and J. N. Pitts, Jr., *J. Phys. Chem.*, **81**, 296 (1977).
- [30] D. G. Hendry, Workshop on Chemical Kinetic Data Needs for Modeling the Lower Troposphere, Environmental Protection Agency and National Bureau of Standards, Reston, VA, May 15-17, 1978.
- [31] D. G. Hendry and R. A. Kenley, *J. Am. Chem. Soc.*, **99**, 3198 (1977).
- [32] K. R. Darnall, W. P. L. Carter, A. M. Winer, A. C. Lloyd, and J. N. Pitts, Jr., *J. Phys. Chem.*, **80**, 1948 (1976).
- [33] J. N. Pitts, Jr., A. M. Winer, K. R. Darnall, G. J. Doyle, and J. M. McAfee, "Chemical Consequences of Air Quality Standards and of Control Implementation Programs: Roles of Hydrocarbons, Oxides of Nitrogen and Aged Smog in the Production of Photochemical Oxidant," California Air Resources Board, contract 4-214, Final Rep., 1976.
- [34] A. M. Winer, personal communication, 1978.
- [35] J. G. Calvert and R. D. McQuigg, *Int. J. Chem. Kinet.*, **S1**, 113 (1975).
- [36] A. M. Winer, personal communication, 1978.
- [37] M. C. Dodge, personal communication, 1979.
- [38] C. J. Hochenadel, J. A. Ghormley, J. W. Boyle, and P. J. Ogren, *J. Phys. Chem.*, **81**, 3 (1977).

Received September 12, 1978

Revised May 25, 1979

Accepted June 5, 1979

10.7 Conclusions

Because of the complex nature of the planetary boundary layer an integral element of any air quality modeling study should be a formal assessment of the effects of uncertainties in the parameterization of the physical processes. In this chapter a variety of methods for performing such sensitivity analyses have been discussed. Particular attention was given to Fourier Amplitude Sensitivity Test (FAST). Unlike conventional methods the FAST procedure is ideally suited to the task of examining the global sensitivity of nonlinear mathematical models. The reason for this is that the technique allows arbitrarily large variations in either system parameters or input variables. This characteristic was exploited in two practical applications involving components of the atmospheric diffusion equation.

CHAPTER 11

EVALUATION OF MODEL PERFORMANCE

11.1 Introduction

Previous Chapters of this study described the formulation and testing of the individual components of the atmospheric diffusion equation. The most critical test however, is the ability of the system as a whole to satisfactorily describe the concentration dynamics occurring in an airshed. This Chapter presents an assessment of the model performance when applied to one urban region, the South Coast Air Basin of Southern California. The particular period to be studied, for which detailed emissions and meteorological information have been assembled, is 26-27 June 1974.

11.2 Performance Evaluation of the Airshed Model

There are three steps that need to be undertaken when evaluating the performance of a model: (1) A basic assessment of model validity; (2) comparison of predictions and observations for past events; and (3) analysis of the sensitivities of the predictions to uncertainties in model components.

Model validity refers to the essential correctness of the model in terms of its representation of the basic chemistry and physics as well as to its accuracy of numerical implementation as measured by adherence to certain necessary conditions such as conservation of mass.

Discrepancies in validity arise as a consequence of the need to employ simplifying assumptions during the mathematical formulation. As the model described in previous chapters was developed, each component, advection and turbulent diffusion, chemical kinetics, emissions and surface removal, was formulated taking into account the latest relevant data and information (Table 11.1). In each section of the report an attempt has been made to test individual model components in a manner that would assess the validity of the basic representation of the atmospheric physics and chemistry. Every effort has been made to include as much state-of-the-art information as possible, and, given the present generation of computing capabilities, the model represents the most valid practical one for an accurate description of urban air pollution.

Most emphasis in model performance evaluation has traditionally been given to step (2), comparison of predictions and observations for past events. Usually it is impossible to ascertain whether discrepancies between predictions and observations are due to errors in input data, such as emissions inventories, or in the representation of the basic physical and chemical processes. While it is imperative to separate the influences of these uncertainties, the practical problems associated with obtaining the necessary emissions and meteorological information virtually precludes a definitive assessment of the formal validity of a model using field data. Nevertheless, comparisons of predictions and observations for past events is probably the crucial component of the model evaluation. If the test conditions are to be

TABLE 11.1

Summary of Model Components, Their Input Data Requirements and Testing Procedures

MODEL COMPONENT	DETAILED ELEMENTS AND INPUT DATA	TESTING PROCEDURES (REFERENCES REPORTING DETAILED RESULTS)
Chemical Kinetics	Reaction mechanism Photolytic rate constants Thermochemical rate constants Hydrocarbon lumping procedures	The chemical mechanism was evaluated by comparing its predictions against data obtained from carefully controlled smog chamber studies. In addition, the mechanism was subjected to a detailed sensitivity analysis that examined the effects of uncertainties in rate constants and stoichiometric coefficients (Falls et al., 1979). The procedures for generating photolytic rate constants were tested against field measurements of NO ₂ dissociation rates (McRae et al., 1982a).
Meteorology	Deposition velocities Mixing height Relative humidity Three-dimensional wind field Temperature Topography Turbulent diffusivities Solar insolation Surface roughness Ultraviolet flux	Much of the basic data used in the model is derived from sparse and discrete ground level observations. The objective analysis procedures that are used to interpolate the data were tested against analytic problems and observed concentration distributions of tracer gases (Goodin et al., 1979a,b, 1981; McRae et al., 1981 and McRae, 1981). Predicted turbulent mixing rates, under convective conditions, were compared against field experiments (McRae et al., 1981). Estimates of surface removal rates, derived from the deposition module, were compared against field and laboratory data.
Numerical Integration Procedures	Solution of advection-diffusion equation for chemically reactive flows Initial and boundary conditions	Problems with known solutions and properties similar to conditions encountered in the atmosphere were used to test the basic numerical technique. In addition, simplified numerical schemes were compared against more detailed approaches (McRae et al., 1982b). The computational procedures were tested for numerical stability, convergence, and mass conservation.

representative of those occurring in an actual airshed then it is important to recognize that the data collection requirements can involve an enormous expenditure of time and resources. Some of the needed information is summarized in Table 11.2. The present chapter is devoted, in large part, to an assessment of the application of the model in reproducing the important features of a two-day smog episode in the South Coast Air Basin (SCAB) of Southern California. This basin, in many respects, is the ideal one for evaluating the performance of an urban model since it has considerable variations in meteorology and emission flux densities and has the most persistently severe photochemical air pollution in the world.

One way to attempt to understand the causes of discrepancies between predictions and observations is to analyze the model to determine to what input parameters and variables the model is most sensitive. When combined with estimates of the levels of uncertainty associated with each input parameter and variable, this analysis, a so-called sensitivity analysis, will indicate how much of the overall uncertainty of the model output is associated with the individual uncertainty in each model input. Then the overall estimated uncertainty in the model predictions can be compared with the differences between predictions and observations in specific applications. Chapter 10, for example, presents the results from a sensitivity analysis of the kinetic mechanism. There have recently been several studies of the sensitivity of photochemical air quality models to input parameter variations or uncertainties (Falls et al., 1979; Dunker, 1980, 1981;

TABLE 11.2
 Summary of Input Data Needed to Carry Out
 A Model Performance Evaluation Study

BASIC INPUT	DETAILED COMPONENTS	RELEVANT CHAPTERS
Meteorology	Three dimensional wind field Mixing depth Topography and surface roughness Turbulent diffusion coefficients Solar insolation Ultraviolet radiation Temperature Relative humidity	3,4,6
Chemical Kinetics	Reaction mechanism Reaction rate constants Reaction stoichiometry Surface deposition velocities Hydrocarbon lumping procedure	6,8
Air Quality Data	Initial and boundary conditions Verification data	3
Emission Inventory	Mobile sources Stationary sources Area sources	7

Seigneur et al., 1981; Tilden and Seinfeld, 1982). These studies, although carried out on models somewhat different from that under analysis here, do indicate the variables to which large photochemical models are most sensitive. Rather than repeating these calculations in this chapter, relevant results from these earlier studies will be cited where appropriate. One aspect of the input uncertainty question did, however, appear to warrant consideration, that of assessing the accuracy of the emissions inventory. For this reason a new technique for evaluating the influence of errors in individual source categories on the overall inventory is presented.

11.3 Definition of the Region of Interest

The SCAB boundaries are shown in Figure 11.1. The grid system origin can be defined accurately on the Universal Transverse Merator (UTM) system. For the present study the origin is located in UTM zone 11 at E 560 km and N 3680 km. The region extends 400 km in a westerly (x) direction and 160 km north (y). The lower right hand corner was chosen for the origin because of the UTM zone change 60 km inside the western border of the modeling region. For the purposes of locating sources, the region has been further subdivided into 5x5 km cells. Once the grid system has been established then it is possible to process much of the model input data. for example, Figure 11.2 is a perspective view of the topography of the South Coast Air Basin. This information is needed for the wind field generation procedures. Extensive use was made of these three-dimensional displays to check data consistency and orientation.

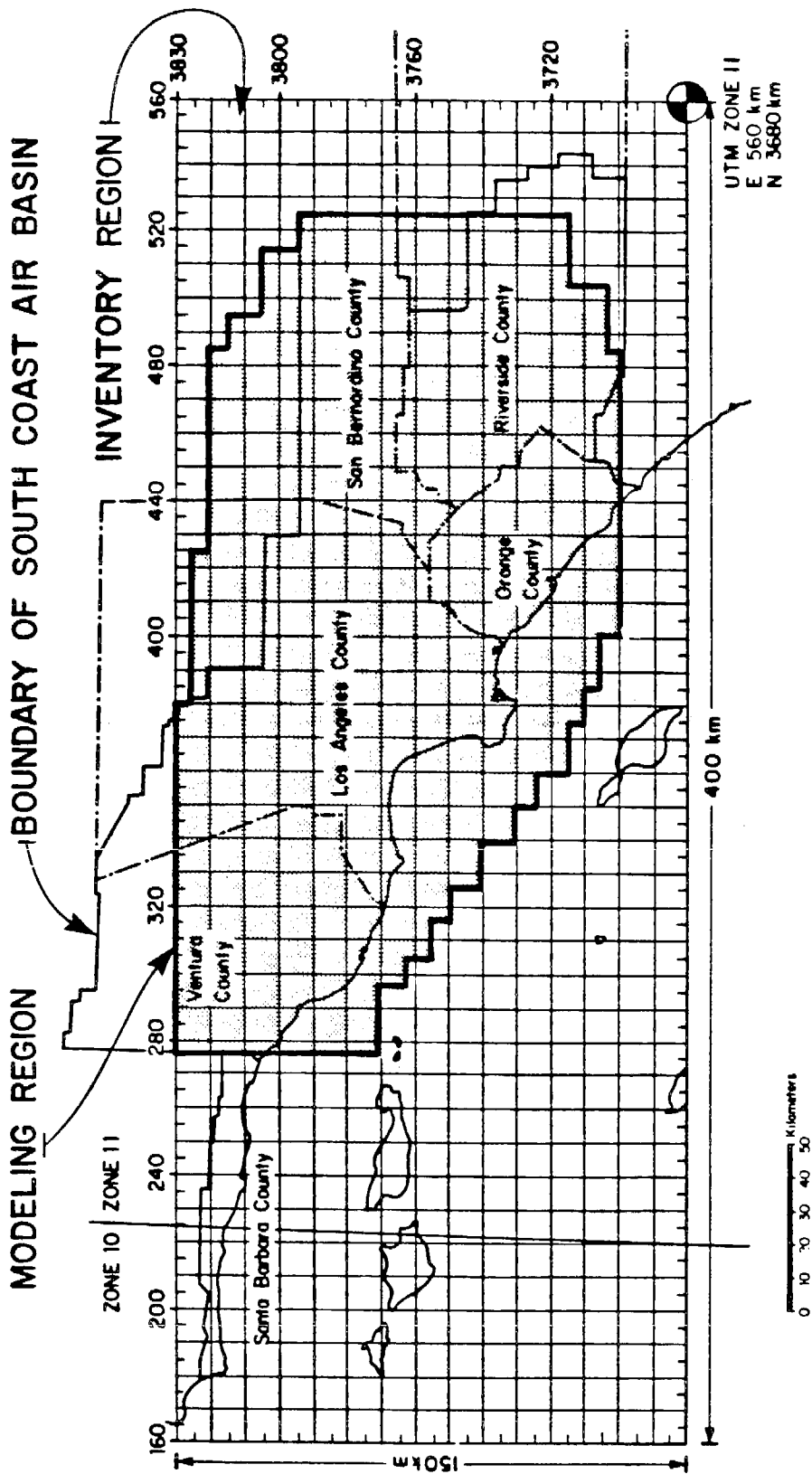


FIGURE 11.1

Definition of Computational Grid System Over the South Coast Air Basin
 The shaded portion corresponds to the area used
 in the model performance evaluation.

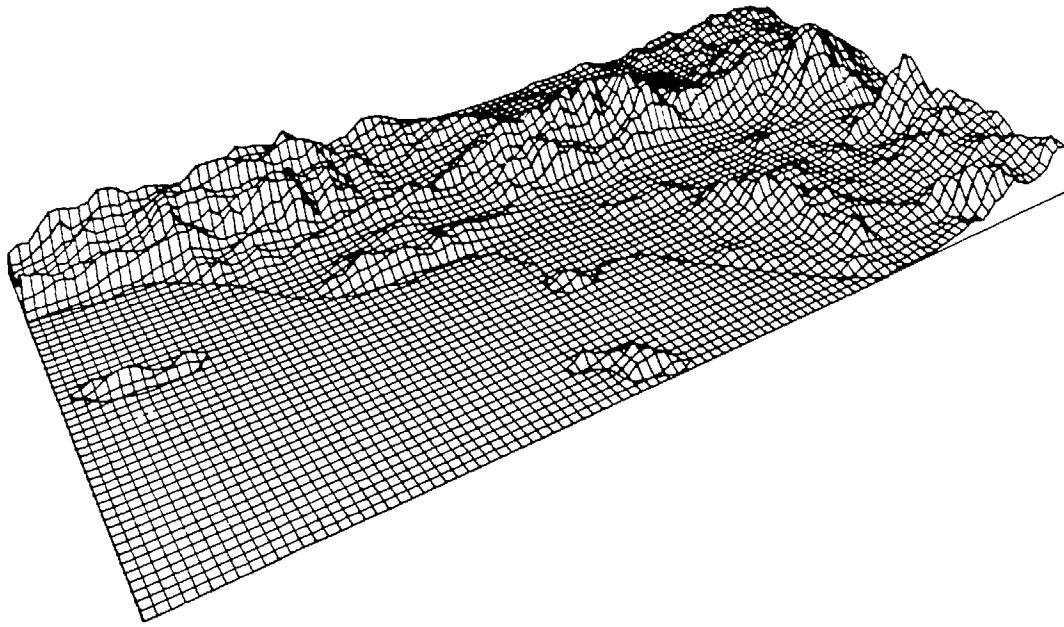


FIGURE 11.2

Perspective View of the Topography of the
South Coast Air Basin. (Vertical Scale 1:10)

11.4 The Episode of 26-28 June 1974 in the South Coast Air Basin

During the week of 26-28 June 1974, a severe air pollution episode was experienced in the South Coast Air Basin of California (CARB, 1974a). Hourly averaged ozone concentrations reached 0.50 ppm in the Upland-Fontana area, and values above 0.35 ppm were reported at 10 other stations. During the period 23-28 June, 1974 wind speeds were considerably lower than normal. (Radiosonde data from Pt. Mugu indicated that the wind speeds averaged about 1.6 m s^{-1} between the surface and 750 mb height; the normal June averaged is about 4.2 m s^{-1} .) At El Monte, the maximum depth of the mixed layer was approximately 750 m on each of the days 26-27 June. This value is unseasonably low. Temperatures between the 300 and 900 m levels reached 30°C during 27 and 28 June, while the surface temperatures dropped as low as 15°C during the night. The intense nocturnal inversion was caused partly by subsidence and partly by radiation from the surface since the dry air aloft kept the sky cloudless (CARB, 1974b). In summary, the low wind speeds, high temperatures and low inversion base produced conditions conducive to the accumulation of precursor emissions, and in turn, to the production of high ozone levels. These high ozone levels provide a stringent test of the ability of the model to reproduce extreme events. Another important reason for choosing the 1974 period was that detailed emissions inventories, commissioned by the State of California Air Resources Board, were available for that year.